

# **Carbon Nanotubes as Near Infrared Laser Susceptors**

**Amir A. Bahrami**  
**Gonville & Caius College**

**This thesis is submitted for the degree of Doctor of Philosophy  
(PhD)**



**Department of Materials Science and Metallurgy**  
**University of Cambridge**

## **Declaration**

The work submitted for the degree of Doctor of Philosophy in this thesis is the result of research carried out in the Department of Materials Science and Metallurgy, University of Cambridge and The Welding Institute in Abington, Cambridge, between October 2006 and June 2010, under the supervision of Prof. Alan H. Windle, *FRS*. No part of this thesis has been submitted for a degree or any other types of qualification at this or any other University. The results described and the conclusions drawn are original except where otherwise stated and referenced. This is entirely my own work and does not include outcome of any work done through collaboration with others except where stated. In accordance with the regulations of the Degree Committee of the faculty of Physics and Chemistry, this thesis does not exceed 60,000 words in total.

Amir A Bahrami

Gonville and Caius College  
University of Cambridge

## **Acknowledgements**

First and foremost I want to thank my father Heshmat and my mother Mehri Bahrami for their love, support and encouragement throughout my life including during the course of preparing for this PhD degree.

However, writing this dissertation has involved exploring new areas, understanding of which would have been impossible without the freely given assistance of colleagues. Firstly I would like to thank my supervisor Prof. Alan Windle for his advice and guidance during the course of this research and all of the people in the macromolecular group for the stimulating discussions.

Furthermore I would like to thank TWI for allowing me the time and freedom of using unique equipment and facilities to conduct this research. I would particularly like to thank Dr Reza Razmjoo for his continuous support and encouragement and Dr Roger Wise my industrial supervisor for his guidance. Also special thanks go to Miss Aurelie Brun of TWI for her help in setting up the welding trials.

I am eternally grateful to the Royal Commission for the Exhibition of 1851 for funding the project and being supportive in all aspects of this research particularly the secretary of the commission Mr. Malcolm Shirley, and Miss Jenifer Parkyn, the commission's senior administrator.

Last but not least I thank my wife Shaz, and son Adam, for their love and support during the course of preparing this thesis and their incredible patience with my much reduced participation in family activities during the course of this time.

## **Abstract**

The coupling efficiency of carbon nanotubes with near infrared laser radiation at 940nm wavelength was investigated. Nanotubes treated with different post processing methods were irradiated at different laser power intensities as dry samples and suspensions in water or ethanol. The interaction with the laser beam was measured and quantified based on the temperature increase in the samples as well as the amount of energy transmitted through them. Parallel experiments using carbon black revealed better performance of carbon nanotubes in terms of coupling efficiency and heat dissipation to their surroundings. It was found that most of the incident radiation on an individual carbon nanotube is absorbed, resulting in extreme local temperature increases proportional to the laser intensity, which can lead to instant tube oxidation in air. Such high thermal energies are efficiently transferred to the material in immediate contact with the nanotubes, increasing its temperature very rapidly. The most intriguing results were obtained in the presence of water where the observations suggested, disintegration of carbon nanotubes with each laser pulse. It is shown that extremely high local temperatures vaporise the water in the immediate vicinity of a carbon nanotube and result in a water-gas reaction. It is further postulated that such effects can be achieved with laser beams at power intensities near the skin tissue's safe exposure thresholds, and therefore can potentially be used as a method of removing nanotubes from living tissue. This has advantages in providing an exit route for nanotubes whether introduced on purpose for reasons of medicine or therapy, or possibly, as a result of inadvertent exposure. Further studies on laser heating and transmission through different dry samples, highlighted that more crystalline structures such as that of a heat-treated nanotube, are more effective in causing extinction of the laser beam and a reduction in the transmitted beam intensity, however the tubes with more defects or with a length comparable to the radiation wavelength are very effective in converting the absorbed laser energy to heat. This effect is exacerbated when the laser beam is polarised parallel to the long axis of the carbon nanotubes. These heating effects were exploited to create welds in high density polyethylene using through transmission laser welding. The resultant welds showed better than or equal mechanical performance to welds made using industrial absorbers such as carbon black or Clearweld®.

## Contents

Declaration.....	I
Acknowledgements.....	II
Abstract.....	III
Contents.....	IV
Nomenclature.....	VII
List of abbreviations.....	VII
Roman letter symbols.....	VII
Greek letter symbols.....	VIII
<b>1.</b> Introduction.....	1
<b>1.1.</b> Motivation.....	1
<b>1.2.</b> Thesis structure and scope.....	4
<b>2.</b> Literature survey.....	7
<b>2.1.</b> Near Infrared radiation and its interaction with materials.....	7
<b>2.1.1.</b> Atomic response to photon absorption.....	10
<b>2.1.2.</b> Electronic absorption processes.....	15
<b>2.1.2.1.</b> Electronic absorption of light in metals.....	16
<b>2.1.2.2.</b> Electronic absorption of light in non-metals.....	17
<b>2.1.3.</b> Non-linear absorption.....	17
<b>2.1.3.1.</b> Two photon absorption.....	17
<b>2.1.3.2.</b> Carrier excitation.....	18
<b>2.1.4.</b> Electron-phonon coupling and lattice heating.....	20
<b>2.1.5.</b> Simultaneous treatment of photons electrons and phonons.....	21
<b>2.2.</b> Carbon nanotubes, their structure and optical properties.....	25
<b>2.2.1.</b> Structure of carbon nanotubes.....	25
<b>2.2.2.</b> Synthesis of carbon nanotubes.....	27
<b>2.2.3.</b> Electronic structure of carbon nanotubes.....	28
<b>2.2.4.</b> Phonon modes in carbon nanotubes.....	30
<b>2.2.5.</b> Optical properties of carbon nanotubes.....	30
<b>2.2.5.1.</b> Raman spectra of carbon nanotubes.....	30
<b>2.2.5.2.</b> Infrared absorption by carbon nanotubes.....	32
<b>2.2.5.3.</b> Optical limiting properties of carbon nanotubes.....	35
<b>2.2.5.4.</b> Plasmons in carbon nanotubes.....	36
<b>2.2.5.5.</b> Laser induced structural changes in carbon nanotubes.....	38
<b>2.3.</b> Summary.....	40
<b>3.</b> Carbon nanotube synthesis, treatment & characterisation.....	43
<b>3.1.</b> Carbon nanotube production, using a chemical vapour deposition method.....	43
<b>3.2.</b> Post synthesis treatments of carbon nanotubes.....	46
<b>3.2.1.</b> Ball milling.....	46
<b>3.2.2.</b> Heat treatment.....	46
<b>3.2.3.</b> Acid treatment.....	47
<b>3.3.</b> Charaterisation of as-produced and treated carbon nanotube.....	48
<b>3.3.1.</b> SEM.....	48
<b>3.3.2.</b> TEM.....	58
<b>3.3.3.</b> Raman spectroscopy.....	60
<b>3.3.4.</b> FTIR.....	63

3.3.5.	Differential scanning calorimetric analysis .....	66
3.3.6.	Thermogravimetric analysis in air and helium .....	67
3.4.	Modulated Thermogravimetric Analysis in water-saturated helium .....	73
3.4.1.	Experimental set up.....	73
3.4.2.	Results and analysis .....	75
3.4.3.	Summary .....	80
4.	Laser induced water-gas reaction in carbon nanotube-water suspensions.....	83
4.1.	Setting limits for laser source properties and exposure times.....	83
4.1.1.	Photo-thermal cancer therapy using nanostructures .....	84
4.1.2.	Safe exposure limits to near infrared laser radiation for the skin .....	86
4.2.	Modelling the heating and water-gas reaction of a single carbon nanotube in a pool of water .....	88
4.2.1.	Nukiyama's boiling curve.....	89
4.2.2.	Film boiling on a carbon nanotube heating element.....	90
4.2.3.	Laser energy requirements and pulse times .....	96
4.2.4.	The diffusion of the generated heat to the surrounding tissue .....	98
4.3.	Multiple pulse laser transmission experimental set up .....	99
4.4.	Removing carbon nanotubes from water suspensions in between layers of bacon.....	109
4.4.1.	Experimental set up.....	109
4.4.2.	Results and analysis .....	110
4.5.	Summary .....	112
5.	Laser absorption and heating of carbon nanotubes.....	114
5.1.	Laser transmission through water and ethanol suspensions .....	114
5.1.1.	Laser transmission experimental set up .....	115
5.1.2.	Water and ethanol suspensions transmission results and analysis.....	115
5.2.	Laser heating and transmission through dry samples .....	118
5.2.1.	Sample types .....	118
5.2.2.	Laser heating experimental set up.....	119
5.2.3.	Results of heating and time dependent saturation for samples with random orientation using a non-polarised laser beam.....	122
5.2.4.	Results of heating and time dependent saturation for samples with polarised light at different orientations.....	125
5.2.5.	Measuring intensity saturation in heat treated carbon nanotubes .....	129
5.2.6.	Laser transmission experimental set up .....	130
5.2.7.	Transmission results.....	130
5.3.	Correlation between absorption and temperature increase with Raman characteristics.....	134
5.4.	Summary .....	137
6.	Through transmission laser welding of high density polyethylene using carbon nanotubes .....	140
6.1.	Laser welding of plastics .....	140
6.2.	Factors affecting laser light absorption and scattering by polymers.....	142
6.2.1.	Relationship between polymer type/crystallinity and laser wavelength.....	142
6.2.2.	Temperature .....	143
6.2.3.	Laser intensity and transmission.....	143
6.3.	Calculating welding parameters.....	144

<b>6.3.1.</b>	Absorber requirements.....	144
<b>6.3.2.</b>	Weld temperature and melt depth calculations.....	149
<b>6.4.</b>	Sample preparation .....	153
<b>6.4.1.</b>	Heating and transmission specimen preparation.....	155
<b>6.4.2.</b>	Weld sample preparation .....	156
<b>6.4.2.1.</b>	Lap shear testing of the welded specimens.....	157
<b>6.5.</b>	Transmission measurements through HDPE specimens.....	158
<b>6.6.</b>	Heating of HDPE specimens .....	159
<b>6.7.</b>	Initial welding trials .....	162
<b>6.7.1.</b>	Microscope images of the initial welds .....	165
<b>6.8.</b>	Design of experiments .....	167
<b>6.8.1.</b>	Lap shear test results.....	168
<b>6.8.2.</b>	Melt depth .....	173
<b>6.8.3.</b>	Scanning electron microscopy .....	178
<b>6.9.</b>	Summary .....	184
<b>6.10.</b>	Outlook .....	192
	References.....	194

## Nomenclature

### List of abbreviations

ACNT	Acid treated multi wall carbon nanotubes
AHCNT	Heat treated and then acid treated multi wall carbon nanotubes
BCNT	Ball-milled multiwall carbon nanotubes
CB	Carbon black
CNTs	Carbon nanotubes
CVD	Chemical vapour deposition
CW	Clearweld®
DoE	Design of experiments
DoS	Density of state
DWNT	Double-wall carbon nanotubes
FCA	Free carrier absorption
HBCNT	Ball milled and then heat treated multiwall carbon nanotubes
HCNT	Heat treated multiwall carbon nanotube carpets
HDPE	High density polyethylene
HCNT	Heat treated carbon nanotubes
IR	Infrared
LTM	Laser transmission measurement
MDSC	Modulated differential scanning calorimetric analysis
MFB	Minimum film boiling
MS	Mass spectroscopy
MTGA	Modulated thermo-gravimetric-analysis
MWCNTs	Multiwall carbon nanotubes
NIR	Near Infrared
RBM	Radial breathing mode
SCNT	Multiwall carbon nanotube carpets
SWNTs	Single wall carbon nanotubes
TTLW	Through transmission laser welding
WCNT	Multiwall carbon nanotubes synthesised on the quartz furnace tube

### Roman letter symbols

$A_f$	Absorption fraction
$B_{12}$	Einstein absorption coefficient
$B_{21}$	Einstein stimulated emission coefficient
$C$	Speed of light ( $\text{m s}^{-1}$ )
$C_{pL}$	Water's specific heat ( $\text{J kg}^{-1} \text{K}^{-1}$ )

E	Electron charge (C)
H	Planck's constant ( $\text{J s}^{-1}$ )
$h_{LG}$	Water's latent heat of vaporization ( $\text{J kg}^{-1}$ )
I	Beam intensity ( $\text{W cm}^{-2}$ )
$J_e$	Current density of electrons ( $\text{A m}^{-2}$ )
K	Wave vector
$k_B$	Boltzmann constant ( $\text{J atom}^{-1} \text{K}^{-1}$ )
$m_e$	Electron mass (kg)
P	Power (W)
q	Momentum ( $\text{kg m s}^{-1}$ )
$Q_c$	Heat loss through conduction (W)
$Q_r$	Heat loss through radiation (W)
$r_{nuc}$	Nucleation radius (m)
$R_f$	Reflection fraction
$T_f$	Transmission fraction
V	Volume ( $\text{m}^3$ )
$V_G$	Steam specific volume ( $\text{m}^3 \text{kg}^{-1}$ )
$V_L$	Water specific volume ( $\text{m}^3 \text{kg}^{-1}$ )
$v_e$	Electron velocity ( $\text{m s}^{-1}$ )
X	Thermal diffusivity ( $\text{m}^2 \text{s}^{-1}$ )
Z	Distance travelled by light (thickness) through the material (m)

### Greek letter symbols

$\alpha$	Absorption coefficient ( $\text{cm}^{-1}$ )
$\beta$	Mass extinction coefficient ( $\text{m}^2 \text{kg}^{-1}$ )
$\varepsilon$	Dielectric function ( $\text{F m}^{-1}$ )
$\varepsilon_0$	Permittivity of a vacuum ( $\text{F m}^{-1}$ )
$\gamma$	Thermal conductivity ( $\text{W m}^{-1} \text{K}^{-1}$ )
$\gamma_G$	Thermal conductivity of steam ( $\text{W m}^{-1} \text{K}^{-1}$ )
$\lambda$	Wavelength (m)
$\mu$	Light scattering coefficient of skin ( $\text{cm}^{-1}$ )
$\sigma$	Electrical conductivity ( $\text{S m}^{-1}$ )
$\sigma_{SB}$	Stephan–Boltzmann constant ( $\text{W m}^{-2} \text{K}^{-4}$ )
$\tau$	Average collision time interval ( $\text{s}^{-1}$ )
$\nu$	Frequency ( $\text{s}^{-1}$ )
$\nu_p$	Plasma frequency ( $\text{s}^{-1}$ )
$\nu_s$	Scattered photon frequency ( $\text{s}^{-1}$ )
$\psi$	Surface tension of water ( $\text{N m}^{-1}$ )

## **1. Introduction**

Carbon nanotubes (CNTs) are molecular-scale carbon fibres and can be thought of as one or many graphene (a single layer of graphite) sheets rolled into single, or multi-concentric cylinders. Their dimensions and properties have attracted an unprecedented amount of research efforts and funding, most of which are aimed at realising their potential in everyday life applications. CNTs are exceptionally black [1] and highly efficient light absorbers. The light absorption factor per graphene layer has been estimated to be 2.3% [2], which means that for multiwall tubes containing greater than 50 concentric tubes, most of the incident light is absorbed and mainly converted to heat. Indeed the consequences of exposing CNTs to radiant energy such as that from a domestic photographic flash have been known for a number of years, with the instantaneous combustion of CNTs when close to a flash gun first being reported by Ajayan et al [3].

This project seeks to lay down the underlying science of using carbon nanotubes as near infrared (NIR) laser energy absorbers. The efficiency of these structures in absorbing the NIR electromagnetic radiation energy will be measured and quantified based on the resultant temperature change and the amount of the incident laser energy transmitted through the sample. These responses will be determined as a function of multiwall carbon nanotube (MWCNT) type, alignment, mass and sample thickness as well as the incident power intensity of the radiation. This provides the basis for exploitation of their embodied properties in downloading energy into predefined regions of targeted structures. The domains of this principle are examined across two specific and distinctively different applications: one is understanding the conditions and energy intensities required for instant disintegration of MWCNTs from aqueous environments such as that of a living tissue and the other, is evaluating the performance of MWCNTs as laser absorbers used in through transmission laser welding (TTLW) of thermoplastics, specifically high density polyethylene (HDPE).

### **1.1. Motivation**

One of the areas of interest and research concerning CNTs is their potential application in the medical field, particularly as diagnostic or therapeutic tools for cancer and

subcutaneous tumours [4, 5, 6, 7]. CNTs are thought to have the potential for use as minimally invasive therapeutics with minimal adverse effects on the patients' quality of life [8 and 9]. However, there is a paradoxical and rising concern on potential health hazards and toxicity of these materials [10, 11, 12]. A prominent concern is based on the parallels drawn between CNTs and asbestos due to the high aspect ratio and stiffness of CNT fibres [13, 14]. Whatever the outcome of the current debate amongst toxicologists, if nanotubes, or indeed nanoparticles in general, have entered human tissue whether intentionally for therapeutic reasons or due to inadvertent exposure, it will be of vital importance to have a fast and minimally invasive method of removal for these materials from the body.

Here a method is proposed, coupled with experimental verification of the principle, for the remote removal of MWCNTs from aqueous environments, including soft tissue, using pulses of NIR laser radiation at 940nm wavelength (photon energy of  $2.12 \times 10^{-19}$  J or 1.32 eV) as human tissue and water are least absorbent in this wavelength as will be discussed in section 4.1. This can be achieved if a localised water-gas reaction can be stimulated at an acceptable laser wavelength, intensity and exposure times for human skin tissue.

The water-gas reaction is a process in which a carbon source can be converted into a 1:1 mixture of carbon monoxide and hydrogen through reaction with water vapour [15].



In industry, water is blown through hot coke and the resulting gas is called water gas, which is a mixture of hydrogen (H<sub>2</sub>, 50%), carbon monoxide (CO, 40%), carbon dioxide (CO<sub>2</sub>, 5%), nitrogen and methane (N<sub>2</sub> + CH<sub>4</sub>, 5%). This reaction is endothermic with activation energy of 80kJ mol<sup>-1</sup> [16], which means that the coke cools down during the reaction therefore energy is constantly supplied during the reaction to keep the coal hot. It is thought that the amounts of the carbon monoxide and hydrogen produced as a result of the reaction of small amounts of carbon nanotubes with water, are small and therefore are easily dispersed and removed from the tissue with minimum risk of asphyxia [17].

Another prominent area of research concerning CNTs is the production of nanocomposites, which have better thermal and electrical conductivity and structural strength over virgin polymer materials [18]. An area, which is related to this topic and has been somewhat over looked, is the potential use of CNTs in laser welding of thermoplastics. There is very little published work directly related to the use of carbon nanotubes as a multifunctional material for through transmission laser welding of plastics. There have been some references made to the use of microwave radiation and CNTs for melting of polymers [19], however the reported work does not explore the potential for welding of plastics. There is very little, and only recent, work published on the use of lasers for joining carbon nanocomposites [20], however this report specifies the use of nanocarbon at high concentrations (10 wt%) with dimensions much closer to that of carbon black (which has been used for a long time as an absorber of laser radiation for purposes of heating and welding plastics) than fibrous CNTs.

MWCNTs have absorption bands in the NIR, where the absorption of most thermoplastic polymers are low and, if dispersed in the part further from the laser, they will absorb large fractions of the irradiated energy at the joint interface. Their efficient coupling to the incident radiation and subsequent temperature increase means that they do not require large amounts of laser energy or high concentrations to heat the polymeric substrates above their melting point and create a weld under appropriate amounts of pressure (e.g. clamping pressure applied during a welding process). This means that through transmission laser welding (TTLW) of semi-crystalline thermoplastics, through which most of the incident laser radiation is scattered by the crystallites and, only a fraction reaches the weld interface, is possible with only small concentration of MWCNTs at the joint. The tubes' high thermal conductivity would enable uniform and rapid heat transfer into the centre of the weld line, resulting in a strong joint with sufficient melt depth. In addition, the presence of these fibres with very high aspect ratios ( $>10^5$ ) and mechanical strength, could enhance the integrity of the welded joint through tube entanglement and fibre reinforcement at the interface. Here the mechanical integrity of laser welds made in HDPE substrates are evaluated and compared with those prepared using conventional absorbers such as carbon black (CB) and Clearweld® (CW) absorber.

## **1.2. Thesis structure and scope**

A report summarising and evaluating the accessed published literature is given in Chapter 2. In the first instance, a review on the nature of electromagnetic radiation and the principles of its interaction with materials is explained. This is further expanded to the structure, properties and characteristics of CNTs, their optical properties and interaction with laser radiation, particularly in the NIR region. Following this, and as described in Chapter 3, MWCNTs were produced using a chemical vapour deposition (CVD) process. Some of the produced MWCNTs were then treated using different methods to either change their dimensions (e.g. shorten their length through ball milling) and crystallinity (e.g. via heat treatment) or to improve their dispersion properties in matrices such as water or ethanol (e.g. via acid treatment and functionalisation). The resultant MWCNTs (both treated and as produced) were then characterised using a scanning electron microscope (SEM) to determine their appearance and dimensions, including length and diameter. The SEM was coupled with chemical analysis in some cases, to qualitatively identify the elements present on the surface of the tubes. A transmission electron microscope (TEM) was used to get a better view of the structure of the as-produced MWCNT sample. The samples were analysed using Raman spectroscopy to identify any characteristic structural and vibrational modes and how these vary for MWCNTs that have been subjected to different treatment processes. Fourier transform infrared spectroscopy (FTIR) analysis was also used to evaluate the absorption properties of MWCNTs in the IR spectrum and how these vary with different treatment methods. Thermogravimetric analysis (TGA) was used to identify the oxidation temperature in air for different samples and how this is affected by different post production treatments as well as providing a semi-quantitative measure of the amount of remnant catalyst impurities such as iron and iron oxide in different samples. TGA in an inert, dry helium environment coupled with mass spectroscopy (MS) was used to identify the evolving gas species, to see any oxidation effects of adsorbed contamination such as oxygen, carbon dioxide or trapped water at high temperatures. Finally, modulated differential scanning calorimetric analysis (MDSC) was used to provide a quantitative value of the specific heat capacity of different samples.

Tests were then conducted in a water-saturated helium environment using a modulated TGA (MTGA) method coupled with MS to identify the evolved gasses. This was done to ensure that water-gas reaction does take place between MWCNTs and water vapour and also to measure the activation energy for such a reaction to further verify the energy balance calculations.

Chapter 4 is focused on the theoretical and practical feasibility of removing carbon nanotubes from aqueous environments by using a NIR laser radiation source. This includes an initial literature review on the interaction of lasers with living tissue in medical applications and identifies the limits of allowable energy intensities and wavelengths. This is then followed by a theoretical analysis of removing a single MWCNT from a pool of water and calculations of the associated laser intensity needed and the energy balance considering the heat loss to the surroundings. After the required amount of energy is calculated and compared with allowable exposure limits to the skin, suitable pulse duration to deliver this energy was identified. Incremental increases in transmission of multiple pulses of laser radiation were measured through 0.1wt% water suspensions of MWCNTs. These were compared with experimental results under the same conditions for suspensions in ethanol to ensure that the observed increase in transmission was unique to water suspensions and due to the water-gas disintegration of CNTs. A proof of concept was then demonstrated by removing MWCNTs from water suspensions in between layers of bacon.

Chapter 5 further examines both, the laser absorption of the nanotube samples in dry form and as suspensions in water or ethanol. Laser transmission trials were conducted to evaluate and compare the optical properties of different suspensions. In addition, the dry samples were tested for their heating and absorption behaviour, taking into account the effects of fibre orientation and light polarisation. The results of Chapter 5 were then used to identify the material type used for the laser welding trials that are reported in chapter 6.

Chapter 6 initially describes the TTLW of polymers and factors influencing this process. Combinations of practical results and theoretical calculations are then conducted to estimate the amount of MWCNT absorber that is needed for welding of HDPE, the

possible melt depth and weld temperatures. The results of initial trials on absorber application to the welding interface and the consequent impact on the specimen preparation are briefly described. Heating and transmission through thin specimens are reported and then the final welding trials are described, together with the subsequent lap-shear-tensile test results. The weld integrity achieved using MWCNTs is compared with that achieved with CB or CW using identical welding parameters. Microtome sections of the produced welds are also compared under transmission optical microscopy, while the failed surfaces of the tensile test specimens are examined using SEM.

The work carried out in the thesis and the results are then concluded in Chapter 7, with highlights of the significant findings and a brief discussion on future work and possible next steps. Finally, the bibliographic list of all the referenced published literature is given at the end of this thesis.

## **2. Literature survey**

This chapter begins with a review of NIR radiation and how electromagnetic radiation of this or similar wavelengths interact with different materials. A more detailed description of absorption mechanisms of photons is then given trying to consolidate the different processes responsible for optical heating of materials particularly those with a metallic, electronic structure. Physical, electronic and vibrational structures of CNTs are then reviewed with specific attention to their effects on optical absorption and properties of CNTs. A report of the surveyed published literature is then given concerning interaction of the laser and other light sources at or close to NIR wavelength with carbon nanotubes. This provides a basic understanding of the mechanisms responsible for laser light absorption and subsequent heating of CNTs and how this affects the CNTs structure and their interaction with the surroundings. This made the basis for a series of experimental work and an associated specific literature search, which is reported in subsequent chapters.

### **2.1. Near Infrared radiation and its interaction with materials**

In the classic sense and as described by Maxwell, electromagnetic radiation is considered to be wave-like, consisting of electric and magnetic field components that are perpendicular to each other and to the propagation direction. Such radiations are created by oscillatory electric charges, and the frequency of oscillation and its wavelength provides a method of dividing the electromagnetic radiation spectrum into different regions. Infrared (IR) radiation covers a range of wavelengths from 0.750  $\mu\text{m}$  to 1000  $\mu\text{m}$  and spreads in between visible light and microwave frequencies. As illustrated in Figure 1, this region is divided into three sections; near, mid and far IR. The region of main interest in this study is the NIR, because as will be discussed later, both skin and most thermoplastics have a window of minimum absorption in this range, which would provide an advantage in laser removal of CNTs with minimum tissue absorption and TTLW of thermoplastics with minimum scattering of light by the samples to be welded.

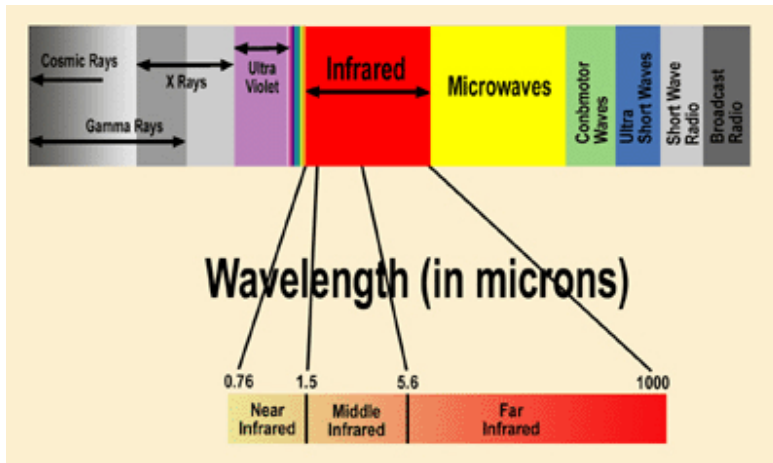


**Figure 1, the wavelength span of the infrared region of the electromagnetic radiation spectrum [21].**

In general when a beam of electromagnetic radiation is incident on a material's surface it can be reflected, transmitted or absorbed by the material. The main factor determining the type of interaction is the energy of the incident radiation, which is determined by the amount of energy carried in small packets known as photons which in turn are dependent on the radiation frequency via Planck's equation, shown below:

$$E = h\nu \quad (2)$$

Where E is energy (J), h is Planck's constant ( $6.63 \times 10^{-34} \text{ Js}^{-1}$  or  $4.13 \times 10^{-15} \text{ eVs}^{-1}$  [22] ) and  $\nu$  is the radiation frequency ( $\text{s}^{-1}$ ).

Radiation absorption is the main mechanism leading to beam heating of a material. The far-IR region has photons with low frequencies, which can be absorbed by the rotational motions of molecules which also have low frequencies. The mid-IR couples with the fundamental vibrations and associated rotational-vibrational structures, whilst the higher energy NIR can interact with electrons, either through electron cloud polarisation (for bound electrons) or electronic excitation (for free electrons), as well as some high frequency phonons [22].

The increase in electrons' oscillation due to the radiation electric field, causes the incident wave's intensity to decrease, so the wave travels more slowly in the material. The material property which determines the phase velocity of a wave travelling through

it, is the refractive index, denoted by  $n$ . The imaginary part of the refractive index,  $\beta$ , is known as the extinction coefficient and determines the attenuation of the wave along the propagation direction, while travelling through the material. This extinction is contributed to by both; scattering of light by defects, inclusions etc, as it traverses the material and absorption of light by the material. The scattering process is not necessarily inelastic, which means that it does not always contribute to energy transfer from the light beam to the material, whereas the absorption process is always inelastic and draws energy out of the beam and into the material. If  $I_0$  ( $\text{Wcm}^{-2}$ ) is the intensity of the incident light at the material surface, then the intensity  $I$  ( $\text{Wcm}^{-2}$ ) at depth  $z$ , inside the material, is given by:

$$I(z) = I_0(1 - R)\exp^{-\alpha z} \quad (3)$$

Where  $\alpha$  is the absorption coefficient ( $\text{cm}^{-1}$ ) and governs the spatial change of the beam and  $R$  is the reflectivity coefficient.

The external field is periodically changing its direction resulting in an electric field being produced by the oscillating electrons, which re-radiate their kinetic energy, unless they undergo frequent collisions with the atoms. This re-radiation of energy is a cause of reflection.  $R$  and  $\alpha$  are related to  $n$  (refractive index) and  $\beta$  (extinction coefficient) by:

$$R = \frac{(n - 1)^2 + \beta^2}{(n + 1)^2 + \beta^2} \quad (4)$$

$$\alpha = \frac{4\pi\nu\beta}{c} = \frac{4\pi\beta}{\lambda} \quad (5)$$

Where  $\lambda$  is the wavelength of the radiation.

Both sets of parameters,  $n$  and  $\beta$  or  $R$  and  $\alpha$  are equivalent in describing a material's optical properties and they all depend on the incident wave's frequency. Sometimes due to the fluctuation in density of atoms (e.g. thermal motion in solids) the incident light beam intensity is reduced without absorption, this extinction of the incident light by atoms is called Rayleigh scattering.

### 2.1.1. Atomic response to photon absorption

The simple first order explanation of the interaction of atoms with photons was made by Einstein. No explicit quantum mechanics was used in Einstein's theory except that the atomic energy levels were assumed discrete, and it was convenient (not necessary) to regard the electromagnetic radiation as quantised to photons. Considering thermal equilibrium within a material, the three Einstein coefficients, namely; stimulated absorption, stimulated emission and simultaneous emission govern the transitions between the different energy levels when the material is exposed to an external radiation source [23].

Considering low photon intensities and, an atom in state  $N_1$  with energy  $E_1$  in absorbing a quantum of radiation energy moves to the excited state  $N_2$  with energy  $E_2$  ( $B_{12}$ ). The atom can then return to its initial state by either stimulated emission ( $B_{21}$ ), which has the same phase properties as the incident light, or spontaneous emission ( $A_{21}$ ), which is coherent with the incident light but out of phase (random) and therefore causes scattering of the incident light and attenuation of the beam [24].

The absorption coefficient  $\alpha$  has units of 1/length and  $\alpha z$  gives the fraction of intensity absorbed for a light beam at frequency  $\nu$  while traveling distance  $z$  through the material. Figure 2 shows a schematic of absorption of a photon ( $B_{12}$ ) and the resultant spontaneous and stimulated emissions.

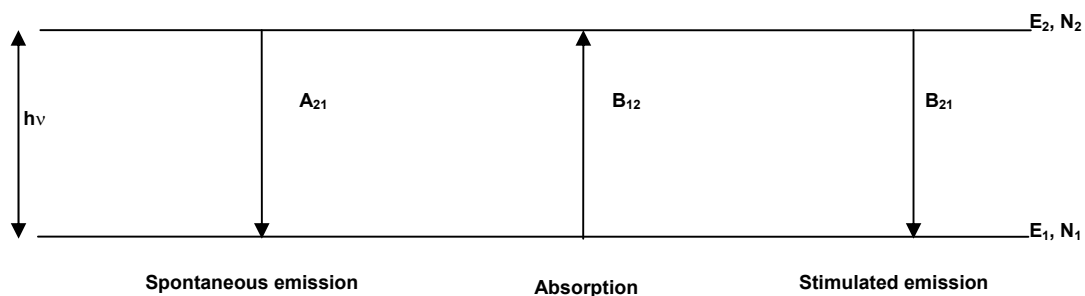


Figure 2, schematic of atomic energy levels and the transition between them.  $B_{12}$  denotes the absorption process, when an atom from state  $N_1$  with energy  $E_1$  absorbs a quantum of energy and moves to state  $N_2$  with energy  $E_2$ .  $A_{21}$  and  $B_{21}$  denote the relaxation processes for the atom due to; spontaneous and stimulated emissions respectively.

The spontaneous emission coefficient gives the probability per unit time that an electron in state 2 with energy  $E_2$  will decay spontaneously to state 1 with energy  $E_1$ , emitting a photon with an energy  $E_2 - E_1 = h\nu$ . The change in the number density of atoms in state 1 per unit time due to spontaneous emission will be:

$$\left(\frac{dn_1}{dt}\right)_{A21} = A_{21}n_2 \quad (6)$$

The stimulated emission coefficient gives the probability per unit time per unit spectral radiance of the radiation field that an electron in state 2 with energy  $E_2$  will decay to state 1 with energy  $E_1$ , emitting a photon with an energy  $E_2 - E_1 = h\nu$ . The change in the number density of atoms in state 1 per unit time due to stimulated emission will be:

$$\left(\frac{dn_1}{dt}\right)_{B21} = B_{21}n_2I_0 \quad (7)$$

Where  $I_0$  ( $\text{Wcm}^{-2}$ ) is the radiation intensity and is defined by Planck's law as:

$$I_0 = \frac{2h\nu^3}{c^2(e^{h\nu/k_B T} - 1)} \quad (8)$$

Where  $T$  is the temperature of the material,  $K_B$  is Boltzmann's constant ( $1.38 \times 10^{-23}$  J  $\text{atom}^{-1}\text{K}^{-1}$  or  $8.62 \times 10^{-5}$  eV  $\text{atom}^{-1}\text{K}^{-1}$  [22]) and  $c$  is speed of light (approximately  $3 \times 10^8$   $\text{ms}^{-1}$  [22]).

The absorption coefficient gives the probability that an electron in state 1 with energy  $E_1$  will absorb a photon with an energy  $E_2 - E_1 = h\nu$  and jump to state 2 with energy  $E_2$ . The change in the number density of atoms in state 1 per unit time due to absorption will be:

$$\left(\frac{dn_1}{dt}\right)_{B12} = -B_{12}n_1I_0 \quad (9)$$

The number of atomic species  $n_1$  and  $n_2$  is dependent on the energy supplied by the photons ( $h\nu$ ) and the materials thermal energy ( $k_B T$ ). The ratio between the spontaneous

and stimulated emissions will be proportional to the amount of energy available and can be written as [23]:

$$\frac{A_{21}}{B_{21}I_0} = \exp^{(h\nu/k_B T)} - 1 \quad (10)$$

For radiations in the NIR frequency,  $h\nu \gg k_B T$  and therefore  $A_{21} \gg B_{21}I_0$ , as a result the spontaneous emission rate far exceeds the thermally induced emission rate. Therefore the thermal energy density can be ignored for  $\nu \geq 10^{13}$  Hz and the only contribution to emission is due to the external source. At equilibrium, the net change in the number of excited atoms is zero, as the loss and gain due to all processes are balanced.

$$A_{21}n_2 + B_{21}n_2I_0 - B_{12}n_1I_0 = 0 \quad (11)$$

If the two atomic levels are non-degenerate, as is the case in two permanent energy levels, then the two B coefficients are the same. The change in the estate population with time can therefore be written as:

$$\frac{dn_1}{dt} = -\frac{dn_2}{dt} = n_2A + (n_2 - n_1)BI_0 \quad (12)$$

Assuming light is switched on at  $t = 0$ , when all the  $n$  atoms are in the ground state and then integrating Equation 12 with respect to  $t$ , it is found that  $n_2$  depends on time as shown in Equation 13 and Figure 3.:

$$n_2 = \frac{nBI_0}{A + 2BI_0} \{1 - e^{-(A+2BI_0)t}\} \quad (13)$$

For short irradiation times, e.g.  $(A+2BI_0)t \ll 1$ , the number of excited atoms increases linearly with time  $t$  and  $n_2 = nBI_0t$  [23]. While for long irradiation times  $(A+2BI_0)t \gg 1$ , the number of excited states approaches steady state and  $n_2 = nBI_0 / (A+2BI_0)$ .

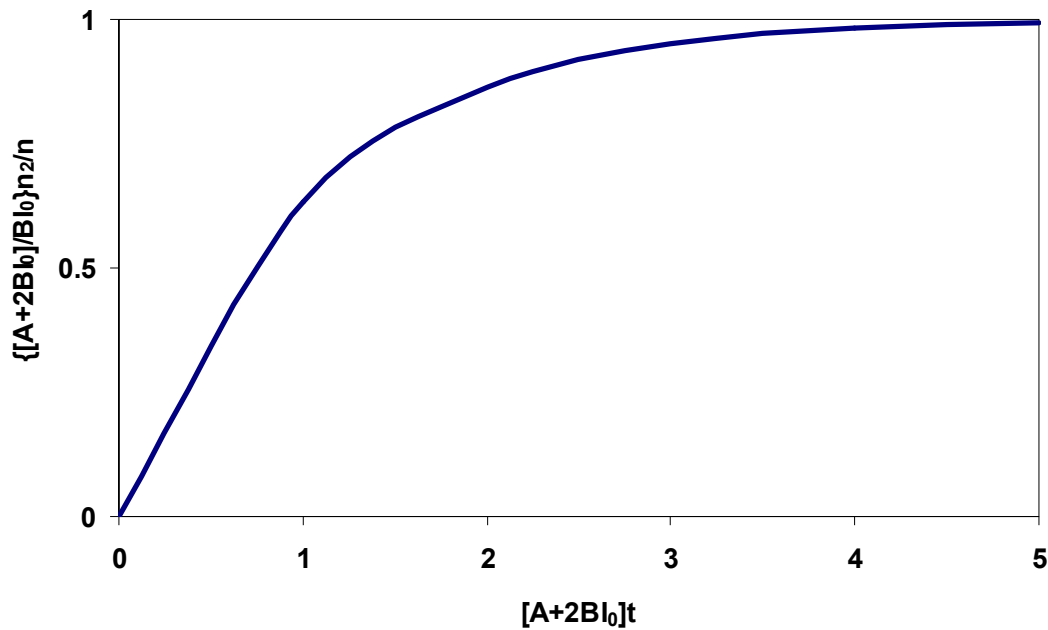


**Figure 3, change in the number of excited atoms (i.e. increase in the number of atoms in state N<sub>2</sub>) with increase in radiation exposure time for a given quantised atomic state.**

When the light is first turned on atoms are lifted into their excited states and energy is transferred from the light to the atoms. After the steady state is reached the atoms contain a constant amount of stored energy and the transfer of energy from the radiation ceases. When  $BI_0 \ll A$ ,  $n_2$  is much smaller than  $n$  and most of the atoms are in their ground state. In this case  $n_2$  is proportional to the energy density of the light beam. For powerful lasers where  $BI_0$  approaches or exceeds  $A$ , the dependence of  $n_2$  on intensity becomes non-linear and the graph of  $n_2/n$  bends over to reach  $\frac{1}{2}$  for  $BI_0 \gg A$  as shown in Figure 4. This is called the saturation of the atomic transition.  $BI_0/A \geq 1$  and is not easily achieved with conventional light sources as the light intensity required for this is very high and only a laser beam can provide it [25]. The required intensity for such a light source was estimated by Loudon [25] to be  $20\text{Wcm}^{-2}$ . This value is similar to the laser intensities used in this study as explained later and therefore a non-linear response is likely to be seen in our experiments.

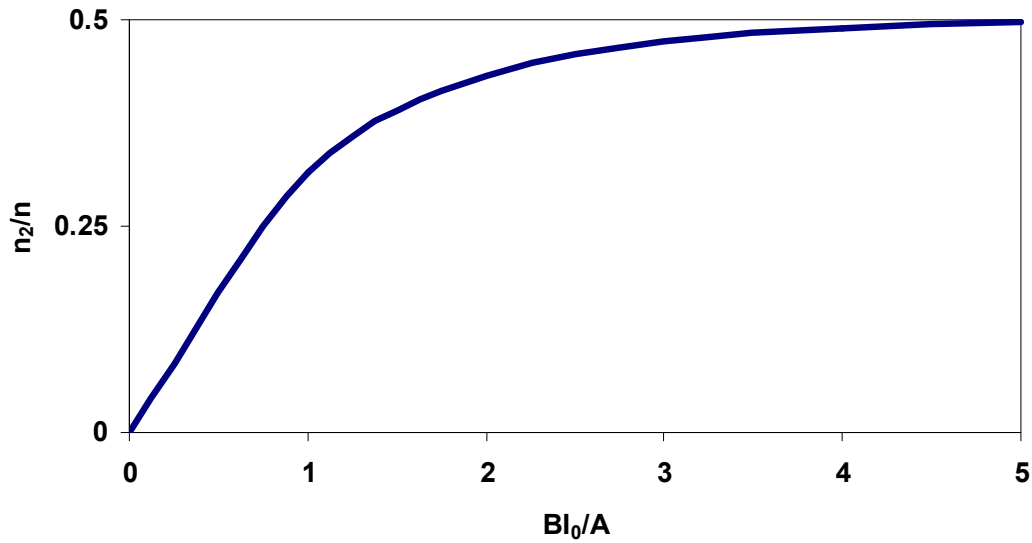


**Figure 4, change in the number of excited atoms (i.e. increase in the atomic number in state N<sub>2</sub>) with increase in radiation intensity for a given quantised atomic state.**

Now supposing significant attenuation and assuming a steady state has been reached Equation 12 can be rearranged as:

$$n_2 A = (n_2 - n_1) B I_0 \quad (14)$$

The rate of energy scatter from the beam is  $n_2 A h \nu$  and the rate of energy loss from the beam is;  $n_1 B I_0 h \nu - n_2 B I_0 h \nu$ . The laser beam intensity thus falls off linearly with distance through the material at a rate determined by the A coefficient instead of the more rapid exponential fall off determined by the B coefficient at lower intensities. The decrease in absorption as the atomic transition approaches saturation is due to the approach of the rate  $n_2 A h \nu$  of scattering energy out of the beam to its maximum value  $\frac{1}{2} n A h \nu$ . Any further increase in the beam intensity cannot lead to a proportionate increase in the scattering rate and the fractional change in  $I_0$  in traversing the material decreases [25]. The implications of this in the practical work presented in this thesis is that, when heating carbon nanotubes using a laser source a maximum intensity will exist, above which any further increase in the laser intensity will not produce a corresponding increase in the temperature of the tubes.

### 2.1.2. Electronic absorption processes

Now that a general description of interaction of an incident radiation with atoms is given the next step is to have a more specific look at the process of absorption, which is the principal reason for laser beam heating of materials.

Photon absorption for a laser with a NIR wavelength mainly occurs through the incident laser light interaction with electrons. Generally bound electrons respond only weakly to the incident electromagnetic wave and mainly affect its phase velocity, whereas free electrons are accelerated by the incident wave and extract energy from it. To understand the interaction of light with bound electrons a quasi-classical approach is used, which models a solid as a set of harmonic oscillators with resonant frequency  $\nu_0$  (Lorentz Model) [26]. Considering a bound electron in a solid irradiated by a laser beam of frequency  $\nu$ , with electric field  $E(x,t)$  and magnetic field  $H(x,t)$  the forces exerted on an electron by the magnetic field is:

$$F = e\mathbf{v} \times \frac{\mathbf{H}}{c} \quad (15)$$

Where  $\mathbf{v}$  is the electron velocity (in the order of  $10^6 \text{ ms}^{-1}$ [25]) and  $e$  is the electron charge ( $1.602 \times 10^{-19} \text{ C}$  [22]). The force exerted by the electric field is:

$$F = eE \quad (16)$$

In a light field,  $H$  and  $E$  are the same and the effect of the magnetic field is less by  $v/c$ . The velocity of an electron is 100 times less than the velocity of light, so the effect of the magnetic field is 100 times weaker and can be ignored. Therefore for monochromatic light with wavelength of  $\lambda$  over the atomic distance  $x$ , the electric field effect is [27]:

$$E(x,t) = \epsilon_0 \cos(2\pi\nu t - \frac{2\pi x}{\lambda}) \quad (17)$$

Where  $\epsilon_0$  is permittivity of a vacuum  $8.85 \times 10^{-12} \text{ farad m}^{-1}$  [22].

If the atomic dimensions are much less than  $\lambda$  (e.g. for UV, Visible, IR etc...) the phase variation within an atom can be neglected and:

$$E(x, t) = \varepsilon_0 \cos \omega t \quad (18)$$

To model the interaction of a free electron with the electric field of an electromagnetic wave, the resonant frequency of the Lorentz model should be set to zero (Drude model). Since the dominant damping mechanism for a free electron is the electron-lattice collision [28] and assuming electron lattice collision period of  $t_c$  seconds, the damping term can be written as  $1/t_c$  ( $10^{-12}$ s). The real ( $\varepsilon_1$ ) and the imaginary ( $\varepsilon_2$ ) parts of the metals' dielectric function ( $\varepsilon$ ) can then be written as [28]:

$$\varepsilon_1 = n^2 - \beta^2 = 1 - \frac{\nu_p^2 t_c^2}{1 + \nu^2 t_c^2} \quad (19)$$

$$\varepsilon_2 = 2n\beta = \frac{\nu_p^2 t_c}{\nu(1 + \nu^2 t_c^2)} \quad (20)$$

Where  $\nu_p$  is the plasma frequency and can be thought of as the frequency of the collective oscillations of all the electrons.

$$\nu_p = (N_e e^2 / m \varepsilon_0)^{1/2} \quad (21)$$

Where  $N_e$  is the electron number density.

At radiation frequency  $\nu = \nu_p$  and assuming  $\nu^2 t_c^2 \gg 1$ ,  $\varepsilon_1$  tends to zero, the phase velocity of light inside the material is infinite as all the electrons are oscillating in phase and majority of the incident light is absorbed. At  $\nu > \nu_p$  the interaction of light with electron plasma becomes weaker and the material becomes transparent. When  $\nu < \nu_p$  absorption is low and reflectivity is high and tends towards unity at long radiation wavelength.

### 2.1.2.1. Electronic absorption of light in metals

The optical properties of metals are dominated by free electrons. Vacant energy sites exist above the Fermi energy level and the upper most electrons near this level are of such low inertial mass that they can be freely excited by radiation over a wide range of frequencies. When the photon energy  $h\nu$  is comparable with the relativistic electron rest

mass energy ( $mv^2$ ) of free electrons, energy is transferred to the electron as a result of inelastic scattering of the incident photon. The scattered photon will have energy of  $h\nu_s < h\nu$ , where  $\nu_s$  is the scattered photon frequency. Photon absorption by free electrons involves absorption or emission of a phonon to conserve momentum [29].

#### **2.1.2.2. Electronic absorption of light in non-metals**

For insulators ( $E_g > 3\text{eV}$ ) and semiconductors ( $E_g < 3\text{eV}$ ), the valence band is full and separated from the conduction band by a gap. Therefore unlike metals, the absorption of the incident radiation does not happen over a wide range of frequencies, because the electrons need to jump this gap to draw energy from the incident beam [30]. Here photons can induce two kinds of electronic transitions: intraband (occurs between confined quantum states or bound to continuum states, either in the valence band or in the conduction band) and interband [28]. Band to band transitions can take place when the photon energy is comparable to the band gap. This also involves absorption or emission of a phonon to conserve momentum. If the photon energy  $h\nu$  is much less than the band gap energy ( $E_g$ ) then intraband transitions are possible (to be transparent to IR the band gap should be larger than  $0.75\text{-}1.2\ \mu\text{m}$ ), which are weak interactions and unfavourable for beam heating. When the photon energy approaches  $E_g$ , the degree of absorption increases as band to band transitions become available. For energies higher than  $E_g$  the response is similar to that of metals.

#### **2.1.3. Non-linear absorption**

At high beam intensities such as beams produced by laser radiation, there are additional mechanisms influencing the absorption of light by a material. Two particular non linear absorption mechanisms namely: two photon absorption and carrier excitation (significant for non-metals) can lead to significant lattice heating.

##### **2.1.3.1. Two photon absorption**

Under low incident beam intensities, atoms interact with light by going through one or more intermediate states and then returning to their initial states and the absorption and emission quanta have the exact same energy. The quanta are coherent and the entire process is characterised by phase memory. However if the frequency of the incident light

is such that the intermediate state coincides with a stationary state, the interaction is very strong and resonant absorption takes place [29]. If the intermediate state is not stationary, phonon emission can occur and the atom will then decay back by spontaneous radiation, no phase memory is associated with spontaneous radiation.

If the atom does not de-excite by giving off a quantum of radiation it may interact with light again and go through intermediate and final states. Here the re-emitted final light will have a frequency higher than the exciting radiation (anti-Stokes). The anti-Stokes intensity will depend on concentration of the excited atoms, photon flux and the square of the exciting intensity. For a multiphoton absorption, if both photons have the same frequency then the probability of absorption is intensity dependent. The time delay between the two participating photons can be as long as the lifetime of a photo-generated free carrier (100s of ns) [29].

The coherence property of light influences the two photon absorption. Second order coherence is a function of materials thickness ( $z$ ) and is related to the magnitude of fluctuations in the instantaneous beam intensity, each time two photon absorption takes place the change in intensity with material depth can be estimated as [29]:

$$\frac{dI}{dz} = -2Nh\nu/V\tau \quad (22)$$

Where  $\frac{dI}{dz}$  is the fluctuation in the instantaneous beam intensity over a given depth in the material,  $\tau$  is the probability per unit time that a quantum  $h\nu$  is absorbed and  $N/V$  is the number density of atoms.

### 2.1.3.2. Carrier excitation

In non-metals when a beam of photons has energy higher than  $E_g$ , excited carriers (electron-hole pairs) are generated with the rate of  $1/t_g$ . These carriers can relax via collision with the lattice or recombination, the rates of which are  $1/t_c$  ( $\sim 10^{-12} \text{ s}^{-1}$ ) and  $1/t_r$  ( $\sim 10^{-7} - 10^9 \text{ s}^{-1}$ ) respectively [28]. Electron-hole pairs can relax to the bottom of conduction band and the top of the valence band by emission of phonons, which will then

interact with other phonons and dissipate as random lattice vibration. They can recombine after phonon emission or before phonon emission although electron-phonon coupling is much faster than the recombination process.

The band to band relaxation can be radiative or non-radiative ( $10^{-6}$  to 1 s) [31]. There could also be Auger emissions where an electron hole pair releases its energy to another electron or hole pushing them to higher energy states in the band, which will then release its energy by phonon emission. (electron -electron relaxation time  $10^{-13}$  to  $10^{-14}$  s) [31].

If  $1/t_g > 1/t_r$ , significant numbers of free carriers are built up leading to optically induced free carrier absorption (FCA), therefore an absorption coefficient can be thought of as the sum of FCA and normal interband transitions. Only photons absorbed by FCA are available for instantaneous lattice heating while the energy release by interband absorption is through recombination. Above a certain threshold intensity, free carriers can have sufficient energies to cause impact ionisation and create an avalanche of free carriers, which increases the absorption coefficient by orders of magnitude.

If  $1/t_g \gg 1/t_c$ , hot carrier plasma is created before the lattice is appreciably heated. Collision of the carriers creates a thermal equilibrium between them. Recombination processes establish equilibrium between electrons and holes but do not reduce the carrier density for the duration of the laser pulse. After the pulse ends the hot carriers first collide with the lattice and then recombine. This hot plasma limits the rate of local energy deposition as it reflects the light at sufficient carrier densities (e.g.  $10^{20}$   $\text{cm}^{-3}$  for visible light) and increases the heating volume by diffusing away from the absorbing surface. FCA is dependent on the number of free carriers and the radiation intensity. Plasma formation needs high intensity, ultra-short-pulses, to result in a laser induced optical breakdown. Radiative heating of free electrons, accelerates the electrons which then collide with ions and gas phase atoms. This in turn produces more electrons and more ionisation and is a source of sample shielding

#### 2.1.4. Electron-phonon coupling and lattice heating

As a free electron is moving through the lattice, it encounters cells of uneven length due to the lattice thermal motions and it gets scattered. This leads to an irreversible exchange of energy between electrons and the lattice, which is a cause of lattice heating [28]. Many energy exchange processes such as those between electrons and phonons are intrinsically inelastic and will lead to dissipation of all or most of the energy as lattice vibrations and heat. The exchange of energy amongst photons, electrons and phonons can in principle be determined by evaluating the collision integral in the Boltzmann's transport equation [31]. This equation applies to analysis of the general currents within a system, as well as the transport coefficients and the relationships between them in a non-equilibrium state. To be able to write an equation for photons, electrons and phonons interaction based on Boltzmann's equation and understand the heating caused by a beam of light in a material microscopically, it is essential to briefly look at the scattering processes that contribute to this heat generation. The interaction of electrons with photons have already been discussed therefore the proceeding section will focus on electron-phonon scattering.

The wave function of an electron inside a crystal extends over the entire crystal but the distortion of the potential from perfect periodicity reduces the spatial extension of the wave function. However, the mean free path can still be 100s of nanometres, and could have between  $10^6$  to  $10^8$  atoms. Electrons get scattered by other electrons and by phonons. Electron-electron (e-e) interaction is weak but electron-phonon (e-ph) interaction is the main scattering process resulting in creation or annihilation of phonons.

Long wavelength acoustic phonons cover many unit cells and the atomic displacement caused by them changes the lattice constant. Transverse phonons have zero probability of scattering electrons as the product of their allowable wave vectors and displacement in the atoms is zero. So only longitudinal phonons create instantaneous variations in the lattice constant and scatter electrons [31].

Scattering of an electron in an initial state with momentum  $k$  and energy  $E$  by phonons to a new state with momentum  $k'$  and energy  $E'$  will create (-) or annihilate (+) a phonon

with momentum  $q'$ , and energy  $h\nu'$ . The conservation of energy and momentum requires that:  $E \pm h\nu = E'$  and  $k \pm q = k'$ .

### 2.1.5. Simultaneous treatment of photons electrons and phonons

It is assumed that a non-equilibrium state can be described by a non-equilibrium distribution function, which depends on time. Such a function describes how electrons or other types of particles are distributed in real and momentum space through the course of time. The Boltzmann transport equation expresses the global non-equilibrium distribution of a particle in terms of local equilibrium distributions. The equation enables application of properties of equilibrium systems to the study of a non-equilibrium system.

This equation considers one particle in a system with coordinate  $r$  and momentum  $q$ . The particle distribution function ( $f$ ) for a system of  $N$  particles where each particle has generalised coordinate  $r$  ( $x,y,z$ ) and momentum  $q$  can be written as [31]:

$$\left(\frac{\partial f}{\partial t}\right) + \frac{dr}{dt} \cdot \nabla_r f + \frac{dq}{dt} \cdot \nabla_q f = \left(\frac{\partial f}{\partial t}\right)_c \quad (23)$$

Where  $\frac{\partial f}{\partial t}$  is the particle distribution function,  $\frac{dr}{dt} \cdot \nabla_r f$  is the change in the velocity of the particle due to the external force,  $\frac{dq}{dt} \cdot \nabla_q f$  is the change in particle momentum due to the external force and  $\left(\frac{\partial f}{\partial t}\right)_c$  is the change in the particle distribution due to collision of the incoming photon.

The collision integral is thus defined as the rate of change of the distribution function, and is the change of the electron number per unit time in the phase space volume due to scattering. The right hand side of this equation lumps the interaction of one electron with the incoming photons and the left hand side is the scattering term describing the interaction of the one particle with other particles.

The energy exchange in absorption and scattering of photons by electrons, energy exchange between electrons themselves and the scattering of electrons by phonons, can

be simultaneously evaluated using Boltzmann's transport equation. At high laser intensities the inelastic rapid scattering processes dominate and as the recombination processes are a few orders of magnitude slower than electron-phonon and electron-electron scattering such processes will be ignored for the purpose of simplicity. The phonon distribution function is assumed to change only due to phonon-electron collisions and direct absorption of the laser energy by phonons is neglected. Also, only one phonon mode is considered and phonon-phonon collisions are neglected, although they are one of the main processes by which the generated heat is distributed through the bulk of the material.

The process can therefore be simplified as a free electron, absorbing energy from the laser light while the lattice remains cold. On a femto-second time scale the energy is distributed amongst the free electrons by electron-electron collisions leading to the thermal equilibrium (thermalisation) of the electron gas. By emission of phonons the electron gas cools down and although the electron-phonon collision time  $t_c$  may be as short as the electron-electron collision time the energy transfer from the hot electrons to the lattice will last much longer than the thermalisation of the electron gas due to the large mass difference of electrons and phonons [31].

The right hand side of equation 23 is the collision integral. In metals the largest contribution to photon absorption is mediated by electron-ion collisions [32]. The radiation's electric field, exerts a force on the electrons, this force alters the electron's Fermi energy ( $E_f$ ) as the electrons accelerate in the direction of the applied field ( $E_f = 1/2mv^2$ ). The external field therefore induces an electric current in the material (a detailed discussion is given by Gang [31]). This can be written as:

$$(E + \nabla E_f / e) \cdot J_e \tag{24}$$

Where  $\nabla E_f / e$ , denotes the change in the Fermi energy as an electron is accelerates under the external field.  $J_e$  is the current density of electrons, which is equal to  $\sigma E$  for metals, where  $\sigma$  is the electrical conductivity of the metal.

Only electrons close to Fermi level contribute to electrical conductivity so at light frequencies smaller than the electron lattice collisions, the electrical conductivity can be written as:

$$\sigma = (Ne^2 / m)\tau_F \quad (25)$$

Where N is the electron number density ( $m^{-3}$ ), m is electrons mass, and  $\tau_F$  is the electron-electron relaxation time at Fermi level.

This gain of electron energy under an external electric field is balanced by an increase in the electrons internal energy, the energy loss due to electron-phonon coupling and the energy loss to the heat current carried by electrons, all of which comprise the change of distribution function with time, which is the left hand side of the equation.

After the electrons are excited to energy levels above Fermi energy, they will decay and many electron-electron collisions are needed to establish another Fermi distribution. Therefore their internal energy increases with time during irradiation. This can be denoted as  $\frac{du_e}{dt}$  where  $u_e$  is the electron internal energy. Also the excited electrons will carry some of the excess energy due to the induced current as a hot electron gas carrier. This can be denoted as  $Q_e$ , which is the heat flux carried by electrons and the net flow of hot electrons is denoted as  $\nabla \cdot Q_e$  using the divergence operator  $\nabla \cdot$ . This would have a positive value, during irradiation pulse and as the pulse ends the electrons cool down and it becomes negative. In a high carrier density metal, the electronic contribution to thermal conductivity is significant and is described as below:

$$\eta_e = \frac{k_0 k_B^2 \sigma}{e^2} \quad (26)$$

Where  $\eta_e$  is the electronic thermal conductivity,  $k_0$  is a constant,  $k_B$  is the Boltzmann constant.

E-ph interactions lead to heating of the phonon gas, analogously to the cooling of the electron gas. The electron group velocity is usually much greater than the speed of sound therefore the phonon energy is negligible compared with the electron energy and the electron energy change after scattering by a phonon is small. Therefore one electron-phonon collision changes the energy of the electron gas only slightly and many electron-phonon collisions are necessary to decrease the amount of kinetic energy stored in the electron gas (20 phonons must be created for the transfer of 1eV to the lattice from carriers) [31]. In addition, e-ph interactions have an equilibration effect on the electron gas. The e-ph scattering term can therefore be written as  $G(T_e - T_p)$ , which defines the energy transfer due to e-ph coupling, where G is the coupling coefficient and at high temperatures when the electronic and phonon temperature are the same it can be written as:

$$G = \frac{\pi^2}{6} \frac{m_e v_s^2 n_e}{\tau(T_e) T_e} \quad (27)$$

Where  $m_e$  is the effective electron mass ( $9.11 \times 10^{-31}$  kg [22]),  $v_s$  is the speed of sound,  $n_e$  is the number density of the electrons, and  $\tau(T_e)$  is the electron relaxation time.

The e-ph scattering is proportional to the inverse of the phonon temperature and, under the condition of  $T_e = T_p$ ,  $\tau(T_e)$  is proportional to  $1/T_e$  [33]. The Boltzmann equation can therefore be written as [31]:

$$\frac{\partial u_e}{\partial t} + \nabla \cdot \mathbf{Q}_e - G(T_e - T_p) = (E + \nabla E_f / e) \cdot \mathbf{J}_e \quad (28)$$

Meaning that, the energy transferred to the material during laser irradiation and the resultant Joule heating is balanced by the increase in internal energy of the electrons, the heat transferred by the electron gas and the energy transferred from the excited electrons to phonons.

## 2.2. Carbon nanotubes, their structure and optical properties

### 2.2.1. Structure of carbon nanotubes

CNTs are molecular scale carbon fibres and can be thought of as a graphene sheet rolled into a cylindrical shape. They have hexagonal lattices consisting of  $sp^2$  hybridised carbon atoms, giving rise to three  $\sigma$  orbitals in one plane with one  $\pi$  orbital in a plane perpendicular to it. They can be single (SWNT), double (DWNT) or multiwall (MWCNT), having one dimensional (1D) structures with high aspect ratios. The long tubes are usually terminated by caps, which are hemispheres of a fullerene, each with six pentagons and an appropriate number of hexagons to fit the cylinder. Each individual tube exhibits spiral conformation called chirality, which is given by the chiral vector  $C_h$ . The primary symmetry of CNTs is either achiral (symmorphic) whose mirror image is the same as the original such as zigzag and armchair structures or chiral (non-symmorphic), which exhibit spiral symmetry (see Figure 5).

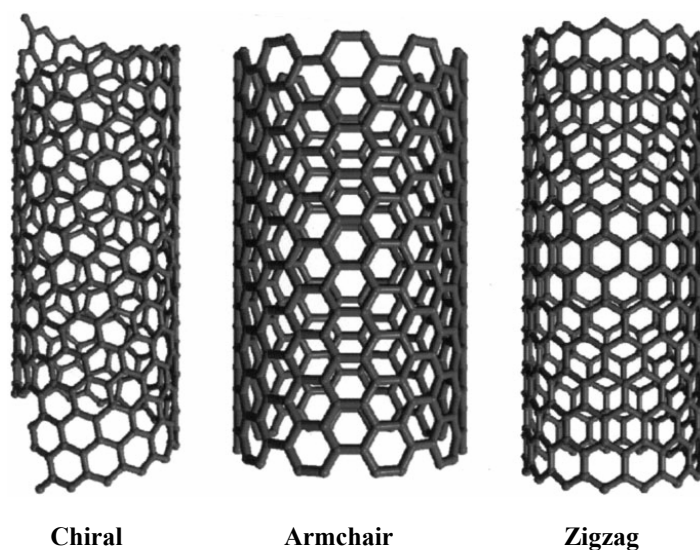


**Figure 5, schematic of different spiral conformations (chiralities) in a single wall carbon nanotube (SWNT) [34].**

The chiral structure is determined by the chiral angle ( $\theta$ ) and  $C_h$  (see Figure 6).

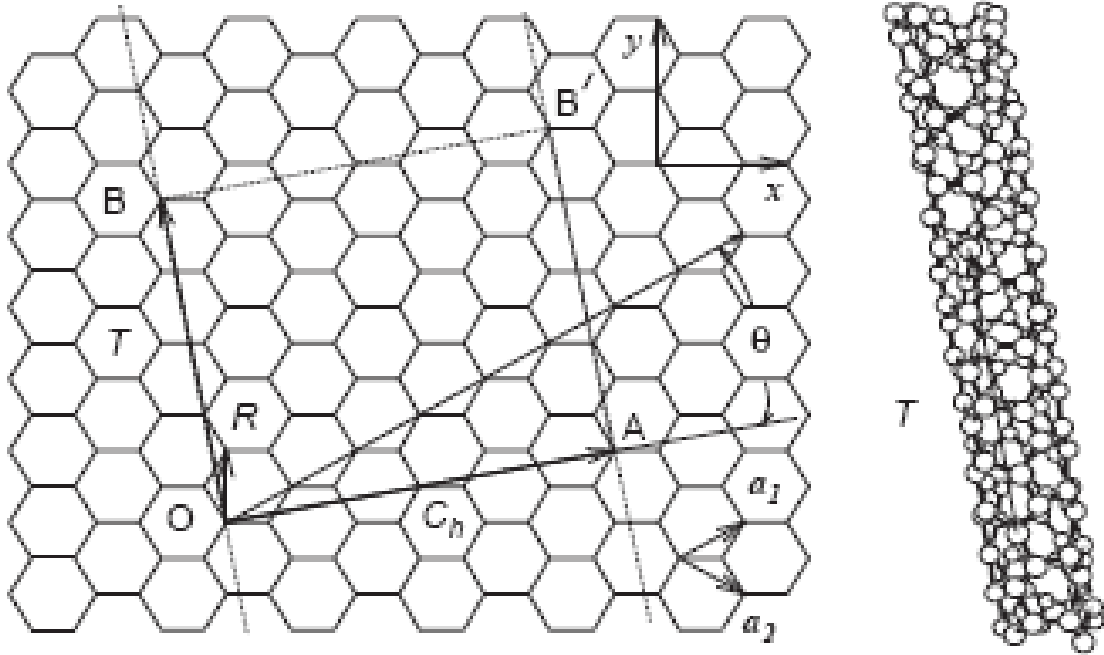


**Figure 6, unrolled honeycomb structure of a single wall carbon nanotube (SWNT) showing the chiral vector ( $C_h$ ), chiral angle ( $\theta$ ) and the translation direction (T) [35].**

In Figure 6 T is the axis direction (translational vector) and  $a_1$  and  $a_2$  are real space unit vectors of the hexagonal lattice. The chiral vector can be written in terms of these unit vectors and integers; n and m:

$$C_h = na_1 + ma_2 \equiv (n, m) \quad (29)$$

Where m and n are integers and  $0 \leq |m| \leq n$ .

The tube diameter  $d = L/\pi$  where L is the tube's circumferential length and equal to the absolute value of  $C_h$ :

$$L = |C_h| = \sqrt{(C_h \cdot C_h)} = a \sqrt{(n^2 + m^2 + nm)} \quad (30)$$

Where  $a = |a_1| = |a_2|$  is the lattice constant (width of the unit cell).

The value of a is calculated as:  $1.42\text{\AA}$  (c-c bond length in graphite)  $\times \sqrt{3} = 2.46\text{\AA}$  for graphite. As the C-C bond length in CNT is slightly larger than graphite ( $1.44\text{\AA}$ ) the

lattice constant  $a$ , for an armchair tube is equal to  $2.49\text{\AA}$  and for a zigzag tube is equal to  $\sqrt{3}a = 4.31\text{\AA}$  [36].

$\theta$  is the angle between the vectors  $C_h$  and  $a_1$  with values in the range of  $0 \leq \theta \leq 30^\circ$  because of the hexagonal symmetry of the honeycomb lattice (for a zigzag nanotube  $\theta = 0$  and for an armchair nanotube  $\theta = 30^\circ$ ). This angle denotes the tilt angle of the hexagons with respect to the direction of the nanotube axis, and specifies the spiral symmetry and  $\cos \theta$  is defined as:

$$\cos \theta = C_h \cdot a_1 / |C_h| |a_1| = (2n + m) / 2\sqrt{(n^2 + m^2 + nm)} \quad (31)$$

When considering concentric tubes the chiral vectors of the individual tubes can be determined separately, this gives the radii of individual tubes and the spacing between them. Such spacing was calculated as  $\sim 0.352\text{nm}$  and  $\sim 0.34\text{ nm}$  for a zigzag and armchair tubes in a DWNT respectively ( $0.334\text{nm}$  for graphite) [37]. The structure of the tubes will not be commensurate to each other in almost all concentric tubes unless they are achiral.

### 2.2.2. Synthesis of carbon nanotubes

Between carbonisation ( $650^\circ\text{C} - 750^\circ\text{C}$ ) and graphitisation temperatures ( $\sim 2300^\circ\text{C}$ ) carbon can transform from an amorphous carbon to a stable planar graphite structure by cutting and reconnecting  $sp^2$  bonds. Therefore the basic principle for the synthesis of CNTs is straightforward: a carbonaceous feedstock has to be brought into the gas-phase at an appropriate temperature and then cooled where the evaporated species can subsequently self-assemble into the tubular structures [38]. There is vast amount of literature on the production of carbon nanotubes. Some of the methods developed so far include: arc discharge [39], pyrolysis [40], laser ablation [41], and chemical vapour deposition [42] [43]. Other methods which can produce CNTs at room temperature have also been reported including plasma enhanced CVD [44] and use of excimer lasers [45]. Although production of specific tubes (SWNT, MWCNT, etc...) with narrow diameter distribution is now possible [46, 47, 48] and synthesis of monochiral tubes have also been

reported [49] the controlled production of nanotubes with consistent and perfect structures on large scales still remains a challenge [50, 51].

The growth mechanisms of CNTs have also been a subject of vast research and debate. One mechanism put forward by Iijima et al [52], is that the tubes are open during growth and carbon atoms are added at the open ends. Others including Endo and Kroto [53] suggested that the tubes are always capped and the pentagonal defects assist the absorption of carbon atoms. The large aspect ratio of nanotubes implies that growth along the length (whether opened or capped) is more likely than growth in the diameter and coaxial tubes are thought to grow spontaneously (Russian doll as opposed to Swiss roll configuration) [36].

### **2.2.3. Electronic structure of carbon nanotubes**

A SWNT has energy bands with a set of 1D dispersion relations that are a cross section of those for graphene [54]. The 1D confinement of the electronic structure gives rise to van-Hove singularities (vHs) in the density of state (DOS) and the optical absorption of SWNT, particularly the semiconducting tubes, are greatest when the excitation energies correspond to the energy difference of these singularities [55].

Close to the Fermi energy, the band structure of graphene is dominated by the  $\pi$  states and since there are two atoms in the unit cell (see Figure 7) there are two  $\pi$  bands, a bonding ( $\pi$ ) below the Fermi level and an anti-bonding ( $\pi^*$ ) above the Fermi level [56]. Electrons can be optically excited from the valence  $\pi$  to the conduction  $\pi^*$ . For metallic tubes transitions occur close to the K points, where the valence and conduction bands touch [35].

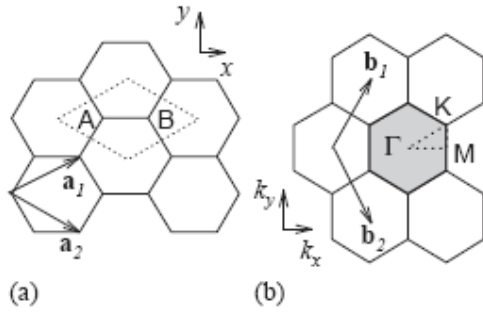


**Figure 7 (a) the unit cell (dotted rhombus) and (b) the Brillouin zone (shaded hexagon) of graphene where  $b_1$  and  $b_2$  are reciprocal lattice vectors.  $\Gamma$ ,  $K$  and  $M$  are the high symmetry points [35].**

For a  $(n, m)$  CNT the Bloch vectors (the wave vectors of electrons in the periodic potential) are discrete due to the periodic boundary conditions along the circumference [56]. If they cut through  $K$  points the 1D energy band has a 0 energy gap and a finite DOS at the Fermi level, such tubes are therefore metallic. In metallic nanotubes  $n-m = 3q$  (where  $q$  is an integer) therefore all armchair ( $n=m$ ) CNTs and those zigzag ( $m=0$ ) tubes with  $n = 3q$  are metallic. It is estimated that 1/3 of chiral tubes are also metallic [36]. It should be noted that although graphitic materials are known to be good conductors the carrier density of graphite is  $10^{18} \text{ cm}^{-3}$ , i.e. about one carrier per  $10^4$  atoms, compared with copper's 1 carrier per atom. The low carrier density is offset by high mobility. The phonon scattering is low at low temperatures for highly crystalline graphite and results in low resistivity [37].

If the vectors do not pass through the  $K$  points, then, the tube is semiconducting with a finite band gap where the DOS is zero. This gap varies with the tube chirality and diameter with a primary value of 1eV (which is close to photon energy at  $1\mu\text{m}$  wavelength), scaling with  $1/r$ , where  $r$  is the tube radius. In one case where  $n \equiv m$ , this gap is thought to be very small ( $\sim 10 \text{ meV}$ , scaling with  $1/r^2$ ) being induced by the tube curvature; this secondary gap vanishes only in metallic tubes [48]. In very small diameter tubes the curvature of graphene sheets results in band shifts that move their band edges into the semiconducting energy gap, suggesting that all very small diameter tubes should be metallic [57]. In large diameter tubes with many concentric constituents as the diameter increases, more wave vectors become allowed for circumferential direction and

the tube becomes more 2D and the semiconducting band gap decreases. Therefore although some of the constituent tubes may have semiconducting properties, MWCNTs with diameters larger than 20-30nm, can be taken as metallic [58].

The electronic structure of CNTs can be influenced by the presence of magnetic fields. In a uniform external magnetic field if the field is parallel to tube axis, the energy gap of the tube will change as a function of the magnetic field and a semiconducting carbon nanotube can become metallic and vice versa. If the field is perpendicular to the tube axis, since all the magnetic flux which comes in one side leaves from the other side the net penetrating flux to the surface is zero. A decrease in electronic resistance has been observed by increasing the strength of an external magnetic field [36].

#### **2.2.4. Phonon modes in carbon nanotubes**

The Raman spectra of SWNT and their phonon dispersions have been comprehensively studied by many researchers [35, 36, 37 and 59] and a particularly detailed description is given by Dresselhaus et al [35]. At first approximation SWCNT phonon dispersion is obtained by folding the phonon dispersion relation of a graphene layer. This gives 6N dispersion relations for the x, y and z vibration for each atom and phonon dispersion depends on chirality and diameter. There is also a large amount of sharp structure in the phonon DOS, reflecting the quantum confinement of the phonon states into vHs. Thus there are 6N-4 optical phonons, with their energy gaps proportional to  $1/r^2$  [60].

#### **2.2.5. Optical properties of carbon nanotubes**

Some of the optical properties of carbon nanotubes related to absorption and scattering of light are described below starting with their Raman spectra.

##### **2.2.5.1. Raman spectra of carbon nanotubes**

Out of the 6N phonon dispersions possible, only a few are Raman and IR active. This is due to the small wave vectors of the photons, where only k vectors close to  $k = 0$  couple to incident light based on the energy-momentum conservation requirements. Therefore only the zone centre at  $\Gamma$  point ( $k = 0$ ) needs to be considered. If the excitation energy is close to the energy of high optical absorption, the Raman intensity is enhanced and this is known as resonant Raman. Raman spectra are not chirality dependent although the

phonon dispersion is, which shows in the absolute intensity. The electron - phonon coupling constant for CNTs is reported to be  $0.5\text{eV}/\text{\AA}$  [36]. Figure 8 shows a typical Raman spectrum for a carpet of MWCNTs.

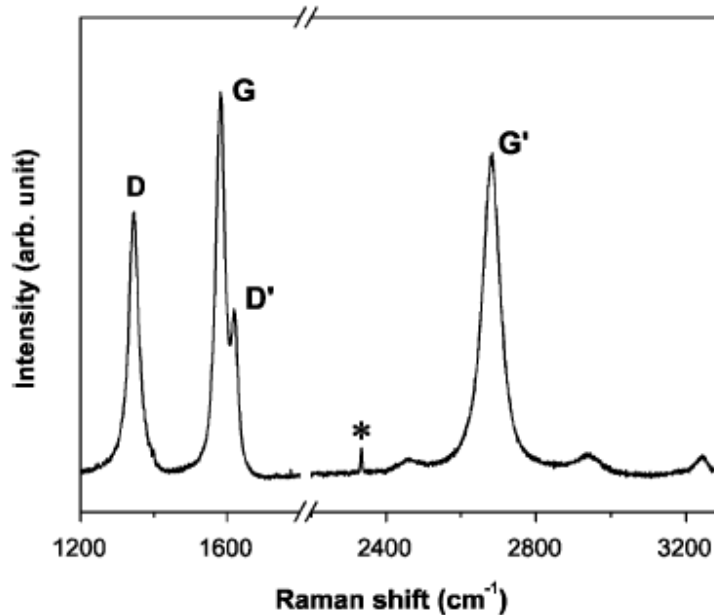


**Figure 8, Raman spectrum of a multiwall carbon nanotube sample, showing the main Raman features, the D, G, D' and G' bands taken with a laser excitation energy of 2.41 eV (514.5 nm wavelength). The peak denoted with \*, comes from the Raman mode of N<sub>2</sub> gas (2330 cm<sup>-1</sup>) present in the air surrounding the sample [61].**

The stretching of the C-C bond in graphitic materials gives rise to the G peak, which is common to all sp<sup>2</sup> carbon systems [62]. This band is sensitive to strain effects, such as that induced by external forces or by one graphene layer on another in multiwall nanotubes. In graphite and SWNTs, the D peak at 1350cm<sup>-1</sup> and the G' peak at 2700cm<sup>-1</sup> are due to one and two-phonon, second-order Raman scattering processes respectively. G' is a second-order two-phonon process and exhibits a strong frequency dependence on the excitation laser energy and is an overtone of the D. It is also very sensitive to the stacking order of the graphene sheets along the c axis [61].

The D band has a dispersive behaviour whereby its frequency changes with the energy of the incident laser ( $E_{\text{laser}}$ ), and up-shifts with increasing  $E_{\text{laser}}$  linearly over a wide laser energy range. D and D' peaks have been related to the presence of defects [35] in the tube structure and disorder induced by lattice distortion [63] respectively. Qualitative

evaluation of the amount of disorder in a graphene monolayer is usually made by analyzing the  $I_D/I_G$  intensity ratio between the disorder-induced D band and the Raman allowed G band.

Important for coupling electrons to the lattice are the three low-lying optical modes at the center of the Brillouin zone. The most notable of these is the radial breathing mode (RBM), which corresponds to the motion of carbon atoms radially in and out of plane. The RBM has frequency of  $\nu_{\text{RBM}} = 100\text{--}500 \text{ cm}^{-1}$  and is inversely proportional to the tube diameter through:  $\nu_{\text{RBM}} = 248/\text{diameter} \text{ cm}^{-1}$  [35]. It has been indicated that Raman scattering is diameter selective (as the tube curvature will affect the phonon DOS) and changes with the laser field [64]. Therefore some of the characteristic peaks of SWNTs are not so evident in MWCNTs spectra. An example is the RBM feature which can only be seen for very small inner tubes accompanied by a good resonance condition [65].

MWCNT's phonon structure is affected by the inter-tube interactions and the large diameter, which creates effectively a 3D system similar to graphite with only longitudinal acoustic (LA) and transverse acoustic (TA) phonon modes [66].

#### **2.2.5.2. Infrared absorption by carbon nanotubes**

The IR absorption of carbon, from carbon black (CB) [67] to graphite [68] has been researched for many years. However, unlike vast amounts of literature on Raman spectroscopy of CNTs the IR spectroscopy of CNTs is not so intensely investigated. One reason could be due to high absorption of CNTs, which makes sample preparation and accurate measurements difficult.

Transmission FTIR measurements of CNT/KBr pellets, have shown one broad and asymmetric line at  $1575\text{cm}^{-1}$  and a weaker line at  $868\text{cm}^{-1}$  [69]. However, the authors did not specify whether the samples were MWCNTs or SWNTs but the lack of RBM peaks in their Raman spectra could suggest that the samples were MWCNTs. IR optical absorptions of SWNT have been reported to have broad peaks at 0.68 eV ( $\lambda = 2 \mu\text{m}$ ) and 1.2 eV ( $\lambda = 1\mu\text{m}$ ) photon energies, both of which are near-IR and correspond to  $5000\text{cm}^{-1}$  and  $10000\text{cm}^{-1}$  wave numbers respectively. The authors suggested that the peaks are due

to diameter distribution in the film of SWNTs, as opposed to individual tubes. IR reflectance of SWNTs is reported to have three distinct features; a low energy mode positioned below  $400\text{cm}^{-1}$  and varying considerably with diameter, and two phonon modes at around  $874 \pm 2\text{cm}^{-1}$  and  $1598 \pm 3\text{cm}^{-1}$  [70]. The latter two peaks were described as footprints of SWNTs as they appeared in all samples regardless of diameter distribution and symmetries.

It has been suggested that, parallel to the tube axis, CNTs are optically isotropic and similar to amorphous carbon, and perpendicular to the tube axis their properties depend on light polarisation [37]. IR reflectance of un-oriented SWNT films consisting of metallic and semiconducting tubes revealed that the reflectivity, monotonically decreases as photon energy increases [71]. The optical transitions were thought to be well-aligned along the tube axis with strong interband transitions dominating the far-IR region and masking the contributions from excitons. Using a magnetic field to align SWNT the measured IR spectral range comprised of the free-carrier absorption due to metallic tubes in the far-IR, and the first interband transition of the semiconducting tubes in the near-IR [72].

Wang et al. [73] studied the role of excitons in electromagnetic excitations of semiconducting SWNT, using a two photon absorption process, arguing that conventional linear optical measurements only access one-photon transitions for which a vHs and a broadened excitonic resonance exhibit qualitatively similar features. As described earlier two-photon excitation is a nonlinear optical effect that requires the simultaneous absorption of a pair of photons (see Figure 9). This required high intensity and they provided this by femtosecond (fs) laser pulses with the fluence of  $5\text{Jm}^{-2}$  ( $0.5\text{mJcm}^{-2}$ ) and monitored the induced light emission. Only when the excitation energy was substantially greater than the emission energy did two-photon absorption occur, which is a signature of the presence of excitons with significant binding energy.

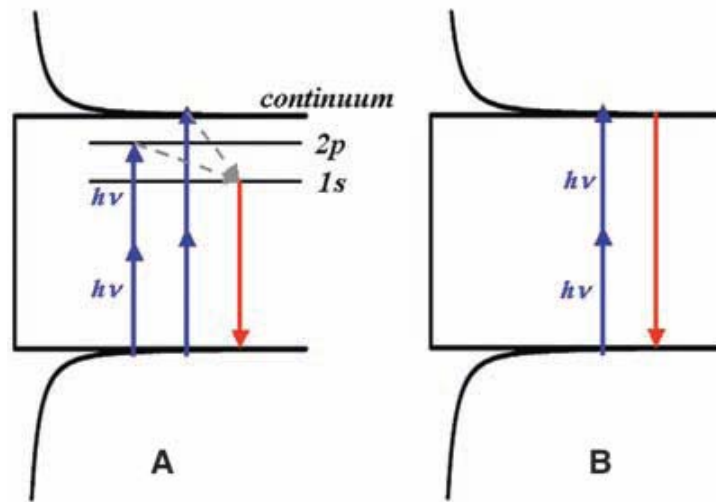


**Figure 9, schematic representation showing excitation (blue arrows) with photon energy  $h\nu$  and subsequent fluorescence emission (red arrows). (A) Is the exciton picture and (B) is the band picture where the threshold for two-photon excitation lies at the band edge, where the relaxed fluorescence emission also takes place [74].**

Photoconductivity of SWNT has absorption peaks in the IR region [74]. Prolonged irradiation causes a change in conductivity, which is thought to be bolometric (caused by heating of the SWNT network) [75]. Electron-phonon interactions lead to ultrafast relaxation of the photo-excited carriers and the energy of the incident IR radiation is efficiently transferred to the crystal lattice which causes a change in resistance.

Measurements on the photon-to-current conversion efficiency of MWCNT have been reported to be 7%, which is about 50 times higher than that of SWNTs [76], suggesting that charge transfer is more effective due the large number of concentric tubes. Randomly oriented MWCNTs have been shown to have high IR absorption efficiency, acting as IR detectors, with interaction manner compared to that of simple dipole radio antenna [77]. The idea of using MWCNTs as infrared detectors have been further reported using a 250W IR lamp perpendicular to the axis of aligned MWCNT and measuring the conductivity increase as a function of intensity [78]. Authors suggested that IR radiation causes band to band transitions of electrons in MWCNTs and increases the conductivity. The observations may be accurate but the effects of excitons and lattice heating is ignored. Furthermore direct coupling of IR to high frequency phonons is possible as the

IR source used had a spread of wavelength from far to near IR. Both of these should influence the conductivity as they would act as scattering mechanisms.

### **2.2.5.3. Optical limiting properties of carbon nanotubes**

Optical limiters are effective devices to decrease transmittance at high intensity. There are many reported experiments on optical limiting effects of multiwall carbon nanotubes in the visible and infrared spectral regions with nanosecond laser pulses. CNT samples in different matrices have been examined, Sun et al. reported samples suspended in distilled water and embedded in polymethylmethacrylate (PMMA) films. The reported limiting thresholds were 1, 5, and 13 Jcm<sup>-2</sup> at 532, 700, and 1064 nm, respectively [79].

Optical limiting has also been observed in carbon black suspensions in water. This has been attributed to a nonlinear scattering process. The expansion of the micro-plasmas formed in the matrix as a result of heating the carbon particles, and their rapid expansion to the surrounding liquid, is thought to strongly scatter the incident laser light. Consequently, the light energy in the propagation direction is decreased, leading to the limiting behavior [79].

Other investigations have used laser pulses of 7ns duration produced by a *Q*-switched Nd:YAG laser at 1064nm wavelength. At incident fluence of less than 0.06 Jcm<sup>-2</sup> the energy transmittance was constant. However, in excess of 0.06 Jcm<sup>-2</sup>, the transmittance decreased as the incident fluence increased. Experiments with 532 nm, 15 ns duration laser pulses showed that the threshold for carbon nanotubes is much less than that for carbon black (7 Jcm<sup>-2</sup> as opposed to 50 Jcm<sup>-2</sup>) [80] and optical limiting occurs mainly due to nonlinear scattering, and is host liquid dependent. Authors suggested that the scattering originated from micro-bubbles, formed due to absorption-induced heating of the host liquid.

Izard et al [81] investigated the role of carbon nanotubes' structure on their optical limiting properties. They suggested that length is not a structural parameter that influences the optical limiting properties of a nanotube. However, the wavelength used in their study ( $\lambda= 530\text{nm}$ ) was much shorter than the length of the shortest tube they used (a

few microns long), which could suggest a slight error in their conclusions. They also studied the influence of diameter on nanotubes optical limiting properties and reported improving efficiency with increasing diameters. They analyzed different bundle sizes and attribute their observations to the effect of bundle diameters on nucleation and growth of bubbles in the solvent, where more energy is required for nucleation of bubbles in small diameter bundles or individual tubes. This explanation is plausible however based on bubble growth dynamics [82] the initial growth is very fast, limited only by the momentum available to displace the surrounding liquid from its path. As the bubble grows in size, the effect of inertia becomes negligible, and growth continues by virtue of diffusion of heat from the superheated liquid to the interface, although at a much slower growth rate than during the inertia-controlled stage of growth. Therefore directly relating the bubble size with the size of the nanoparticle nucleus is not straight forward as the most important factor will be the amount of heat supplied (the energy of the light source) and the time during which it has been delivered (pulse duration). A more reasonable alternative theory was also suggested by the authors, based on plasmonic absorption of carbon nanotubes and possible plasmon coupling between carbon nanotubes inside bundles that may induce significant absorption enhancement and subsequent heating. This could result in faster superheating of the water and possibility of formation of small bubbles.

#### **2.2.5.4. Plasmons in carbon nanotubes**

In MWCNTs the large diameter range leads to a uniform optical absorption as a function of wavelength. A more compact nanotube bundle exhibits stronger absorption mainly owing to more  $\pi$  electrons. Parallel to tube axis CNTs are optically isotropic and similar to amorphous carbon. Perpendicular to tube axis their properties depend on light polarisation [37]. If light is polarised parallel to the tube the dielectric function is similar to graphite as the surface resembles planar graphite, if it is polarised perpendicular to the tube, the dielectric function is a mixture of both parallel and perpendicular dielectric functions of the graphite sheet [36]. Although metallic and semiconducting tubes are expected to laser heat differently, the effective heat dissipation and averaging effects will mask this. Laser heating occurs through the energy transfer from highly excited electrons

to the lattice via electron-phonon scattering. A high concentration of excited electrons weakens the covalent bonds and this can induce structural transformations.

Plasmons are collective oscillations of the free electron gas density and can couple with photons as long as the photonic frequency is in the same order as the plasmonic frequency. The plasmon frequency can often be estimated in the free electron model as described earlier using Equation (21). Studies on the IR optical properties of well-aligned MWCNT bundles revealed that the loss function has a prominent  $\pi$ -plasmon peak and is dependent on the polarization direction of the incident light [83]. However the authors suggested that the absorption is diameter and chirality independent. This may be correct for bundles of MWCNTs due to group effects but for individual tubes absorption will definitely depend on the diameter and chirality, as they are directly related to the electronic structure of the nanotubes.

Work done by Azuma et al, on photo-excitation using a Ti:sapphire laser at 800 nm wavelength with an average power of 300 mW suggested that the Fe impurities or the vacancies left by removing metal particles during the purification process would act as trap centers for electrons or holes and at high temperatures photo-excited carriers become long-lived due to the repetition of the trapping and de-trapping processes. They also reported highest achieved absorption when the CNTs longitudinal axis was parallel to the incident laser field [84].

This has been explained by the assumption that unlike the classical plasmon in a 3D electron gas, the plasmon in a carbon nanotube bundle is anisotropic and can be excited only along the tube axis. The lower energy mode is in the 5–8 eV range and has been identified as the  $\pi$  plasmon, while the higher energy mode in the 20–30 eV range has been identified as the  $\pi + \sigma$  plasmon. However if tunneling between nanotubes is permitted, the classical plasmon can then be excited in a direction perpendicular to the nanotubes [85]. Carbon nanotubes possess a very rich spectrum of plasmon modes and it has been shown that defects as well as formation of nanotube bundles can dramatically enhance the coupling of electromagnetic radiation with plasmons [86]. At intermediate frequencies, there is a series of plasmon modes each related to a specific inter-vHs

electron transition. These weakly dispersive modes occur in the range of frequencies between 0.5 to 3 eV [86].

#### **2.2.5.5. Laser induced structural changes in carbon nanotubes**

There have been several reports on using laser radiation for pruning CNTs. A 26mW circular laser beam of 1.24mm diameter ( $\sim 2.2 \text{ Wcm}^{-2}$ ), at 632nm wavelength was reported as the power needed to remove tubes in air environment parallel to their axis. This value reduced to 13mW ( $1.1 \text{ Wcm}^{-2}$ ) when the tubes were upright. The local temperature during irradiation was reported to have exceeded 1750K, and the authors suggested that, based on their calculations, the achieved temperature would have been sufficient to melt the remnant iron catalysts, initially used during the production of the CNTs [87]. Other reports used an excimer laser at 248nm and fabricated an area of patterned CNT arrays with power density of  $17 \text{ mWcm}^{-2}$ . They found that the laser beam did not usually burn the entire lengths of the long CNTs and the length reduction can be controlled by varying the laser power [88].

Excimer laser radiation (248 nm wavelength with photon energy of about 5 eV), operating at a pulse repetition frequency of 10Hz and a pulse length of approximately 20ns was reported to have been used to exfoliate amorphous carbon from carbon nanotubes. The resulting exfoliation was attributed to two factors which may be acting simultaneously. One was  $\pi$  plasmon resonance and the other thermal mismatch between CNTs and the amorphous carbon sheath covering them. The  $\pi$  plasmon represents the collective excitation of the  $\pi$  electron system as discussed earlier and can have energies in the same order as the excimer laser for graphitic carbon. The authors therefore suggested that the resultant resonating  $\pi$ -plasmon can transfer its momentum to the impurity-CNT interface and weaken the physical adhesion between them. It was also suggested that the thermal stresses originating from the sudden temperature rise with each laser pulse could be another cause of exfoliation, as MWCNTs have a negative coefficient of thermal expansion (CTE) ( $-1.3 \times 10^{-6} \text{ K}^{-1}$ ) along the length direction and hence tend to contract, while the amorphous carbon layer surrounding the MWCNT has a positive CTE value ( $2 \times 10^{-6}$  to  $7 \times 10^{-6} \text{ K}^{-1}$ ) and tries to expand [89].

A study on laser irradiation of highly oriented pyrolytic graphite, reported that the threshold energy fluence for ablation was much lower for picosecond (ps) pulses than nanosecond (ns) pulses with a minimum of  $0.25 \text{ Jcm}^{-2}$  [90]. A similar study using ns laser pulses and mass spectrometer analysed the constituents of the resultant plume [91]. The laser plume constituents were identified as neutral carbon species for low power densities while the signal was suppressed by the ion signal at high power densities.

Heating of DWNTs deposited on glass surfaces and submerged in methanol as a function of continuous-wave-laser has been reported [92]. At powers higher than  $10 \text{ Wcm}^{-2}$  the methanol started to vaporise and the authors compared this with CB in water where the same effects could not be observed and they attributed this to a stronger plasma excitations for CNTs. Although the coupling of CNTs with IR could be more prominent, the reason for their observation could also be the fact that methanol's boiling point is some 36K below waters boiling point. They also reported no difference in heating of metallic and semiconducting tubes and this was attributed to the effective heat dissipation and averaging effects in the bundle. Also larger laser heating was reported when using shorter wavelength and this was related to the population of several higher lying excited states which multiplied the energy transfer to the lattice via electron phonon scattering.

Dumitrica et al. [93] have presented an interesting model, describing the response of SWNTs to fs lasers. The sample used in their model was a SWNT with 1 nm diameter, which had detectable RBM vibrations with a 133 fs period. They quoted coherent RBM oscillations in response to  $<10$  fs laser pulses and electron-phonon relaxation times in the order of ps, implying that non-thermal effects will dominate the initial stages of a SWNT's response.

They suggested the presence of two coherent RBM excitations, localized in the cap and nanotube body and a soft longitudinal excitation that couples with the tubular CNT length. Under high absorbed energies but below  $2.9 \text{ eV atom}^{-1}$  (the graphite's ultrafast fragmentation threshold), the resulting oscillatory motions lead to expansion of the caps and contraction of the tube body that causes bond breakage and cap fragmentation.

Elastic response of SWNTs to short pulse lasers have also been reported, with bundles having elastic strain of about 20% [94]. However these have been due to thermal effects and related to the CNT bundles CTE. Analytical calculations on the CTE of SWNT have shown [95] that CTE in the radial direction is less than the axial direction for armchair carbon nanotubes, but the opposite holds for zigzag tubes. Furthermore, the CTE in the radial direction is independent of the carbon nanotube chirality, while the axial CTE strongly depends on the chirality.

Use of a laser to produce thermally induced changes in CNTs' structure e.g. welding [96] or to cause ablation of materials in which CNTs have been embedded [97] have been further reported and all of such effects rely on lattice heating in the tubes as a result of electron-phonon coupling. This coupling has been investigated by many researchers [98, 99, 100, 101] and it has been suggested that, in CNTs it is strongly chirality dependent [101]. The effect of e-ph couplings in nanotubes have also been observed through investigations on the field emission properties of CNTs [102, 103, 104] and have been specified as main contributors to Joule heating where fast traveling electrons interact with the lattice and lose some of their kinetic energy as heat. Electronic mean free path of MWCNTs due to phonon emission is estimated to be  $\sim 10$  nm and each optical or zone boundary phonon emission is approximately at  $\sim 180$  meV [105] so that most of the energy provided by the electric field to each electron is converted into phonons within the nanotube. By correlating the electron resistivity to the phonon population, measured by Raman spectroscopy, the high-energy electron - phonon scattering length in metallic SWNTs was determined to be  $\sim 30$  nm [106].

### **2.3. Summary**

Absorption of near IR radiation by a material is mainly due to its interaction with the materials bound and free electrons. The microscopic cause of absorption is the extraction of energy by free electrons from the radiation and change of phase velocity of incident photons as a result of inelastic scattering by bound electrons. The extinction of light may also be due to scattering effects which do not lead to absorption such as those caused by spontaneous emission and may act as a self limiting process with regard to absorption. Furthermore extrinsic factors such as the number of defects and amount of impurities can

alter the optical absorption properties of a material. Most of the absorption processes will lead to lattice heating either due to direct collision of excited electrons with the lattice or due to emission of phonons to conserve momentum in electron-photon inelastic scattering processes. High intensities such as those produced by a laser can lead to non-linear absorption processes such as two photon absorption or free carrier excitation, both of which will exacerbate the heating of the lattice. This effect is time dependent and can also reach an intensity saturation limit. This is called the saturation of the atomic transition and is not easily achieved with conventional light sources as the light intensity required for this is very high and only a laser beam can provide it. The required intensity for such a light source was estimated by Loudon [25] to be  $20 \text{ Wcm}^{-2}$ . This value is similar to the laser intensities used in this study as explained later and therefore a non-linear response is likely to be seen in our experiments.

The complex non-equilibrium interactions between all the individual processes involved in heating a material with a beam of light can be simplified through the Boltzmann transport equation, where the collision term is the Joule heating effect that the external electric field has on the electrons and this is balanced by the rate of change of the electron energy due to interaction with other electrons, increase in internal electronic energy and coupling with lattice phonons. However due to the difference in the electronic velocity and hence electron energy, compared with speed of sound and energy of phonons, the amount of energy transferred from the electron gas due to interactions with one phonon is small and many e-ph interactions need to take place to transfer a significant amount of energy to the lattice from electrons. To transfer 1eV of energy from electrons to the lattice 20 phonons need to be created.

The interaction of light with carbon nanotubes varies based on their metallic or semiconducting properties. The semiconducting tubes are reported to have a band gap of 1eV which decreases with increase in diameter and the large diameter MWCNT are thought to have an overall metallic property. The laser radiation interacts primarily with conduction  $\pi$  electrons although the photon energy of near IR radiation at 940nm ( $1.32\text{eV} > E_g$ ) would mean that it can also interact with semiconducting tubes, as it would with metallic tubes in addition, CNTs have been shown to have absorption peaks in the NIR at

around 1.2eV. Although the number of carrier electrons in CNTs is not as large as what is expected for metals (the carrier density of graphite is  $10^{18} \text{ cm}^{-3}$ , i.e. about one carrier per  $10^4$  atoms, compared with 1 carrier per atom for copper.), their large mean free path (10nm) compared to their length would mean rapid transfer of the irradiated energy by the electrons and electron gas thermalisation prior to lattice heating. The absorption properties are also dependent on the nanotubes orientation and are enhanced for those beams that are polarized parallel to the tube axis. This is partly because of the  $\pi$  Plasmons directionality, which enhances absorption in tube bundles. These vibrations are in the order of 0.5 - 3 eV. Efficient absorption of near IR by CNTs has initiated research for a variety of applications including; as optical limiting materials, where significant light scattering has been observed at intensities as low as  $0.06 \text{ Jcm}^{-2}$ . This has been attributed to both effective optical absorption properties of CNTs as well as nonlinear scattering, such as, micro-bubble formation, which shows host liquid dependence. Furthermore, light absorption by carbon nanotubes can be enhanced by extrinsic effects. Fe impurities or the vacancies left by removing metal particles during the purification process would act as trap centers for electrons or holes and at high temperatures, photo-excited carriers become long-lived due to the repetition of the trapping and de-trapping processes. The effective optical absorption properties as well as the anisotropic coefficient of thermal expansion of carbon nanotubes have enabled the development of methods using a variety of lasers to alter their structure in different environments.

### **3. Carbon nanotube synthesis, treatment & characterisation**

A single batch of MWCNTs was produced and used for all the experiments reported in this thesis to remove the possible batch to batch variations in the multiwall carbon nanotube (MWCNTs) properties, which were observed to have a significant effect on their optical properties during the initial trials. This batch was then either used as-produced or was treated using heat treatment, ball milling, acid treatment or a combination of each to examine the effects of structural variations on NIR laser absorption and heating. The as-produced and treated tubes were characterised using SEM, Raman, TGA and DSC. Some of the as-produced samples were also examined under TEM to have a closer look at their structure. Small particle graphitised Carbon black (CB) was procured from Sigma Aldrich (14028-U) and single wall carbon nanotubes (SWNTs) were procured from Thomas Swan (PR0925, Elicarb SW) to be used and analysed as a comparison with the produced and treated MWCNTs.

#### **3.1. Carbon nanotube production, using a chemical vapour deposition method**

Aligned carpets of MWCNTs were grown on the walls of a quartz tube placed inside a 4-zone heater furnace (Figure 10), as well as on rectangular quartz substrates of 25 mm by 150 mm placed inside the quartz tube. Ferrocene powder was first sublimed at 90°C to reduce impurities and then 6 g of the sublimed ferrocene was stirred in 94 g of toluene for an hour, producing a 6 wt% ferrocene (98% Sigma-Aldrich F40-8, Lot-S05391-016) in toluene (99.5% Sigma-Aldrich) solution. The mixture was filtered using a 0.2 µm filter to remove any large remnant-un-dissolved particles, and 44.8 ml of the filtered mixture was then injected at the rate of 5.6 ml h<sup>-1</sup> using a 50 ml Hamilton syringe. The solution was injected to a preheated tube as droplets, which were vaporised at 200°C and carried into the furnace by argon gas flowing at 1.4 L min<sup>-1</sup>. The furnace was set at 760°C and flushed with flowing argon for 2 hours, prior to injection. The MWCNTs were grown for 8 hours, after this time, the needle of the Hamilton syringe was removed and the argon flow rate was increased to 3L min<sup>-1</sup> to assist with the cooling of the quartz tube and the substrates. The furnace lid was then opened and the quartz tube was allowed to cool down.

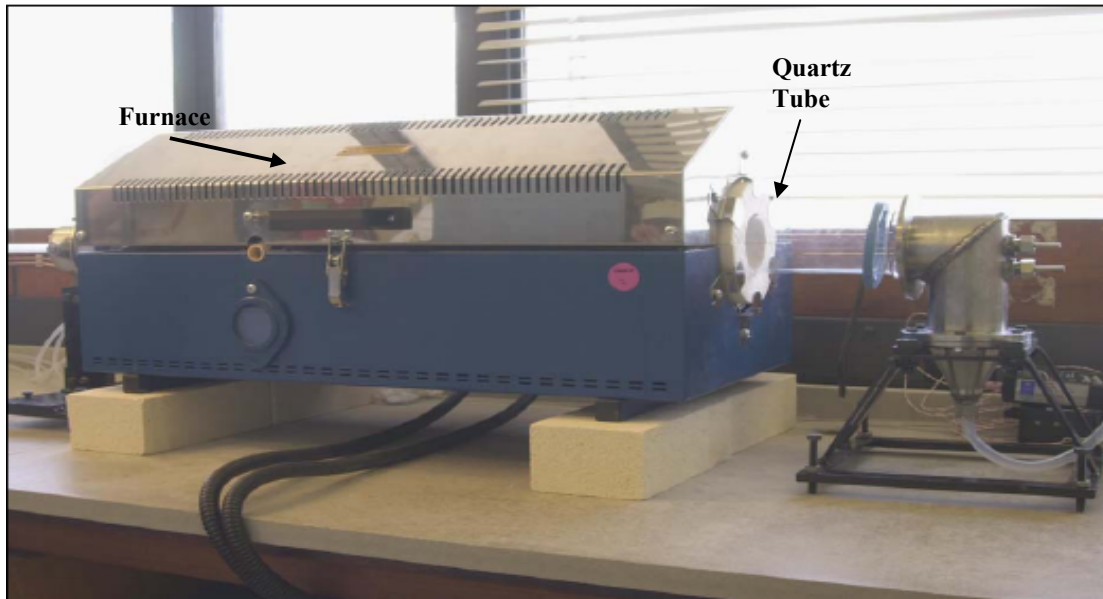


**Figure 10, the horizontal four zone heating furnace used for chemical vapour deposition (CVD) growth of multiwall carbon nanotubes (MWCNTs) in this study [107].**

The carbon nanotubes were then removed from the quartz tube in a fume cupboard. The MWCNT carpets grown on rectangular flat substrates were removed with a fine razor blade retaining their shape as shown in Figure 11, while the tubes grown on the walls of the quartz tube were scraped out only retaining some of their alignment but not completely as shown in Figure 12.

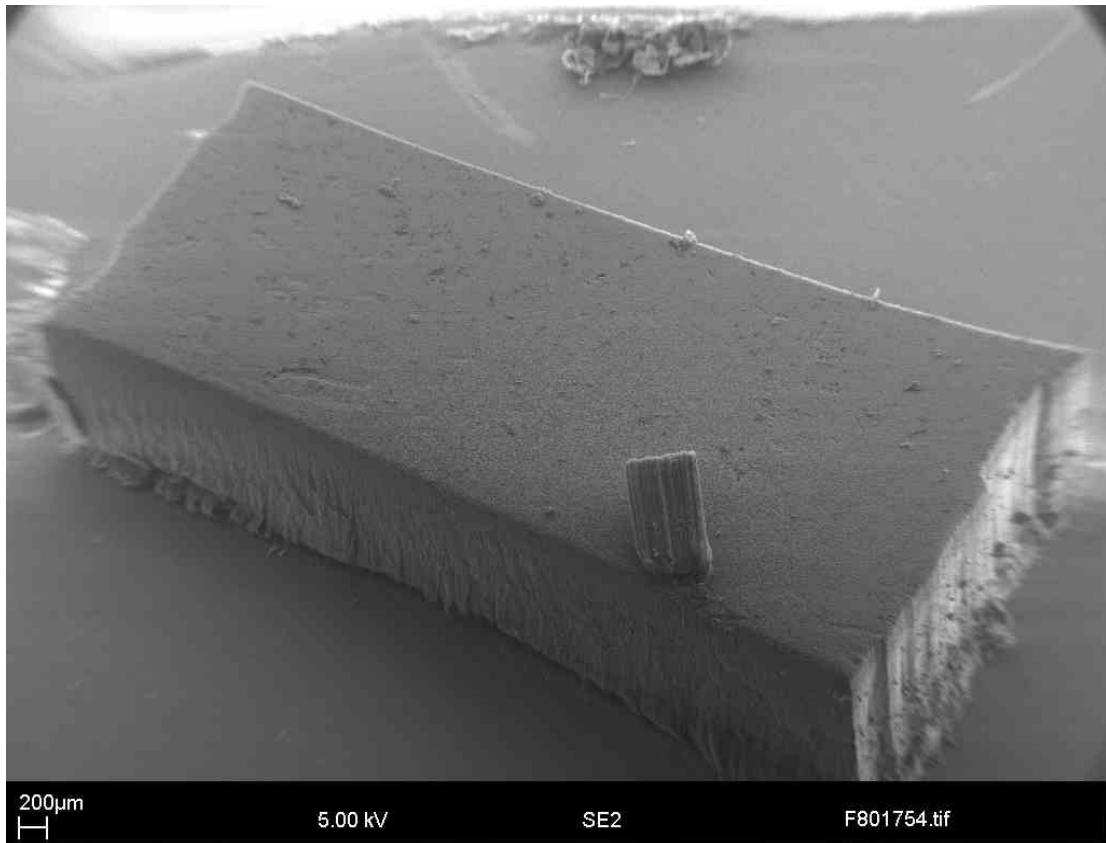


**Figure 11, an as-grown carpet of multiwall carbon nanotubes (MWCNTs).**

The process produced 8.65g of MWCNTs grown on the wall (WCNT) and 0.75g carpets grown on substrates (SCNT).

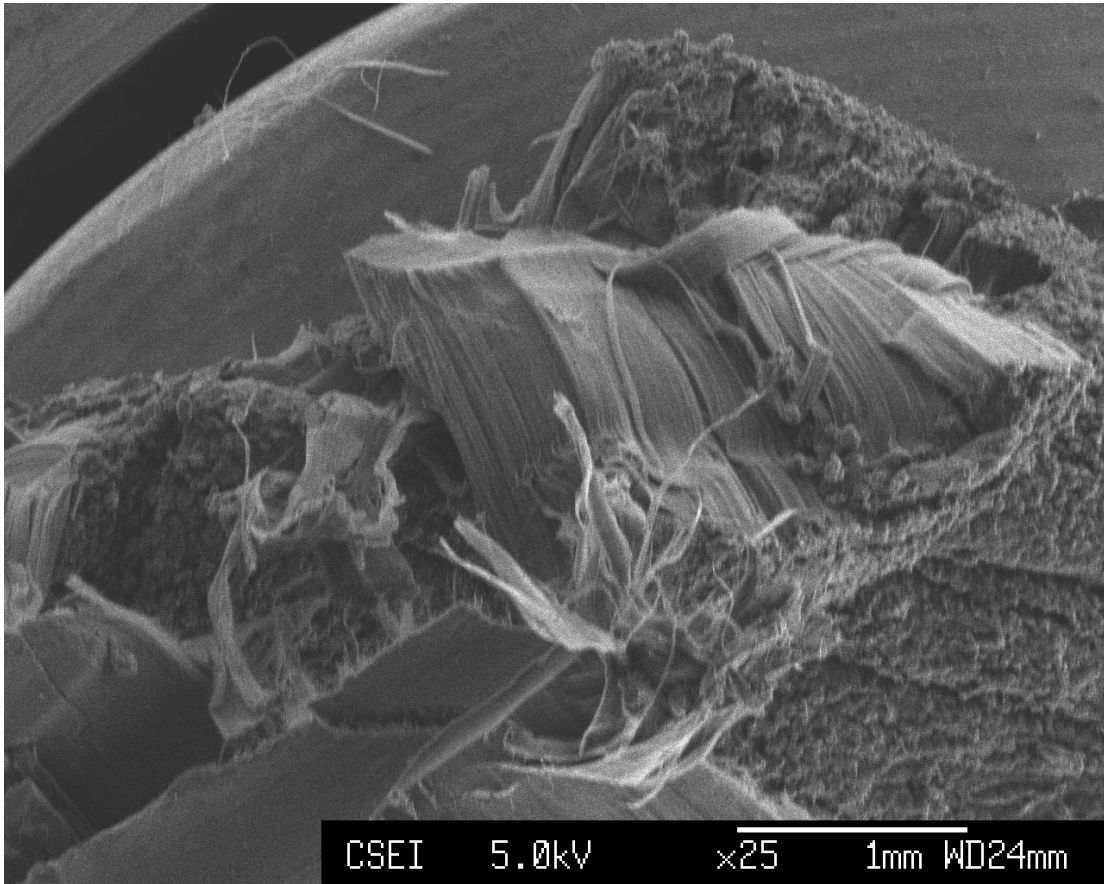


**Figure 12, as-produced multiwall carbon nanotubes (MWCNTs) grown on the quartz tube walls (WCNTs).**

Different treatments were performed on the resultant tubes post-production, which are described in the following sections

### **3.2. Post synthesis treatments of carbon nanotubes**

#### **3.2.1. Ball milling**

Three grams of the as-produced MWCNTs were ball milled using a high speed, double container, ball mill and 6 steel balls of approximately 10 mm diameter in each cylindrical container. The containers were partially filled and the samples were ball milled for 1 hour to produce shortened nanotubes (BCNTs).

#### **3.2.2. Heat treatment**

Heat treatment at high temperatures in an inert environment is believed to remove almost all the remnant iron particles of the catalyst precursor [108, 109] as well as improving the crystallinity of the tubes. Furthermore thermogravimetric analyses (TGA) have shown

that the oxidation temperature of SWNTs can be increased by 350K after 1800°C heat treatment, and the metal content (originally around 30%) can be reduced to about 2% after such treatment [110]. Other researchers have measured the change of the interlayer spacing as a result of heat treatment on MWCNTs and reported that the spacing at the mid longitudinal section of the MWCNT reaches interlayer spacing of graphite, while that at the tube apex, 0.348 nm is still slightly larger compared to that in a turbostratic graphite [111].

Heat treatment in the work presented here was carried out by placing SCNTs, WCNTs and BCNTs in a graphite crucible and then heating them at 25 Kmin<sup>-1</sup>, up to 1900°C in an argon-filled Astra graphite furnace. The tubes were then left at 1900°C for 7 hours, after which the furnace was cooled down to room temperature at the same rate.

### **3.2.3. Acid treatment**

CNTs are highly hydrophobic, thus to be able to disperse them in water they are usually functionalised. Initially an acid reflux method was used based on a publication by Shaffer et al [112]. This method is thought to remove much of the remnant iron particles as well as introducing oxygen-containing functional groups onto the surface. One gram of WCNTs were added to a mixture of 10 ml concentrated nitric (70% Fisher Scientific) and 30 ml sulphuric (95%-98%, Fisher Scientific) acids in a round-bottomed flask and refluxed for 30 minutes. On cooling, the mixture was washed with distilled water on a sintered glass filter until the washings were neutral. Acid treatment using this method proved inefficient in terms of yield and time; therefore an alternative method was sought. Other methods of facilitating CNT dispersion in matrices have been reported, which are not based on covalent functionalisation [113, 114, 115]. One report claimed the use of dodecyl sulphate sodium (DSS) salt as a surfactant [116]. This was tested using a variety of concentrations followed by prolonged periods of ultrasonication and resulted in only very poor dispersions.

The use of plasma treatment has also been reported [117] to enable wetting of CNTs with water. This method was therefore explored using a glow discharge chamber (Emitech K1050X Plasma Asher) on WCNT samples. This was done at 10 W for 10 minutes in a

mixture of 25% oxygen and 75% argon environment at  $6 \times 10^{-1}$  mbar pressure. After the treatment a drop of water was placed on the surface of the carpet and it seemed to wet the carpet well and soak through it due to capillary forces. However the process is thought to cause extensive damage to the tubes and therefore was not used for the main trials [118, 119].

A simpler chemical treatment was therefore carried out in a mixture of concentrated sulphuric and nitric acids (3:1 by volume) under sonication for 8 hours at 40°C in a round bottom flask placed in a water bath. The tubes were then filtered and washed with deionised water until the filtrate reached pH of  $\sim 7$  and then dried overnight at 100°C on a hot plate. The process was carried out on as-produced WCNT as well as heat treated MWCNTs. It should be noted that the sonication process also causes mechanical damage to the MWCNTs by shortening their length; [120] however, the damage produced by the plasma process is based on ablating lots of the carbon atoms from the nanotube randomly, and leaves behind a highly disordered and almost perforated structure.

### **3.3. Characterisation of as-produced and treated carbon nanotube**

#### **3.3.1. SEM**

A JSM 6430 FEGSEM microscope was used to examine the treated and as-produced MWCNTs. The first and rather most important observation was the presence of carbon nanotubes, as shown in Figure 13 (the bottom of a SCNT carpet) and 14 (the side view of a SCNT carpet). All tubes seemed to have imperfections along the length possibly due to the presence of defects and non-hexagonal lattices in the crystal structure. The top view of the fibres was very similar for all samples showing many curly tube ends, as opposed to the bottom of the samples, which had straight ends. None of the treatments had destroyed the fibre like appearance of the tubes.

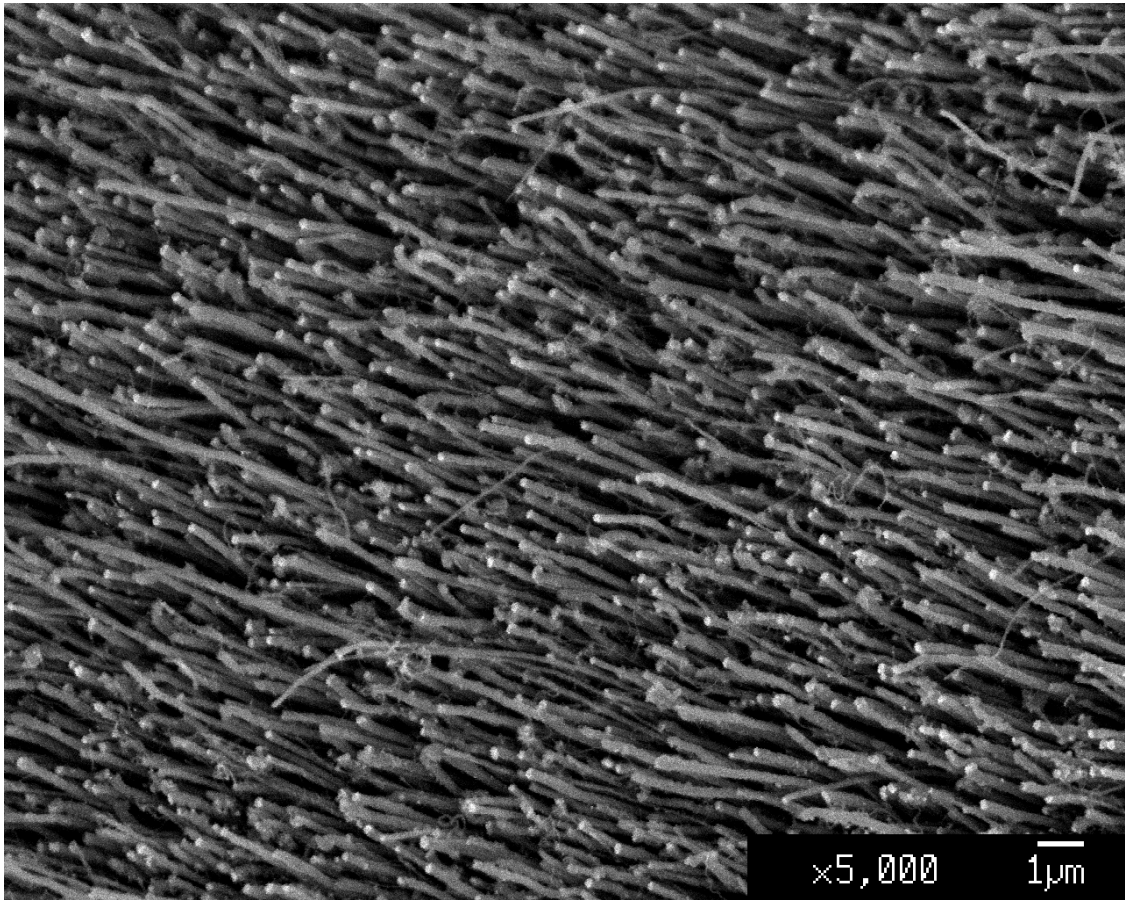


**Figure 13, SEM image from the bottom (where the tubes where originally connected to the substrate) of an as-produced carpet of multiwall carbon nanotubes. These carpets were grown on quartz substrates placed inside the furnace (SCNT).**

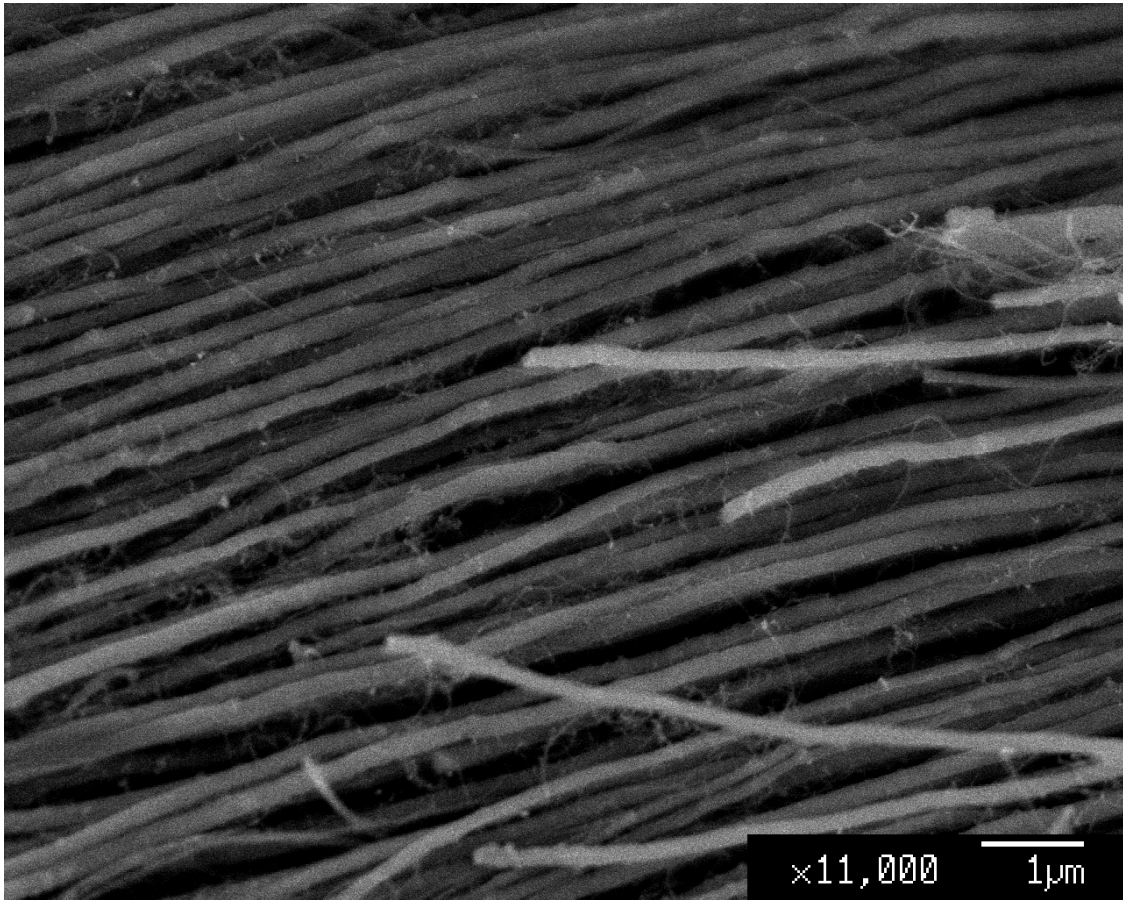


**Figure 14, SEM image of an as-produced aligned carpet of multiwall carbon nanotubes grown on quartz substrates (SCNT).**

The diameters and length of more than 100 tubes per sample type were measured. The length of as-produced (SCNT) and heat treated (HCNT) carpets were measured using a digital micrometer. The length of the other samples and the diameter of all samples were measured using Image J software on SEM images of identical magnification, and the results are presented in Table 1.

**Table 1, Diameter and length of different multiwall carbon nanotube samples, measured using SEM and the Image J software.**

Sample	Average diameter/nm	Standard deviation	Average Length/ $\mu\text{m}$	Standard Deviation
SCNT	88	36	1313	36
HCNT	73	55	1394	26
HBCNT	73	55	1	1
ACNT	64	37	116	16
AHCNT	60	36	124	17
SWNT	9	54	-	-
CB	78	36	-	-

SCNTs and HCNTs appeared highly aligned with a degree of entanglement at the top of the fibres (opposite position to where the growth would have started on the substrate) terminating with non-fibrous clusters of materials (possibly a mixture of amorphous carbon and iron particles) as can be seen in Figure 15. This was seen in all samples regardless of type or treatment.

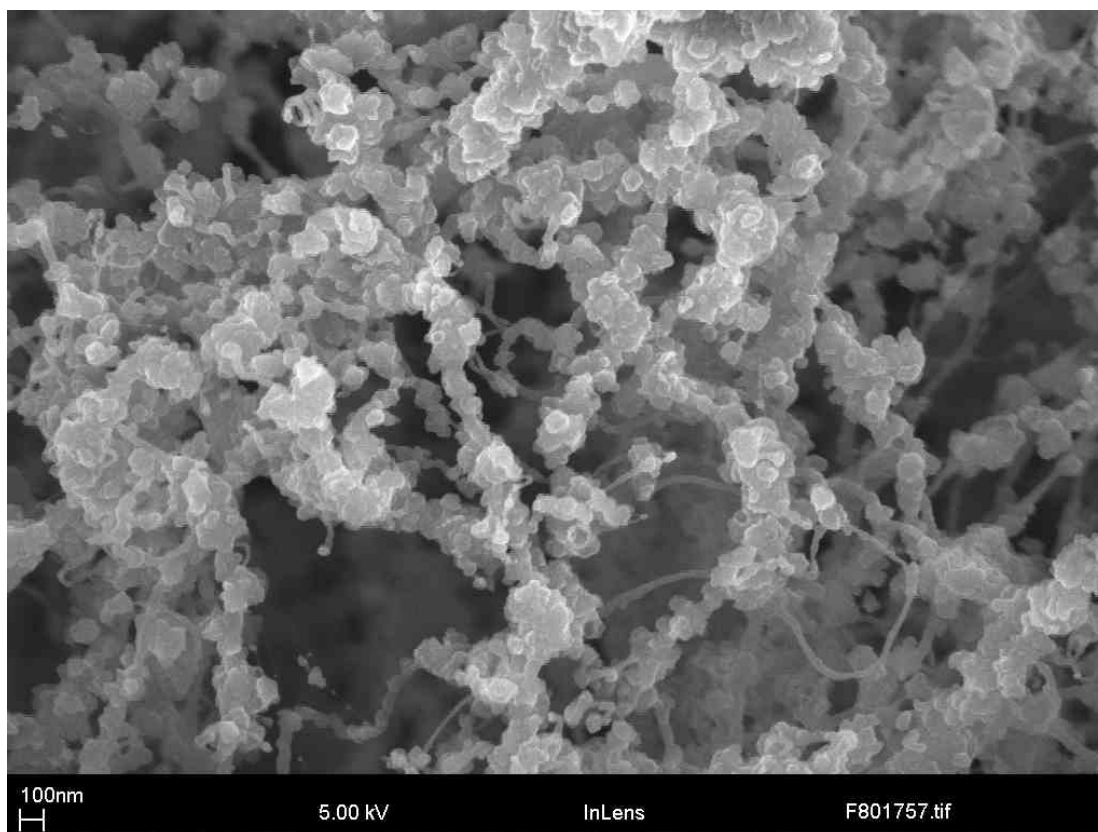


**Figure 15, SEM image from the top of a heat treated multiwall carbon nanotube carpet (HSCNT).** Chemical analysis of the samples using EDX, showed peaks of carbon, oxygen and iron for SCNT samples as shown in Figure 16, whereas the HCNT samples only showed

carbon peaks and very small oxygen peaks as can be seen in Figure 17. The heat treatment did not affect the fibre alignment and there were no differences in the appearance of the tubes compared with their as-produced counter parts. There were however, some differences measured in terms of the diameter of the tubes, which seemed smaller on average after heat treatment, and their length, which appeared to be slightly longer. It should be noted that the standard deviations were very large for these measurements, however as well as statistical variations, slight reduction in diameter can be due to the removal of impurities such as amorphous carbon from the outer radius of the tubes, either due to vaporisation or exfoliation based on different coefficient of thermal expansion (CTE) of graphitic carbon nanotubes and amorphous carbon as is reported in the literature [89]. The longer length is also thought to be either variation in length distribution in the original MWCNT carpets or possibly due to the high temperature heat treatment in the presence of the remnant catalyst particles (before they are removed for example during the temperature ramp up), which could have continued the CNT growth by using the un-reacted carbon or the amorphous carbon around the tubes.

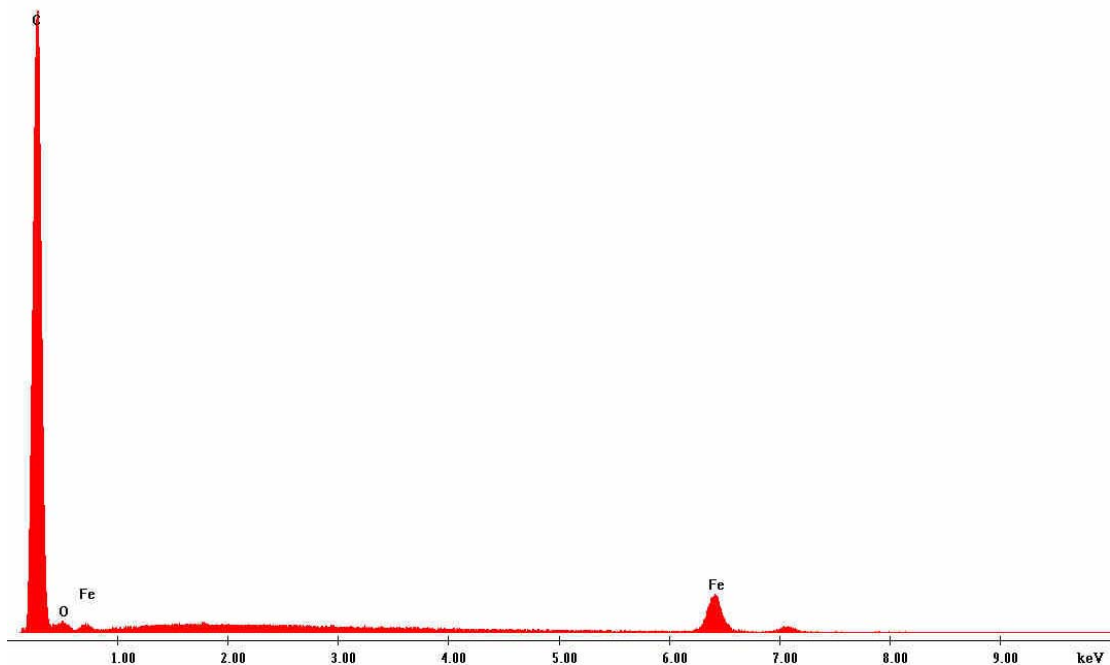


**Figure 16, a typical EDX element trace for the bottom of an as-produce aligned multiwall carbon nanotube (SCNT) carpet, showing an intense peak for carbon and two smaller peaks for iron and one for oxygen.**



**Figure 17, a typical EDX element trace from the top surface of a heat treated aligned multiwall carbon nanotube (HCNT) carpet, showing an intense peak for carbon and a very small peak for oxygen similar to figure 16, however, there are no detectable traces of iron in these samples.**

Acid treated carbon nanotubes (ACNTs) did not retain their alignment, as they had been subjected to severe agitation during the acid treatment process. These tubes, however, seemed to be more compacted, which is mainly due to wetting and subsequent drying that creates densely packed bundles [121]. Length measurements showed that acid treatment shortens the tubes considerably, mainly as a result of the mechanical damage caused by sonication [120]. The acid-treated tubes' structure also appeared slightly different from the structure of as-produced CNTs, as shown in Figure 18. Some tubes were joined or cross-linked through what is likely to be amorphous carbon and had coatings on them. The EDX signal highlighted the presence of carbon, oxygen and sulphur as well as two different iron signals on the surface of these tubes. The samples that were heat treated prior to acid treatment (AHCNT) seemed to have retained their alignment and compactness as shown in Figure 19 although shortened in length and reduced in diameter, more than both, only heat treated and only acid treated tubes. The external sheathing that had connected the ACNTs could not be seen in the AHCNTs, which increases the possibility of their origin being from the amorphous carbon and higher degree of its

functionalisation in ACNTs, hence a more intense sulphur signal. AHCNTs would have less amorphous carbon and more crystalline structure as a result of heat treatment and therefore will be more resistant to the acid treatment process. The EDX showed traces of both oxygen and sulphur on AHCNTs but no peaks for iron. The remnant iron catalyst from the production process is either inside the tubes and can only be removed by heat treatment at high temperatures or outside the tubes and can be washed away by the acid treatment process, this is why some traces of iron can be detected on ACNTs while there are no detectable traces of iron on AHCNTs.

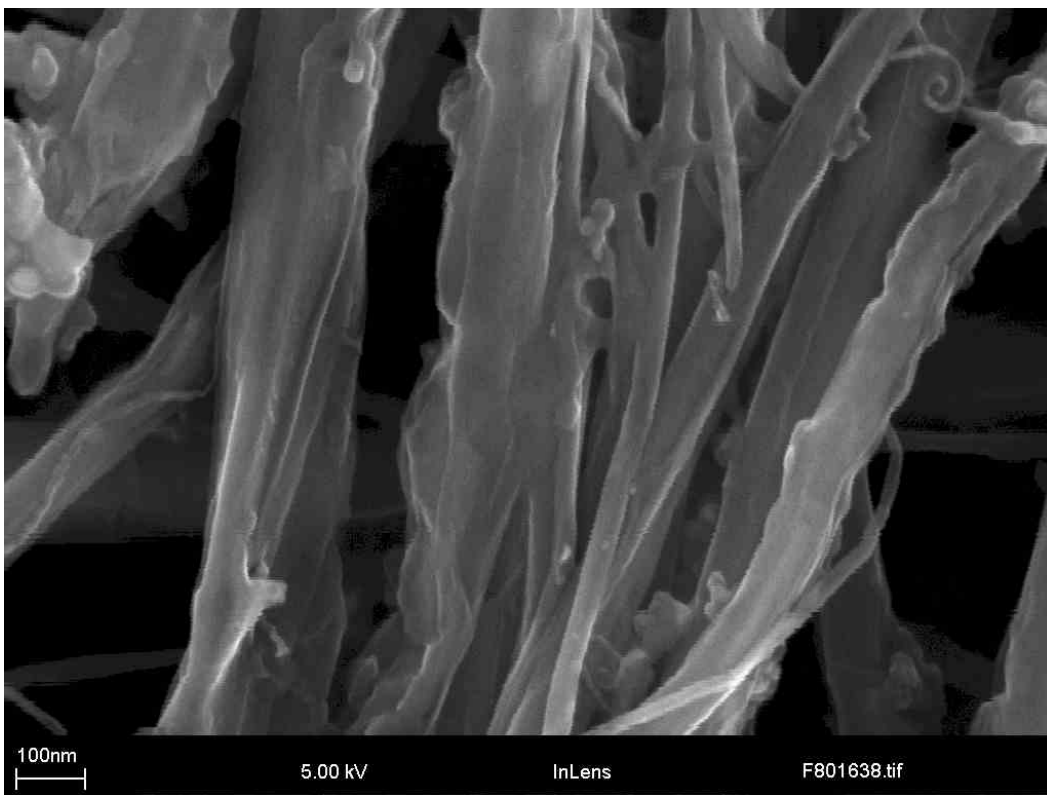


**Figure 18, side view of some of the acid treated multiwall carbon nanotubes (ACNTs) with a visible sheath of a material coating them.**

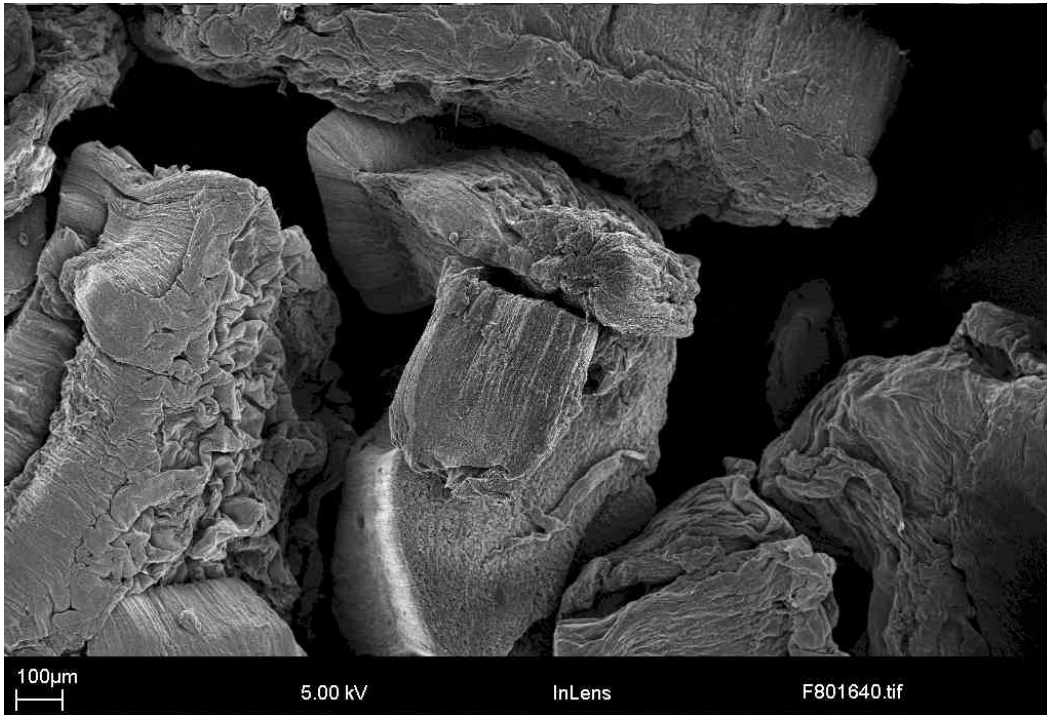


**Figure 19, SEM image of heat treated and then acid treated (AHCNT) multiwall carbon nanotube carpet fragments that have kept some degree of their alignment even after acid treatment.** The ball milling process produced very short tubes with an average length in the same order as the wavelength of the NIR laser used for the experiments in these trials i.e.  $\sim 1\mu\text{m}$ . The ball milling process was very severe and was found to mechanically shorten and break the tubes. The diameters of the ball milled tubes after heat treatment were very similar to that of the heat treated tubes, which had not been ball milled. An SEM image of the HBCNTs is shown in Figure 20. The EDX traces showed signals of carbon and oxygen.

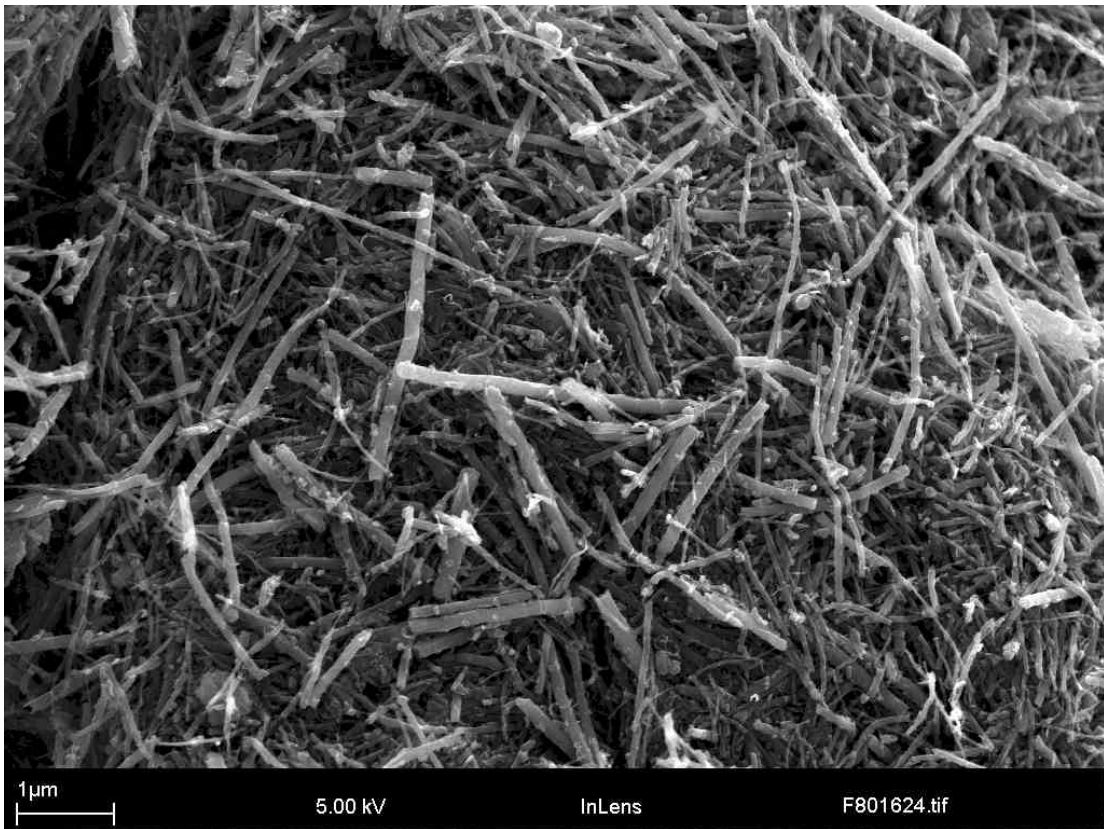


**Figure 20, SEM image of ball milled and then heat treated multiwall carbon nanotubes (HBCNTs).**

One possible explanation for the oxygen signal on heat treated tubes including those that were not ball milled, is the presence of adsorbed oxygen or CO<sub>2</sub>. An infrared spectroscopy of CO<sub>2</sub> that becomes permanently trapped in carbon nanotube bundles during thermolysis of partially oxidized samples has been reported by Matranga et al [122]. Their results pointed to a sequential filling of adsorption sites in opened nanotubes. Some reports also suggested that CO<sub>2</sub> at high temperature can act as an oxidizing agent for removing carbon based impurity species from CNTs [123].

Images of CB and SWNT particles were also taken for structural comparison. The CB particles were in an agglomerated form as can be seen in Figure 21, consisting of particles with diameters of approximately 75nm on average. The EDX traced oxygen, small amount of silicon (possibly due to the manufacturing methods which could have used silica) and sulphur in addition to carbon on the sample's surface.

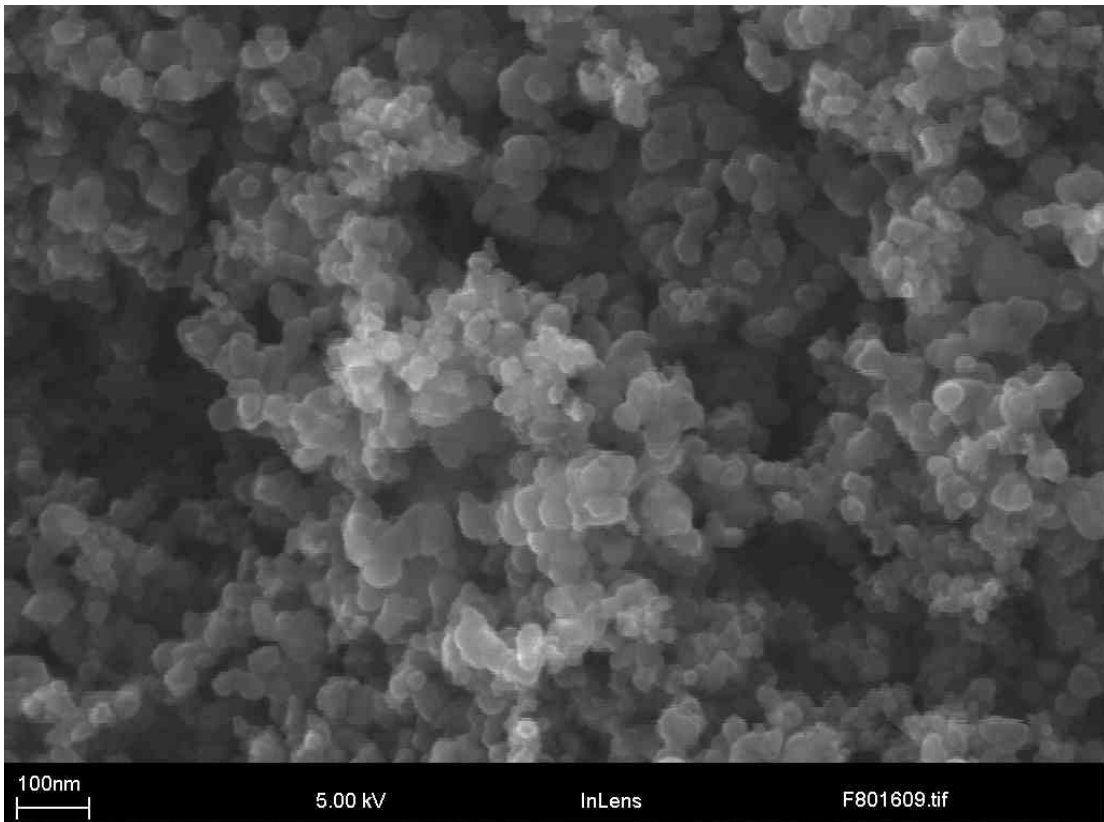


**Figure 21, SEM image of carbon black (CB) particles.**

The presence of sulphur and oxygen on carbon black and the acid treated samples can be due to the treatment and purification process used, which involves the use of different chemicals, particularly sulphuric acid.

The SWNT fibres had a spindled-yarn-like structure as shown in Figure 22. They had small diameters and the EDX trace showed the presence of sulphur and oxygen as well as the main carbon peak on their surfaces.

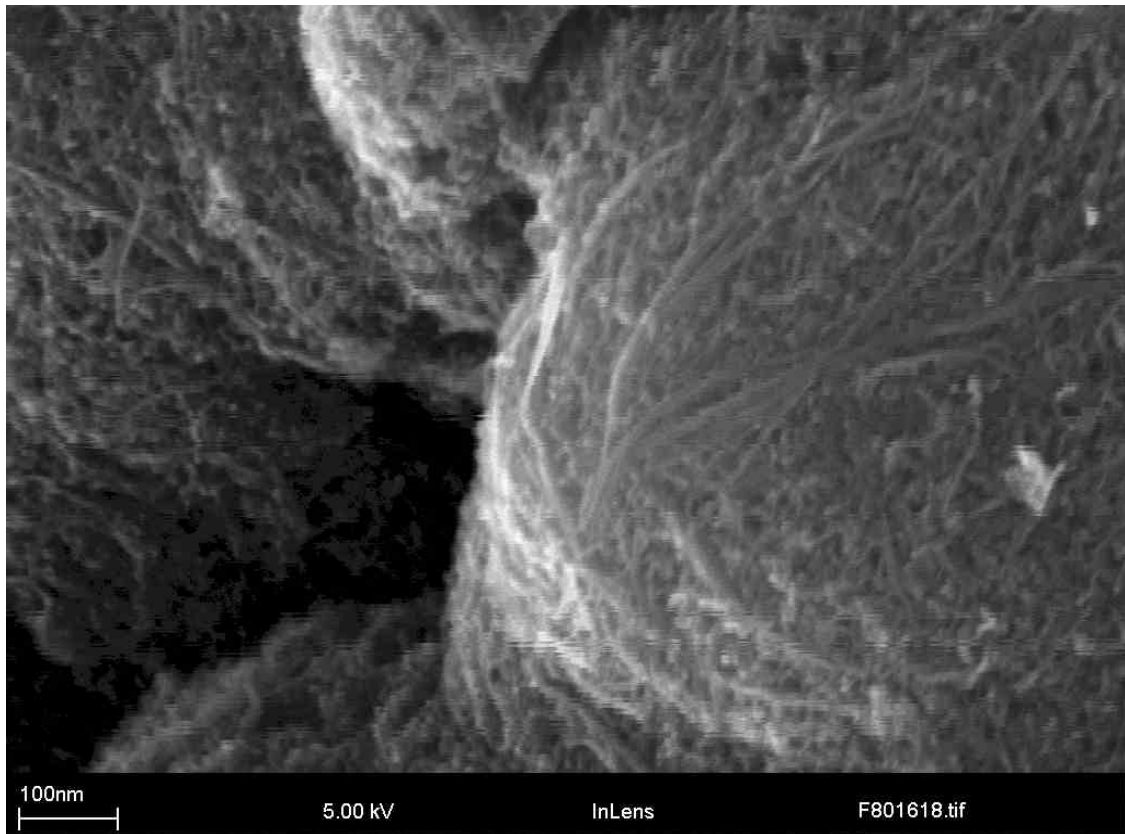


**Figure 22, SEM image of single wall carbon nanotubes (SWNT).**

FTIR studies have shown that SWNTs contain adsorbed oxygen in the form of oxide or hydroxide species, some of which can be removed at temperatures of 450°C in an ultra high vacuum environment, although it would be difficult to remove all traces of oxygen even at much higher temperatures [124].

### **3.3.2. TEM**

A few samples were prepared by dispersing WCNTs in ethanol using an ultrasonic bath for 2 minutes. A small amount of the dispersion was then removed and diluted in more ethanol. A carbon-coated copper grid was dipped into the solution and a few tubes were picked up by the grid and examined using a JEOL CX 200 TEM (Figure 23).

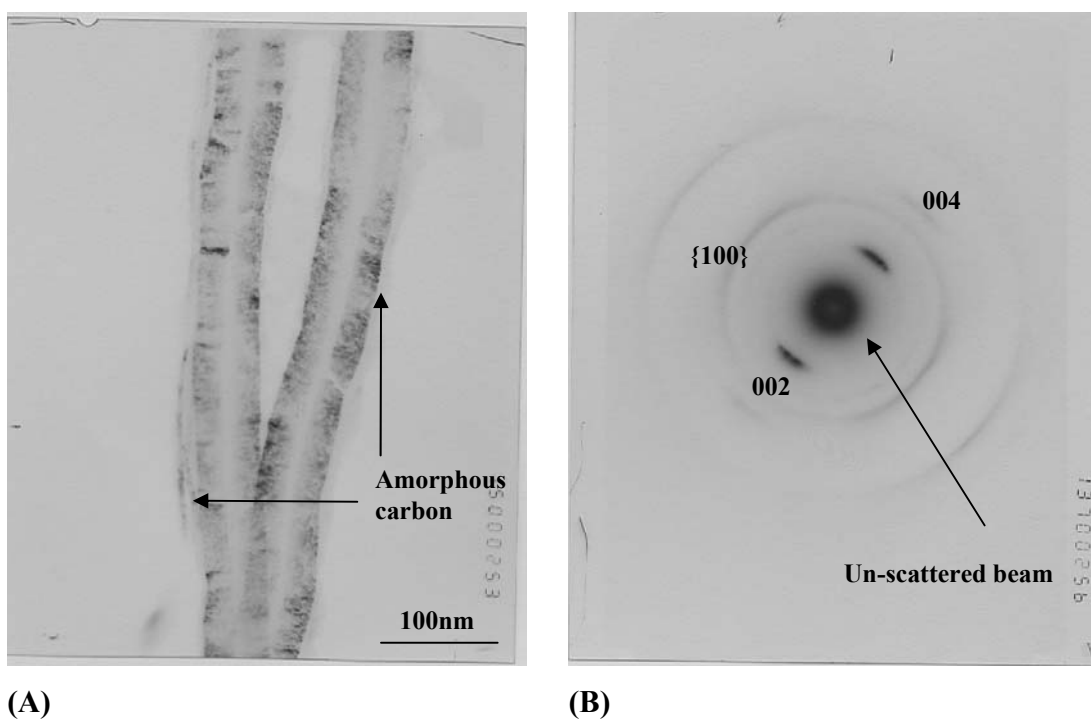


**Figure 23, (A) dark field TEM image of two WCNTs at 150K magnification and (B) the corresponding diffraction pattern for the tube in (A).**

The TEM images showed thick wall sections with an opening in the middle of the tubes indicating that the material produced were multiwall tubes. The diameter of the MWCNT in 23(A) was approximately 60 nm, with the hollow core having a diameter of 14 nm approximately. Taking the carbon atomic radius for  $sp^2$  hybridisation as 0.073 nm [125] and the interlayer spacing in graphite as 0.334 nm [126] there will be approximately 50 concentric nanotubes in the MWCNT imaged by the TEM. The light regions could be attributed to by the presence of vacancies and defects in the crystal structure. The tubes were not perfectly straight and a thin layer of coating, possibly amorphous carbon, was observed on their surface as well as defects along the their length. The diffraction pattern of the tubes (Figure 28B) showed short arcs in the equator which are the (002) first order and (004) second order diffraction planes perpendicular to the nanotube axis. They are produced by electron diffraction from each and two sets of parallel quasi-planar graphene sheets. Such planes seen edge on act as two parallel line gratings for the electron waves. The continuous circles are the diffractions from the rest of the two stacks of honeycomb lattices. The first continuous line from the centre could be due to {100} planes

corresponding to the basal plane of the unit cell in graphite. This is a continuous line as opposed to discrete spots, indicating different chiralities amongst the layers [49].

### 3.3.3. Raman spectroscopy

A Renishaw 1000 Ramascope spectrometer with a 514 nm wavelength (green visible light) excitation laser was used and several spectra were taken from different samples. Figure 24 shows a spectrum for HBCNT samples. The intensities and wavenumber of the main peaks are listed in Table 2.

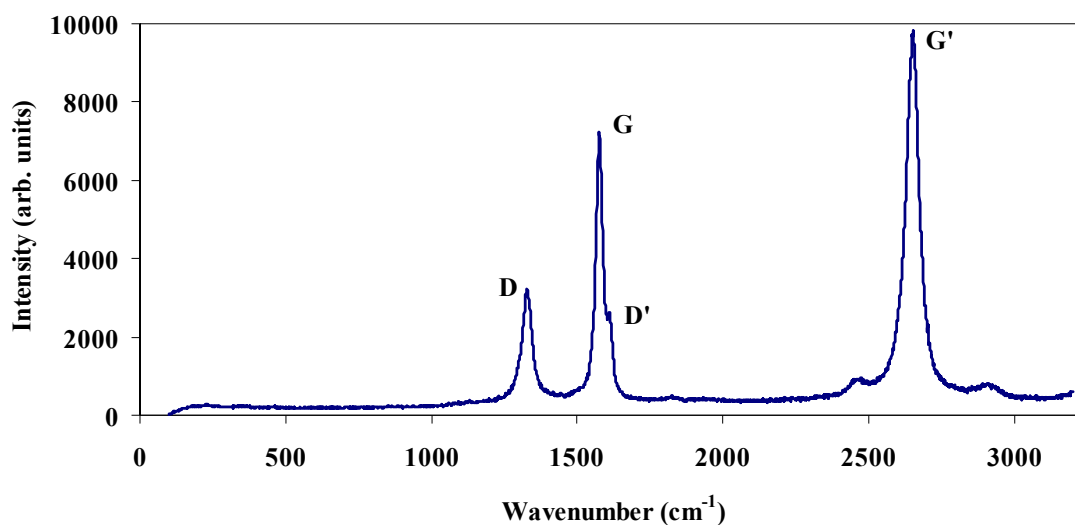


Figure 24, the Raman spectrum of ball milled and then heat treated multiwall carbon nanotube samples (HBCNT) using a 514nm wavelength laser radiation.

The main features of a typical MWCNT, namely G', G, D and D' peaks were identified in the spectra of all MWCNTs. The lack of radial breathing mode (RBM) peaks was another confirmation of the existence of MWCNTs with rather large diameter inner tubes. There were however, low intensity peaks at 150 cm<sup>-1</sup> wave numbers and below for some of the multiwall samples. Such peaks have been previously reported to indicate the presence of more than 10 walls in MWCNTs [76], which is indeed the case in our samples.

**Table 2, Summary of Raman spectroscopy results on all of the samples, including intensities (arbitrary units) and wave numbers ( $\text{cm}^{-1}$ ) for various observed peaks.**

Sample	$\text{Wn}^*$ / $\text{cm}^{-1}$	$I_D$ /arb. units	$\text{Wn}$ / $\text{cm}^{-1}$	$I_{D'}$ /arb. units	$\text{Wn}$ / $\text{cm}^{-1}$	$I_G$ /arb. units	$\text{Wn}$ / $\text{cm}^{-1}$	$I_{G'}$ /arb. units
HBCNT	1327	3195	1613	2586	1577	7247	2648	9668
HCNT Bottom	1334	4074	1613	2676	1583	7221	2662	8423
HCNT Side	1331	3909	1613	2747	1581	6699	2656	8279
SCNT Bottom	1328	2565	1613	2963	1581	6243	2656	7457
SWNT	1322	3985	1613	4113	1590	8175	2613	3637
SCNT Side	1334	3187	1613	3529	1578	6911	2661	8818
HCNT Top	1330	6828	1613	3650	1581	6635	2659	6449
AHCNT	1333	7435	1613	4727	1584	8270	2663	10576
SCNT Top	1325	5215	1613	3385	1577	5112	2646	3212
ACNT	1336	10103	1613	8665	1583	1100	2661	10464
CB	1340	1366	1613	1076	1587	1332	NA	NA

\* wavenumbers

Carbon black's spectrum did show D and a single G peak with no clear G' or D', as shown in Figure 25. Although the D and G peaks for carbon black had very similar wave numbers as D and G peaks for the MWCNTs samples, the intensity (I) of both peaks were very similar. The  $I_D/I_G$  ratios are thought to be a qualitative indication of the amount of defects present, the results for carbon black samples, therefore, are not surprising.

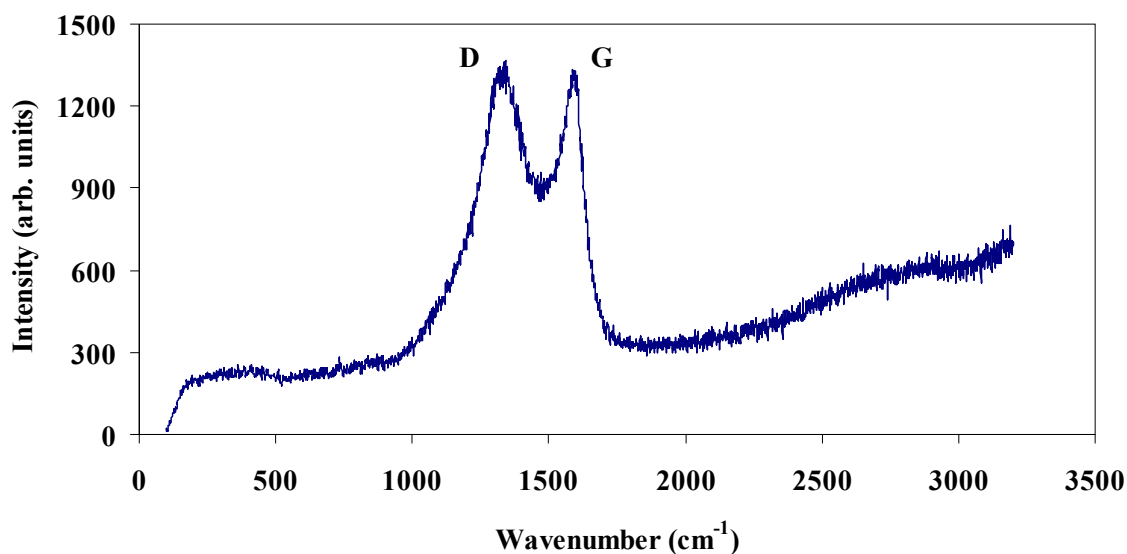


Figure 25, Raman spectrum of carbon black (CB) using a 514nm wavelength laser radiation.

The spectrum from SWNTs also showed the expected peaks. The RBM peak was also visible as shown in Figure 26.

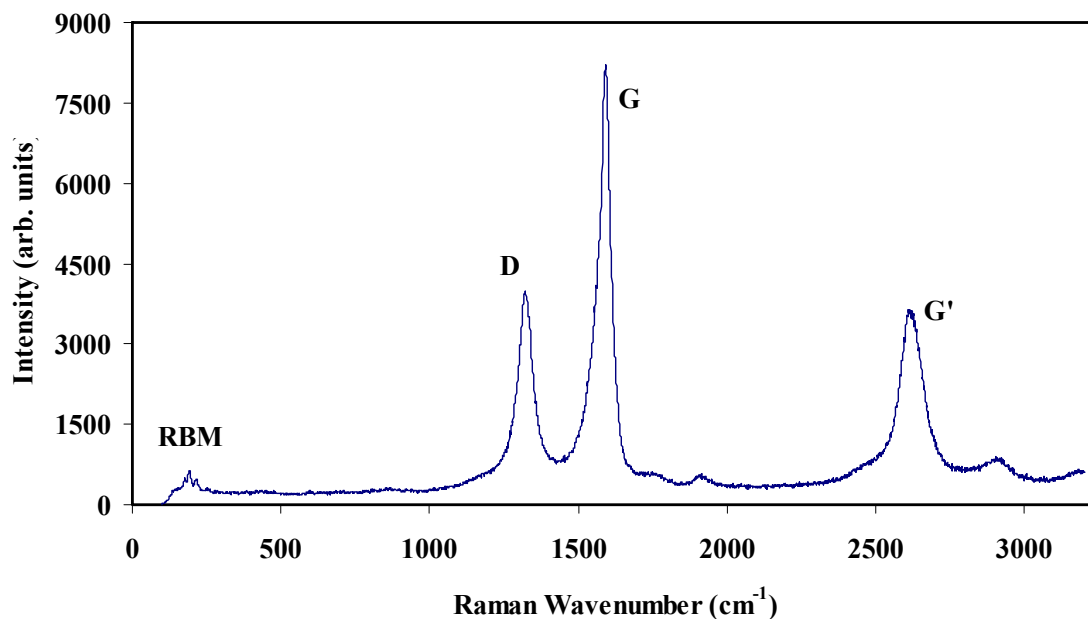


Figure 26, Raman spectrum of SWNT using a 514nm wavelength laser radiation.

The intensities of the peaks varied in all samples, which could be particularly seen by measuring the  $I_{G'}/I_G$  ratio, this ratio seemed to be higher for heat treated multiwall tubes particularly those with shorter length suggesting that a better resonance was achieved as

well as a higher degree of graphitisation in these samples. The  $I_D/I_G$  (a qualitative measure of imperfections or presence of defects in the tubes) and  $I_{D'}/I_G$  (a qualitative measure of the reduction in alignment in the graphitic layers such as distortion and strains in the structure) ratios are given in Table 3.

**Table 3,  $I_D/I_G$  and  $I_{D'}/I_G$  ratios for the different samples and sample orientation.**

Sample	$I_D/I_G$	$I_{D'}/I_G$
HBCNT	0.36	0.44
SCNT Side	0.51	0.46
SWNT	0.51	0.49
HCNT Bottom	0.37	0.56
SCNT Bottom	0.47	0.41
HCNT Side	0.41	0.59
AHWCNT	0.57	0.90
AWCNT	0.79	0.92
SCNT Top	0.66	1.02
HCNT Top	0.55	1.03

The  $I_D/I_G$  ratios seem to be small for heat treated tubes and large for acid treated tubes. Also when the beam was incident to the top of the tubes, the ratios are largest regardless of any post production treatment, than for the Raman laser incident to the bottom and the side of the tubes. If this ratio is taken as a measure of the degree of disorder in the crystalline structure or the amount of imperfection and defects, then the samples that have been heat treated in general have better crystallinity and fewer impurities and are more graphitised. Possible correlation between these structural characteristics and the NIR laser absorption and heating of the samples are explored in section 5.3.

#### **3.3.4. FTIR**

FTIR transmission measurements were made with a Bruker Tensor 27 FTIR equipment, by preparing MWCNT/KBr (99+% Acron Organics) pellets at many different MWCNT wt% concentrations. Many attempts were made to get a clear spectrum, however this was difficult due to the high IR absorption of MWCNTs, consequently the lowest concentration of pellets at 0.027wt% produced the best results. The pellets were examined under SEM to ensure presence of MWCNT fibres as shown in Figure 27.



**Figure 27, SEM image of a specimen taken from a pellet of multiwall carbon nanotubes (MWCNTs) and KBR.**

More than 50 spectra were taken and apart from atmospheric corrections no other manipulations were performed. Figure 28 shows a spectrum of as-produced MWCNTs covering the complete spectral range from  $500\text{cm}^{-1}$  to  $4000\text{cm}^{-1}$ .

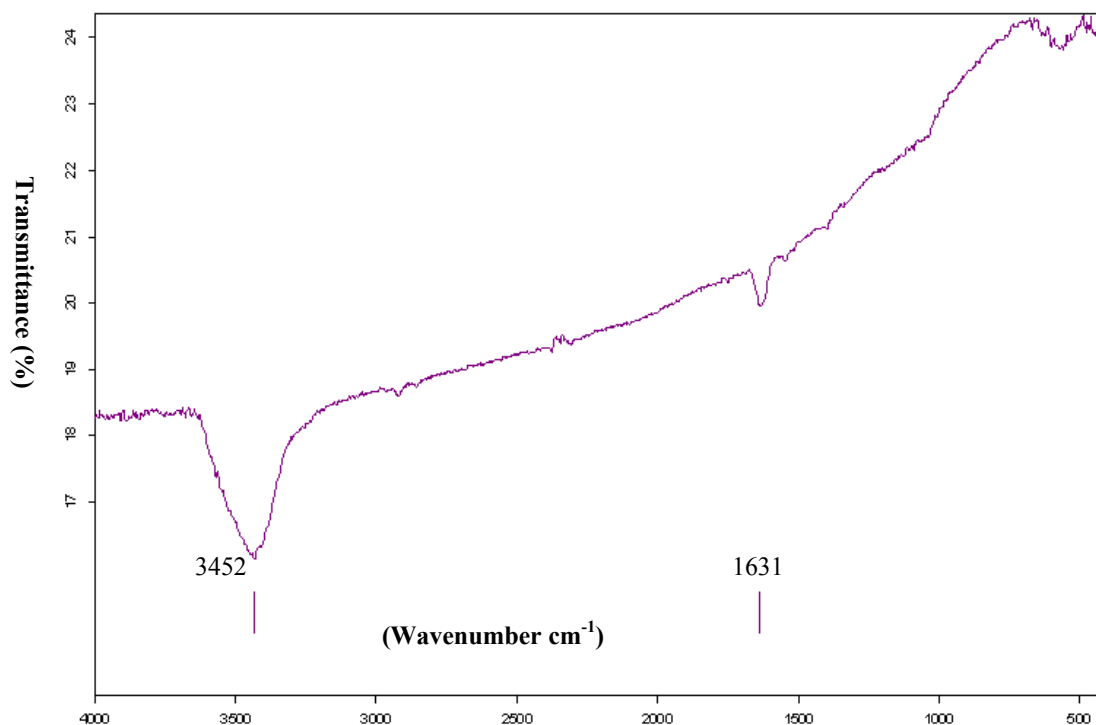


**Figure 28, a FTIR spectrum of as-produced multiwall carbon nanotube samples (MWCNTs).**

Due to the intrinsically high IR absorption by MWCNT samples across the spectral range, the transmittance spectrum is generally very flat. However, a small peak could be seen at  $1631\text{cm}^{-1}$  for all samples, which has been previously attributed to adsorbed water [112], this peak was present in all samples including those that had been dried at  $120^{\circ}\text{C}$  prior to taking the FTIR measurements. Another prominent peak was the free water peak at  $3452\text{cm}^{-1}$  and was more intense for ACNT samples.

The IR absorption of MWCNT samples was observed to be more prominent at lower wavelengths in the IR spectrum, (4000 wavenumber) in the FTIR analysis, which corresponds to  $2.5\ \mu\text{m}$  wavelength (twice as much as the laser wavelength used in our experiments) showed a smaller transmittance percent than the longer wavelength of  $20\ \mu\text{m}$  (500 wavenumber).

### 3.3.5. Differential scanning calorimetric analysis

One of the important properties of the samples that needed to be evaluated was their heat capacity to ensure accurate estimation of laser heating. The heat capacity of different samples were measured using TA Instruments Q1000 equipment and modulated DSC method [127]. The DSC signals used, included, heat flow and heat capacity as measured in the standard mode plus reversing heat capacity as measured by Modulated DSC (MDSC). In the standard mode, heat flow is continuously converted to heat capacity as described in Equation 33.

$$C_p = \frac{\text{Heat Flow}}{\text{Heating Rate}} \times K \quad (32)$$

Where  $C_p$  is specific heat capacity ( $\text{Jg}^{-1}\text{K}^{-1}$ ), heat flow is in  $\text{Wg}^{-1}$ , heating rate is in  $\text{Kmin}^{-1}$  and  $K$  is a calibration constant.

Reversing heat capacity (MDSC mode) is measured in the same experiment used to measure DSC heat capacity and is usually more accurate and reproducible because of the way it is measured and provides a check of the heat capacity as measured in the faster DSC single-run approach.

$$\text{Reversing heat capacity} = (\text{Amplitude of modulated heat flow}/\text{Amplitude of modulated heating rate}) \times K \quad (33)$$

By using amplitudes (total change) rather than absolute values for the heat flow and heating rate signals, the effects of baseline curvature are eliminated. Nitrogen was used as the purge gas at  $50 \text{ mLmin}^{-1}$  flow rate. Sapphire was used for calibration standard at  $20^\circ\text{Cmin}^{-1}$  from  $0$  to  $300^\circ\text{C}$ . MDSC isothermal was then performed on the samples at  $56.8$  and  $256.8^\circ\text{C}$ . The results are shown in Table 4.

**Table 4, Resultant heat capacity values for different sample from the modulated DSC analysis.**

Sample name	Pan weight/mg	Lid weight/mg	Sample weight/mg	Cp/ Jg <sup>-1</sup> K <sup>-1</sup>	Comments
WCNT	12.446	10.179	1.233	0.440	Random orientation
HCNT	12.173	10.037	2.152	0.727	Straight carpet was used
HWCNT	12.370	10.263	1.674	0.721	Random orientation
ACNT	12.232	10.325	3.879	0.851	Random orientation (weight fluctuations, at the start due to the presence of water )
AHCNT	12.304	10.288	4.547	2.225	Random orientation (weight fluctuations, at the start due to the presence of water )
HBCNT	12.231	10.242	3.578	0.732	Random orientation
SWNT	12.177	10.101	3.119	0.801	Random orientation
CB	12.171	10.070	5.755	0.788	Random orientation

The results for most of the samples showed heat capacity values similar to that of graphite, varying from 0.72 to 0.85 JK<sup>-1</sup>g<sup>-1</sup> (with an average value of 0.757 JK<sup>-1</sup>g<sup>-1</sup>) for different samples apart from AHCNT and WCNT, which showed values of 2.23 and 0.44 JK<sup>-1</sup>g<sup>-1</sup> respectively. In the case of the WCNTs it is possible that the heat capacity is influenced by the presence of remnant iron catalyst particles (the heat capacity of iron is 0.45 Jg<sup>-1</sup>K<sup>-1</sup> [127]). The reason for a large variation in the AHCNT samples is not clear. One possible explanation is the presence of trapped water due to the acid treatment process. Some fluctuations in weight of the sample were recorded as it was heated during the test, however similar fluctuations were also observed for the ACNT samples but did not result in such high heat capacity values. Another reason could be that the structure of the tubes had changed due to the sequence of the treatments. Initially, the heat treatment would have had increased crystallinity and removed iron particles and impurities such as amorphous carbon and then the acid treatment would have reduced their length and introduced some chemical bonds and defects to their structure. The combination and the sequence of these treatments may have contributed to the increase in heat capacity of the AHCNT samples.

### 3.3.6. Thermogravimetric analysis in air and helium

A TA instruments Q500 TGA was used to analyse the mass loss with temperature for the samples in air with ramping rate of 25 K min<sup>-1</sup> up to 1000°C. The balance gas for all experiments was He with the flow rate of 80 ml min<sup>-1</sup>. The sample gas flow rate was set as 120 ml min<sup>-1</sup> and platinum pans were used to hold the sample in the furnace. This

analysis was also used to measure the amount of residual iron in the samples. Figure 29 shows the TGA results for some of the samples heated in air while the total weight loss and an arbitrary 5% weight loss temperature are listed in Table 5.

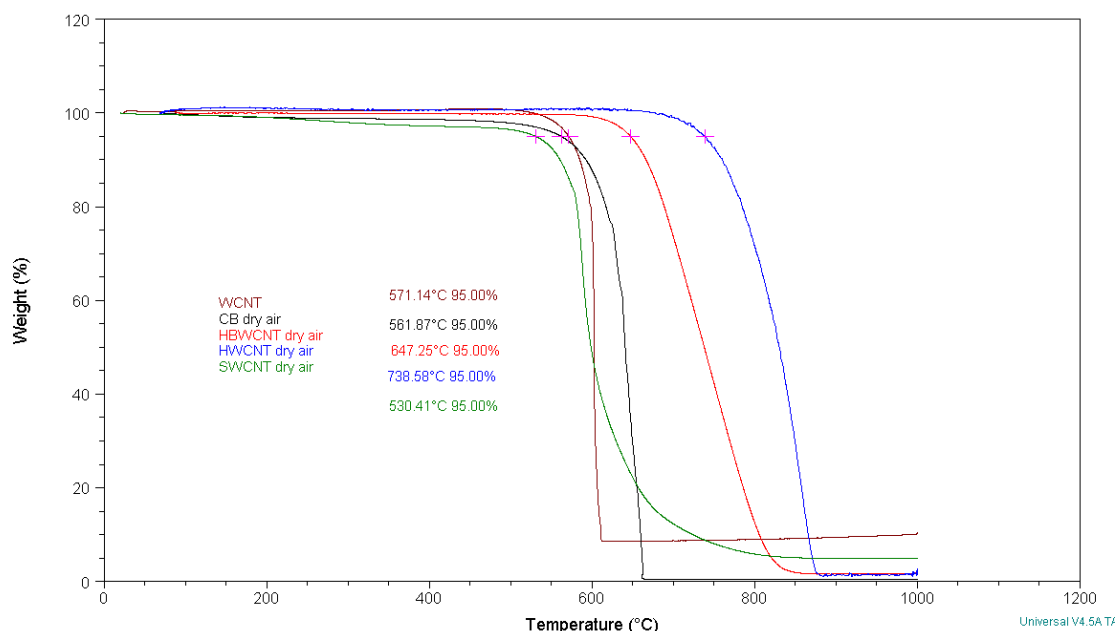


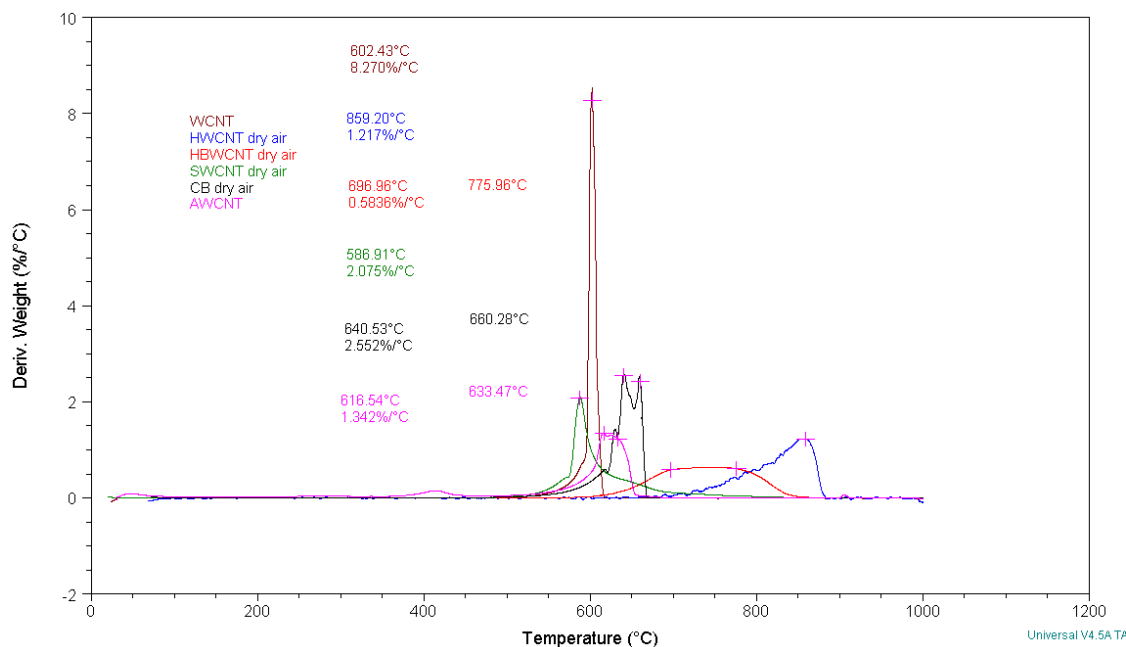
Figure 29, TGA results in terms of weight loss with temperature for heating different samples in air.

Table 5, Results of TGA analysis in air in terms of oxidation temperature and mass residue.

Sample	Mass residue/%	Mass residue/mg	5% Mass loss temperature/°C
WCNT	6.1	0.1	571
ACNT	5.3	0.4	NA due to high water content
SWNT	4.6	0.3	530
HBCNT	0.5	0.0	647
HCNT	1.3	0.0	738
CB	0.5	0.0	561
AHCNT	0.2	0.0	NA due to high water content

The results showed a slight initial decrease in weight for almost all samples at less than 200°C which is due to the evaporation of adsorbed water and possibly related to the peak of free water in the IR spectra at 3450 cm<sup>-1</sup>. SWNTs had the lowest oxidation temperature followed by CB and then WCNT, although the rate of oxidation was highest for WCNT (based on the slope of the curves) amongst all samples, as can also be seen from the plot in Figure 30. The heat treated tubes had higher oxidation temperatures than other samples with the pristine heat treated tubes (HCNT) being oxidised at some 100°C above the ball

milled ones. The residual weight in the samples is thought to be mainly from remnant iron particles initially used as catalysts as has been reported in the literature [128] and as confirmed by the EDX analysis on the residues from WCNT samples as shown in figure 31.



**Figure 30, in air TGA results in terms of derivative mass with temperature against temperature.**

AHCNTs had lower amounts of residues than as-produced samples or the samples that had been through only one treatment process i.e. either heat or acid treatment. AHCNTs had gone through two processes that would have reduced the iron content both from the surface and from the inside of the tubes significantly. The heat treatment process would reduce both the iron inside the tubes and the iron particles on the surface of the tubes, while the acid treatment would remove the iron particles remnant on the surface. CB and HBCNTs had more residues than AHCNTs but less residues than HCNTs. It is possible that due to the shortening of the tubes during the ball milling process in HBCNT, previously trapped iron particles are exposed in the subsequent heat treatment process, and are consequently removed easier by the heat treatment process. SWNTs had a considerably higher amount of residues than HCNTs, however, even higher amounts of residues were seen in ACNTs and the maximum amount was associated with WCNTs. The samples with higher iron content showed slight weight gains after they had lost most of their mass due to oxidation. This slight weight gain is thought to be due to the

oxidation of remnant iron particles, resulting in an increase in weight. A similar regime was seen for the heat treated tubes with the difference that the annealing had removed majority of the amorphous carbon and it had improved the crystallinity, which subsequently increased the oxidation temperature. The remaining weight due to very small amounts of iron particles in the heat treated samples was therefore negligible and increased only slightly by producing a small amount of iron oxides. The initial mass loss for ACNT and AHCNT could not be recorded accurately as both samples contained some dampness from the acid treatment process and the initial mass loss was very large at low temperatures (above 100°C) due to water evaporation.

By plotting the derivative weight against temperature as was shown in Figure 30, the rapid weight loss of WCNTs can be observed from the intense peak at around 600°C. The other samples have a shorter, right-shifted peak. It can be seen that carbon black has two peaks which are some 20°C apart and HBCNT has a plateau between 696°C and 775°C. This is thought to be due to the variation in length of the HBCNTs in the sample, leading to the spreading of weight loss over a larger temperature range. In general it can be seen that samples with higher iron content and defects (based on the Raman results) have a sharper weight loss peak and lower oxidation temperatures. The residue from the WCNT sample, was examined using EDX analysis and it was confirmed that the remnants are mainly iron oxide as can be seen in Figure 31.

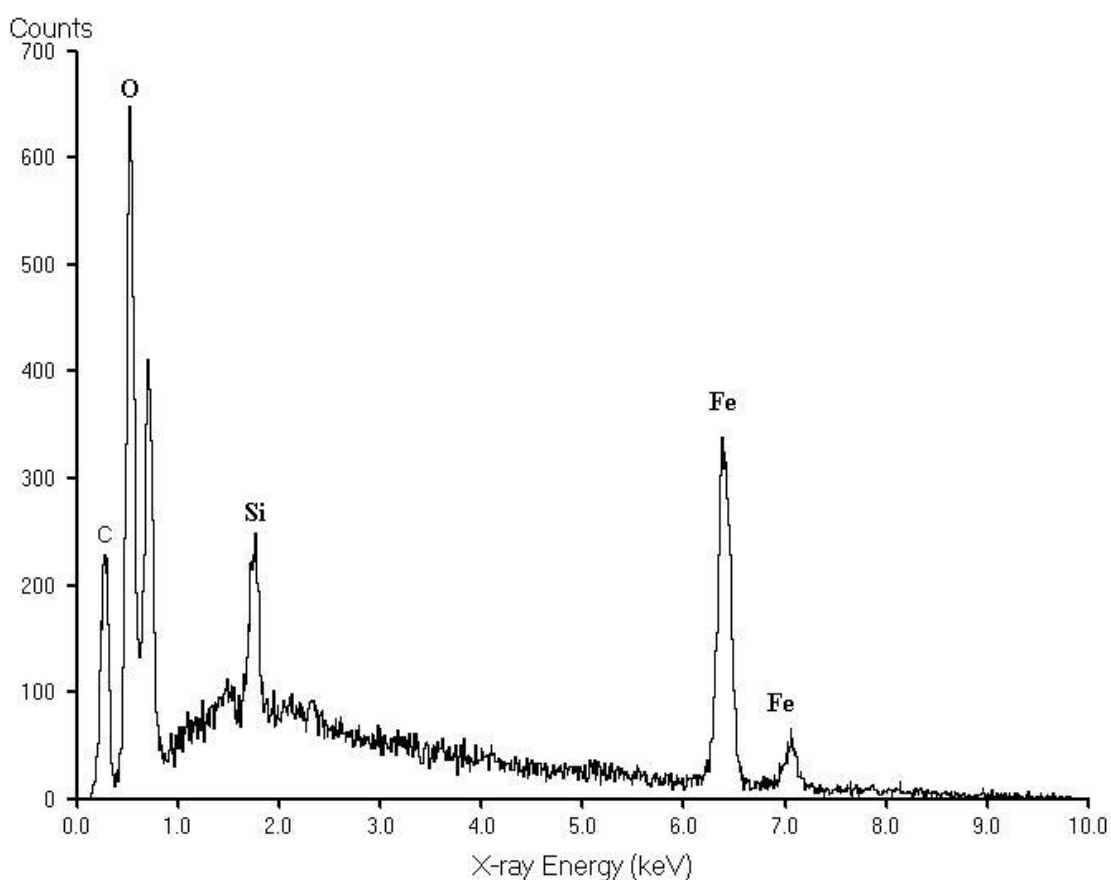


**Figure 31, EDX from the as-produced multiwall carbon nanotube remnants after TGA in air environment.**

Conducting a TGA analysis on the samples in He under the same parameters did not show any significant weight changes. The TGA test temperature was then increased to 1000°C and dwelled at this temperature for 30 minutes, after the dwell time some small weight changes could be seen in the samples as shown in Figure 32.

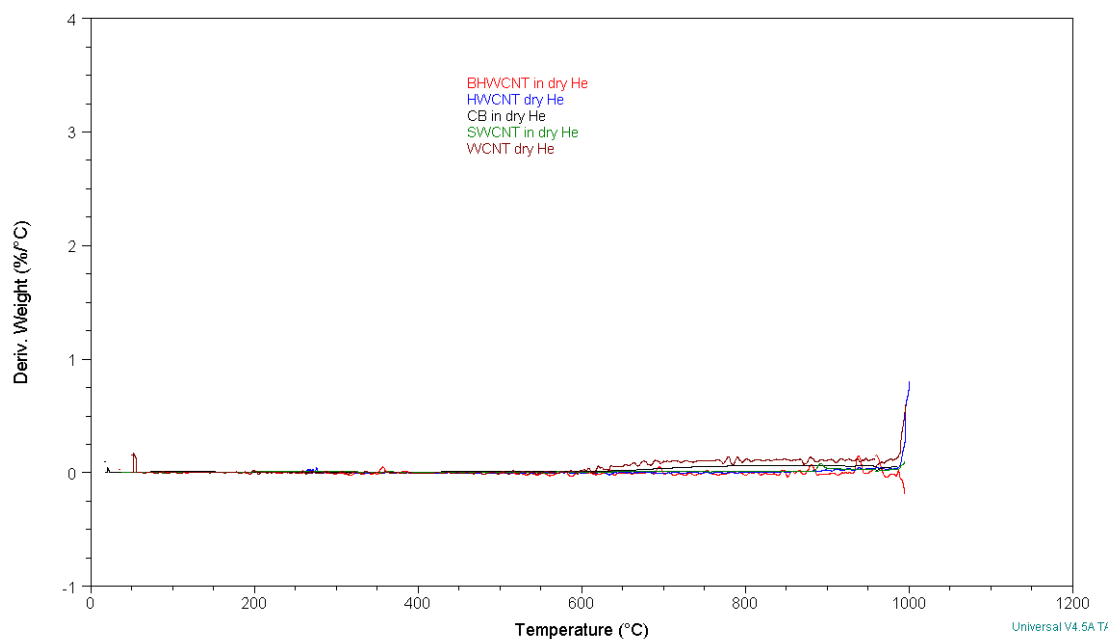


**Figure 32, plot of the derivative of weight with temperature against temperature for the samples analysed by TGA in He environment, showing weight changes towards the end of the dwell period of 30min at 1000°C.**

The small mass change at very high temperatures is thought to be due to the reaction of the samples with water, oxygen or carbon dioxide present as adsorbed species as described earlier and reported in the literature [123,124]. The MWCNTs have a large surface area and will be highly reactive with even small amounts of any oxidising agent at high temperatures. The presence of iron particles in materials such as ACNTs and WCNTs can further catalyse this reaction. The tests were repeated with a mass spectrometer (MS) connected to the TGA chamber and collecting the evolved gasses carried through by the flowing He, the results of which are shown in Figure 33.

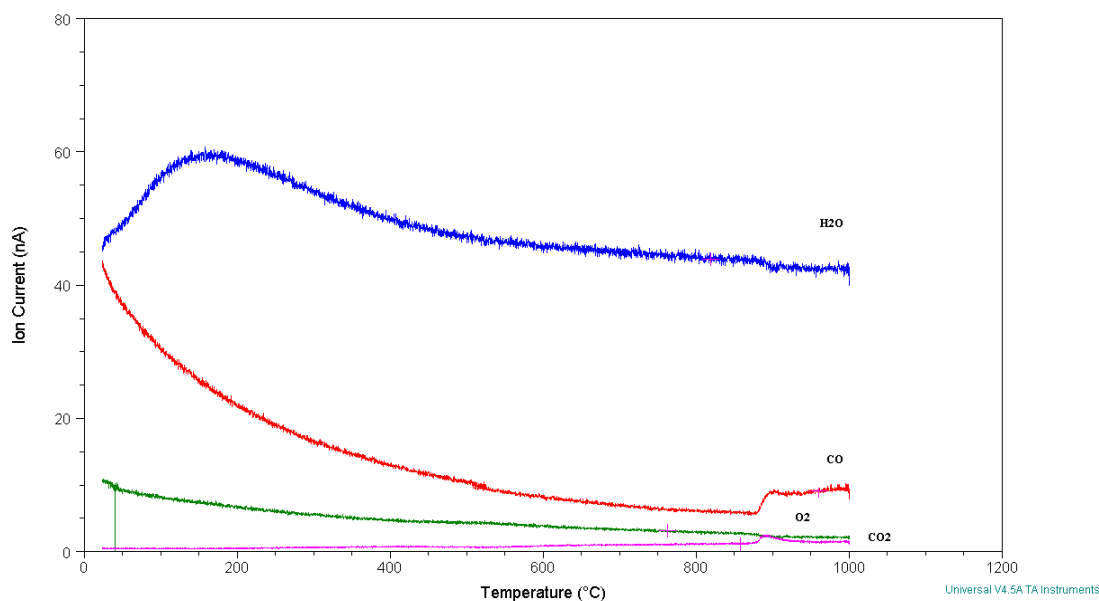


**Figure 33, mass spectrometer signal for the gases evolving from the TGA furnace when conducting TGA on as-produced carbon nanotubes in He environment. The signals show an increase in the amounts of CO and CO<sub>2</sub> and a corresponding reduction in the amounts of H<sub>2</sub>O and O<sub>2</sub>, as a temperature of around 900°C is reached and following a dwell period at this temperature.**

The mass spectrometer showed an increase in CO and CO<sub>2</sub> signals and a reduction in O<sub>2</sub> and H<sub>2</sub>O. It can be seen that the water signal is more prominent than others showing the presence of moisture in the TGA furnace or the He gas. The presence of CO signal and its associated increase at high temperatures, corresponding to a reduction in intensity for the water signal, indicates the possibility of a water-gas reaction taking place. This was further investigated using a modulated TGA (MTGA) method as described in the following section

### **3.4. Modulated Thermogravimetric Analysis in water-saturated helium**

Before testing the response of aqueous suspension of MWCNTs to NIR laser radiation, the validity of the water-gas reaction model for MWCNTs was tested by heating some of the MWCNTs in an environment of helium saturated with water vapour in TGA and monitoring the resulting liberated gas with a mass spectrometer.

#### **3.4.1. Experimental set up**

Helium gas from a bottle was first passed through a sealed bubbler filled with boiled deionised water and the resultant wet helium was then run through the TGA as the

sample gas. The TGA was connected to a Pfeiffer Vacuum ThermoStar mass spectrometer, which was continuously collecting samples from the TGA furnace. A schematic of the experimental set up is given in Figure 34.

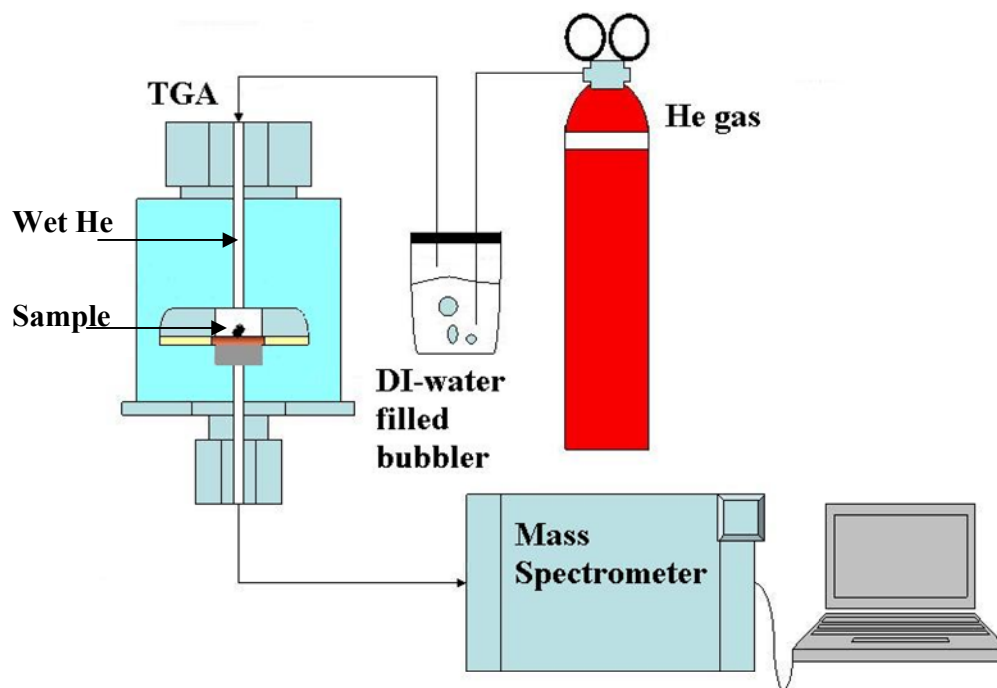


**Figure 34, schematic of the Modulated TGA in water saturated helium experimental set up**

MTGA makes use of an oscillatory temperature programme to obtain kinetic parameters during a mass loss [129]. MTGA was performed using a TG Q500 V6.7 analyser from TA Instrument. The TGA was equipped with a standard (Hi-Res<sup>TM</sup>) furnace to provide the close coupling between the test specimen, furnace and temperature sensor required for rapid temperature modulation. A sample of the produced MWCNT, weighing 4.214mg, was loaded on the platinum pan of the instrument. The balance gas was helium at a flow rate of 40.0 ml min<sup>-1</sup> and the sample gas was water-saturated helium from the bubbler at a flow rate of 60.0 ml min<sup>-1</sup>. The mass spectrometer was continuously monitoring the gases in the TG furnace and registering signals for water, hydrogen, carbon monoxide, carbon dioxide and oxygen, even before the TGA furnace was turned on. After the signals had reached a plateau the initial isotherm at room temperature started for 30 minutes to further flush the system with the sample gas. The high resolution MTGA was then started with a modulation amplitude of  $\pm 5$  K, over a period of 200s and

an underlying heating rate of  $4.00\text{ }^{\circ}\text{C min}^{-1}$ . The MTGA was continuously altering the heating rate in response to the sample's measured rate of mass loss. In temperature ranges where the mass was stable, the sample was heated rapidly at  $25^{\circ}\text{Cmin}^{-1}$ , while at the onset of a mass loss, the heating rate slowed in response to the increasing rate of mass loss. As the reaction reached completion, the heating rate increased (in response to the decreasing rate of mass loss). The experiment continued until it reached  $1000^{\circ}\text{C}$  and was followed by an isotherm at this temperature for 10 minutes before terminating. Meanwhile, the mass spectrometer was continuously recording signals from the furnace to identify the gaseous species that were evolving or being consumed while the sample was being heated.

### 3.4.2. Results and analysis

The initial purging signals taken from the mass spectrometer for oxygen, carbon dioxide, hydrogen and water are shown in Figure 35.

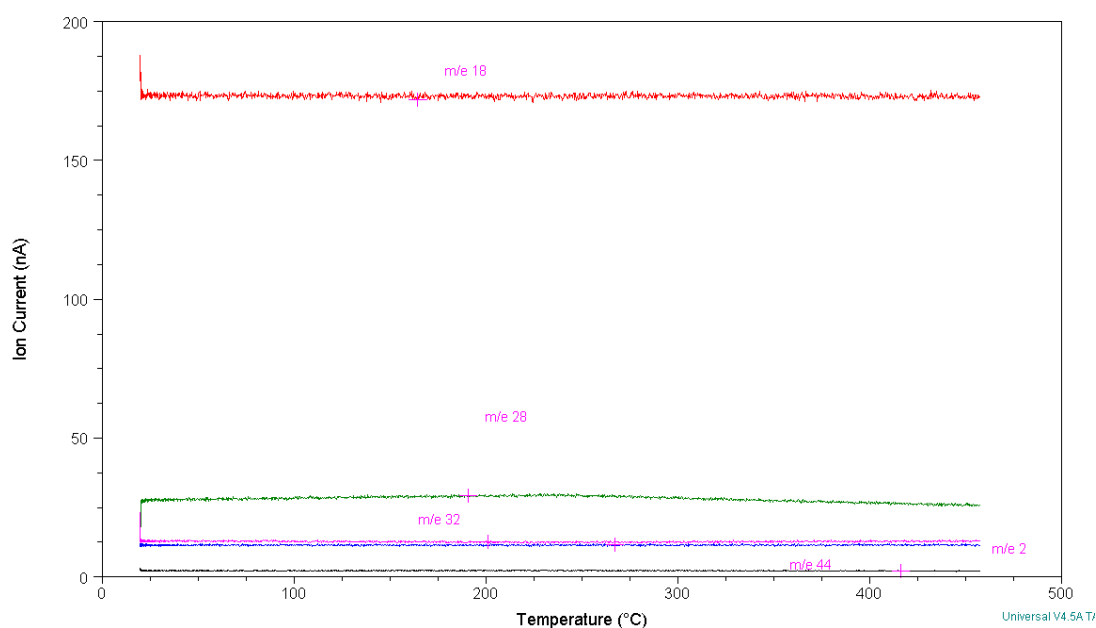


**Figure 35, mass spectrometer signals from the TGA furnace being flushed with water-saturated-helium, after 2 hours of purging and before the start of the experiment.**

It can be seen that after an equilibrium is reached the water signal in red ( $m/e\ 18$ ) is the highest while the signals for CO in green ( $m/e\ 28$ ),  $\text{O}_2$  in pink ( $m/e\ 32$ ),  $\text{H}_2$  in blue ( $m/e\ 2$ ) and  $\text{CO}_2$  in black ( $m/e\ 44$ ) are much smaller. After the plateau was reached the MTGA

test started. Figure 36 shows the combined weight loss and liberated gas plots for as-produced carbon nanotubes (WCNTs). The weight loss commences at 670°C and it is accompanied by the liberation of hydrogen, carbon monoxide and carbon dioxide with a transient reduction in the water vapour content. This behaviour is entirely consistent with the water-gas reaction and in dry helium there was no significant weight loss or emitted gasses at this temperature as described in section 3.3.6. After the reaction has taken place the amounts of the detected species start to equilibrate as the endothermic reaction comes to an end.

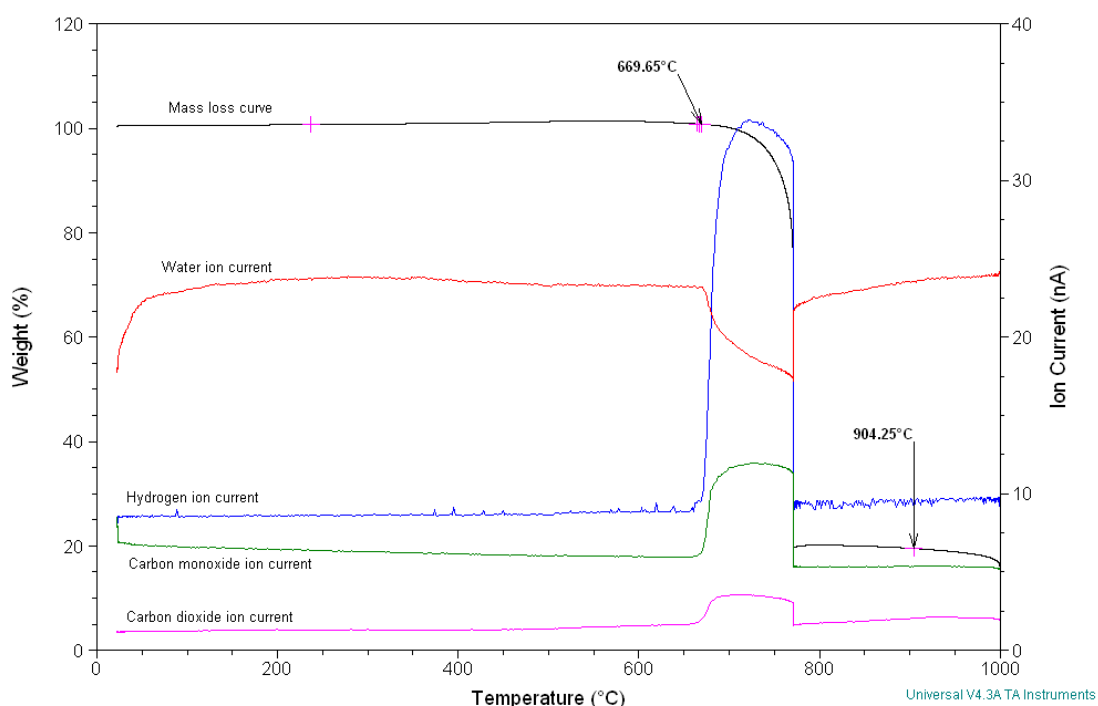


**Figure 36, Modulated TGA results in terms of variation in weight on the left Y axis and the results of the mass spectrometer as ion current signals on the right Y axis against temperature. The results are for as-produced multiwall carbon nanotubes (WCNTs) heated to 1000°C in water-saturated-helium.**

MTGA provides continuous measurement of kinetic parameters (not energy) during the whole of the decomposition process, permitting the important kinetic parameter of activation energy to be continuously plotted as a function of conversion, temperature and time. In addition, the use of controlled rate TG provides for the average temperature to be increased during the experiment so that multiple decomposition steps of a material may be observed in the same experiment. The continuous activation energy curve resulting from the high resolution TGA experiment is shown in Figure 37.

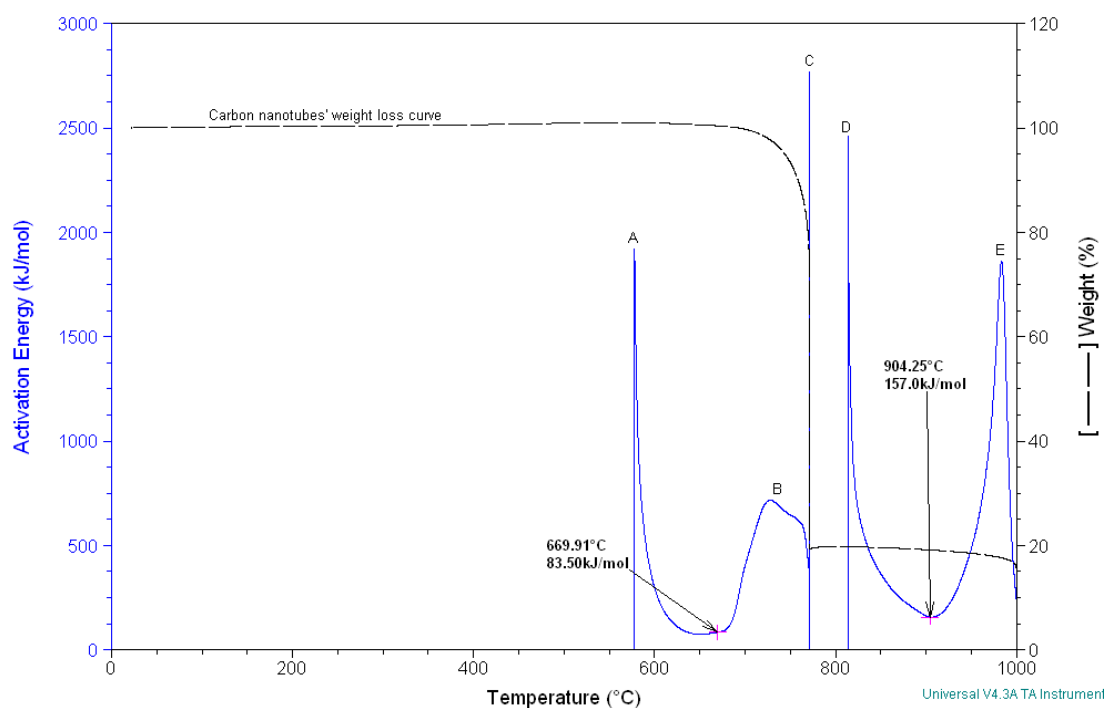


**Figure 37, activation energies plotted against test temperature for the water-gas and the water-gas shift reactions in as-produced multiwall carbon nanotubes (WCNTs) measured using the modulated TGA method.**

When there is no mass loss, the value for activation energy is set to zero. Once the onset of mass loss is observed (near 600°C), calculation of the kinetic parameters is initiated. Because it takes several cycles to produce reliable data, the first few data points are unrealistically high (peak A) [129]. The calculated values become constant once a few cycles are achieved; this is at 669°C with activation energy of 83 kJmol<sup>-1</sup>. This value is very close to the literature value (80 kJmol<sup>-1</sup>) for the water-gas reaction [16], which is another confirmation that this reaction is taking place between the carbon nanotube sample and the water vapour in the saturated test gas. At the end of the mass loss region, the kinetic parameter once again goes to an unrealistically high values (peak C) as the sine waves (oscillatory heat flow proportional to the mass of the test specimen) become distorted by the lack of reacting material. In Figure 37 however there is a slight hump (B) before the expected spike at C. The broad peak B with the modest appearance of carbon dioxide provides evidence for the water-gas-shift reaction as shown in Equation 34.



This reaction would commence once carbon monoxide becomes available, which will pertain here as a result of the water-gas reaction. The broad B peak is then due to the shift reaction overlapping with the water-gas reaction and becoming dominant due to its lower activation energy. The graph of activation energy against time confirms the overlapping shift reaction as shown in Figure 38, with activation energy of  $43 \text{ kJmol}^{-1}$ , which is very close to the literature value ( $41 \text{ kJmol}^{-1}$ ) for the water-gas-shift reaction [16]. As the heating continues, another reaction takes place (after the D peak), which reduces the weight of the sample slightly while producing small amounts of  $\text{CO}_2$ . This is thought to be due to the reaction of the remnant WCNTs with oxidizing species such as the products of the water-gas and the shift reaction or adsorbed gases at relatively high temperature ( $\sim 1000^\circ\text{C}$ ), similar to the results seen in dry helium TGA in section 3.3.6. The activation energy of this reaction is  $157 \text{ kJ mol}^{-1}$ , which is close to the literature value of  $159 \text{ kJ mol}^{-1}$  for graphite oxidation [130].

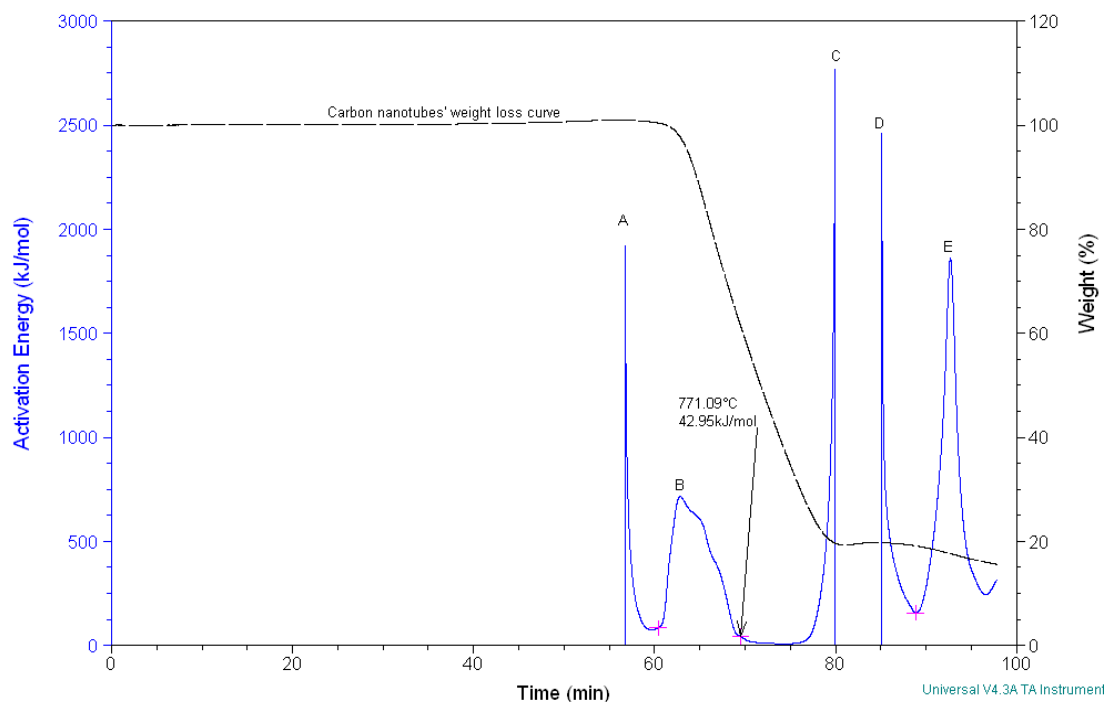


**Figure 38, plot of the activation energy against time for the modulated TGA experiment in water-saturated-helium, showing three clear activation energies, highlighted by a + and from left to right are thought to be due to water-gas, water-gas-shift and oxidation reactions respectively.**

The same trials were conducted on other samples to see whether the water-gas reaction can also be seen in post production treated MWCNTs. Figure 39 shows the results as a

derivative mass loss against temperature. A distinct peak was seen for WCNT, with smaller and right shifted peaks for the other samples. The maximum weight loss temperature and the corresponding mass loss rate ( $\% \text{ } ^\circ\text{C}^{-1}$ ) is also shown on Figure 39.

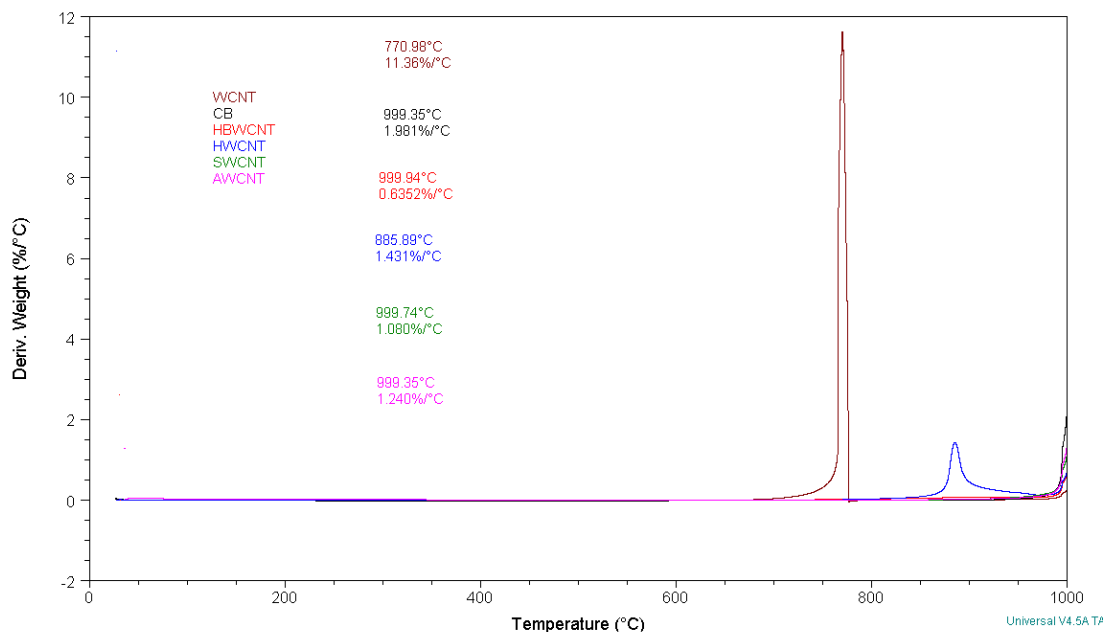


**Figure 39, derivative of mass with temperature against test temperature for different samples analysed using the TGA method in a water-saturated-helium environment.**

The activation energies and reaction temperatures were derived from the experiment and are listed in Table 6.

**Table 6, water-gas reaction activation energies for different samples, obtained using the modulated TGA method.**

Sample	Activation energy / kJ/mol	Reaction temperature / °C
AHCNT	322	1000
ACNT	205	929
CB	203	956
HBCNT	59	876
HCNT	59	906
SWCNT	91	676
WCNT	83	669

The activation energies and reaction temperatures for all the acid treated tubes and CB were higher than other samples. Previously similar EDX signals were observed for these materials, which indicated presence of non-carbonaceous elements that had been incorporated in their structure as a result of the acid treatment methods in MWCNTs and production and processing methods during CB manufacture [131]. The presence of

additional molecules on the surface, could affect the ability of the underlying carbon to react with water until much higher temperatures have been achieved and a majority of the functionalised bonds have been removed. This can also be one of the reasons for these materials' higher heat capacities as observed in section 3.3.5. The heat-treated tubes react at much higher temperatures than as-produced tubes, however, the activation energies are much smaller than for all the other samples. This could be because the heat treated tubes have much more crystalline structures and are more stable at lower temperatures; however, as the temperature increases they become more and more active, and once high enough temperature are reached, they can undergo this reaction. The lower reaction energies could be due to the high temperature affecting the kinetics of the reaction. SWNT and WCNTs have much lower reaction temperature than all the other samples and lower reaction energies than AHCNT, ACNT and CB. The reason for this is thought to be due to the presence of iron in these materials, as was indicated earlier from the remnants of TGA in air, as iron acts as a catalyst for the water-gas reaction by lowering the reaction temperature and activation energy. In addition, both of these materials have a higher number of defects and imperfections and therefore could undergo the water-gas reaction at lower temperatures due to their less stable structures as opposed to the heat treated tubes. The next chapter considers the possibility of inducing the water-gas reaction of MWCNTs using a near infrared laser as the heat source, with pulse energy and duration within acceptable exposure limits of skin. The concept is first examined by establishing the possibility of removing the tubes from water suspensions and then proved as a possible minimally-damaging remote tool for removing MWCNT, from tissue by conducting laser trials on layers of bacon.

### **3.4.3. Summary**

The CVD process is a reliable route for producing MWCNTs using a hydrocarbon source and ferrocene catalyst. The produced tubes usually have an entangled appearance at the top, where the growth has ceased at different lengths for different MWCNTs and the applied forces from the adjacent tubes have reduced, resulting in growth in random directions. However the bottom part of the MWCNTs from where the growth has initiated, appears straight and regular. The structure of the produced carbon nanotubes can be modified through different post processing methods, such as ball milling, acid and

heat treatment. None of these methods essentially alter the fibrous characteristics of the tubes, but they can increase the amount of structural imperfections, such as those produced as a result of the acid treatment process, leading to more defects or addition of functionalised molecules. In some cases they reduce the amount of impurities, such as remnant iron catalyst particles on the MWCNT and MWCNT bundle surfaces as seen post acid treatment. Reduction in such impurities is more significant when using heat treatments at high temperatures in an inert environment, resulting in the removal of most of the remnant iron catalysts from both inside and outside of the MWCNTs. The process also reduces the amount of weakly bound amorphous carbon from the surface of the tubes and improves the crystallinity of the MWCNTs as was highlighted by the EDX, TEM and Raman spectroscopy results. It was observed that these treatment processes and consequent structural and chemical changes affect the physical properties of the MWCNTs including, changing their heat capacity and oxidation temperatures. Also more crystalline structures, such as those subjected to heat treatment, have higher heat capacities and oxidation temperatures as opposed to samples with higher iron content and defect densities (qualitatively measured by the  $I_D/I_G$  ratio). It was also observed that the samples which had been heat treated and had aligned orientation, produced more intense Raman peaks, which could be due to the resonance vibration and coupling of the samples to the Raman laser beam. The MWCNTs are highly reactive towards either oxygen or water to the extent that parts of their structure (perhaps lattices with imperfections and vacancies or amorphous regions) can react with even very small amounts of oxygen or water as long as temperatures as high as 900°C are achieved and sustained for a period of time. Such species may exist as adsorbed or trapped molecules on or in between carbon nanotube carpets, or as contaminations in the otherwise inert environment, for example, as impurities in the test gas. Such effects, however, are not seen at lower temperatures. The process may have also been further catalysed by the presence of iron impurities. Finally MWCNTs have unfavourable absorption characteristics for transmission FTIR analysis in the mid to far IR region. This is because most of the beam is absorbed by the sample and it is extremely difficult to distinguish between individual peaks resulting from rotation or vibration of atomic bonds. Therefore FTIR did not prove to be a useful characteristic method for the purposes of this work, it however emphasised the fact that

MWCNTs have high and prominent optical absorption characteristics across the IR spectrum.

The validity of the water-gas reaction model for carbon nanotubes was tested using MTGA in a water-saturated helium environment and showed that carbon nanotubes can undergo the water-gas reaction in water-saturated environments. The MTGA results highlighted this fact and the mass spectroscopy analysis confirmed the by-products of this reaction as hydrogen and carbon monoxide. The amount of energy and the temperature needed for the tubes to undergo such a reaction depends on two main factors one is the structure and degree of crystallinity and the other is the presence of iron particles that could act as a catalyst for the reaction. Carbon nanotubes, which were more crystalline and had been heat treated required longer dwell times at 900°C to react with water. The tubes that had not been treated and carried remnant iron from the production process reacted with water at temperatures around 670°C, which is similar to the expected reaction temperature for the water-gas reaction (674°C) [16]. The analysis also revealed the activation energy for the reaction to be 83kJ mol<sup>-1</sup>, which is again very close to the quoted literature values (80 kJ mol<sup>-1</sup>) [16]. Samples that had been subjected to chemical treatments, such as the acid treatment process, had higher reaction temperature and energy. This is due to the presence of chemical impurities which will hinder the reaction of carbon with water.

#### **4. Laser induced water-gas reaction in carbon nanotube-water suspensions**

As mentioned in the introduction section, one of the main objectives of this study was to examine the possibility of removing carbon nanotubes (CNTs) from an aqueous environment and therefore provide the basis for methods of removing them from living tissue without causing detrimental temperature changes and at allowable laser exposure times and radiation wavelengths. The first step was to define the laser parameters permitted for safe exposure to skin and then to understand how such parameters relate to the energy densities needed to initiate the water-gas reaction in a carbon nanotube immersed in a pool of water. The concept was then verified with experimental work on aqueous suspensions.

##### **4.1. Setting limits for laser source properties and exposure times**

McKenzie [132] gives a complete review illustrating the diversity of laser applications in medicine where thermal processes play the leading role. Here, however, a brief overview aims to highlight the aspects, which would set a limit on laser parameters chosen for heating of MWCNTs as aqueous suspensions in this study. The literature states that the specific energy dose required to achieve a laser-induced biological transformation is nearly constant [133] and therefore, the exposure duration that delivers this dose of energy is the single parameter distinguishing the transformation process. The laser-tissue interaction can therefore be categorised according to the exposure time as follows:

- Electromechanical interaction (10 ps to 100 ns).
- Photo-ablative interaction (10 ns to 100 ns pulses of ultraviolet).
- Thermal interaction (1 ms to 10 s exposure, quasi continuous wave i.e. the type of laser parameters used in this thesis).
- Photochemical interaction (10 s to 1000 s continuous wave).

Excessive heating of living tissue will cause transformations and tissue death starting at temperatures as low as 45°C [133]. To avoid this, the radiation wavelength should be selected to minimise direct tissue absorption. The best approximation of a suitable

wavelength is one at which water (approximately 70% of the body mass) is least absorbing. Water has strong absorption bands in long IR wavelengths with a typical absorption depth of 10 $\mu$ m in the far IR; however a window exists between 600 nm to 1200 nm where water is least IR absorbent [133]. Furthermore biological systems are known to be highly transparent to this spectral range [4,134, 135]. The wavelength chosen also determines the radiation penetration depth, which is usually impeded by both; optical scattering and absorption of the tissue. In general, greater tissue depth penetration is possible with longer wavelengths, until the near-infrared absorption bands of water near 2000 nm are reached. In this study a near infrared diode laser source at 940 nm was used. It was also intended to deposit the energy required for initiating the water-gas reaction in the MWCNTs in time frames much shorter than the time needed for the heat to diffuse through the tissue and raise the surrounding tissue temperature, to, or above thresholds with deleterious effects.

#### **4.1.1. Photo-thermal cancer therapy using nanostructures**

Nanomaterials have the potential to be used in minimally invasive therapeutics with only small effects on the patients' quality of life [5]. Their main advantage in cancer therapy is their multifunctionality [8]. A concept currently being pioneered at Houston Medical Centre is based on nanoparticles of silica coated with gold (named Nanoshells by the authors), which are stable in the bloodstream and will concentrate in tissues with poorly formed vascular system, such as the regions around a tumour. Different Nanoshell particle size and coating thickness, result in different optical properties, which can be tailored for either diagnostic purposes or therapeutic purposes via radiation absorption [136, 137].

There are, however, three significant disadvantages with the use of Nanoshells; one is that the nanoparticles are left remnant in the body, the effects of which are unknown, secondly they are not targeted to a specific cell but are instead delivered systematically. Finally, the high laser power (35W) and exposure times (7minutes) reported by the authors as the required parameters to heat up the Nanoshells sufficiently, could cause severe irreversible damage to healthy tissues. SWNTs have also been investigated following the same principles as Nanoshells, the ability of attaching sensing molecules to

the tube walls allows a multifunctional material which can target only specific and predefined molecules [4,6]. Most intriguing results were reported by Panchapakisan et al [5]. They irradiated breast cancer cells in phosphate-buffered-saline solution laid in trenches made of functionalised SWNTs for 60 seconds using  $200 \text{ mWcm}^{-2}$  of power. It was observed that the cells were removed after irradiation and the authors attributed this to explosions caused by the SWNTs. They explained that adsorbed water molecules in SWNT sheets were heated inside the tubes to temperatures greater than  $100^{\circ}\text{C}$ , which caused pressure build up and explosion of the tubes. Figure 40 is from the same publication.

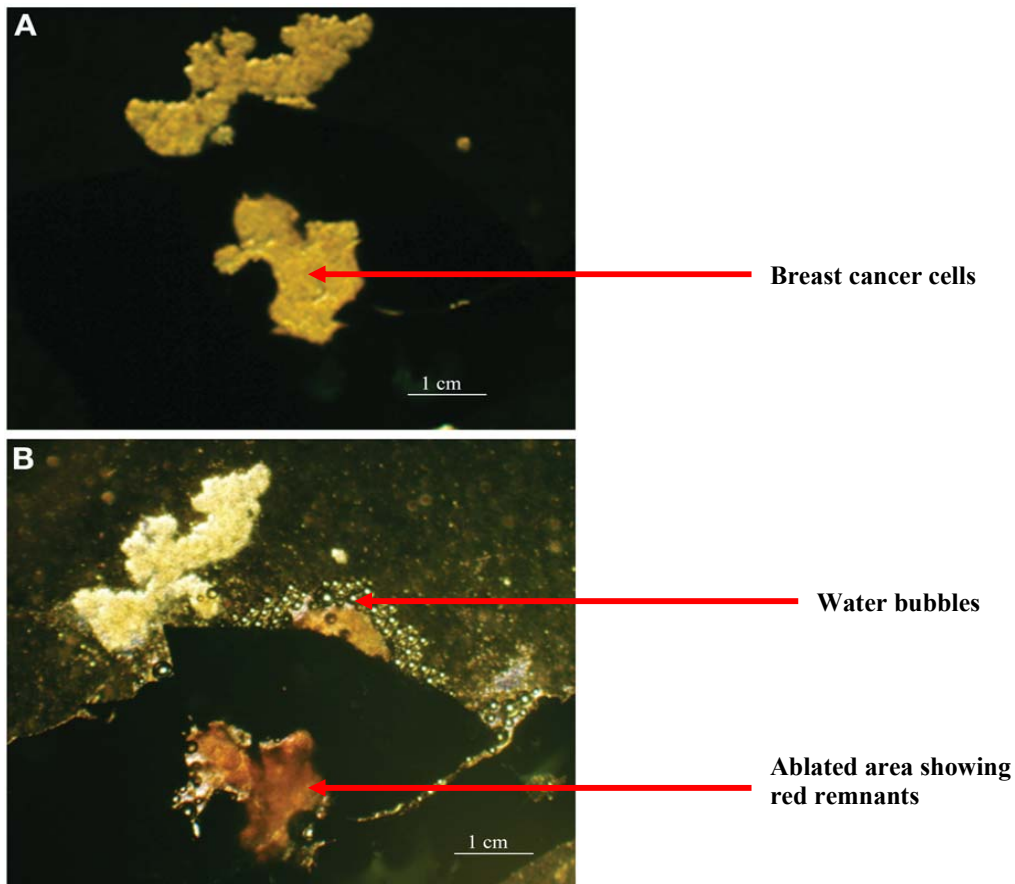


**Figure 40, (A) breast cancer cells placed inside two etched holes on SWCNT sheet before light exposure; (B) same cells after exposure to  $200 \text{ mW/cm}^2$  of light intensity [5].**

Although the idea of confined water in CNTs has been practically and theoretically demonstrated [138, 139, 140], it is more likely that the laser has heated up the SWNT substrate, and the resultant heating of the cell culture for 60 seconds has simply boiled the

solution off, hence the presence of bubbles in the vicinity of the radiation spot. The cause of SWNT removal is then simply oxidation due to high local temperatures and presence of oxygen as has also been observed by Ajayan et al [3]. The presence of red coloured remnants in place of the SWNT is another confirmation of the tube burning and leaving the catalyst iron particles behind. Therefore any successful remote removal of CNTs from tissue can only be achieved by minimizing damage to the surrounding tissue through ensuring that the laser power densities and the pulse durations used, are within acceptable exposure limits. Furthermore the generated heat, which is diffusible to the surrounding tissue, should not cause aggressive temperature changes. Therefore the safe exposure limits of skin to laser radiation, based on both intensity and exposure time are calculated in the following section.

#### **4.1.2. Safe exposure limits to near infrared laser radiation for the skin**

The laser safety standard PD IEC TR 60825-14:2004 (Safety of laser products - Part 14: A user's guide) is published by IEC (International Electrotechnical Commission, Geneva) and is also issued as a national document in the UK by BSI (British Standards Institution, London). According to this standard the safe exposure limit for the skin at 940 nm, for an exposure of 10 s or more is  $604 \text{ mWcm}^{-2}$  and for a single pulse of between 20 and 100 ms at 940 nm the radiant exposure should not exceed:

$$\text{Maximum allowable radiation exposure} = 3.3 \times t^{0.25} \text{ Jcm}^{-2} \quad (35)$$

Where t is the pulse duration in seconds.

Another point to consider is the amount of energy delivered to a certain depth of the skin (penetration depth). The light intensity change in tissue depends strongly on the relative magnitude of the scattering and absorption coefficients [141]. At the wavelength under consideration (i.e. 940 nm) the absorption ( $\alpha$ ) and scattering ( $\mu$ ) coefficients will be similar to that of an Nd: YAG laser ( $\lambda = 1064 \text{ nm}$ ) as shown in Table 7.

**Table 7, skin absorption and scattering characteristics for a 1064 nm wavelength laser beam [141].**

	$\alpha / \text{cm}^{-1}$	$\mu / \text{cm}^{-1}$
Un-pigmented	0.1-1.0	5-10
Pigmented	5-10	5-10

The effective attenuation coefficient of tissue ( $\varphi$ ) is given by Equation 36 [141]:

$$\varphi^2 = 3\alpha\mu \quad (36)$$

For example, for an un-pigmented skin and considering an average value for absorption and scattering (e.g. 0.5 and 7.5  $\text{cm}^{-1}$ ),  $\varphi = 3.35 \text{ cm}^{-1}$ . Now assuming that the laser has to travel through the thickness of skin ( $z = 0.1\text{cm}$ ) before reaching its target (MWCNTs under the skin) and that the reflection fraction is zero the transmission fraction can be estimated by replacing  $\alpha$  with  $\varphi$  and in equation 3 as shown in Equation 37, to be 72%.

$$I = I_0^{-\varphi z} \Rightarrow \ln T_f = -\varphi z \quad (37)$$

Figure 41 shows the calculated amount of energy transmitted through the skin and the amount of energy illuminating MWCNTs based on laser energy delivered within safe exposure limits for durations of up to 10s.

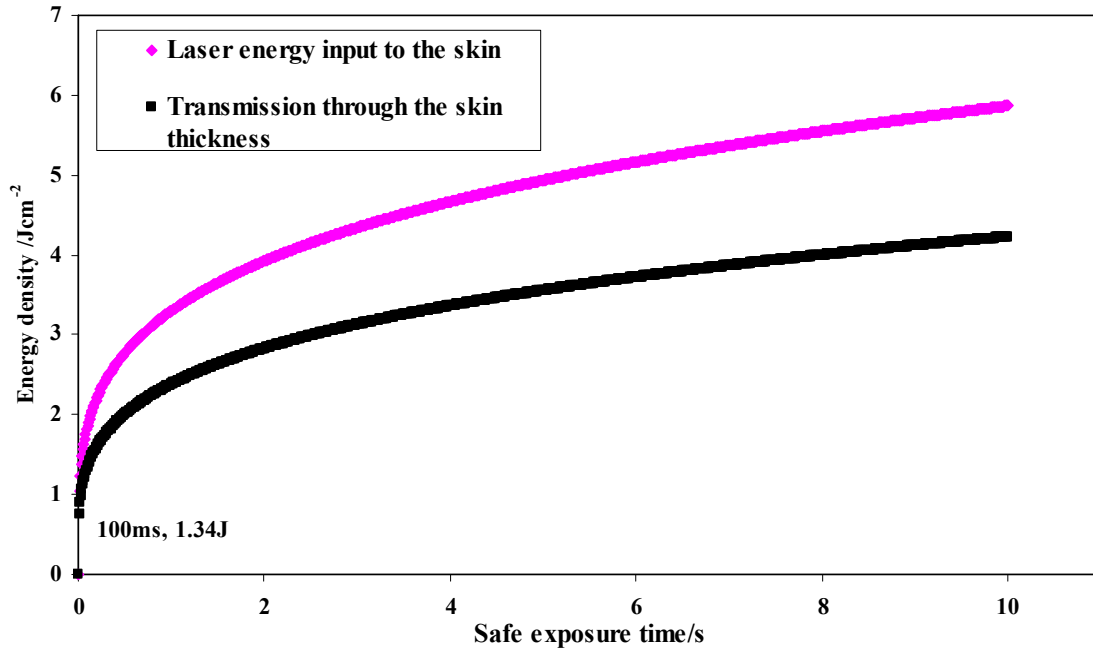


**Figure 41, maximum permissible radiation exposure to the skin and the resultant transmission through the skin (skin thickness ~1mm) for exposures up to 10s.**

From the graph in Figure 41, the safe amounts of energy and the associated pulse time can be deduced. For example a 100ms pulse can safely deliver 1.34 J of energy over 1 cm<sup>2</sup> of skin. It is now important to estimate the required amount of energy to activate a water-gas reaction in a carbon nanotube.

#### **4.2. Modelling the heating and water-gas reaction of a single carbon nanotube in a pool of water**

If the nanotubes are immersed in water to drive the water-gas reaction the supplied energy by the laser beam should be sufficient to rapidly increase the temperature of the tubes, compensate for the greater loss of heat by conduction and radiation from the sample and to convert the water adjacent to the nanotube into steam. It is assumed that both; the laser radiation and the subsequent radiant heat from the sample, pass through the water with negligible absorption. The classic treatment is that of Nukiyama [142] who introduced the so-called ‘boiling curve’. This is described further in the following section.

#### 4.2.1. Nukiyama's boiling curve

When heating a surface in a large pool of liquid, the heat flux  $q$  is usually plotted versus the wall superheat  $\Delta T_{\text{sat}}$ , which is the temperature difference between the surface temperature of the heating element (e.g. the carbon nanotube) and the saturation temperature of the liquid (e.g. the boiling temperature of water). First constructed by Nukiyama, the boiling curve depicted in Figure 42 is also referred to as Nukiyama's curve, where four distinct heat transfer regimes can be identified:

1. Natural convection (AB). This is characterised by single-phase natural convection from the hot surface to the saturation liquid without formation of bubbles on the surface.
2. Nucleate boiling (B'C). This is a two-phase natural convection process in which bubbles nucleate, grow, and depart from the heated surface.
3. Transition boiling (DE). This is an intermediate regime between the nucleate boiling and film boiling regimes.
4. Film boiling (EF). This mode is characterised by a stable layer of vapour that forms between the heated surface and the liquid, such that the bubbles form at the vapour layer and not at the wall.

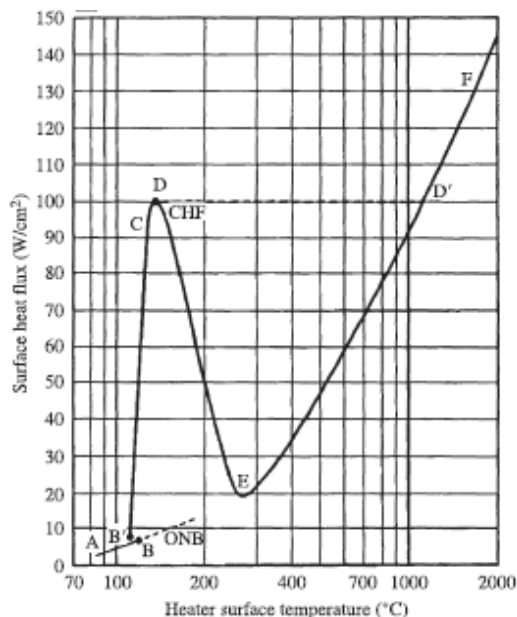


Figure 42, Nukiyama's boiling curve for a steel cylinder in a pool of water [82].

In the natural convection part of the curve, increasing the wall temperature, increases the heat flux from the surface to the liquid, until the first few bubbles appear. As the heat flux is increased, more and more bubble nucleation sites become activated until the surface is

covered with bubbles that grow and depart in rapid successions. The heat flux increases dramatically for relatively modest increases in  $\Delta T_{\text{sat}}$  (defined as  $T_w - T_{\text{sat}}$ ) and increasing the heat flux further causes the departing bubbles to coalesce into vapour jets, changing the slope of the nucleate boiling curve. Further increase in  $q$  eventually prevents the liquid from reaching the heated surface. This is referred to as the critical heat flux (CHF), such that complete blanketing of the surface by vapour occurs parallel to a rapid rise in the surface temperature. This is because dissipation of heat through the steam layer is reduced due to the smaller thermal conductivity of steam compared with water. For heaters that impose a heat flux at the surface, such as electrical-resistance elements, or indeed a carbon nanotube heated by an external radiation source, the process progresses along a horizontal line of constant heat flux so that the wall superheat jumps to point D', where film boiling prevails and vapour bubbles grow and depart from the vapour-liquid interface of the vapour layer, not from the surface. An ulterior increase in  $q$  may bring the surface to the burnout point (F), where the surface temperature reaches the melting point of the heater, or in the case of a carbon nanotube, surrounded by a steam jacket, the water-gas reaction can take place. When reducing the heat flux, the film boiling curve passes below point D' until reaching point E, the minimum film boiling (MFB) point. Here again, the process path depends on the mode of heating. For an imposed heat flux, the process path jumps horizontally at constant  $q$  to the nucleation boiling curve B'C. Consequently, a hysteresis loop is formed when heating a surface up past the CHF.

The decreased energy loss once a stable steam jacket is formed is clearly apparent as long as the critical heat flux (CHF) input of  $1 \text{ MWm}^{-2}$  (in this example for steel) is exceeded, when the temperature will continue to increase until the heat input is balanced by radiative heat loss. This curve corresponds to the gradual heating of a body of water. In the case of 'pool boiling' the temperature is assumed to remain ambient except in the region of the heat source and the CHF is increased by a factor of 3.4 according to Ivey and Morris [143].

#### **4.2.2. Film boiling on a carbon nanotube heating element**

For a heating element as small as a carbon nanotube, the above treatment requires some modifications. The effect of size on the CHF peak has been addressed [144]. It was

shown that for a rod shaped heater, the CHF scaled as (size)<sup>1/4</sup>. While a 1/4 power does not imply a fierce dependence, the reduction of the magnitude of the boiling peak is still a factor of 4 for the nanotube. However, recent studies of the rapid heating of sub micro elements in fluids [145], imply that the mechanism of boiling is very different from that in the bulk, with the mechanism responsible for the boiling peak (i.e. the replacement of discrete bubbles as they leave the heating surface by cooler water) not occurring at all. Instead, for a constant heat flux, the temperature increases continuously with time, although at an enhanced rate once the stable steam jacket is formed around the heater. It is not obvious that there is any critical boiling peak at all in the required heat input, and it is likely that the temperature of nanotubes will increase until an equilibrium temperature is reached consistent with the losses through radiation (which rapidly become dominant above 500°C), and losses through conduction across the micro steam jacket, as well. The factors determined by input power will thus be the equilibrium temperature reached and the time taken to this point.

To achieve a point of “burnout” for the nanotubes, the heating conditions should be met that satisfy the requirements for the water-gas reaction. The precursor for the water-gas reaction is that water vapour is generated around the MWCNT rapidly so that the heating can be confined to the MWCNT and can drive the reaction before being conducted away by the surrounding water. We can, therefore, assume the MWCNT as a nano-scale cylindrical-heat generator with reduced effective thermal conductivity between it and the surrounding water. Figure 43 shows a schematic of a MWCNT being heated using a laser in a pool of water, where  $R_0$  is the radius of the CNT and  $R_1 - R_0$  is the thickness of the required steam jacket to undergo a water-gas reaction with the tube.

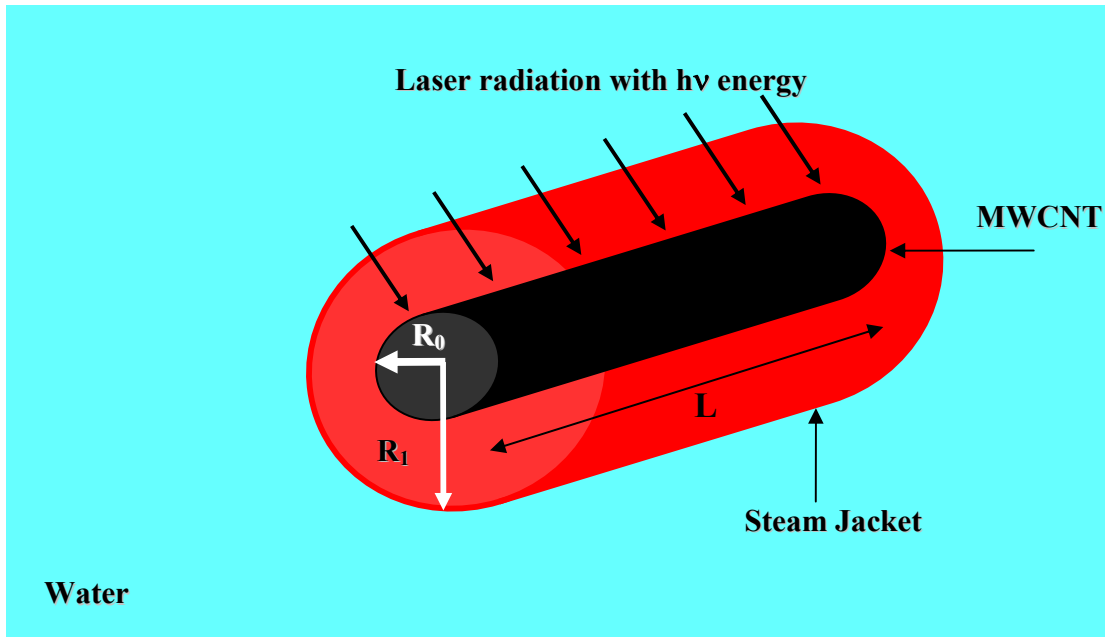


**Figure 43, schematic of laser heating a multiwall carbon nanotube (MWCNT) in a pool of water.**

It is assumed that the nanotube is the only heat source for heating the water and there is no direct laser absorption by the water. An energy balance is required to understand the amount of heat required to drive this reaction and whether sufficient energies can be delivered using a laser source under the safe exposure conditions for skin. Therefore the mass of a MWCNT, the required amount of water for it to undergo the water-gas reaction, and the energy required for the steam jacket to form must be estimated.

For a 100  $\mu\text{m}$  long MWCNT with an outer diameter of 60 nm and an inner core of 14 nm (as was measured by SEM and TEM) and using the available volume of the MWCNT ( $2.65 \times 10^{-15} \text{ m}^3$  excluding the volume of the inner hollow core) and dividing this value by the volume of a single carbon atom will give the number of carbon atoms in the MWCNT. Using Avogadro's number and the molar mass of carbon (12g) the mass of a single carbon atom can be estimated to be  $2 \times 10^{-26} \text{ kg}$  and therefore the mass of the MWCNT is approximated to be  $5.3 \times 10^{-12} \text{ kg}$ , which is equal to  $4.42 \times 10^{-10} \text{ mol}$  of carbon. As the water-gas reaction needs equivalent number of moles of water and carbon to proceed,  $4.42 \times 10^{-10} \text{ mol}$  of water will be used during the reaction. Using the value for the molar mass of water (18g), the mass of the required amount of water to react with a

MWCNT is equal to  $7.95 \times 10^{-12}$  kg. Using the density of water ( $1000.34 \text{ kg/m}^3$  [82]), the volume of this mass of water is estimated to be  $7.95 \times 10^{-15} \text{ m}^3$  using Equation 38:

$$V = \frac{m}{\rho} \quad (38)$$

The thickness of this volume of a cylindrical steam jacket which is  $100\mu\text{m}$  long, can be approximated as  $r_{\text{nuc}} = R_1 - R_0$  in Figure 43 and is estimated to be  $5.33\mu\text{m}$  using Equation 39:

$$V = \pi r_{\text{nuc}}^2 L \quad (39)$$

For nucleation to occur, the temperature must be elevated above the saturation temperature of the liquid to form or activate vapour nuclei. Hence, the vapour jacket does not begin to form at the saturation temperature but instead, when a certain superheat is attained. Typically, nucleation occurs from a vapour nucleus that protrudes into the thermal boundary layer formed at the wall [82]. If  $P_G$  is the vapour pressure inside the nucleus,  $P_L$  the local liquid pressure, and  $\sigma$  the surface tension, since  $P_G > P_L$ , the surface tension balances the pressure difference across the interface and the pressure difference increases with decreasing nucleation radius [82]. The superheat temperature needed for the nucleation ( $\Delta T_{\text{nuc}}$ ) can be calculated by balancing the surface tension as the preventing force with the driving force which is the increase in vapour pressure as the steam jacket nucleates with the increase in temperature using Equation 40 as described by Thome [82]:

$$\Delta T_{\text{nuc}} = \frac{2\psi}{r_{\text{nuc}}(dP/dT)_{\text{sat}}} \quad (40)$$

Where  $\psi$  is the surface tension of water ( $0.0429 \text{ Nm}^{-1}$  [82]).

This is in the case of homogeneous boiling. When there is a wall present heterogeneous boiling takes place, which by nature requires less energy to be driven, however here we assume that the wetting of the CNT surface is minimal and the amount of energy needed

for nucleation will be approximately equal to a homogeneous nucleation, which is a more conservative estimate. Thome also showed that the change in pressure with temperature for a homogeneous nucleation can be calculated using Equation 41:

$$\left(\frac{dP}{dT}\right)_{sat} = \frac{h_{LG}}{T_{sat}(v_G - v_L)} = 301.5 \text{ kJ/Km}^3 \quad (41)$$

Where  $V_G$  ( $0.076 \text{ m}^3\text{kg}^{-1}$  [82]) and  $V_L$  ( $1.12 \times 10^{-3} \text{ m}^3\text{kg}^{-1}$  [82]) are steam and water's specific volume respectively.

Therefore  $\Delta T_{nuc}$  is estimated as  $0.053^\circ\text{C}$ , using Equation 40. The amount of energy required to increase the temperature of the required mass of water to  $\Delta T_{nuc} = 100.053\text{K}$  and convert it to steam from room temperature ( $\sim 20^\circ\text{C}$ ) is estimated to be  $2 \times 10^{-5}\text{J}$  using Equation 42:

$$H = m(C_{pL}\Delta T_v + h_{LG}) \quad (42)$$

Where,  $H$  is the amount of energy required (J),  $m$  is the mass of water to be converted to steam (kg),  $C_{pL}$  ( $4.3927 \text{ J g}^{-1} \text{ K}^{-1}$  [82]) is the heat capacity of water,  $h_{LG}$  is the latent heat of vaporisation ( $2257 \text{ kJ kg}^{-1}$  [82]) and  $\Delta T_v$  is the superheat temperature (K).

The activation energy of the water-gas reaction for the as-produced MWCNTs was measured using the modulated TGA and was found to be very close to the value quoted in published literature. This provided further confidence that the water-gas reaction is taking place between the carbon nanotubes and the water-saturated-helium environment. However for calculating the total amount of energy needed to drive the water-gas reaction between carbon nanotubes and their surrounding water using a laser source, the important value which needs to be considered is the heat of reaction. For an endothermic reaction such as the water-gas reaction this is the energy absorbed as a result of a complete chemical reaction of molar amounts of reactants. The heat of reaction for the water-gas reaction is quoted by Kotz et al [146] to be  $+131 \text{ kJ mol}^{-1}$ , and the energy absorbed for the reaction of one MWCNT ( $4.42 \times 10^{-10} \text{ mol}$  of carbon) can be estimated to be  $5.79 \times 10^{-5} \text{ J}$ . Therefore, the total energy needed for reacting one MWCNT with its

surrounding water is approximately  $7.8 \times 10^{-5}$  J, which is the sum of the energy needed to convert the required amount of water to steam and the heat of reaction.

Assuming that the only source for this energy is the MWCNT, we can calculate the temperature that the MWCNT needs to reach for the required amount of energy to have been transferred to the surrounding water. The thermal transfer regime will be a combination of conduction and radiation. The conduction heat transfer can be calculated using Equation 43 [82]:

$$Q_c = \frac{(T_w - T_s) \times A \times \gamma_G}{R} \quad (43)$$

Where  $T_w$  is the MWCNT temperature,  $T_s$  is the saturation temperature, A is the surface area of the MWCNT, R is steam layer radius and  $\gamma_G$  ( $0.04 \text{ Wm}^{-1} \text{ K}^{-1}$  [82]) is the thermal conductivity of steam.

This is the main source of energy transfer from the MWCNT to the surrounding water as the radiative heat transfer which can be estimated using Equation 44 [82] is mainly lost.

$$Q_r = \varepsilon \sigma_{SB} [T_w^4 - T_A^4] \quad (44)$$

Where  $Q_r$  is the radiative heat loss,  $\varepsilon$  is the emissivity taken as 0.95 and  $\sigma_{SB}$  is the Stephan - Boltzmann constant ( $5.67 \times 10^{-8} \text{ Wm}^{-2} \text{ K}^{-4}$  [22]).

The radiative heat transfer is the greatest source of energy loss and can happen not only through the outer layer of the MWCNTs but even through the inner layers. Therefore, the total amount of energy needed to be supplied to the MWCNT is the energy needed to raise its temperature as per Equation 45 (taking the value of MWCNTs heat capacity as the average of the DSC results as  $0.757 \text{ Jg}^{-1} \text{ K}^{-1}$ ) to a sufficient amount so that it provides the required energy for the water-gas reaction, as well as the energy that is needed to be supplied to compensate for the radiative heat losses.

$$E = mc_{cnt}\Delta T \quad (45)$$

The total amount of energy needed to be conducted to the water to create the required steam jacket was calculated and is plotted on the left Y axis against the required surface temperature in Figure 44 (MWCNT's boiling curve). In addition, the sum of the energies needed to be supplied to the MWCNT to increase its temperature sufficiently to satisfy the conduction heat transfer requirements, and the energy needed to counter-balance the radiative losses are plotted on the right Y axis.

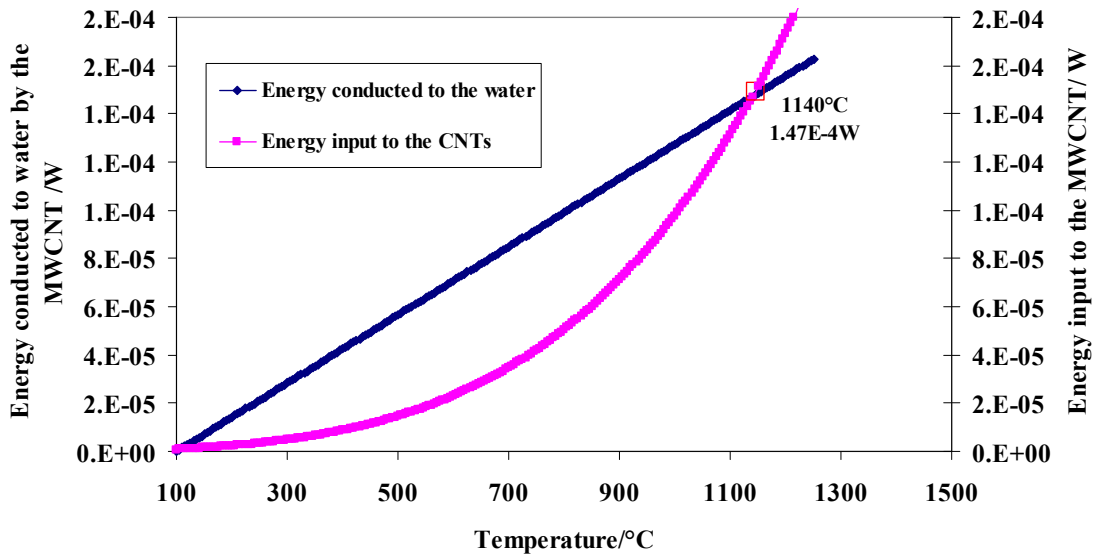


**Figure 44, a multiwall carbon nanotubes (MWCNT) boiling curve. The energy conducted to the surrounding water by the laser irradiated MWCNT is on the left Y axis, with the blue curve showing the change in the value of this energy with the increasing temperature of MWCNT. The right Y axis is the laser energy input to the MWCNT required to balance both; the conduction heat losses to the water as well as the radiative heat losses from the MWCNT.**

It can be seen from the graph, that only when the MWCNT has reached temperatures of around 1140°C does the supply of energy meet the energy demand to drive the water-gas reaction and compensate for the radiative heat losses. This temperature is proportional to  $1.47 \times 10^{-4}$ J of energy that should be supplied to MWCNTs by the laser.

### 4.2.3. Laser energy requirements and pulse times

A MWCNT can be modelled as a 2D structure built from several graphene layers, with the outer tube being counted as two parallel graphene sheets separated by subsequent inner graphene layers (i.e. inner concentric tubes). The space between the graphene layers

(tube interlayer spacing) is empty and constant. It is assumed that there is zero reflection [1] from the graphene sheets and that the incident radiation is either absorbed or transmitted through to the subsequent graphene layers. The laser light intensity after passing through the first layer of graphene ( $I_1$ ) can be estimated as:

$$I_1 = I_0 - A_f I_0 \quad (46)$$

Where,  $I_0$  is the initial incident laser intensity ( $\text{Wcm}^{-2}$ ) and  $A_f$  is the absorption fraction by the graphene layer.

The light intensity after passing through  $n$  layers of graphene can be estimated by putting  $R = 0$  and  $n$  instead of  $z$  in equation 3 as shown in equation:

$$I(n) = I_0 \exp^{-\alpha n} \quad (47)$$

Using the interlayer spacing and the atomic radius values of 0.073nm [125] and 0.0334 nm respectively [126] the number of layers in a 60 nm diameter MWCNT is estimated to be 50 and the surface area of each layer can be calculated using Equation 48:

$$A = 2\pi RL \quad (48)$$

The MWCNT with 50 concentric tubes can be considered as 100 parallel sheets of graphene. Now assuming literature quoted value for absorption fraction of a graphene layer  $\sim 2.3\%$  [2] and using  $1.47 \times 10^{-4} \text{ J}$  as  $I_0$  and 100 as the number of layers in Equation 46, the remaining light intensity after passing through the MWCNT is negligible and it can be assumed that the entire incident beam is absorbed by the MWCNT. Assuming that all the absorbed light is converted to heat, we need to estimate the laser absorbing surface area of the MWCNT to be able to estimate the amount of energy required to be delivered by a laser source, either as a single pulse, multiple pulses or a continuous beam to provide the energy required to drive the water-gas reaction for one MWCNT. It should be noted that in the case of pool boiling, energy conduction only occurs through the outer shell of the MWCNT, where as the surface area available to absorb the laser radiation is

considerably higher, as optical absorption can take place through all the exposed surfaces of the concentric layers. Although the conduction losses only happen through the outer layer. The total surface area of the concentric tubes exposed to the beam is estimated to be  $6.3 \times 10^{-6} \text{ cm}^2$ . Using the amount of energy required to drive the reaction and compensate for the radiation losses in one MWCNT, the laser beam intensity required to illuminate a  $1 \text{ cm}^2$  area can be estimated as  $23 \text{ Wcm}^{-2}$  ( $23 \times 10^4 \text{ W m}^{-2}$ ). If the entire  $1 \text{ cm}^2$  illuminated area is covered with MWCNTs then this amount of energy will be sufficient to remove  $15.6 \times 10^4$  MWCNTs. Therefore, a 100ms pulse of  $23 \text{ Wcm}^{-2}$  beam delivers sufficient energy (2.3J) to remove  $15.6 \times 10^3$  carbon nanotubes. If this is to be delivered within safe exposure limits then 2 consecutive pulses of 1.32 joules and 100ms duration (as is highlighted in Figure 41) can provide more than sufficient amount of energy. Due to the system limitations of the available lasers in this research, in terms of producing stable, low power pulses, the trials in the practical parts of this thesis concerned with removing MWCNTs from aqueous solutions were conducted using pulses of 23W delivering 2.3J of energy over a single 100ms long pulse.

#### 4.2.4. The diffusion of the generated heat to the surrounding tissue

Finally, the effects of the heat generated by the MWCNT on the surrounding tissue prior to the water-gas reaction taking place, should be considered. The temperature change in the tissue in immediate vicinity of a MWCNT at this point can be estimated by using thermal properties of subcutaneous tissue [141] as follows:

- $\gamma$ , Thermal conductivity (subcutaneous tissue) =  $0.19 \text{ Wm}^{-1} \text{ K}^{-1}$
- $\rho$ , Density (subcutaneous tissue) =  $1000 \text{ kg m}^{-3}$
- $C_p$ , Specific heat (subcutaneous tissue) =  $2.675 \times 10^6 \text{ Jkg}^{-1} \text{ K}^{-1}$
- Depth (subcutaneous tissue) = 18mm

Subcutaneous tissue's thermal diffusivity  $X$  is estimated to be  $7.1 \times 10^{-8} \text{ m}^2\text{s}^{-1}$  using Equation 49 [28].

$$X = \gamma / \rho C_p \tag{49}$$

Considering the required beam intensity (I) of  $23 \times 10^4 \text{ Wcm}^{-2}$  over a pulse duration ( $t_p$ ) of 100ms and assuming absorption fraction ( $A_f$ ) to be one (all the radiation is absorbed and nothing is transmitted or reflected) and that all of the absorbed energy is converted to heat, then absorption fraction multiplied by the intensity (I) and the pulse duration ( $t_p$ ) is the total amount of thermal energy dissipated to the tissue by the MWCNTs. The heating rate of tissue can then be calculated using Equation 50 [28]:

$$\Delta T = \frac{alt_p}{C\rho(Xt_p)^{1/2}} = \frac{23 \times 10^4 \times 0.1}{2.675 \times 10^6 \times 1000 \times \sqrt{7.1 \times 10^{-8} \times 0.1}} = 0.1 \text{ K.} \quad (50)$$

Therefore, the total temperature rise in the tissue as a result of the heat generated in the MWCNTs during exposure to the 100ms long laser beam is negligible. This means that the tubes can be safely removed from under the skin without any noticeable temperature change or subsequent damage to the tissue.

#### 4.3. Multiple pulse laser transmission experimental set up

The laser used for all the experiments was a Laserline diode laser operating at a wavelength of 940nm. An Ophir laser transmission measurement (LTM) device (i.e an energy meter), which acts as a black body and absorbs all the incident radiation, was placed directly underneath the samples, to measure the amount of energy transmitted through them. The samples were placed inside a clear glass beaker on the LTM directly under the laser as illustrated in Figure 45. The laser was set to the nominal power of 30W delivering 100ms pulses each time with a spot size of  $0.88\text{cm}^2$ . The exact amount of energy delivered by a 0.1s long pulse was accurately measured using the calibrated LTM device and was recorded to be around 2.266J and slightly less than the expected nominal energy of 3J.

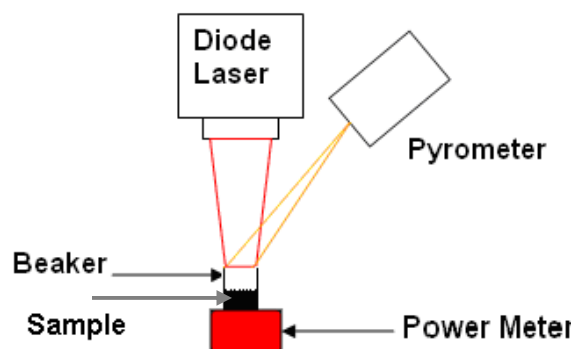


Figure 45, schematic of the laser transmission measurement trials.

The IR laser beam was directed vertically down into a beaker containing 1ml of aqueous suspensions of the required sample. Measurements were made of the transparency of the water, ethanol and the beaker to ensure there will be no contribution to energy loss from the matrices or the glass beaker, and the results of these trials are given in Table 8. Transmission measurements for a succession of twenty 100 ms pulses through a 0.1wt% suspension of ACNT in water were conducted by monitoring the proportion of the incident intensity transmitted through the sample and reaching an energy meter placed directly under the beaker holding the sample. A 0.1wt% sample of ACNT suspension in ethanol was also examined under the same conditions as a comparison with water suspension experiments and to validate that the increase in transmission with consecutive pulses is due to the removal of the MWCNTs as a result of the water-gas reaction, which is only possible in an aqueous environment.

Table 8, transmission measurement results through 1ml of water, ethanol and the sample holder.

Sample	E delivered to the power meter/ J	E transmitted/ J (average of three trials)	Transmission Fraction (T)
Air	2.266	2.266	1.000
Empty beaker	2.266	2.261	0.998
Beaker with 1ml of water	2.266	2.232	0.985
Beaker with 1ml of ethanol	2.266	2.231	0.985

The results show that there was no significant reduction in the transmitted radiation energy through water, ethanol or the beaker holding the samples, therefore, the absorption losses through the suspending medium and beaker can be taken as zero at the wavelength used; thus the absorption of light in the experiments is attributed solely to the ACNTs.

The laser pulse was calibrated and measured to deliver 2.27J over 100ms. The area over which this energy was delivered was equal to the area of the glass container i.e. 0.88cm<sup>2</sup>, and therefore illuminated the entire sample. Twenty consecutive pulses were delivered to each sample and temperature changes in the samples were measured using a non-contact pyrometer. The laser was operated from outside of the laser cell for health and safety reasons and standard thermocouples proved impractical for temperature measurements due to the sample size, experimental set up and rapid temperature rise of the samples. Thermography has been used for variety of laser operations as a reliable tool and its use has even been recently reported for measurements of temperature change in MWCNTs [147]. Therefore IR cameras or pyrometers were used, which measure the radiated heat from the sample and calculate the sample's surface temperature. An Impac infrared pyrometer (IPE 140) was sought following trials with a number of IR cameras and pyrometers. This device had a spectral range of 3 – 5  $\mu\text{m}$  capable of measuring temperature changes from the surface of the sample (without any influence from the laser beam at about  $\sim 1\mu\text{m}$ ). The pyrometer had a circular spot size that was set using a laser targeting beam to cover the same area as the laser beam spot on the sample and was coincided with the laser pilot beam prior to irradiation. Therefore the temperature was being taken from the whole sample surface directly under the laser beam. The pyrometer's temperature range was 30°C to 1000°C with  $\pm 0.1^\circ\text{C}$  accuracy and sampling rate of 100 frames per second. The resultant transmission measurements and the maximum temperatures recorded are listed in Table 9.

**Table 9, transmission measurements made on 1ml of 0.1wt% suspensions of ACNT in water and ethanol.**

<b>Sample</b>	<b>ACNT</b>	<b>ACNT</b>
<b>Max T</b>	<b>94.9</b>	<b>113.4</b>
<b>Volume</b>	<b>1ml</b>	<b>1ml</b>
<b>Liquid height cm</b>	<b>1.1</b>	<b>1.1</b>
<b>Medium</b>	<b>Water (0.1wt% ACNT)</b>	<b>Ethanol (0.1% ACNT)</b>
<b>Beam spot on material</b>	<b>11mm × 8mm</b>	<b>11mm × 8mm</b>
	<b>Transmission (%)</b>	
1 pulse	0.662	4.148
2 pulses	0.750	4.369
3 pulses	0.794	4.369
4 pulses	1.103	4.457
5 pulses	1.280	4.325
6 pulses	2.207	4.192
7 pulses	3.266	4.325
8 pulses	4.722	4.237
9 pulses	6.443	4.281
10 pulses	6.664	4.325
11 pulses	6.705	4.191
12 pulses	7.319	4.233
13 pulses	7.404	4.231
14 pulses	7.885	4.229
15 pulses	8.454	4.139
16 pulses	8.803	4.137
17 pulses	9.635	4.136
18 pulses	11.478	4.222
19 pulses	13.319	4.132
20 pulses	15.378	4.130

A graph of transmission % against number of pulses is shown in Figure 46.

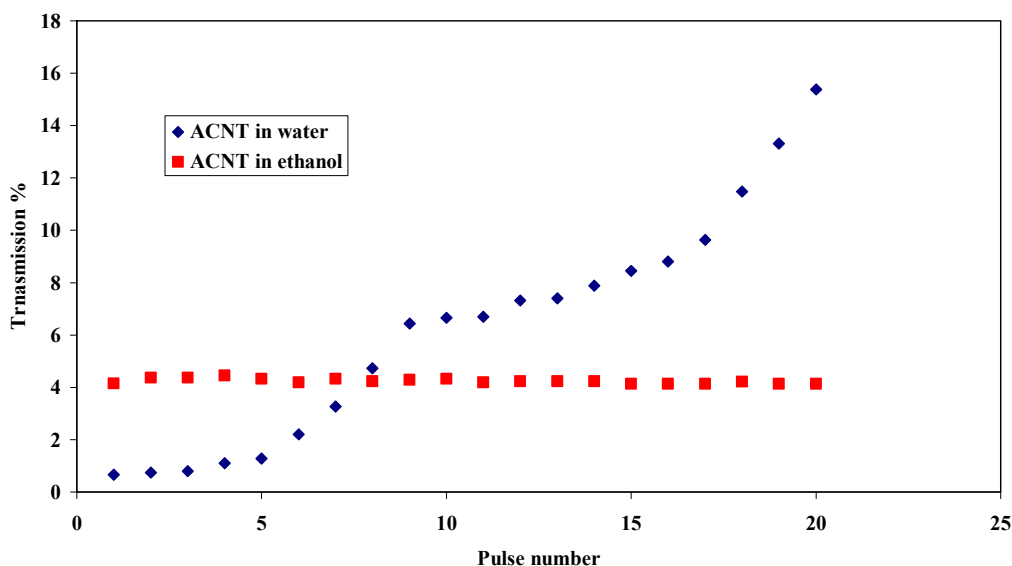


**Figure 46, increase in transmission through a 0.1wt% suspension of multiwall carbon nanotubes and water with 20 consecutive pulses of 100ms long and 2.27J of energy. Identical tests conducted in ethanol show no change in transmission.**

There is a clear increase in transmission through the water suspension with increasing number of pulses, suggesting a reduction in concentration of the absorbing ACNTs. This is due to the removal of ACNT particles by the water-gas reaction. Such a trend cannot be seen when irradiating ACNT suspensions in ethanol as the transmission properties remain constant.

It can be seen from figure 46 that 20 pulses has increased the transmissivity by 15%. It was therefore interesting to see the effect of larger number of pulses or indeed pulses with higher energy. It was found that there is a correlation between pulse power, number of pulses, bulk heating and an agglomeration effect on the MWCNT clusters.

The reason is that when using high power pulses (e.g. 35W over 100ms) or large number of pulses (more than 20), a visible change in the blackness of the suspension is observed. This is because the MWCNTs in the water suspension are not perfectly dispersed as individual MWCNTs, particularly at 0.1wt%, instead they are dispersed as small clusters. When the energy input to the sample is high per pulse or at high number of pulses (conditions currently under consideration as ongoing work within the authors research

group), initially the outer MWCNTs in the clusters react with the surrounding water converting to CO and H<sub>2</sub> and there are then fresh MWCNTs exposed from the clusters. The fresh MWCNTs would have had been exposed to some radiation (although not sufficient to drive a reaction-between them and the surrounding water) and therefore will have slightly modified structures (as has been observed using TEM). This modification means that most of the functionalisation bonds would have been altered and removed and therefore the resultant structure is more hydrophobic and will repel the surrounding water. The increase in the number of pulses particularly at higher energies will cause the sample bulk to heat up and the water starts to evaporate. On the other hand and at the same time the current induced in these clusters (mostly parallel conductors in the radiation field) will induce an attraction force and bring the clusters together. Indeed sparks can be seen with increasing number of pulses, which is thought to be due to the discharging between the MWCNT clusters when they come into contact. Now this effect is more pronounced if the pulse energy is higher due to a stronger current induction. Also it will start to play a dominant role when the number of pulses has been sufficient to expose enough MWCNTs and cause bulk heating and therefore disturb the suspension. Bulk bubble formation and aggressive heating will have two specific effects on bringing the MWCNT clusters together; one is that the bubbles depart from the MWCNT cluster surface producing a suction force between the clusters. The other is the agitation caused by the motion of the water between the hot and cold regions.

When using lower powers and smaller number of pulses (as reported in this work) this effect is minimal, because the heat generated by each pulse during the first few pulses is initially used to remove the exposed MWCNTs and experience showed that if the experiment is stopped after the first 20 pulses no bulk heating would take place and there was no contribution to sample disturbance due to agitation of heating and boiling to bring the clusters close together. The temperature changes in the sample were measured using the pyrometer and the recorded temperature profile for ACNT suspensions irradiated with a maximum of 20 pulses in water is shown in Figure 47.

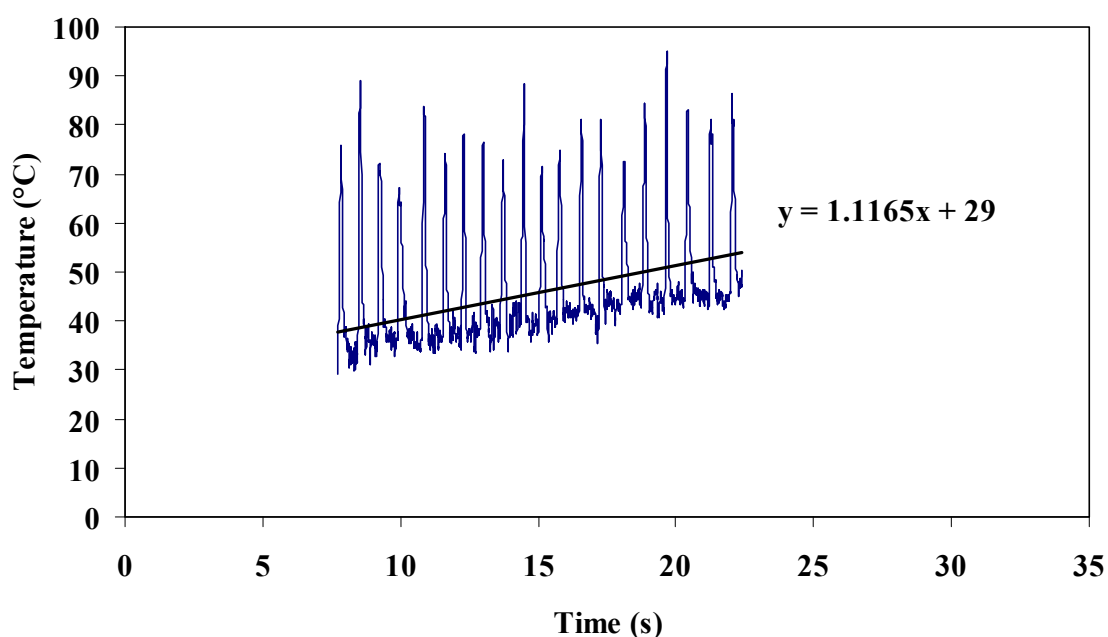


**Figure 47, temperature profile of the 0.1wt% multiwall carbon nanotube and water suspension irradiated with 20 successive pulses of 100ms long and 2.27J energy.**

The graph shows that there is a corresponding temperature peak for each pulse, which for the first few pulses almost reduces back to room temperature immediately after the pulse is finished. After a large number of pulses have been delivered to the sample the base temperature starts to increase as shown by the best linear fit in Figure 47 with the intercept set at 29°C which is the lowest measurable temperature by the pyrometer.. This is because the ACNTs are being disintegrated to CO and H<sub>2</sub> with most of the incident beam being consumed to provide the required energy to drive this reaction. The temperature conducted to the water is highly confined to the immediate vicinity of the tubes, as described earlier, and then used to create a steam jacket, which will subsequently react with the ACNTs. Therefore, only a small amount of the heat is conducted to the bulk of the water.

The radiative losses are also mainly transmitted through the water and collected by the pyrometer. The single pulse temperature analysis for ACNTs in ethanol is shown in Figure 48. It is clear that the temperature is rapidly increased at the application of the pulse and then abruptly reduced by dissipation to the surrounding ethanol as soon as the pulse is finished.

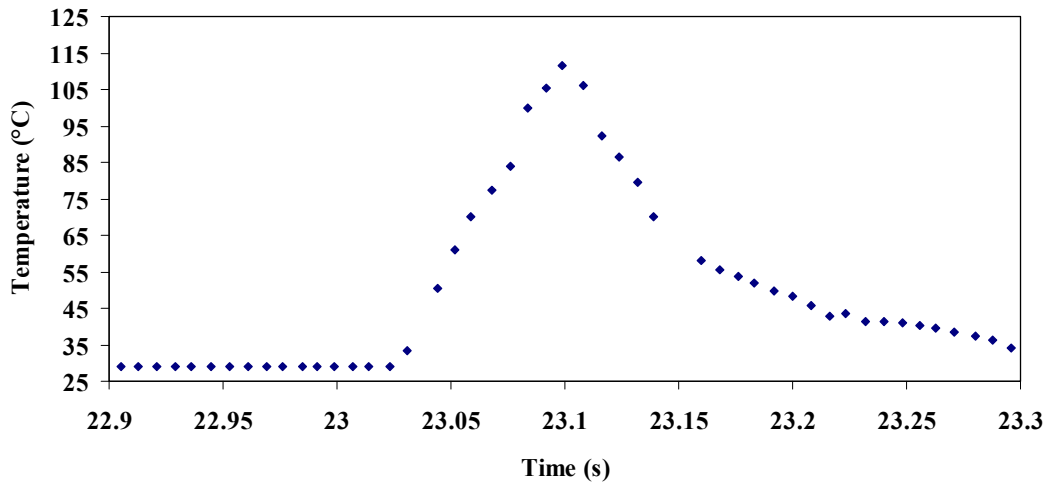


Figure 48, single pulse temperature profile for 1ml of a 0.1wt% multiwall carbon nanotube suspension in ethanol.

However, resolving the temperature profile for a single pulse in water provides a different shape of curve, as shown in Figure 49.

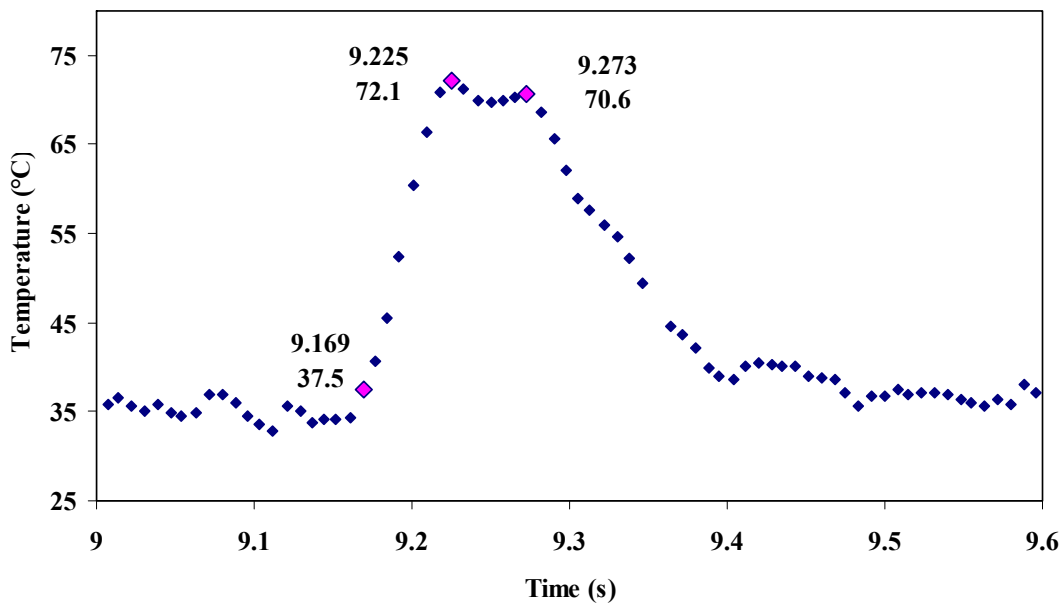


Figure 49, heating curve from an IR pyrometer of 0.1wt% suspension of multiwall carbon nanotube in water for a single 100ms pulse of 2.27J energy.

The reflection fraction ( $R_f$ ) of the ACNT samples were estimated to be 0.086 (see Table 12 section 5.1.5) and the transmission fraction ( $T_f$ ) was measured to be 0.048. The absorption fraction ( $A_f$ ) of the sample can therefore be calculated using the following rule:

$$R_f + A_f + T_f = 1 \quad (51)$$

The absorption fraction of the ACNT suspensions can therefore be estimated as 0.866. Therefore the amount of energy absorbed by the tubes is  $(0.866 \times 2.27\text{J})$  which is 1.97 J. As can be seen in Figure 49, the laser pulse starts at 9.169 seconds and the sample temperature increases rapidly to  $72.1^\circ\text{C}$  by 9.225s (after 56 ms). This is thought to be due to the absorption of the laser radiation energy by the tubes closer to the water surface, which reduces the transmission of laser radiation to tubes in subsequent layers. At this point the exposed tubes at the surface are hot enough to undergo water-gas reaction (total energy delivered to the tubes is 1.27J and the total energy absorbed by the tubes is 1.1J). The temperature then drops slightly (to  $70^\circ\text{C}$ ) and remains the same (plateaus) despite the fact that the beam is still on for a further 48ms until the pulse ends at 9.273s. The reason for the plateau is thought to be the reduction in the amount of absorbers due to their consumption by the water-gas reaction, which has also consumed heat, as it is an endothermic reaction. The sample temperature therefore does not increase despite the laser providing heat (the amount of energy delivered during this phase is 1J and the energy absorbed by the tubes or consumed by the reaction is 0.87J). After the pulse ends, the temperature decreases rapidly and falls back to ambient temperatures.

Using the initial concentration of the MWCNTs and the Beer-Lambert law, the change in ACNT suspension concentration as a result of successive pulses can be estimated. The Beer-Lambert law is a logarithmic relationship between the transmission of light and the absorption coefficient ( $\alpha$ ) and thickness of a material ( $z$ ) as in Equation (52).

$$T_f = \frac{I}{I_0} = 10^{-\alpha z} \quad (52)$$

The absorption coefficient of a liquid is equal to the molar absorptivity or extinction coefficient ( $\beta$ ) of the absorbers and their concentration ( $C$ ), therefore:

$$-\ln T_f = \beta z c \quad (53)$$

This is known as absorbance of a material. The initial mass in 1ml of the ACNTs in the 0.1wt% water suspension was 0.0001g (for 1g of water using water's density value of 1000kgm<sup>-3</sup>). The extinction coefficient for ACNT suspensions was calculated to be 4.22 × 10<sup>4</sup> the details of which is given in Table 12 in section 5.1.2. Therefore using the values of transmission for each pulse, the amount of ACNTs removed after each pulse can be calculated. These results are listed in Table 10.

**Table 10, calculated change in concentration with consecutive 100ms laser pulses of 2.27J each.**

<b>Pulse number</b>	<b>E delivered by the laser/J</b>	<b>E transmitted/ J (average of three trials)</b>	<b>Transmission Fraction (T<sub>f</sub>)</b>	<b>-ln T<sub>f</sub> or A</b>	<b>Transmission %</b>	<b>Concentration of the suspension after each pulse (g cm<sup>-3</sup>)</b>	<b>Amount of nanotubes removed with each pulse/ g</b>
1	2.266	0.015	0.007	5.018	0.662	1.082E-04	7.818E-04
2	2.266	0.017	0.008	4.893	0.750	1.055E-04	2.698E-06
3	2.266	0.018	0.008	4.835	0.794	1.042E-04	1.232E-06
4	2.266	0.025	0.011	4.507	1.103	9.716E-05	7.082E-06
5	2.266	0.029	0.013	4.358	1.280	9.396E-05	3.200E-06
6	2.266	0.050	0.022	3.814	2.207	8.221E-05	1.174E-05
7	2.266	0.074	0.033	3.422	3.266	7.376E-05	8.451E-06
8	2.266	0.107	0.047	3.053	4.722	6.581E-05	7.950E-06
9	2.266	0.146	0.064	2.742	6.443	5.911E-05	6.700E-06
10	2.266	0.151	0.067	2.708	6.664	5.839E-05	7.259E-07
11	2.267	0.152	0.067	2.702	6.705	5.825E-05	1.328E-07
12	2.268	0.166	0.073	2.615	7.319	5.637E-05	1.890E-06
13	2.269	0.168	0.074	2.603	7.404	5.612E-05	2.487E-07
14	2.270	0.179	0.079	2.540	7.885	5.476E-05	1.358E-06
15	2.271	0.192	0.085	2.470	8.454	5.326E-05	1.502E-06
16	2.272	0.200	0.088	2.430	8.803	5.239E-05	8.705E-07
17	2.273	0.219	0.096	2.340	9.635	5.044E-05	1.947E-06
18	2.274	0.261	0.115	2.165	11.478	4.667E-05	3.773E-06
19	2.275	0.303	0.133	2.016	13.319	4.346E-05	3.207E-06
20	2.276	0.350	0.154	1.872	15.378	4.036E-05	3.099E-06

The change in concentration with the first pulse is almost 100 times larger than that of the subsequent pulses. It is likely that due to the high absorption properties of the CNTs the tubes are removed almost layer by layer from the top surface of the sample inwards with each successive pulse. Therefore, at the top surface more tubes would have been removed because the very top layer would have been closer to the surface, and therefore a layer of air, whereas the subsequent layers can only react with the water.

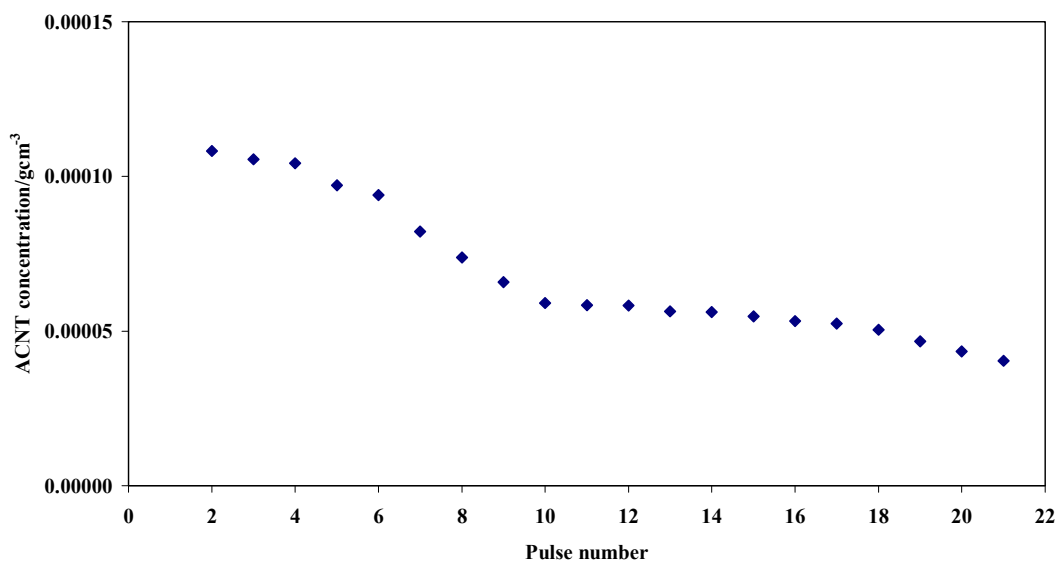


**Figure 50, change in multiwall carbon nanotube water suspension concentration with sequential laser pulses.**

#### **4.4. Removing carbon nanotubes from water suspensions in between layers of bacon**

##### **4.4.1. Experimental set up**

The next step is to assess whether MWCNTs could indeed be removed from body tissue. A first order experiment is conducted here in which a 0.1wt% water suspension of nanotubes is placed between two bacon slices (~ 1.7 mm thick) and irradiated through the upper one. Five ml of the 0.1wt% ACNT water suspension was placed between two slices of bacon and irradiated with 100ms laser pulses 2.27J and spot size of 0.88cm<sup>2</sup>. The same experimental set up as Figure 45 was used with the bacon slices placed on the power meter instead of the beaker. The bacon used was 90% pork meat with no other additives apart from 10% water and traces of salt as indicated in the ingredient list. Prior to testing,

the thickness of each slice was measured at three points and averaged. Furthermore the transmission of the laser pulses through stacks of bacon layers was also measured.

#### 4.4.2. Results and analysis

Using Equation 54 the  $\ln T$  is plotted against thickness in Figure 51. As can be seen, the transmission decreases with increasing in thickness.

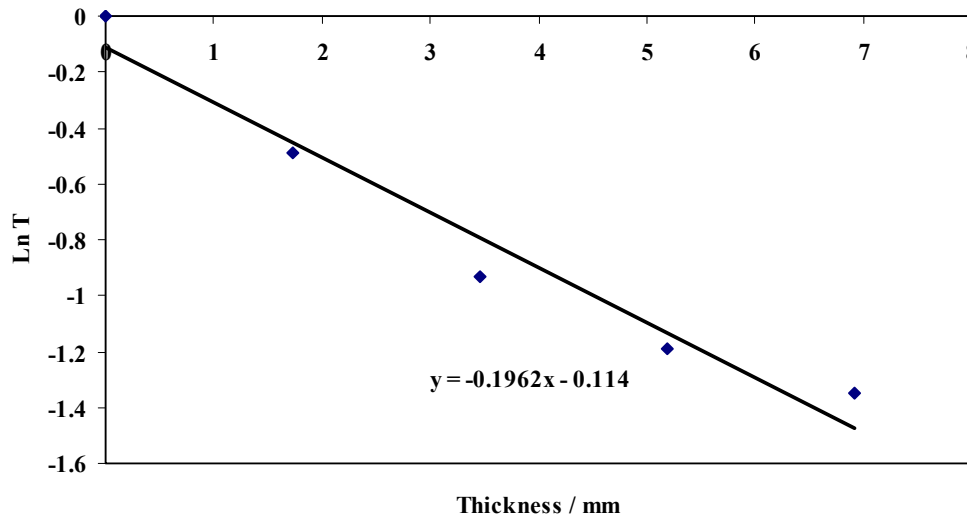


Figure 51, logarithmic regression of transmission with thickness of bacon layers.

Logarithmic regression analysis using Equation 54 gives the following values:

$$\ln T = \ln(1 - R_f) - \alpha z \quad (54)$$

$R = 0.108$  and  $\alpha = 0.163 \text{ mm}^{-1}$ . The fraction of energy absorbed by the layers of bacon can be calculated using Equation 55:

$$A = 1 - R_f - ((1 - R_f)e^{-\alpha z}) = (1 - R_f) \times (1 - e^{-\alpha z}) \quad (55)$$

This gives the blue absorbance curve in Figure 52.

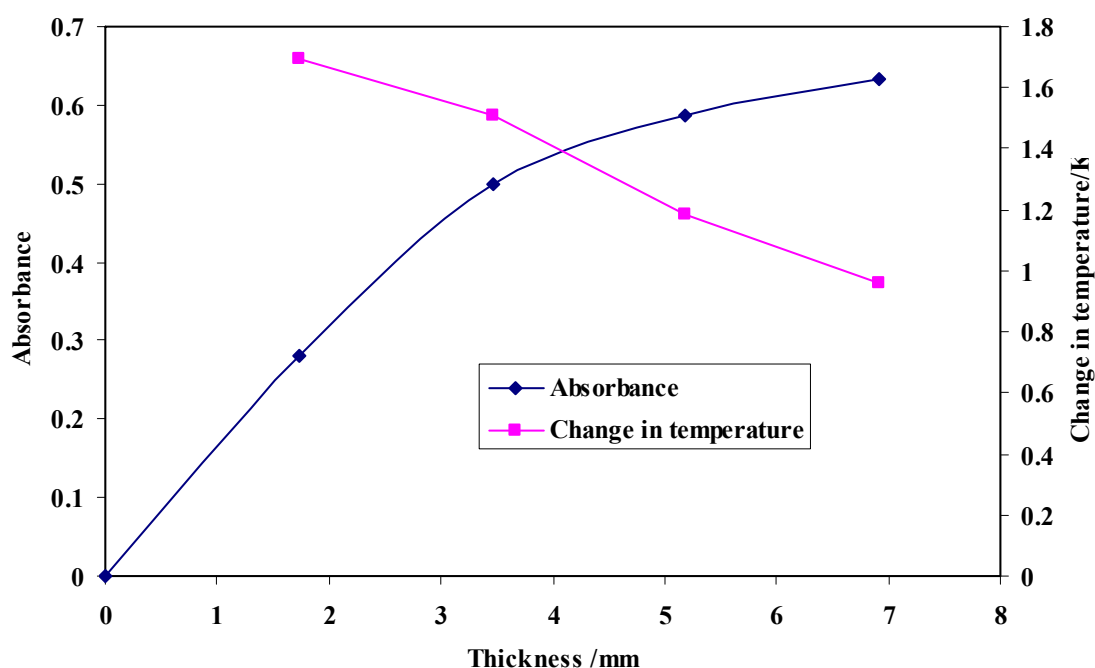


**Figure 52, direct absorption of light by different thicknesses of bacon layers (blue curve and the left Y axis) and the associated temperature change (pink curve and the right Y axis).**

As can be seen in Figure 52, direct absorption of the beam does not significantly raise the temperature of the bacon layers. The value of the small temperature change further decreases with thickness as the mass that needs to be heated increases. Real-time temperature measurements using the pyrometer confirmed the lack of any measurable increase in temperature when two layers of bacon were irradiated.

Five ml of ACNT water suspension was then added between two layers of bacon. The sample was irradiated with a 2.27J pulse of 100ms long over a 0.88cm<sup>2</sup> spot. Fifteen consecutive pulses (with 3 second time interval) were delivered and the resultant transmission measurements (after deducting losses due to the two bacon rashers) are shown in Figure 53.

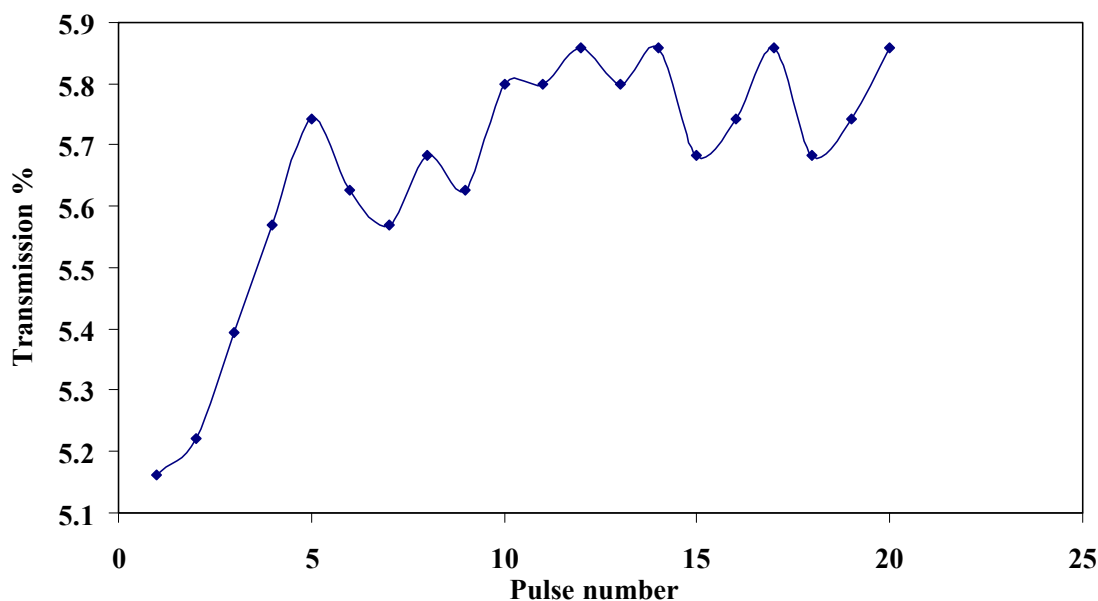


**Figure 53, change in transmission with pulse number for 5ml of 0.1wt% multiwall carbon nanotube-water suspension between two slices of bacon. Transmission through 2 slices of bacon with 5ml of 0.1wt% ACNT-Water suspension in between.**

Figure 53 shows that the transmittance increases with consecutive pulses. The increase is small but it is quite rapid through the first 5 pulses, almost 0.8%, and then fluctuates slightly. However, it seems likely that the overall transmission is gradually increasing. Simultaneous temperature measurement using the pyrometer on the upper surface, where the laser radiation enters the top layer of bacon showed no detectable change in temperature, indicating that any heat transfer from the CNTs does not diffuse too deeply into the bacon. Examination of both bacon layers showed no visible damage, in terms of change in texture or discolouration. There was, however, some clear patches void of any nanotubes, on top of the lower bacon layer, where the MWCNTs were originally deposited.

#### **4.5. Summary**

As the remote removal of nanotubes from living tissue is one of the main objectives of this work, a radiation source was selected with sufficient power intensity to turn the nanotubes into gas, but not so much power and for such duration that it would exceed permitted doses for the skin in particular. The wavelength was also chosen to be as close as possible to that for the maximum penetration of soft tissue, with minimum amount of

scattering and absorption by the tissue. The skin tolerance curves and the relationship between tissue penetration and wavelength curves coupled with the need to heat the nanotubes towards 1140°C led to the use of a 940 nm near IR laser capable of illuminating an area of 0.88cm<sup>2</sup> at a power density of 23 W/cm<sup>2</sup> which for a 100ms pulse was close to and slightly exceeded the published safe limit.

It was possible to initiate the water-gas reaction in aqueous suspensions of ACNTs using the NIR laser source at 940 nm wavelength using 100ms long pulses of 23 Wcm<sup>-2</sup>. It was observed that most of the energy absorbed by the tubes is re-radiated and only a small part of it is consumed to drive the reaction; therefore the reaction can be driven at very small energy inputs and potentially within safe exposure limits for skin. The overall temperature rise of the aqueous sample after heating the ACNTs is small after each pulse and below the temperature threshold damage to the tissue. This was practically demonstrated by using layers of bacon, with dispersed suspensions of ACNTs in water between them. When irradiated with multiple pulses, no change in temperature or appearance of the bacon was observed; however, the transmission through the samples gradually increased indicating the reduction in the amount of absorbers in the beam path, i.e. removal of the ACNTs from in between the bacon layers by the laser beam.

## 5. Laser absorption and heating of carbon nanotubes

### 5.1. Laser transmission through water and ethanol suspensions

The absorption characteristics of MWCNTs and the influence of structural variation in the samples were investigated and compared with that of CB and SWNTs. The MWCNTs used were acid treated to enable uniform dispersion in water or ethanol. Both types of acid treated samples (ACNT and AHCNT) were used to investigate the influence of remnant iron catalyst particles as well as structural disorder on laser absorption. ACNTs have structural disorder and added chemical bonds due to the acid treatment as well as some remnant iron catalysts particles (particularly inside the tubes). AHCNT are almost free from remnant iron catalysts due to the heat treatment but have structural disorder and added chemical bonds due to the acid treatment process, although to a lesser extent than the ACNTs.

The Laserline diode laser was used operating at a wavelength of 940 nm. Identical laser intensities (power /spot size) were used for all the experiments so that results would be comparable.

The laser transmission properties of different concentrations of absorbers in water and ethanol suspensions were then investigated to evaluate absorption coefficients and compare that with their heating efficiency. The test matrix for the wet transmission trials are given in Table 11.

**Table 11, test matrix for heating and transmission measurements through suspensions of different samples in water or ethanol.**

Test	Absorber/ 1ml	Intensity /Wcm <sup>-2</sup>	Matrix	Concentration/ wt%	Laser spot size/cm <sup>2</sup>	Pulse/s	Sample area/cm <sup>2</sup>
Transmission	ACNT, AHCNT, CB	30	Water, Ethanol	0.005, 0.01, 0.05, 0.1	1	0.1	1

### 5.1.1. Laser transmission experimental set up

The laser transmission measurements were conducted as described in section 4.3. The laser was delivering 23W for 100ms pulses each time with a spot size of  $0.88\text{mm}^2$ . The measuring device was calibrated and gave a reading of 2.3J per pulse. The experiments were conducted using a single pulse and measuring the intensity of the transmitted beam through the sample.

### 5.1.2. Water and ethanol suspensions transmission results and analysis

The test were done as triplicates and it was seen that for water suspensions the transmission progressively increase in triplicate tests done consecutively on the same sample due to the removal of the tubes via the water-gas reaction with each pulse. The triplicate tests on water suspensions were therefore conducted on a fresh sample each time. Using the value of density for water and ethanol (1 and  $0.79\text{ g/cm}^3$  respectively) and the concentration of the absorbers tested (i.e. 0.005, 0.01, 0.05 and 0.1 wt%) the concentration of the absorbers where calculated in  $\text{g/cm}^3$  and are plotted against transmission ( $\ln T$ ) in Figure 54.

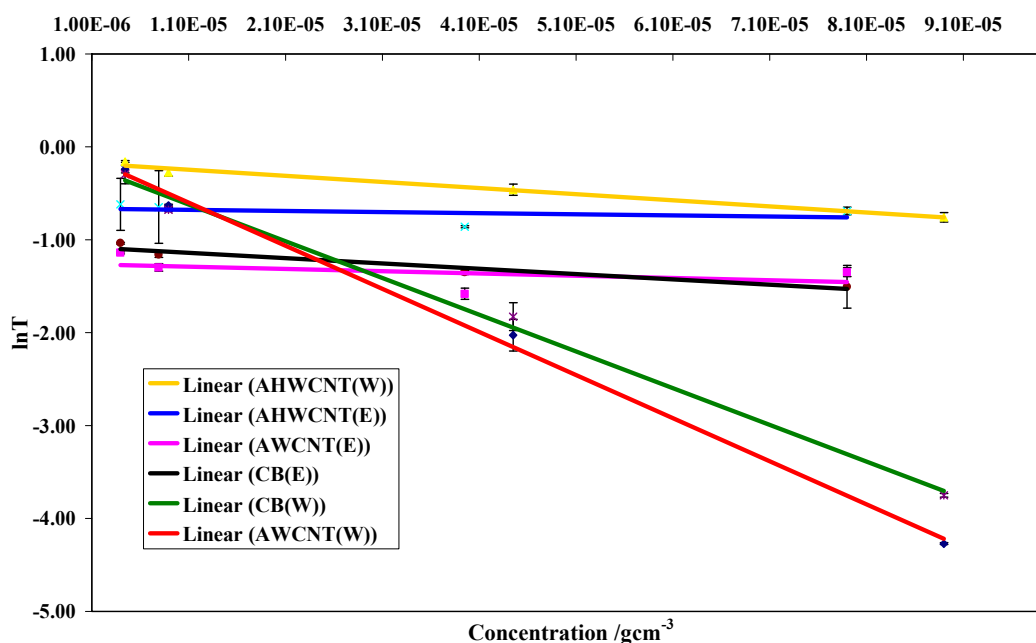


Figure 54, change transmission with increasing concentration for different suspensions of multiwall carbon nanotube and carbon black in water and ethanol.

A linear trend line was fitted to the data. It can be seen that the transmission in ethanol stays almost constant with concentration while in water it decreases dramatically with increase in concentration for all the absorbers. Using the straight line equations for each absorber in each matrix and using Equations (54) and (55) the optical properties of the different suspensions were calculated and are presented in Table 11:

**Table 12, optical properties of different suspensions.**

Suspension	$\ln(1-R_t)$	$R_t$	$\beta x/\text{cm}^3 \text{g}^{-1}$	$x/\text{cm}$	$\beta/\text{cm}^2 \text{g}^{-1}$
ACNT(Water)	-0.089	0.086	46388.0	1.1	42170.1
ACNT(Ethanol)	-1.264	0.717	2419.9	1.1	2199.9
AHCNT(Water)	-0.171	0.157	6619.4	1.1	6017.6
AHCNT(Ethanol)	-0.667	0.486	1178.5	1.1	1071.4
CB(Water)	-0.188	0.171	39487.0	1.1	35897.3
CB(Ethanol)	-1.077	0.659	5746.0	1.1	5223.6

It was observed that the extinction coefficients in water are higher than in ethanol and higher for ACNT than CB than AHCNT. This is thought to be due to the water-gas reaction taking place, which causes extinction of the laser light due to absorption by the reacting material.

The change in the samples temperature was measured using the Impac Infrared equipment as described in the heating trials. Figure 55 shows the results of the temperature measurements plotted against concentration for different samples.

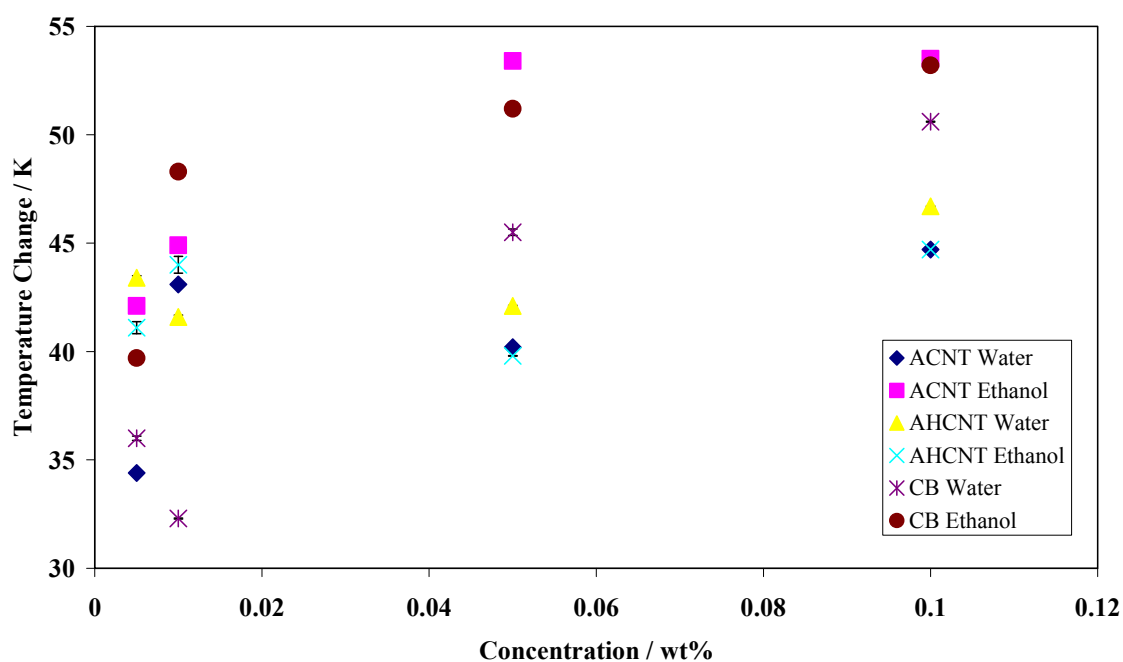


**Figure 55, change in samples' temperature with concentration using a 100ms laser pulse of 2.27J. Maximum temperature variation for 1ml of different absorbers at different concentrations in different media are shown.**

The general trend for ACNT and CB in ethanol is that the temperature increases logarithmically with concentration until about 0.02 w% where the temperature increase tends towards a plateau. This could be due to the percolation threshold being reached at around 0.02wt% loadings. Percolation is the formation of long range connectivity in a random system as with dispersed MWCNTs in ethanol or water and this threshold is inversely proportional to the aspect ratio of the conductive filler [148]. The effect of percolation threshold on heating MWCNT suspensions has also been reported in the literature [149]. It is therefore not unexpected that ACNTs and CB should show a similar threshold, as the measurement of their length highlighted that the ACNT tube length are in the same order as the CB particle clusters. It has been shown that electromagnetic energy absorption increases slowly with carbon nanotube concentration up to the percolation threshold, this absorption greatly increases at electrical percolation. Indeed the percolation threshold has been reported previously for MWCNTs in silicon oil to be around 0.022 to 0.026 wt% [149].

A similar trend can be seen for the other absorbers where the heating is increased exponentially and then plateaus, however the maximum heat generated is not as high for

the AHCNTs. The heat generated in water suspensions is less and this is due to the water-gas reaction taking place which removes heat from the system hence showing less heating while having higher extinction coefficient.

The effects seen in transmission measurement are contributed to by; the absorption properties of the MWCNTs as well as the thermal properties of the matrix and their interaction. Furthermore only absorption properties of samples could be examined that were dispersible in water and ethanol with minimal agglomerations namely acid treated samples or CB. However, the structures of such MWCNTs are altered by the acid treatment process, which would consequently affect their optical properties. It is therefore essential to examine the absorption properties of our materials independent of the effects of the surrounding matrix and expand this to all the produced and post treated MWCNT samples to identify the best parameters and material type combination for generating heat by using a NIR laser source. This work is described in the following section.

## **5.2. Laser heating and transmission through dry samples**

### **5.2.1. Sample types**

These tests included laser heating and transmission through all the samples in a dry form either as powder or as aligned carpets to understand and compare their coupling efficiency in terms of the heat generated and the amount of intensity transmitted, as well as the effects of orientation and light polarisation. This gives a ranking of the different types of MWCNTs in terms of absorption and heating efficiency per unit mass or thickness for a given laser intensity and a comparison with CB and SWNT, which were procured and not manufactured in house. The materials used are listed in Table 13.

**Table 13, list of materials used in dry heating and transmission trials.**

<b>Abbreviation</b>	<b>Material</b>	<b>Sample form</b>
WCNT	Multiwall carbon nanotubes grown on the walls of the quartz furnace	Randomly oriented fibres
SCNT	Multiwall carbon nanotubes grown on the substrates placed inside the quartz furnace	Aligned carpets
HCNT	Heat treated SCNT	Aligned carpets
ACNT	Acid treated WCNTs using the ultrasonic method	Randomly oriented fibre agglomerates
AHCNT	Heat treated and then acid treated WCNTs	Randomly oriented fibre agglomerates
HBCNT	Ball milled and then heat treated WCNT	Randomly oriented fibres
CB	Carbon black	Spherical particles
SWNT	Single wall carbon nanotubes	Randomly oriented fibre agglomerates

### **5.2.2. Laser heating experimental set up**

Laser powers were chosen following initial test results at different intensities both in air and argon to avoid oxidation of the samples and the need of complex experimental set up in inert gas, which would have compromised the quality of the temperature measurements. Triplicate tests were carried out to provide statistical confidence in the results with test durations of 60 seconds.

All the trials with ACNT, SWNT, AHCNT, HBCNT and CB were made using a laser intensity of  $2.5\text{Wcm}^{-2}$ . The trials with HCNT and SCNT were made using  $1.25\text{Wcm}^{-2}$  of intensity, because for the latter tests a polariser was used and its damage threshold limited the maximum laser power that could be used for the tests in combination with sample geometry and the required beam size.

The specimens to be laser heated were placed directly under the beam with the centre of the laser spot on the centre of the sample. A typical set up is shown in Figure 56.

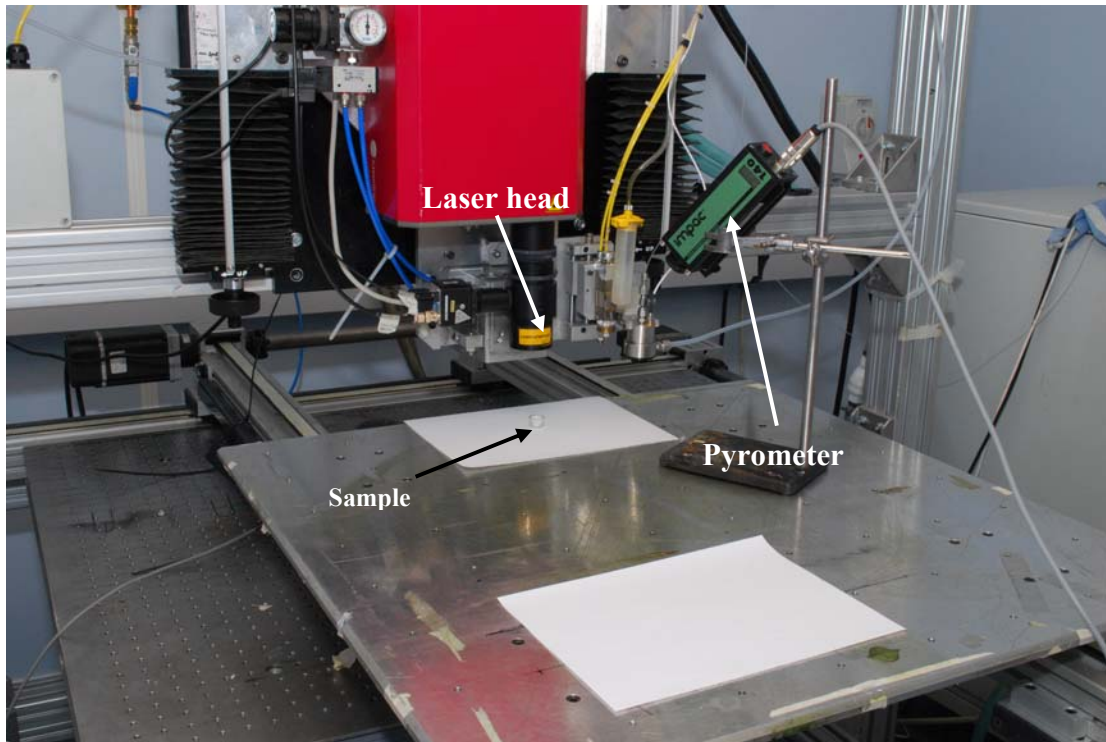


**Figure 56, a typical laser heating experimental set up, during the experiments the pyrometer is generally moved much closer to the sample and the laser.**

The laser was set to the selected nominal power of 5W; this was then calibrated using an Ophier energy meter to measure the exact amount of energy delivered by the beam, which was confirmed to be  $5 \text{ Js}^{-1}$ . The laser was operated from outside of the laser cell for health and safety reasons and thermography, using an Impac Infrared pyrometer was used as explained earlier to measure temperature changes. ACNT, AHCNT and HBCNT were in powder form and were compared to CB and SWNT as dry powders. CB was used mainly as control and SWNT was used to see the effect of diameter and other structural variance. Table 14 shows the test matrix used for dry heating tests.

**Table 14, heating of dry samples at 940nm with a 5W nominal power and 60 seconds pulse duration.**

Sample	Weight/ mg	Surface area/ cm <sup>2</sup>	Thickness /mm	Laser spot /cm <sup>2</sup>	Laser intensity /Wcm <sup>-2</sup>	Sample orientation/ Light polarisation
AWCNT	237	1	12	2	2.50	Random
AHCNT	661	1	12	2	2.50	Random
HBCNT	210	1	12	2	2.50	Random
SWNT	328	1	12	2	2.50	Random
CB	570	1	12	2	2.50	Random
HCNT	9.6	0.2	2	4	1.25	↑ / Random
HCNT	9.6	0.2	2	4	1.25	↓ / Random
HCNT	9.6	0.2	2	4	1.25	⊥ / Polarised
HCNT	9.6	0.2	2	4	1.25	/ Polarised
SCNT	3.2	0.2	2	4	1.25	↑ / Random
SCNT	3.2	0.2	2	4	1.25	↓ / Random
SCNT	3.2	0.2	2	4	1.25	⊥ / Polarised
SCNT	3.2	0.2	2	4	1.25	/ Polarised

HSCNT and SCNT were used to investigate the effect of laser beam polarisation and the nanotubes orientation on photo-thermal effects as described below:

- The carpets were irradiated from the bottom (denoted by ↓ in the text) and the laser beam was not polarised. The bottom of the carpets is taken as the root of the MWCNTs, which was originally connected to the glass substrates during growth.
- The carpets were irradiated from the top or the opposite end to the root (denoted by ↑ in the text) and the laser beam was not polarised.
- The carpets were irradiated from the side and the laser beam was polarised parallel (denoted by || in the text) to the nanotubes' long axis using a polariser.
- The carpets were irradiated from the side and the laser beam was polarised perpendicular (denoted by ⊥ in the text) to the nanotubes' long axis using a polariser.

HCNT were further used to investigate the saturation intensity. This was taken as the laser power density beyond which no additional heating was achieved and the temperature time curve would reach a plateau, this test matrix is shown in Table 15.

**Table 15, intensity saturation limit, test matrix.**

Absorber	Medium	Power/W	Spot Size/cm <sup>2</sup>	Sample Size/cm <sup>2</sup>	Pulse Duration/s
HCNT	Argon	1	1	1	10 and 60
HCNT	Argon	5	1	1	10 and 60
HCNT	Argon	10	1	1	10 and 60
HCNT	Argon	15	1	1	10 and 60
HCNT	Argon	20	1	1	10 and 60
HCNT	Argon	25	1	1	10 and 60
HCNT	Argon	30	1	1	10 and 60
HCNT	Argon	35	1	1	10 and 60

### 5.2.3. Results of heating and time dependent saturation for samples with random orientation using a non-polarised laser beam

The average maximum temperatures achieved from each set of three experiments for different samples are shown in Table 16, along with the weight specific maximum temperature ( $\text{Kmg}^{-1}$ ). All the temperature-time profiles recorded by the pyrometer showed the same trend (see Figure 57) with a similar plateau to that discussed earlier when considering atomic state saturation with time in section 2.1.1. The sample temperature increases rapidly when the beam starts at  $t = 0$  and then reaches a plateau when steady state conditions are reached for the excitation and relaxation of atomic species.

**Table 16, heating results for dry samples in air using a 5W continuous laser beam for 60s.**

Sample	Pulse duration/s	Laser intensity on the sample/W	Average $T_{\text{Max}} / ^\circ\text{C}$	Standard deviation	Weight specific $T_{\text{Max}} / (\text{Kmg}^{-1})$
ACNT	60	2.5	217.3	0.04	0.92
AHCNT	60	2.5	55.0	0	0.08
HBCNT	60	2.5	310.0	0.06	1.47
SWNT	60	2.5	183.9	0.03	0.56
CB	60	2.5	390.7	0.03	0.69

The weight specific temperature profiles for 250mg of each sample are plotted in Figure 57. It can be seen that the variation between triplicate tests is very small and the average values are good representation of the temperature of each sample. For samples with random orientation it can be seen that maximum heat in descending order is generated by HBCNT, ACNT, CB, SWNT and finally AHCNT.

The multiwall carbon nanotube samples coupled with IR instantly and much faster than CB based on the gradient of the initial part of the curve. This could mean that the initial absorption is influenced by the carbon atoms' ordered and possibly quasi-1D structure. MWCNTs had an immediate increase in temperature and then reached a plateau after approximately 1 second. This can be attributed to the atomic state saturation with time for the given beam intensity. In CB the surface temperature is raised rapidly but as the heat conduction is not as good as the tubes the heating of the subsequent layers in a sample relies on the beam and the generated heat diffusing through contacts between the individual particles. It seemed that HBCNTs' temperature change exceeds that of ACNTs and the coupling is more efficient due to better crystallinity and less impurities. HBCNTs have the same length as that of the radiation wavelength therefore they could couple and resonate with the radiation [150 and 151], in addition they have a graphitised structure, which could increase their absorption properties. ACNT is again more graphitised than CB and shows better coupling and heat generation. CB and SWNT have similar dimensions and show similar heating effects. AHCNT is consistently the least heat generating sample. This sample has been through a graphitisation process and then acid treated. It is possible that the acid treatment has changed the structure of the previously heat treated sample more than those that had not been heat treated. In addition the presence of additional chemical molecules due to the acid treatment might further affect the obtained temperature change in this material. It is possible that at shorter pulses the behaviour of AHCNT is not that much different to ACNT however it reaches time saturation for the excited states much faster and therefore any extended exposure times does not increase its temperature significantly. This hypothesis is examined in the transmission measurements by using short pulses and measuring the associated heating effects

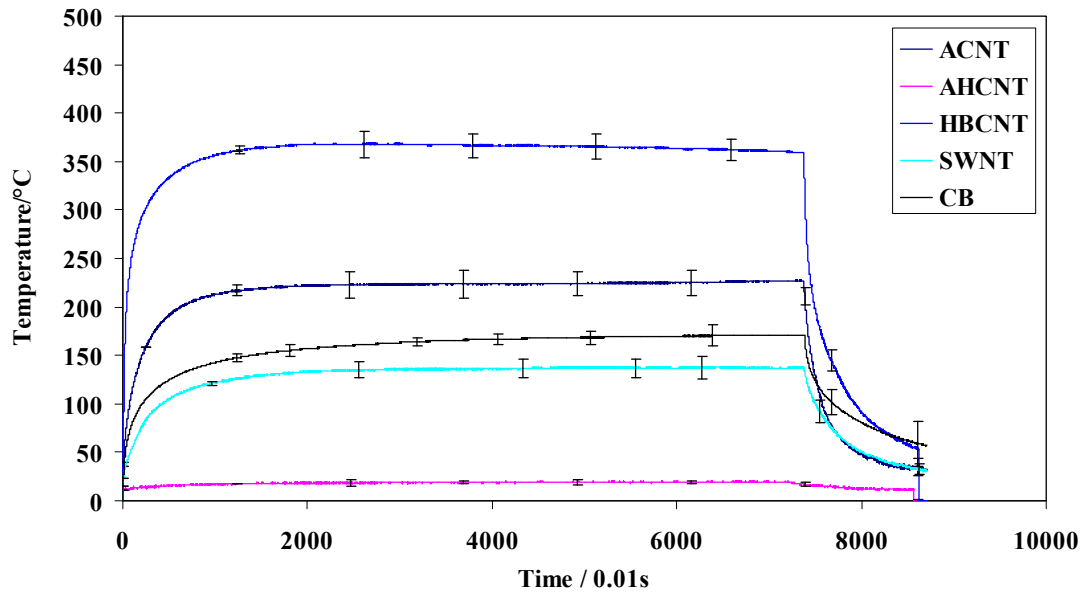


**Figure 57, normalised (for 250mg of each absorber) temperature profile for samples with random orientation.**

The photon frequency of the laser beam was calculated to be  $3.2 \times 10^{14} \text{ s}^{-1}$  with an energy of 1.3eV. Now considering the MWCNTs as an ensemble of many tubes, which themselves are made up of concentric tubes with semiconducting or metallic properties any of the following processes and most probably a combination of all, contributes to the heating of the nanotubes.

For metallic tubes the photon energies are absorbed by the electrons in the conduction band and the gained energy causes these low inertial-mass electrons to flow along the length of the tube. Due to the small electron mean free path most of the energy provided by the electric radiation field to each electron is transferred to phonons via collisions with the lattice and ultimately is converted to heat in the nanotube (Joule heating). This transfer of energy to the lattice is enhanced at sites with defects and impurities such as broken HBCNT or defected structure of ACNT.

In semiconducting tubes the high intensity radiation has photon energies higher than  $E_g$  (reported between 2meV to 1eV [35]) and causes free carrier excitations and band to band transitions. The interaction of these carriers with the lattice in picosecond time

scales increases the lattice temperature instantaneously. However band to band transitions in nanosecond time scales will relax through recombination and give rise to photon emissions. The reradiated energy will have lower frequencies than the absorbed energy as the excited electrons will relax via lattice collisions, which is an inelastic scattering process before undergoing emissions of photons with lower energies than the incident photons. As the lattice heats up the density of high frequency phonons are increased hence the electron mean free path is shortened, leading to increased absorption and heating. Heat conduction is highest along the length of the tubes and the confinement of heat in the tube length is another contribution to the extremely fast temperature rise.

#### 5.2.4. Results of heating and time dependent saturation for samples with polarised light at different orientations

The average maximum temperatures for each set of three experiments for different samples are shown in Table 17 along with the weight specific maximum temperature ( $\text{Kmg}^{-1}$ ). All the profiles are the same showing a similar plateau as that discussed with atomic state saturation with time in section 2.1.1 where the samples' temperature is increased exponentially when the beam starts at  $t = 0$  and then reaches a plateau when steady state is reached between the excitation and relaxation of atomic species.

**Table 17, dry heating results for samples irradiated in air, using a continuous laser beam for 60s.**

Sample	Pulse duration/s	Laser intensity on the sample/W	Average $T_{\text{Max}} / ^\circ\text{C}$	Standard deviation	Weight specific $T_{\text{Max}} (\text{Kmg}^{-1})$
HCNT $\perp$	60	0.25	112.3	0.37	11.70
HCNT $\downarrow$	60	0.25	80.0	0.31	8.34
HCNT $\parallel$	60	0.25	135.1	0.68	14.08
HCNT $\uparrow$	60	0.25	107.0	1.31	11.14
SCNT $\uparrow$	60	0.25	118.7	1.53	37.09
SCNT $\downarrow$	60	0.25	85.4	1.63	26.70
SCNT $\perp$	60	0.25	153.5	3.47	49.12
SCNT $\parallel$	60	0.25	160.5	1.77	50.17

The experiments with a polariser showed that there was an influence from the orientation of the MWCNT fibres and the polarisation of the light on the temperature change.

Laser heating HCNT carpets showed that, when the laser beam was random and not polarised, more heat was generated at the top of the carpet than at the bottom. The amount of heat generated by the HCNT increased when the laser beam was polarised as shown in Figure 58 with the maximum amount of heat generated when the laser beam was polarised parallel to the HCNTs long axis. As it was discussed in Chapter two parallel to the tube axis, MWCNTs are optically isotropic and similar to amorphous carbon, and perpendicular to the tube axis their properties depend on light polarisation. If light is polarised parallel to the tube the dielectric function is similar to graphite as the surface resembles planar graphite if it is polarised perpendicular to the tube the dielectric function is a mixture of both parallel and perpendicular dielectric functions of the graphite sheet, the free-carrier absorption is therefore enhanced when the beam is polarized parallel to the tube axis. This is because unlike the classical plasmon in a 3D electron gas, the plasmon in a carbon nanotube bundle is anisotropic and can be excited only along the tube axis. The lower energy mode is the  $\pi$  plasmon, while the higher energy has been identified as the  $\pi + \sigma$  plasmon.

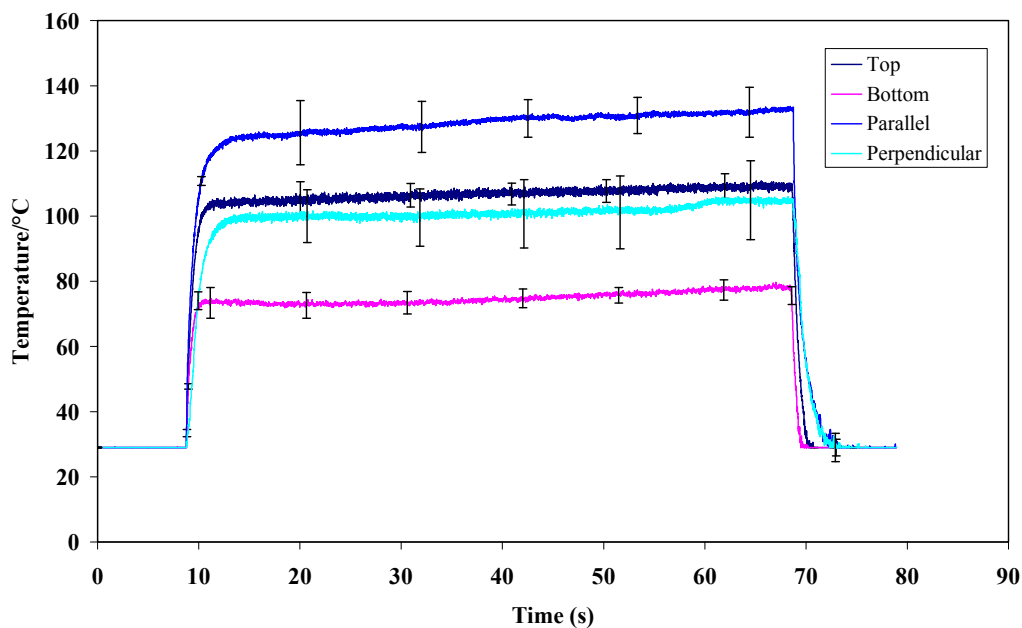


**Figure 58, temperature profile for aligned heat treated multiwall carbon nanotube carpets (HCNT) with light polarisation parallel and perpendicular to their axis when irradiated from the side or randomly polarised when irradiated from the top or the bottom of the carpet.**

When laser heating SCNT, as for the HCNT, more heat was generated when the laser beam was incident on the top of the carpets were rather than the bottom. More heat was

also generated when the laser beam was polarised, although this time, similar amounts of temperature change was observed for both perpendicular and parallel polarisation direction as shown in Figure 59. If tunneling between nanotubes is permitted, the classical Plasmon can then be excited in a direction perpendicular to the nanotubes. This could be the reason why the heating difference in SCNT for parallel and perpendicular directions is similar as the imperfect structure allows tunneling of electrons. It has been shown that defects as well as formation of nanotube bundles can dramatically enhance the optical signatures of this coupling. At intermediate frequencies there is a series of plasmon modes each related to a specific inter-van Hove electron transition. These weakly dispersive modes occur in the range of frequencies between 0.5 to 3 eV. This coincides with the photonic energy of the radiation used in this study with photonic energy of 1.32eV. It is also possible that the magnetic field of the radiation will change the energy gap of the tube and since the presence of an energy gap in a carbon nanotube is determined by whether or not the 1D energy bands cross or not cross at the K or K' points at the corners of the BZ, a semiconducting carbon nanotube can become metallic and the absorption can be enhanced.

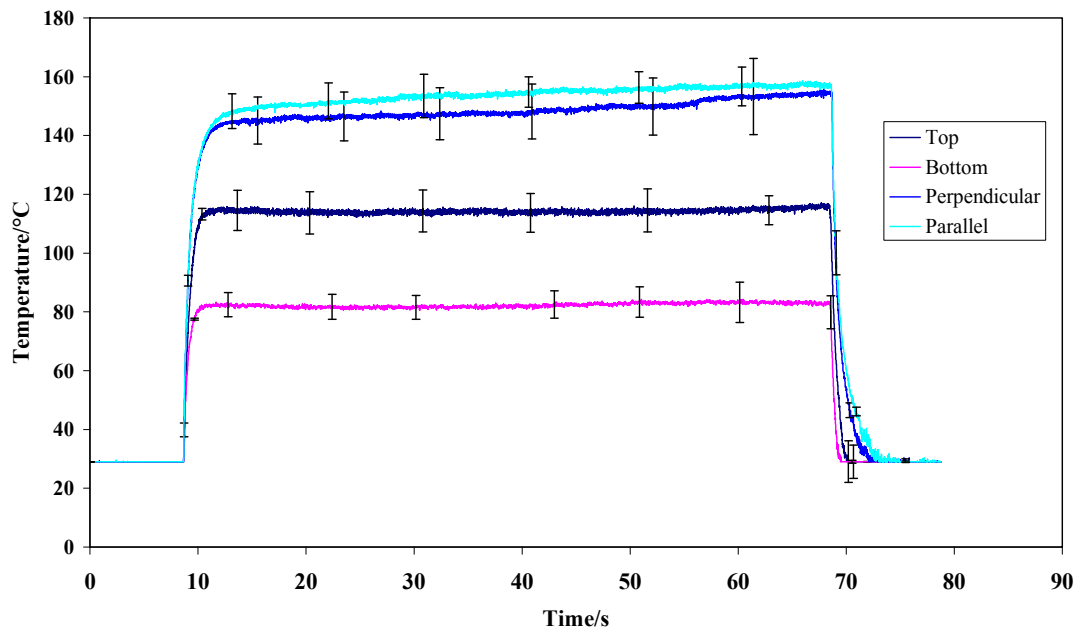


**Figure 59, temperature profiles for SCNT samples with light polarisation. SCNT - effects of fibre orientation and light polarisation.**

To compare the effectiveness of conversion of the laser light energy into heat, weight specific minimum temperatures and the results are shown in Figure 60.

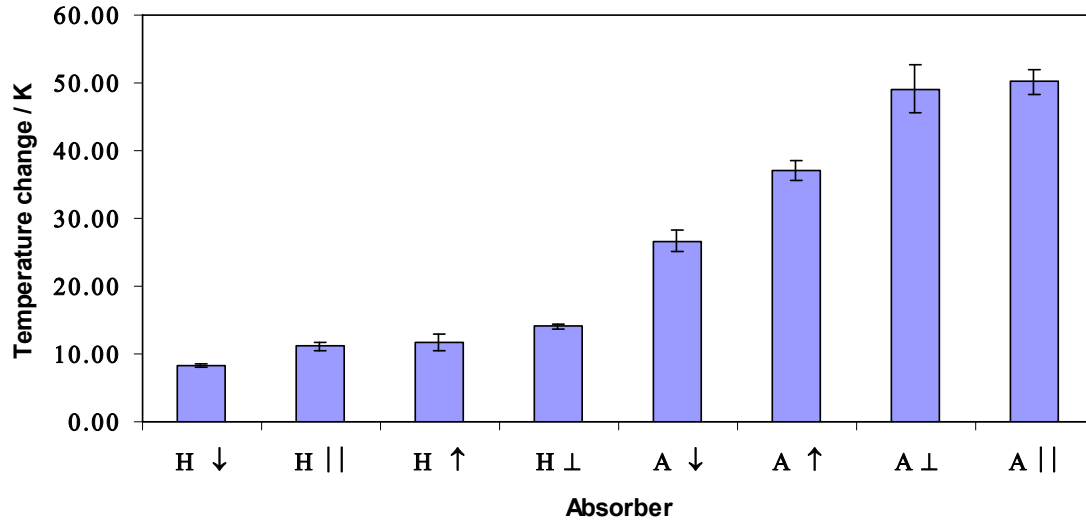


**Figure 60, weight specific temperature change (average  $T_{max}$  for 1mg of sample) for heat treated aligned multiwall carbon nanotube carpets denoted by (H) and as-produced aligned multiwall carbon nanotube carpets denoted by (A) with different orientation and laser beam polarisation (|| means that the beam is polarised parallel to the tubes' axes,  $\perp$  means that the beam is polarised perpendicular to the tubes' axes,  $\uparrow$  means that the light is randomly polarised and the tubes are irradiated on the top end and  $\downarrow$  means that the tubes are irradiated on the bottom end with a randomly polarised light) .**

It is observed that the amount of heat generated by as produced carbon nanotubes is by far greater than that produced by heat treated tubes. The difference is due to the structure of heat treated tubes having fewer defects and scattering points. Also a difference in the heat capacity observed, which can also be shown by calculating the energy input and the resultant change in temperature. However, the absorption properties of the different samples needs to be investigated to further understand whether the resultant heating is due to differences in absorption of the beam or the ability to convert it to heat. Therefore it is possible that HCNTs have better absorption properties due to their crystalline structure, however, the Joule heating term in Boltzmann's transport Equation is reduced due to a reduced electron phonon coupling term. This is examined further in section 5.2.6.

### **5.2.5. Measuring intensity saturation in heat treated carbon nanotubes**

Further tests were carried out on HCNTs by measuring the maximum temperature achieved using different laser powers to examine the intensity saturation limit for HCNTs. The maximum temperature was reached very quickly (recorded in milliseconds due to equipment frame rate limitations) and the tests were done for 10 second durations, because higher laser intensities caused sample degradation and oxidation for longer exposure times, even though the tests were carried out in inert gas (argon) environment. This is because the sample's temperature would have increased until the tubes were hot enough to react with the small amounts of oxygen present as impurities in the argon gas or adsorbed on the tubes. This is why longer exposures than 10s caused oxidation (burning) of the tubes. This is again parallel with the TGA results discussed in section 3.3.6, in dry

helium, where at high enough temperatures (around 1000°C) the MWCNT sample showed weight loss and oxidation due to adsorbed oxidising molecules such as O<sub>2</sub>, CO<sub>2</sub> or trapped water. The results of the intensity saturation experiments are plotted in Figure 61. The heat output (maximum temperature) increases with the laser power, however for intensities greater than 20 Wcm<sup>-2</sup> the temperature rise is beyond the measurement range of the pyrometer and therefore the tests not provide conclusive results, although it is anticipated and has been reported [152] that the tubes can reach much higher temperatures under laser radiation.

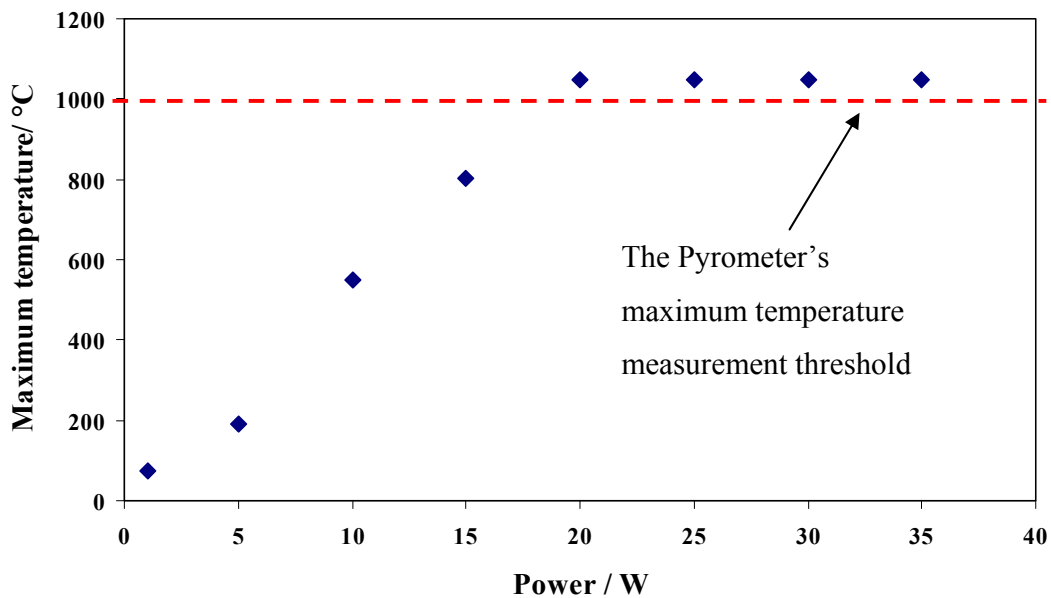


**Figure 61, results of the laser power saturation trials using a 10s long continuous laser beam. The experiment reached the limits of the pyrometer at 20W laser input, which caused an increase in temperature in excess of 1000°C.**

Although the saturation intensity limit could not be measured for the HCNTs the results provided a very important information, that is even at laser power intensity as low as 20W large temperature increases can be achieved in MWCNTs which is very important when conducting and designing the laser welding experiments.

### **5.2.6. Laser transmission experimental set up**

The laser transmission measurements were conducted as described in section 4.4, with the samples placed on a glass substrate (same material as the beaker used in the wet transmission trials in section 4.4). The laser was delivering 100ms long pulses each time with a spot size of  $0.88\text{mm}^2$ . The energy measuring device was calibrated and gave a reading of 2.488J per pulse. The laser absorption by the glass substrate was measured and found to be negligible. The experiments were conducted using a single pulse and measuring the intensity of the transmitted beam through the sample, and the tests were repeated three times to obtain statistical confidence in the results. Simultaneous temperature measurements were conducted using the IR pyrometer.

### **5.2.7. Transmission results**

The transmission test results are shown in Table 18. The associated temperature changes

were also measured and recorded and a typical temperature profile is shown in Figure 62.

**Table 18, dry transmission results using a laser spot size of 0.88cm<sup>2</sup>.**

Sample	Orientation	Energy Delivered/ J	T <sub>max</sub> / °C	Transmission/ %	SD	Weight /mg	Area /cm <sup>2</sup>	Thickness /mm
ACNT	Random	2.488	277.9	8.832	0.003	64	1.5	1.5
AHCNT	Random	2.488	70.3	12.922	0.003	15	1.5	1.4
HBCNT	Random	2.488	617	0.884	0.000	42	2.7	0.6
SWNT	Random	2.488	353.3	6.773	0.001	50	2.3	0.8
CB	Random	2.488	592.7	0.653	0.001	70	2.3	0.5
HSCNT	↑	2.488	797.3	12.821	0.006	34	1.0	1.2
	↓	2.488	1048.5	9.700	0.021	34	1.0	1.2
	Side (Σ)	2.488	1048.5	4.949	0.001	34	1.3	2.8
SCNT	↑	2.488	303.6	47.136	0.091	18	1.0	1.8
	↓	2.488	393.1	39.218	0.008	18	1.0	1.8
	Side (Σ)	2.488	614.2	53.457	0.098	18	0.8	1.8

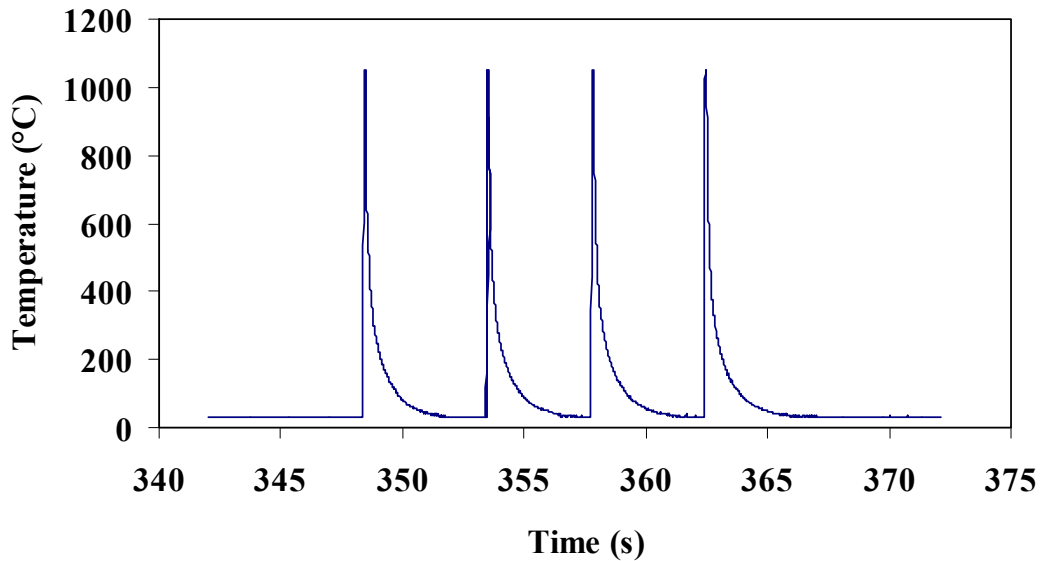


**Figure 62, temperature profile recorded during 4 consecutive 100ms long laser pulses delivered on the length of the parallel nanotubes in the carpet during laser transmission measurements on heat treated aligned multiwall carbon nanotube carpet (HCNT).**

To remove experimental artefacts based on variations in sample geometry and weight. The results of the transmission trials were normalised per unit weight and thickness and are listed in Table 19. The transmission results for the powder form, randomly oriented

samples are plotted per unit thickness and the associated temperature changes are plotted per unit weight in Figure 92 while the results for aligned samples are plotted in Figure 63.

**Table 19, normalised laser transmission results from dry samples per unit weight and per unit thickness.**

Sample	Weight under the 0.88cm <sup>2</sup> beam spot/mg	T <sub>max</sub> per unit weight /K mg <sup>-1</sup>	Weight per unit thickness/ mg.mm <sup>-1</sup>	Transmission per unit thickness/ %
AHCNT	8.80	7.99	6.29	9.23
SWNT	19.13	18.47	23.92	8.47
ACNT	37.55	7.40	25.03	5.89
HBCNT	13.69	45.07	22.82	1.47
CB	26.78	22.13	53.57	1.31
A Side (Σ)	19.80	31.02	11.00	29.70
A ↑	15.84	19.17	8.80	26.19
A ↓	15.84	24.82	8.80	21.79
H ↑	29.92	26.65	25.14	10.78
H ↓	29.92	35.04	25.14	8.15
H Side (Σ)	23.02	45.56	8.22	1.77

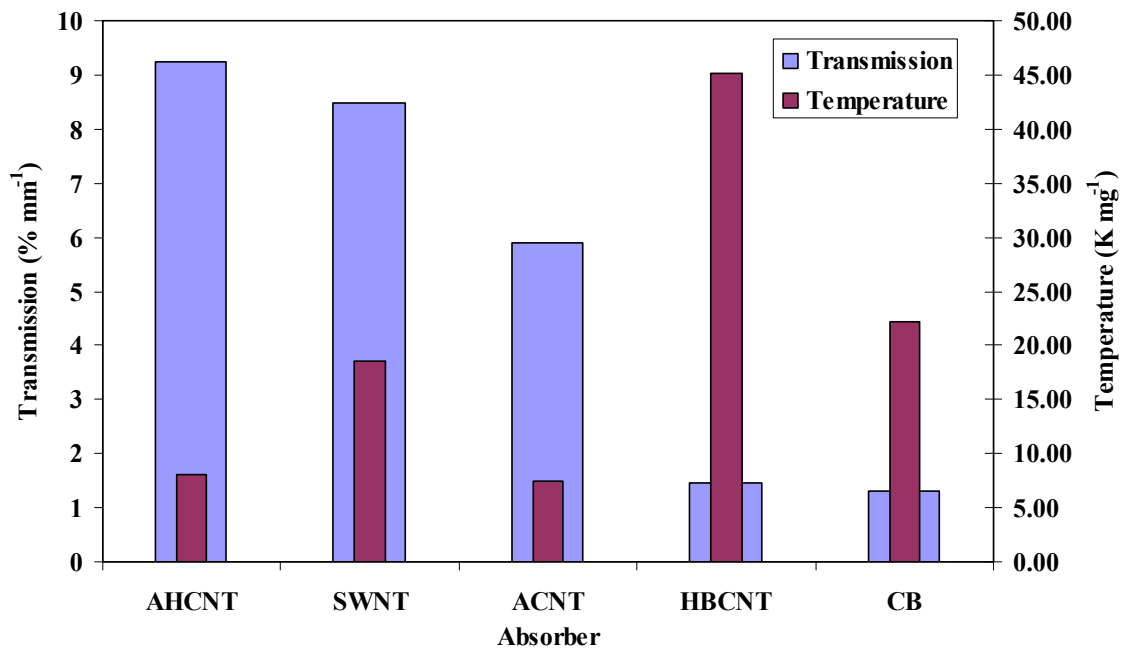


**Figure 63, maximum temperature change and transmission percent for randomly oriented samples per unit weight and for 1mm thickness respectively.**

It is clear that the thickness specific transmission results do not directly correlate to the temperature rise in the sample. This is because the amount of material per unit thickness varies for different samples. Plotting the amount of heat generated per unit weight highlights the effectiveness of each sample in absorbing the laser energy and converting it to heat. Therefore it can be seen that HBCNT and CB with similar transmission (although transmission through HBCNT is slightly higher) properties, heat significantly differently, with HBCNT generating a lot more heat per unit weight. Based on the same principle SWNT generates more heat than ACNT although it transmits a higher percentage of the incident light. ACNT and AHCNT seem to have similar temperature changes associated with them, although AHCNT has higher transmission percent than ACNT. Now considering the results of the heating trials it is possible that for shorter pulses the saturation and equilibrium between excited and relaxed atoms is not reached and the heating rates for ACNT and AHCNT are similar. However due to AHCNTs more graphitised and comparatively less defected structure, the time saturation is achieved much earlier and any increase in radiation does not increase the number of excited states, in return it scatters more light out of the beam than absorbing it.

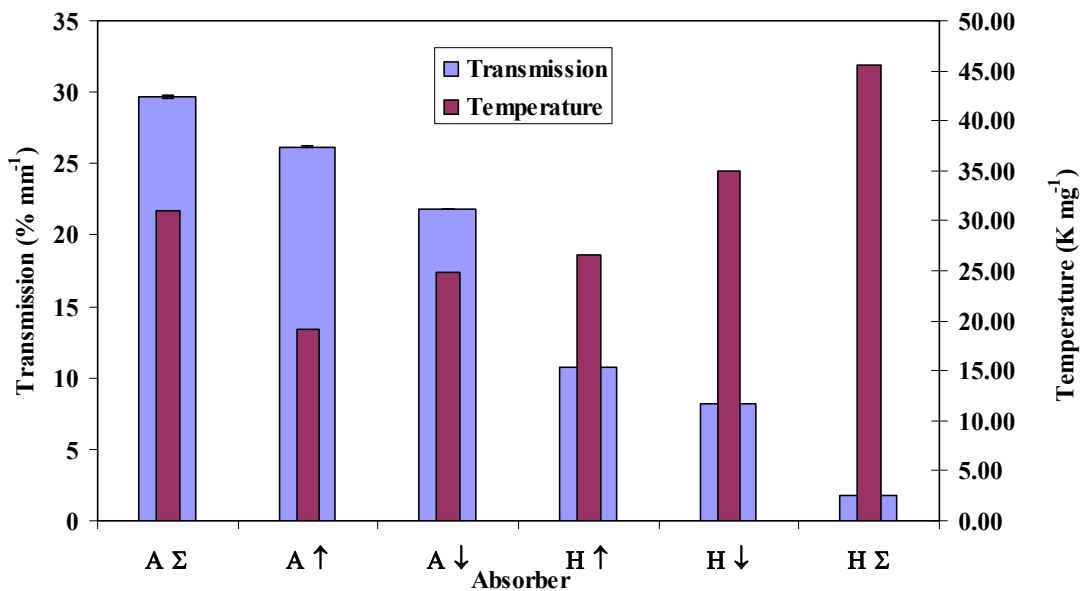


Figure 64, maximum temperature change and transmission percent through aligned samples, per unit weight and for 1mm thick respectively.

Figure 64 revealed a good correlation between the transmissions and associated heating results. Here the sample weight variation was much less due to the block shape of the carpets. Also the SCNT samples on the side produced the third highest amount of heat

per unit weight; while the transmission results showed the maximum amount of transmission from these samples. Again it can be seen that during the heating trials the SCNT samples created much more heat per unit weight compared with HCNT samples. The explanation is two fold one has to do with the faster and lower saturation limit for heat treated tubes resulting in plateaus at lower temperatures, the other is the possibility of removal of the tubes during the transmission trials and therefore increase in transmission with each pulse due to oxidation of the tubes. Indeed as it was shown earlier very high temperatures of about 1000°C was recorded after delivery of each pulse which would confirm the possibility of oxidising samples. This would affect the untreated samples first due to their lower oxidation temperatures as measured by TGA in section 3.3.6.

### **5.3. Correlation between absorption and temperature increase with Raman characteristics**

To further understand how the temperature change and absorption in different samples is related to the structure, the maximum temperature change per unit weight and the average transmission % per unit thickness for each sample are plotted against the  $I_D/I_G$  ratios. The  $I_D/I_G$  should show the influence of the impurities and imperfections as well as the effect of the graphitic or turbostratic structure on heating and absorption characteristics of the samples. Figure 65 shows the change in heating properties with the structural characteristics for the randomly oriented samples.

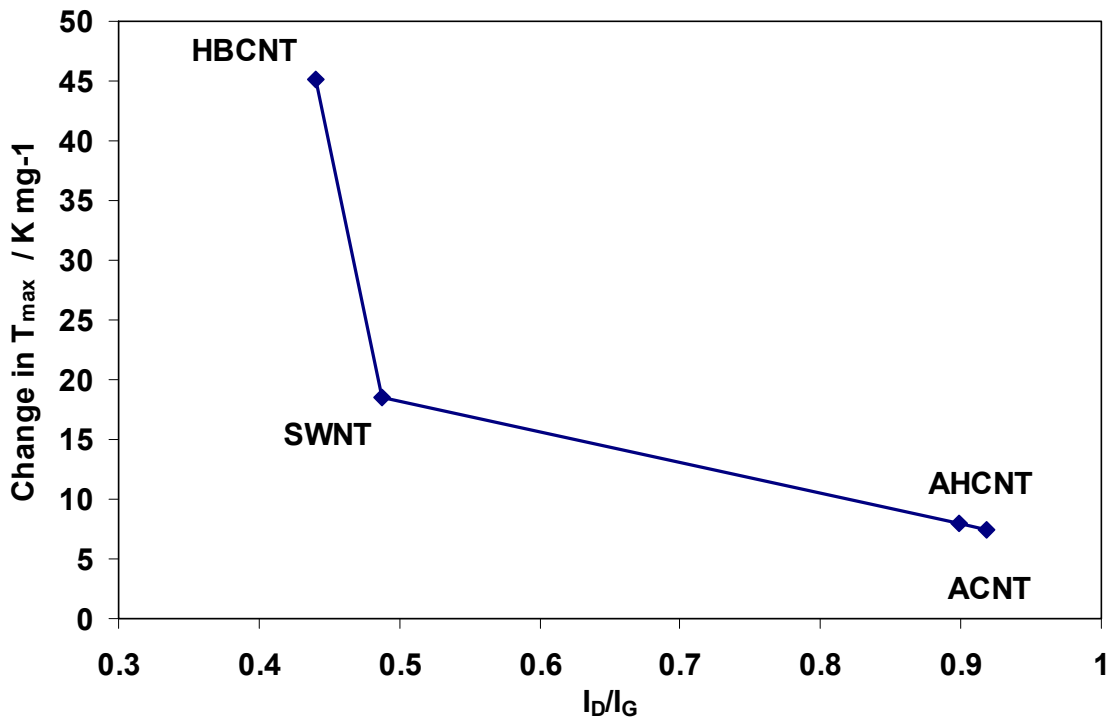


Figure 65, change in the generated heat with structural variations ( $I_D/I_G$  ratio vs average  $T_{max}$  per unit weight).

A direct correlation can be seen between the generated temperature per unit weight of the sample and the degree of disorder and graphitisation. All the number of data points are not sufficient to provide statistical confidence they qualitatively show a temperature decreases with increase in number of defects and impurities. The graphitisation effects seem to tend towards a plateau at about 0.6 where increase in the  $I_D/I_G$  ratio does not change the resultant temperature. The  $I_D/I_G$  ratio seems to change slope at around 0.5 Both ACNT and AHCNT have similar  $I_D/I_G$  ratios and they both have similar  $T_{max}$ . Figure 66 shows the absorption variation as a function of structure for the randomly oriented samples.

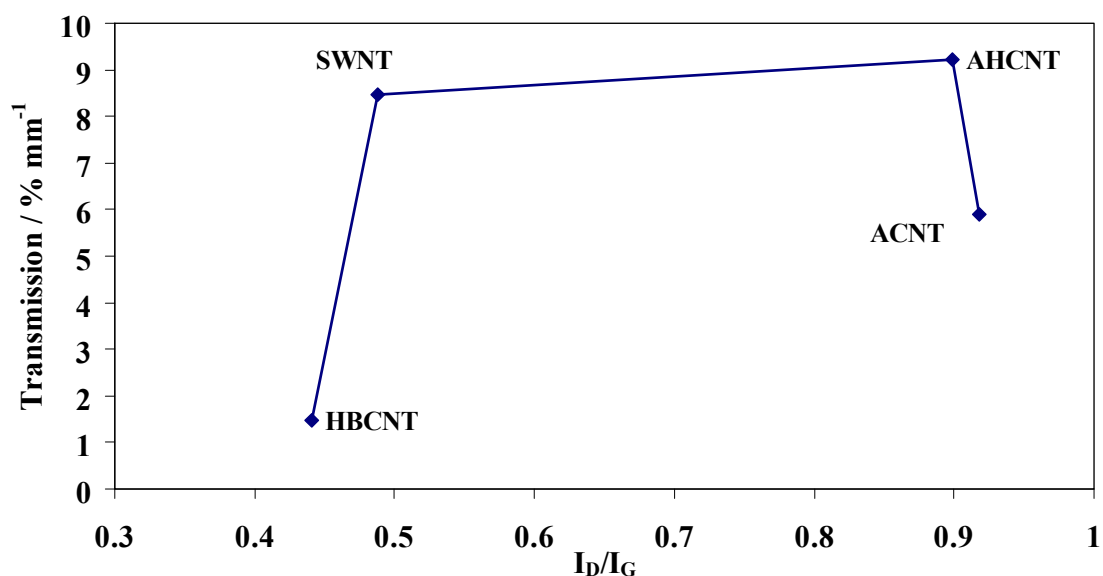


Figure 66, effects of structural variation on transmission percent % per unit thickness.

Apart from ACNT there seems to be a trend in the increase in transmission with structural defects and reduced degree of graphitisation. The reason for the results of the ACNT is unclear however it is thought to be due to the iron impurities present in the sample which would not have a significant effect on the heating of the sample but due to their small sizes act as scattering point for the incident light and reduce transmission on the light through the sample.

No clear correlation between the  $I_D/I_G$  ratio and heating or transmission was seen for the aligned-oriented samples. This is thought to be due to the dominance of the  $\pi$  plasmon effects from these samples parallel and perpendicular to the beam, which would mask effects from imperfections etc. The only observation is that for both HCNT and SCNT samples the bottom of the sample, which is more ordered has lower  $I_D/I_G$  value and seems to produce more heat and absorb more energy than the top of the samples. However the  $I_D/I_G$  showed a clear and linear relationship with heating as shown in Figure 67.

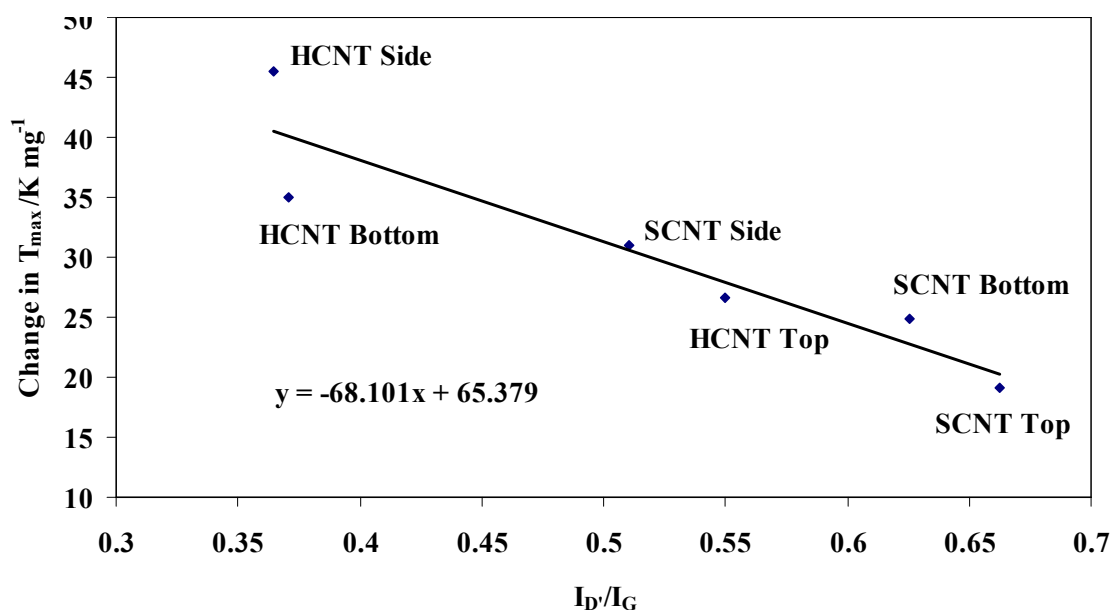


Figure 67, change in the generated heat with structural variations,  $T_{max}$  per unit weight for different  $I_D/I_G$  ratios).

In general heating decreases with increase in distortion and disorder. The presence of distortion and strains would change the electronic structure and therefore as it seems will influence the absorption and heating characteristics of the material.

#### 5.4. Summary

Efficient absorption of near IR by MWCNTs has optical limiting characteristics when in matrices such as water or ethanol, where significant light scattering is observed. This is been attributed to both absorption properties of MWCNTs as well as nonlinear scattering such micro-bubble formation and shows host liquid dependence. Furthermore light absorption by carbon nanotubes can be enhanced by extrinsic effects. Fe impurities or the vacancies left by removing metal particles during the purification process would act as trap centers for electrons or holes and at high temperatures photo-excited carriers become long-lived due to the repetition of the trapping and de-trapping processes. It was seen that ACNTs generate more heat compared with AHCNTs and CB. There seems to be an influence from concentration on the absorption properties and heating behaviour particularly in ethanol, where a clear percolation threshold effect can be seen. However they behave differently when dispersed in water and a percolation threshold effect cannot be seen which is thought to be due to removal of the absorbers form the suspensions via

the water gas reaction. The extinction coefficient measurements showed higher values for ACNT than CB than AHCNT and much higher values for suspensions in water than in ethanol. It seems as combined heat and acid treatment affect the absorption properties of the MWCNTs significantly. The effects seen in transmission and heating experiments on the sample so far are contributed to by; the absorption properties of the absorbers, their thermal conductivity, and dispersion in the matrix as well as the thermal properties of the matrix and its interaction with the absorbers. Furthermore only heating properties of absorbers that could be dispersed in water and ethanol with minimal agglomerations namely acid treated samples or CB could be examined, the structures of which are already adversely altered by the acid treatment process.

Carbon nanotubes are efficient absorbers of IR radiation and they convert the absorbed energy into heat very effectively. The heating is dependent mainly on the structure of the tubes and the degree of graphitisation. More graphitic heat treated tubes seem to heat up more than less graphitised tubes with more defects. There is however a dependence on the energy intensity and the exposure times. For longer exposure times structures with more defects seem to be more effective in generating heat. This is thought to be due to the more crystalline structure of the heat treated tubes having lower saturation thresholds and reaching equilibrium at lower temperatures. For shorter exposures and higher intensities it seems that the more crystalline samples heat up more because they are more effective in heating at lower exposure times. An exception to this are the ball milled nanotubes, which heat significantly better than other samples at all beam intensities and for all beam exposure times. This is thought to be due to their short length in the same order of the radiation wavelength resulting in resonance absorption by the tubes. Impurities do not seem to have much influence on the amount of heat generated but they seem to play a role on scattering of light when incident on the sample surface due to their small sizes. This can be seen in the transmission results where the transmission value increases with increase in structural imperfections unless impurities are present that will add to light extinction but not necessarily absorption. It should be noted that the values and comparisons are made based on transmission other than absorption. This is because deducting the amount of laser energy transmitted and reflected from what was incident on the sample does not correlate directly to absorption and heating. This is because parts of

the beam are extinct from the field without being absorbed to increase the temperature of the sample. These are mainly extinct either due to scattering or out of phase simultaneous emissions as discussed earlier. The transmission seems to increase with reduction in graphitisation. Highly graphitic and crystalline structures are ideal for light absorption and heating however due to their high crystallinity and reduced number of scattering sites as opposed to acid treated or as produced CNTs they seem to reach equilibrium quickly and produce less overall heat. In other words the heat treatment also increases their heat capacity. The absorption is also dependent on the sample orientation and light polarisation. When the laser beam is polarised parallel to the tube axis the coupling effect is exacerbated. For tubes that have not been heat treated some inter-tube tunnelling is allowed and heating parallel and perpendicular to the tube axis give similar results. For graphitised tubes the heating in the perpendicular direction is reduced as the plasma coupling of the tubes mainly happens along the axis. In addition the heating or absorption at 940nm laser wavelength seem to be independent of the samples diameter as the diameters are much smaller than the wavelength. The absorption is also independent of the length of the absorbers unless they are in the order of the radiation wavelength such as HBCNTs. Based on the results in this chapter and as will be explained in the following sections HBCNTs were used as the chosen MWCNT type for the laser welding of high density polyethylene (HDPE).

## **6. Through transmission laser welding of high density polyethylene using carbon nanotubes**

### **6.1. Laser welding of plastics**

The basic requirements for welding thermoplastic materials are heat, time and pressure to ensure there is sufficient inter-diffusion of polymer molecules at the weld interface. Several types of welding processes exist for polymers and the main difference between them is the source of energy used to heat and subsequently melt the polymers.

Laser welding of thermoplastics is suitable for joining films and moulded thermoplastics, and is based on using a laser beam to melt the materials to be welded at the joint interface. The laser provides a very good control of the amount of heat deposited in the material. Two general forms of laser welding are direct laser welding and through transmission laser welding (TTLW). The former process usually uses CO<sub>2</sub> laser radiation, which is readily absorbed by plastics and therefore has a limited depth of penetration and is hence limited to the welding of thin films. TTLW is used to carry out rapid welding of plastics by transmission of light through one of the surfaces to be welded, to an absorbing interface, where localised, precise heating takes place [153]. The welding process therefore relies on both absorption and transmission characteristics of the two parts and their interface, and is capable of welding thicker parts. The typical configuration of the process is shown in Figure 68.

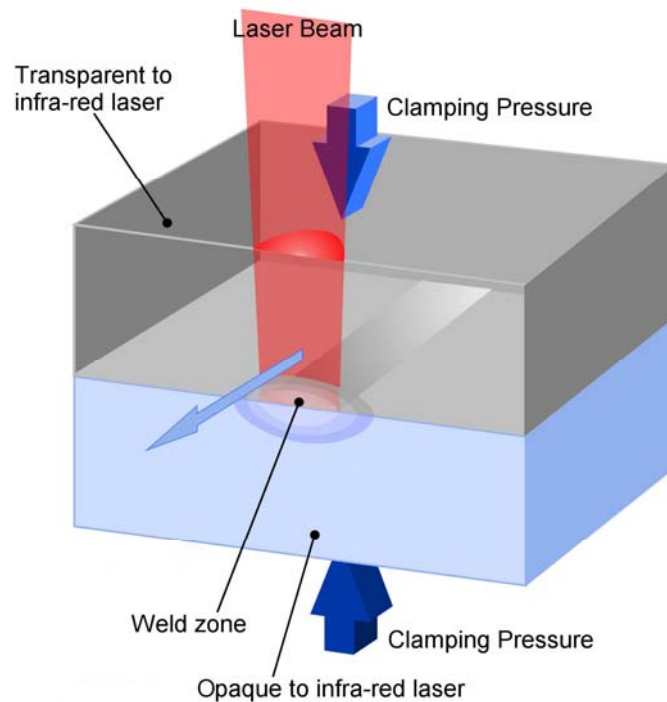


**Figure 68, schematic showing a typical configuration of through transmission laser welding of polymers [154].**

Most unreinforced, un-pigmented polymers allow light energy within a certain wavelength band to be transmitted through them. The light sources that emit in this wavelength band, include Nd:YAG lasers (1064 nm), diode lasers (808 nm or 940 nm) and some infrared lamps. The TTLW process provides means by which thermoplastic polymer parts with different absorption characteristics can be welded with no melt flash, no marking of the outer surfaces and only a small heat affected zone. Infrared lamps can also be used to make similar joints, but the broader wavelength band gives less selectivity in absorption between the two materials to be welded. To enhance the absorbing properties of polymers, the bottom part or the interface can be made opaque to the laser beam by adding an infrared absorber. Usually carbon black (CB) is used, however if the weld is to be between materials that are required to be clear or have a predetermined colour, then the Clearweld® (CW) process is used [155]. CW is a greenish colour dye, which absorbs light at 940nm and generates heat. The generated heat causes discolouration in the dye and it becomes clear and transparent, which is advantageous when welding clear plastics [154]. The laser beam interacts with the absorber at the interface between the two parts, or in the bulk of the lower part and generates heat. The

heat is transferred to the surrounding materials by conduction, causing the substrates to melt and an applied pressure (usually through using a welding clamp), forces diffusion and entanglement of the polymer chains and welds the parts. Due to their strong photo-absorption characteristics and good mechanical properties, MWCNTs are good candidate absorber for TTLW. Their high efficiency in absorption of light means that they will be able to produce larger amounts of heat at the interface compared to similar concentrations of CB or CW and therefore should produce welds at lower energy inputs. Alternatively this will also allow more melting of the material at the interface, and potentially a stronger joint than the other two absorbers for a given laser power. The presence of CNTs, with their fibre-like structure, could further enhance the integrity of the welds as nano-reinforcements across the welded joint. Moreover, their high absorption and efficient photo-thermal conversion characteristics could allow welding of polymers at lower absorber concentration and therefore reduced contamination of the welded joints. This could also allow welding through thicker parts than with CB or CW absorbers, where the intensity of the incident laser beam reaching the interface between the polymers to be welded is significantly reduced. Indeed for semi-crystalline polymers such as high density polyethylene (HDPE), the depth over which the laser radiation is transmitted is restricted by the crystalline structures present in the polymer, limiting the thickness of the material that can be laser welded to around 3 – 6 mm.

## **6.2. Factors affecting laser light absorption and scattering by polymers**

There are many factors that affect the process of transmission laser welding of plastics. These parameters are either related to the properties of the material, such as; polymer type, thickness, crystallinity and temperature, or the properties of the laser radiation and the welding process, such as; wavelength of light, power intensity, or the welding speed [156]. Some of such influencing factors are further described below.

### **6.2.1. Relationship between polymer type/crystallinity and laser wavelength**

The effect of polymer type is prominent. A clear differentiation can be made between the absorption of light at NIR wavelengths by amorphous polymers, such as polymethylmethacrylate (PMMA), and semi-crystalline polymers such as HDPE. The transmission coefficient is reduced by a factor of 10-20 when the polymer bulk contains

crystallites due to scattering of light from these sites [156]. The variation in absorption coefficient between different semi-crystalline materials is also quite marked and is due to two main mechanisms. Firstly, molecular absorption from bond bending and stretching will vary as the molecular constituent changes (hence the use of methods such as FTIR for characterisation of polymers). Secondly, light scattering will vary with the presence of scattering sites in the polymer. These may be filler particulates, crystallites or other heterogeneities within the material. A link might be expected between crystallite size and light scattering, in that maximum scattering occurs when the scattering site is of similar size to the wavelength of the light. It is expected that the molecular resonances are minimal for most thermoplastic polymers at 940nm wavelength as the absorption by polymers tends to increase at longer infrared wavelengths such as those used in FTIR analysers. Scattering from crystallites and other heterogeneities may, therefore, explain the main differences in absorption. This hypothesis was tested by Jones et al [156], by comparing the crystallite sizes to the absorption coefficient of the material for a 1064nm laser wavelength. In these tests, there did appear to be a trend for increasing absorption in materials that had a crystallite size of 2-5 $\mu$ m diameter, and/or contained small particles 2-3 $\mu$ m diameter such as particulate reinforced PP. Thermoplastic polymers with larger scattering sites, such as crystallites of unreinforced polypropylene (PP), HDPE and nylon, and smaller sites such as in PMMA showed lower absorption coefficients [156].

### **6.2.2. Temperature**

In some thermoplastics, at particular wavelengths, the effect of temperature on light absorption is marked. In PMMA some absorption bands disappear as the temperature increases. In PP absorption shows a rapid drop as the melting point is approached [157], due to the melting of crystallites, leading to an essentially amorphous polymer liquid above the melting point.

### **6.2.3. Laser intensity and transmission**

The thermal degradation of polymers is a time and temperature dependent process. Hence degradation can be initiated in polymers either by using a short, high intensity pulse, or by using a series of low intensity pulses over a longer time. There are differences in the behaviour of different thermoplastic polymers; for example, the surface of

polyvinylidene fluoride (PVDF) degrades more readily than either PMMA or HDPE. The degradation process produces carbon, which rapidly increases the laser absorption, leading to more rapid degradation – a runaway situation. This effect can lead to a very distinct transition from transmission to absorption as the laser power intensity is increased. It is clear that knowledge of this transition should be sought while considering laser welding for any particular material. Processing conditions can then be specified that safely avoid degradation regimes. Light transmission, as described by equation 54 ( $\ln T = \ln(1 - R) - \alpha z$ ) is valid only if the power intensity of the light is not too high; if the heat from a high power intensity pulse cannot be dissipated rapidly enough, the material will overheat and degrade.

### 6.3. Calculating welding parameters

It is very important to understand the appropriate parameters for making laser welds. These parameters are mostly interrelated and could provide a complex matrix of tests and variables. Here we first look at a few specific parameters and then explore a method of controlling the number of variables and optimising the number of tests and welds required.

#### 6.3.1. Absorber requirements

Starting from the principles of laser energy absorption in polymers, an estimate of the additives required to enhance the absorption of the laser in the polymer is made below. First the laser absorption properties of HDPE with three different thicknesses were estimated by measuring the through-thickness transmission of a 100ms laser pulse with five different pulse energies, using the Ophier energy meter device as described in earlier; the results are given in Table 20.

**Table 20, results of transmission measurements through virgin HDPE samples with different thicknesses.**

Material	Thickness/mm	Measured energy transmission/J					Fraction transmitted
None	0.00	5.00	4.00	3.00	2.00	1.00	1.00
HDPE	1.42	3.20	2.58	1.93	1.31	0.65	0.65
HDPE	2.90	2.10	1.69	1.28	0.86	0.43	0.43
HDPE	4.71	1.34	1.07	0.83	0.55	0.27	0.27

A linear regression of the transmission results was carried out to give an average fraction of light transmitted (T) through different sample thicknesses and the results are plotted in Figure 69.

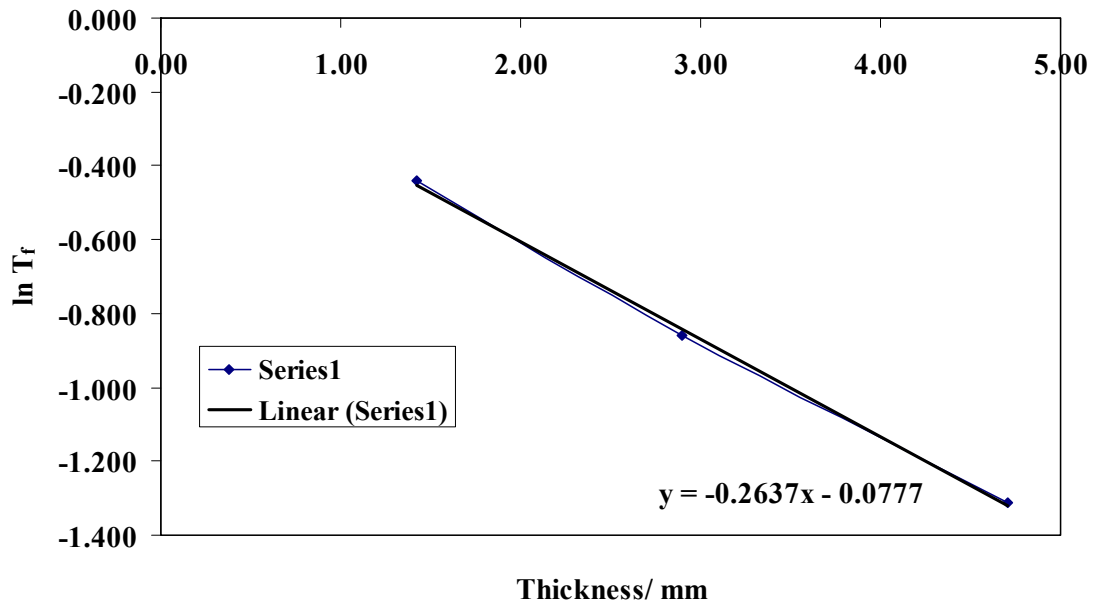
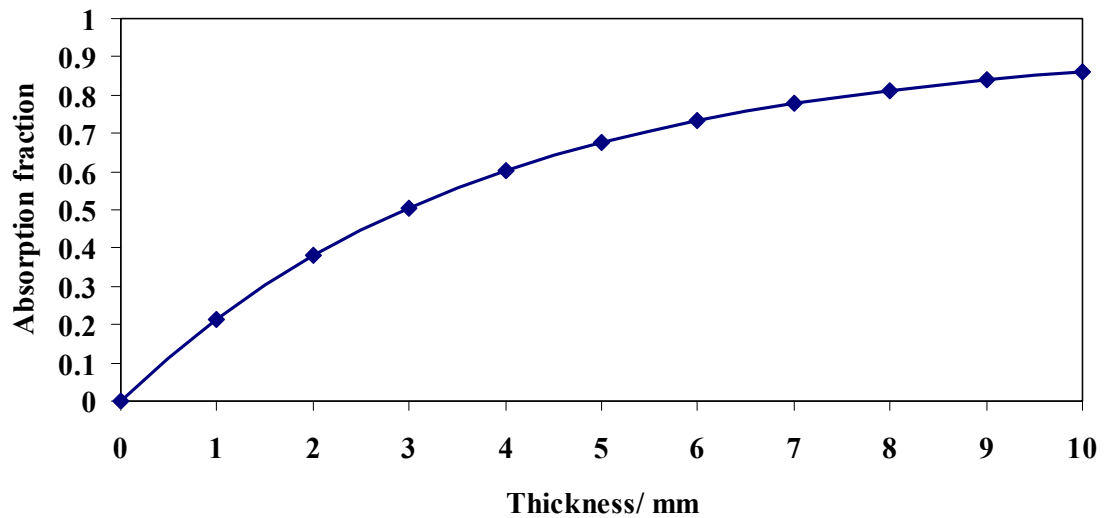


Figure 69, logarithmic regression analysis for HDPE using  $\ln T_f = \ln (1-R_f) - \alpha z$ .

Using the plot in Figure 69 the regression calculation of absorption coefficient were carried out and values of R and  $\alpha$  were found to be 0.075 and  $0.264\text{mm}^{-1}$  respectively these values were find to be close to those quoted by Jones and Rosatmi, 0.05 and  $0.3\text{mm}^{-1}$  [158] respectively. The fraction of energy absorbed by HDPE material can be found using Equation  $\{A_f = 1 - R_f - ((1 - R_f)e^{-\alpha z}) = (1 - R_f) \times (1 - e^{-\alpha z})\}$  and gives the curve in Figure 70 when plotted against thickness using no additional absorbers at room temperature.



**Figure 70, the proportion of the laser energy at 940nm wavelength, absorbed by the HDPE samples of different thicknesses at room temperature, without additional absorbers.**

However it is known that the laser absorption drops significantly at the melting point of semi-crystalline thermoplastics such as PP. It is therefore possible to model how the HDPE sample would behave at or near its melting point based on the behaviour of an amorphous polymer with no crystallites such as clear PMMA. Jones and Olden [156] reported a room temperature value of  $0.01 \text{ mm}^{-1}$  for the absorption coefficient of PMMA and 0.04 for its reflectivity. Now the graph in Figure 70 can be re-plotted to also show the estimated absorption properties of HDPE at its melting point, as shown in Figure 71.

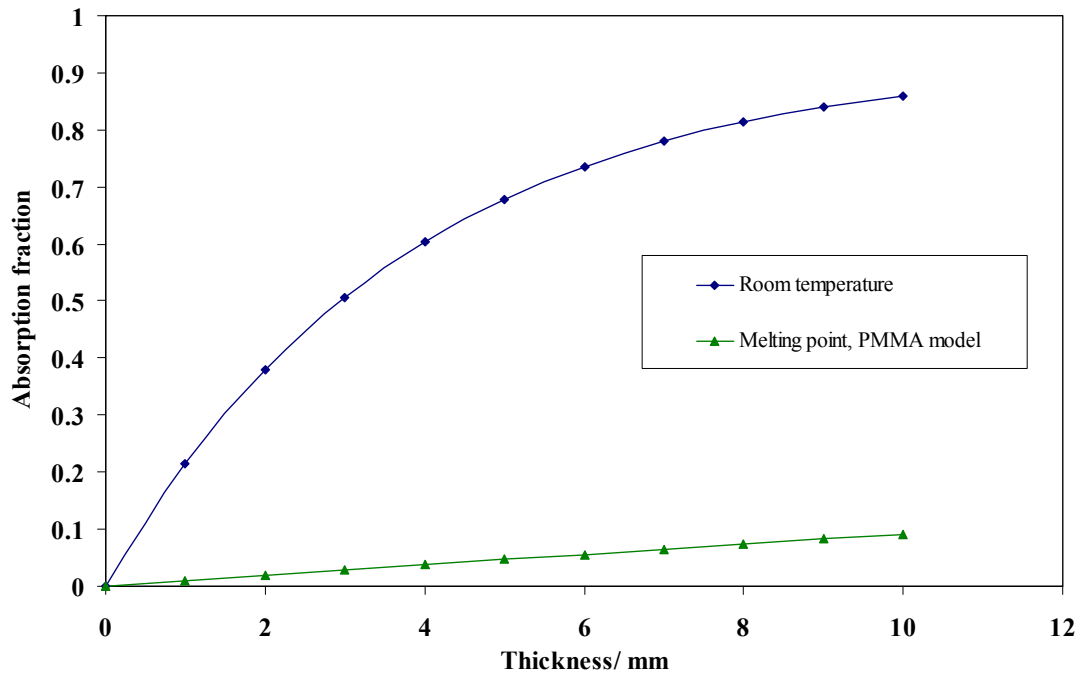


**Figure 71, laser absorption profiles for different thicknesses of HDPE showing the simulated effect of changes that occur upon melting.**

The large decrease in absorption properties at or near the melting point means that additional absorbers are required for laser welding of HDPE. In addition this will focus the heat generation at the weld interface as opposed to bulk heating of the substrates to be welded.

Therefore we now consider the effects of adding MWCNTs as absorbers to the HDPE. The extinction coefficient of our samples were previously estimated to be  $4.2 \times 10^6 \text{ mm}^2\text{g}^{-1}$  (see Table 12), which is very close to the quoted literature value of  $3.2 \times 10^6 \text{ mm}^2\text{g}^{-1}$  [159]. Now using Equation 57, which shows the relationship between absorption coefficient ( $\alpha$ ), extinction coefficient ( $\beta$ ) and concentration ( $C$ ) together with the density of HDPE we can calculate the amount of absorber needed to be incorporated in virgin HDPE (wt%) to achieve a given absorption depth as listed in Table 21.

$$\alpha = 2.3\beta C \quad (56)$$

**Table 21, the estimated amount of multiwall carbon nanotubes needed in wt% in HDPE to give suitable absorption depth.**

$\alpha/ \text{mm}^{-1}$	$C/ \text{g mm}^{-3}$	Wt% in HDPE
0.1	1.0E-08	0.0011
0.2	2.1E-08	0.0022
0.3	3.1E-08	0.0034
0.4	4.1E-08	0.0045
0.5	5.2E-08	0.0056

Assuming an absorption depth of at least 10% of the thickness (3mm thick samples to be welded in this study), the absorption coefficients at room temperature and melting temperature are,  $0.564$  and  $0.31\text{mm}^{-1}$ , respectively. Therefore, absorption fractions expected from room temperature and melted HDPE with carbon nanotubes added at a concentration of  $0.0033\text{wt}\%$  are calculated and plotted against different thickness values in Figure 72.

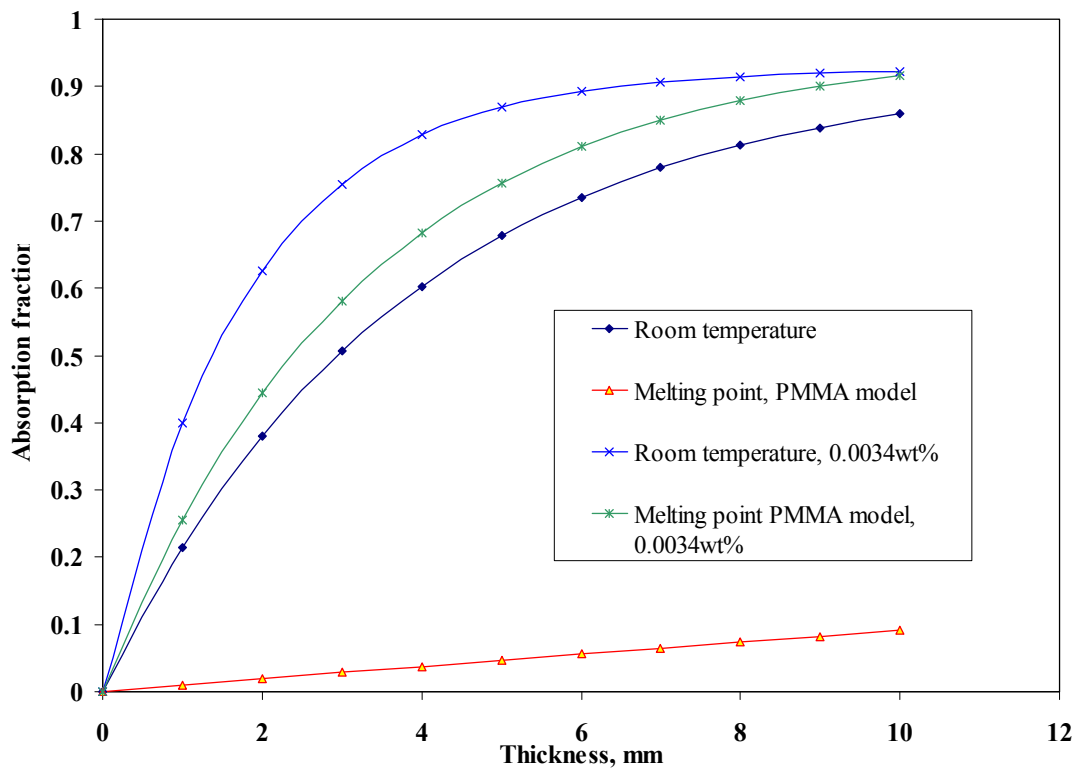


**Figure 72, estimated effect of melting and multiwall carbon nanotube absorber additive on the absorption in HDPE.**

From Figure 72 it can be deduced that the absorption properties of a 3mm thick HDPE sample will be greatly enhanced by the addition of absorbers even at concentrations as low as 0.0034wt%. Following the same principles and calculations and using extinction coefficient values of  $3.6 \times 10^6 \text{ mm}^2\text{g}^{-1}$  for CB (Table 12) and  $5.8 \times 10^6 \text{ mm}^2 \text{ g}^{-1}$  for CW (discussions with the manufacturer) the required wt% concentrations of these absorbers for heating of HDPE to its melting point were estimated to be 0.0039 and 0.0024, respectively. Although the calculated values for the absorbers were very low, practical experience, particularly with processing and dispersion of the CNTs in the virgin polymer, showed that higher concentrations are needed to ensure an even distribution of the required amount of absorber in the HDPE material and therefore more consistent results. The main welding trials in this study were therefore conducted using 0.1wt% absorber addition for all absorbers.

### 6.3.2. Weld temperature and melt depth calculations

It is difficult to routinely measure the temperature at the interface during the welding process. In contrast, the weld depth can be measured after the welding process; by microscopic examination of sectioned specimens as the maximum depth of the heat affected zone (HAZ) from the interface [158]. The weld depth is important to ensure the presence of sufficient amounts of molten polymer to create a weld. It is also useful to have a profile of temperature from the weld centreline through to the deepest part of the HAZ to ensure that very high temperatures and polymer degradation is avoided. Prediction of weld temperature is possible by using a model provided by Shercliff and Ashby [160], where a series of dimensionless variables for temperature, laser power, speed and depth are defined. These are presented below as Equations 57 to 66 as reported by Rostami and Jones [158]:

$$T^* = \frac{(T - T_0)}{(T_m - T_0)} \quad , \quad (57)$$

Where T and T\* are temperature in Kelvin (K) and dimensionless temperature, respectively; T<sub>m</sub> is the melting temperature of the substrate (in K) and T<sub>0</sub> is Room temperature (in K)

$$q^* = \frac{Aq}{r_B \gamma (T_m - T_0)} \quad (58)$$

Where  $q$ ,  $q^*$  are laser beam power (W) and dimensionless beam power.  $A$  is the absorption fraction,  $r_B$  is beam radius (m) and  $\gamma$  is the thermal conductivity of the material to be welded ( $\text{Wm}^{-1}\text{K}^{-1}$ ).

$$v^* = \frac{vr_B}{X} \quad (59)$$

Where  $v$ ,  $v^*$  are the scanning speed of the laser beam ( $\text{ms}^{-1}$ ) and dimensionless beam speed, respectively, and  $X$  is the thermal diffusivity of the material to be welded ( $\text{m}^2\text{s}^{-1}$ ).

$$t^* = \frac{t}{t_0} \quad (60)$$

Where  $t$ ,  $t^*$  are time (s) and dimensionless time, and  $t_0$  is time at the start of beam heating.

$$z^* = \frac{z}{r_B} \quad (61)$$

Where  $z$ ,  $z^*$  are depth coordinate (mm) and the dimensionless depth coordinate.

$$z_0^* = \frac{z_0}{r_B} \quad (62)$$

Where  $z_0$ ,  $z_0^*$  are surface coordinate (mm) and the dimensionless surface coordinate.

The temperature field at the centre of the beam is given by:

$$T^* = \frac{(2/\pi)(q/v^*)}{[t^*(t^*+1)]^{1/2}} \times \exp\left\{-\frac{(z^*+z_0^*)^2}{t^*}\right\} \quad (63)$$

The maximum temperature and weld depth occurs at the beam centre. The dimensionless time to peak temperature is determined using Equation 64 with respect to time.

$$t_p^* = \frac{1}{4} \{2\{z^* + z_0^*\}^2 - 1 + [4\{z^* + z_0^*\}^2 + 12\{z^* + z_0^*\}^2 + 1]^{1/2}\} \quad (64)$$

The dimensionless peak temperature is obtained by substituting  $t_p^*$  from Equation (64) into Equation (63).

In these equations,  $z_0^*$  is used as an adjustable parameter for calibrating Equation (63) to a known surface peak temperature. When a beam of uniform intensity is applied to the surface, at  $z^* = 0$ , for a time equal to the interaction time, it produces a surface peak temperature of [158]:

$$T_p - T_0 = \left( \frac{2Aq}{\pi^{3/2} r_B^2 \gamma} \right) \left( \frac{2ar_B}{v} \right)^{1/2} \quad (65)$$

Or in dimensionless form:

$$\left( T_p^* \right)_{z^* \rightarrow 0} = \left( \frac{2}{\pi} \right)^{3/2} \left( \frac{q'}{v'} \right)^{1/2} \quad (66)$$

The adjustable variable of  $z_0^*$  in Equation (63) is introduced to minimise the difference between  $T_p^*$  that is calculated from Equations (63) and (66). The value of  $z_0^*$  thus obtained is substituted in Equations (64) and (63) respectively to calculate  $t_p^*$  and  $T_p^*$ . Their corresponding surface peak temperature,  $T_p$ , is calculated from Equation (57). By a minute change in the value of  $z^*$  a surface temperature is then calculated in such a way that the difference between  $T_p$  and the surface temperature is minimised. This temperature and its corresponding  $z$  value ( $z = r_B z^*$ ) are calculated using an absorption fraction of 0.564 and thermal properties of HDPE (thermal diffusivity of  $2.5 \times 10^{-7} \text{ m}^2 \text{ s}^{-1}$  and thermal conductivity of  $0.52 \text{ W m}^{-1} \text{ K}^{-1}$ ) [161], stepwise as the value of  $z^*$  is increased until the temperature is higher than the HDPE melt temperature i.e.  $142^\circ\text{C}$  [161]. An example of  $z$  value and corresponding temperature for HDPE samples is plotted in Figure 73. This shows a peak temperature of  $1200^\circ\text{C}$  at the weld centreline reducing to  $\sim 140^\circ\text{C}$  at  $0.7 \text{ mm}$  into the weld. In addition the exposure times to the beam for a given point in the weld were also calculated per unit area ( $\text{mm}^2$ ) by dividing the beam diameter by the welding speed.

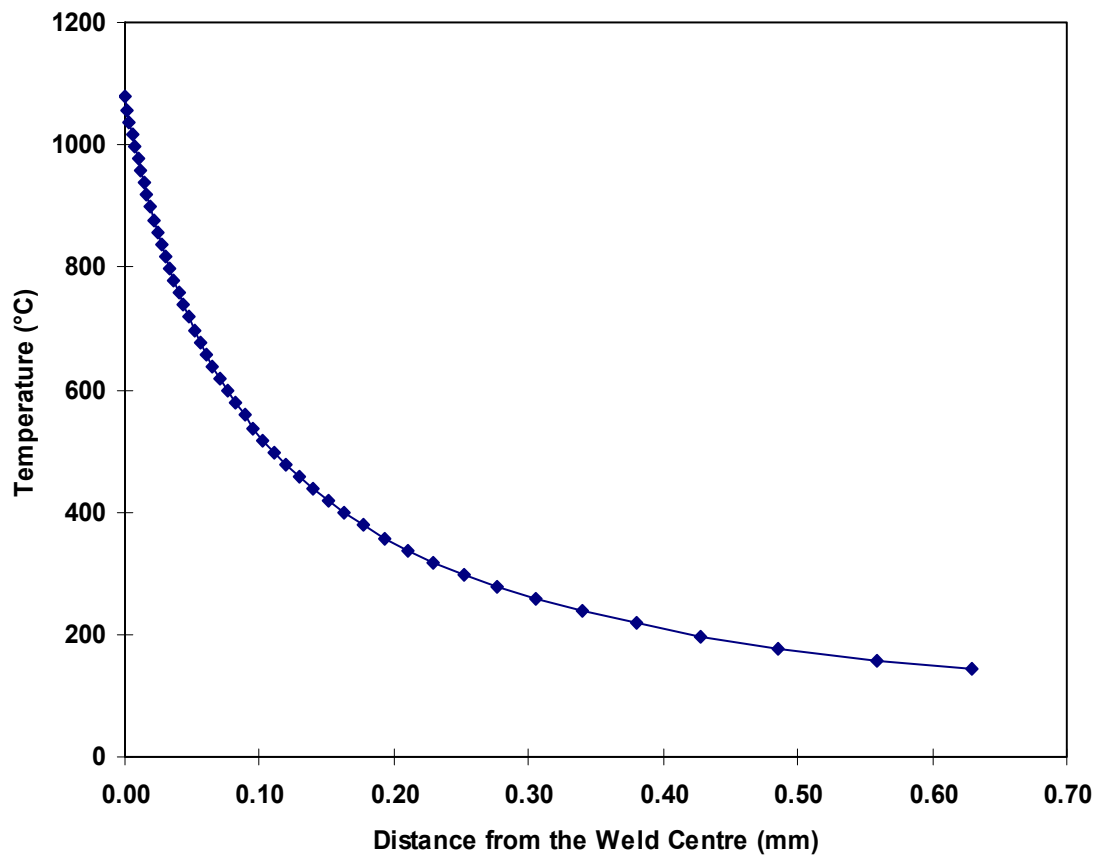


Figure 73, calculated temperature variation as a function of weld depth for laser power of 100W, welding speed of 1000mm.min<sup>-1</sup>, absorption fraction (a) of 0.564 and beam diameter of (r<sub>B</sub>) 2mm.

The resultant melt depth and weld centreline temperatures corresponding to various laser power, welding speed and absorbance are given in Table 22.

Table 22, calculated values of weld depth and temperature for different welding speeds and laser powers.

Laser Power/W	Welding Speed /m.min <sup>-1</sup>	Absorption fraction	Laser beam radius/mm	Exposure time/ms	Temperature at weld centreline/°C	Weld depth/mm
100	1	0.564	2	240	1213	0.71
100	0.5	0.564	2	480	1707	1.23
50	1	0.564	2	240	617	0.34
50	0.5	0.564	2	480	864	0.67

High interface temperatures are the result of low thermal conductivity of the polymer and a short dwell time leading to a steep thermal gradient. Degradation of polymers at such high temperatures is a concern; however, as the dwell times at such temperatures are quite short, this is usually avoided. This has been reported for the Clearweld process on PETG material [162]. The strength of the joints in PETG exceeded that of the parent material and the welds remained optically transparent, indicating that there was no evidence of degradation due to short dwell times.

#### **6.4. Sample preparation**

Use of dry absorbers applied as powders at the weld interface resulted in strong welds even through 9mm thick virgin HDPE samples. However, it was difficult to get a consistent and even amount of absorber introduced to the interface. In addition this method involved handling and manipulating powder nanomaterials and had associated health and safety issues. It was therefore concluded that the most controllable way of making weld preparations was through the use of the specimens, which had the nanomaterials incorporated in them during the manufacturing process, this also mitigated any health and safety issues that may arise when handling the CNTs.

Samples were prepared in two batches using HDPE pellets and HBCNT, CB and CW additives. The first batch of samples were mixed in a twin-screw continuous recycling flow micro-compounder (DSM Micro 15), which enabled mixing of materials at a selected temperature for a selected time. The samples were used for initial heating and transmission trials. An image of the micro-compounder is shown in Figure 74 and the process and sample details are listed in Table 23.



Figure 74, DSM Micro 15, micro-compounder.

Table 23, first batch of material mixes using DSM Micro 15 mixer.

Base Material	Quantity/g	Additive	Wt%	Temperature /°C			Time/min	Screw/rpm	Comments
				Top	Mid	Bottom			
HDPE	12	None	0	180	180	180	3-4	50	Processed well
HDPE	10	HBCNT	0.003	180	180	180	4	50	Grey
HDPE	10	CB	0.003	180	180	180	4	50	Grey
HDPE	10	CW	0.003	180	180	180	4	50	Pale green

The second batch of samples were mixed in a twin-barrel mixing chamber (HAAKE Rheocord R600) to allow larger batches to be made (50g), and when the first mixer became unserviceable. The mixing was carried out under a controlled start temperature, for a selected rotation speed and time. The torque of mixer rotation and temperature of the mix were monitored. An image of the mixer is shown in Figure 75 and the process and sample details are listed in Table 24.

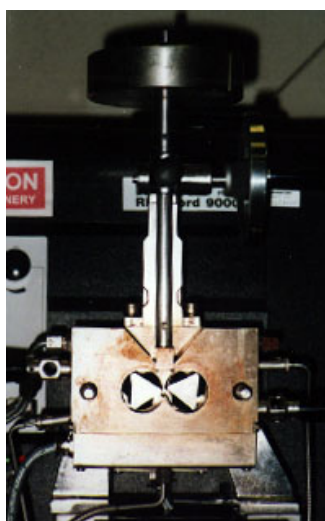


Figure 75, HAAKE Rheocord R600 twin-barrel mixer with continuous measurement of machine rotation speed, temperature and mixing torque.

**Table 24, second batch of material mixes using HAAKE Rheocord R600 mixer.**

Base Material	Quantity/ g	Additive	Wt%	Temperature/ °C		Time/ min	Screw/ rpm	Comments
				Start	Finish			
HDPE	52.00	none	0.00	170	180	5	50	Processed well
HDPE	50.00	HBCNT	0.10	170	180	5	30-50	Black
HDPE	50.16	CW	0.10	170	180	5	30-50	Pale green
HDPE	50.00	CB	0.10	170	180	5	30-50	Black

Samples were prepared by adding an appropriate amount of additive to 10-12g (50g in the second batch) of HDPE pellets. This was added to the pre-heated compounder and mixed for 3-5 minutes typically (up to 10 minutes for some of the carbon nanotubes samples). A short process time was selected to limit any thermally driven changes in the absorber additives and reduce the mechanical damage made to the tubes. Generally well dispersed mixes were achieved with both machines. This could be judged from thin films made from the samples during pressing.

In general CW seemed to be more evenly dispersed in the sample (as it is added in a liquid form) as opposed to CB and HBCNT. CB samples seemed to be more evenly dispersed compared with HBCNT samples, perhaps due to the more severe agglomeration of the fibre- like HBCNTs.

#### **6.4.1. Heating and transmission specimen preparation**

The mixed material from the first batch was initially pressed into a rough pad and then thermally pressed into a 3mm-thick mould. The mould was pre-heated to 180°C for 5 minutes. The polymer was inserted and soaked for 1 to 2 minutes, pressed for 1 minute and transferred to another, water-cooled, press where it was cooled under pressure for two minutes. Natural HDPE sheets, with no addition of absorbers were manufactured in a similar way as control samples. Waisted flat specimens were moulded in this way as shown in Figure 76 for the initial heating and transmission trials. Only the samples with low additive concentration (0.003wt%) were used in the laser heating trials, aiming to provide through-thickness heating.

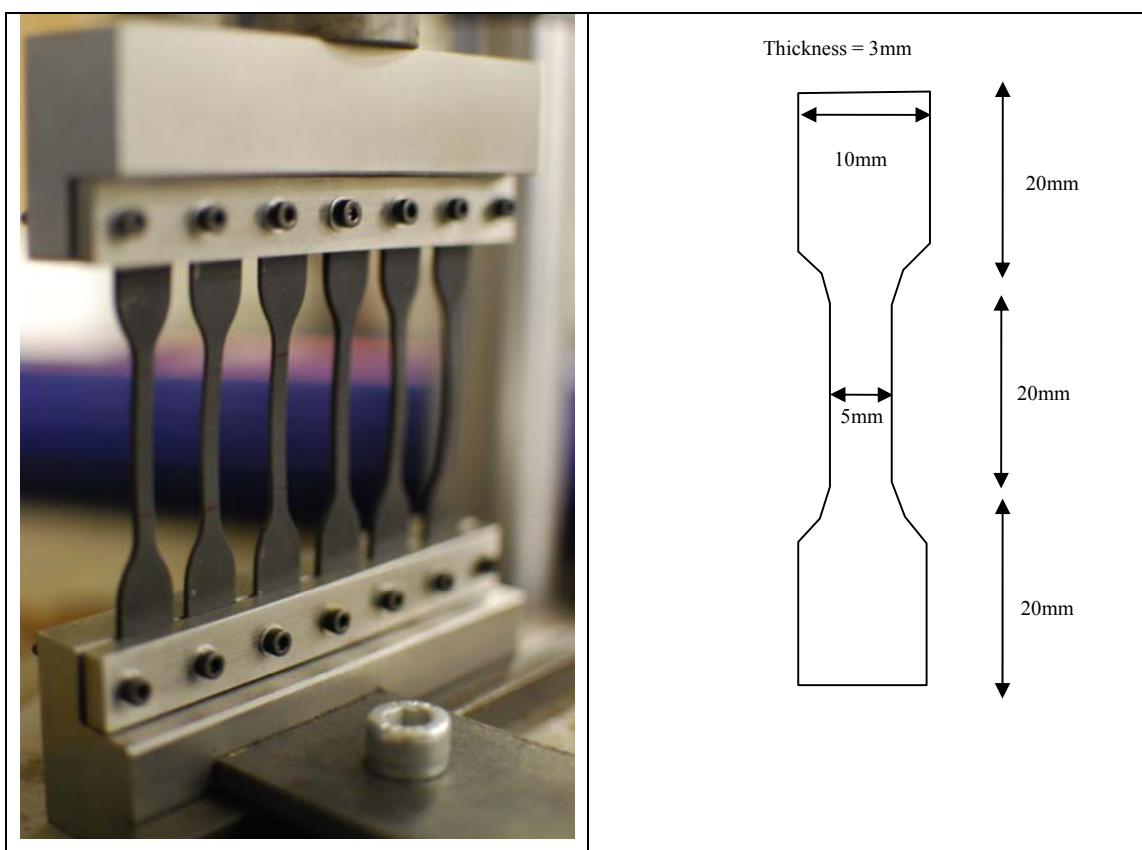


Figure 76, schematic of the flat waisted specimens on the right as well as a picture of them in a sample holder on the left.

#### 6.4.2. Weld sample preparation

The material from the second batch was also pressed into suitable specimens. This time pressing was at around 170°C - 180°C for two minutes to make flat square plaque samples of 100 × 100 mm dimensions with a thickness of 3mm. These samples containing the absorbers were then welded to samples containing no absorber additives with an overlap length of 25mm. Figure 77 shows schematic of the weld specimens and their dimensions.

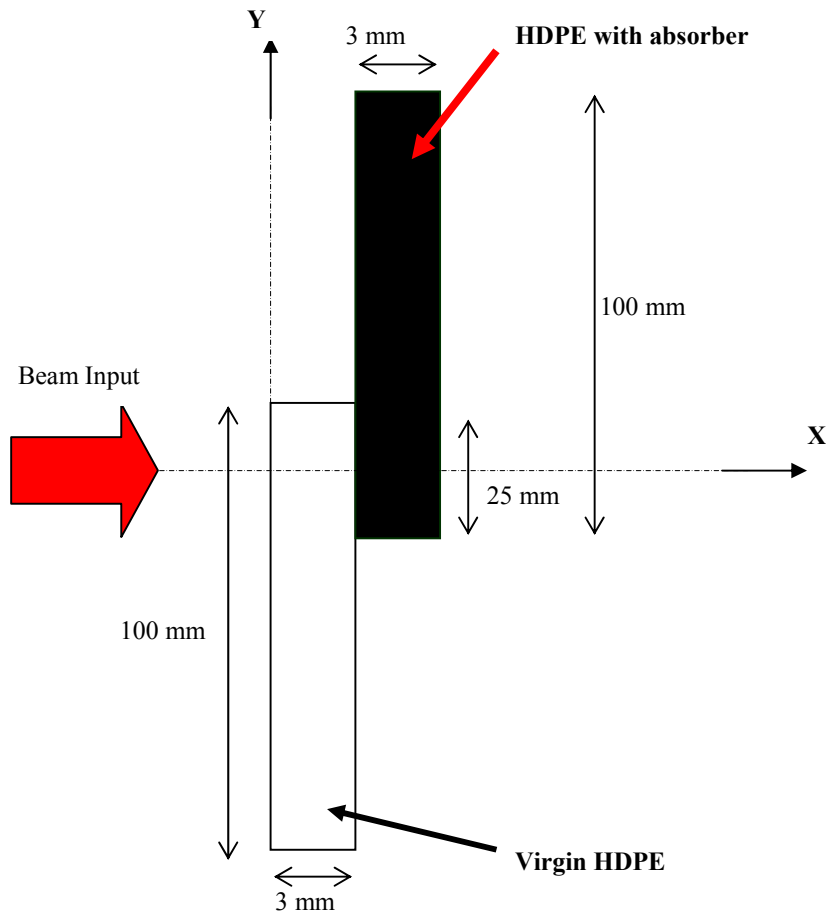
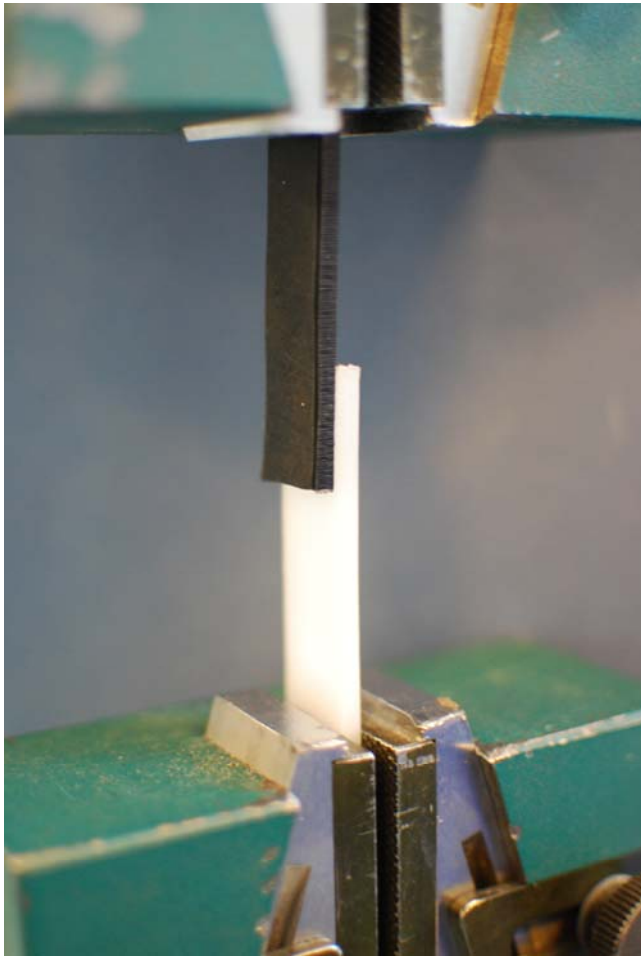


Figure 77, schematic drawing with geometry and dimensions of the samples to be welded for preparing lap shear tensile test specimens.

#### 6.4.2.1. Lap shear testing of the welded specimens

Three lap shear specimens, 25mm wide were cut from each set of welded plaques avoiding the weld ends. These were mounted in grips, with spacers of the same material thickness to promote pure shear at the start of the test, at a gauge length of 120mm. The samples were tested following standard EN 12814-2:1998 at a cross-head speed of  $5\text{mm}\cdot\text{min}^{-1}$ . The location of failure was noted in addition to the peak tensile load. Figure 78 shows a picture of a welded test specimen in a tensile testing machine.



**Figure 78, a typical welded specimen in a tensile testing machine.**

### **6.5. Transmission measurements through HDPE specimens**

The measurements were conducted, using a 50ms pulse at a power of 15W (0.75J). These short pulse measurements were made at a temperature below the HDPE melting point, when the material still contained crystallites and scattered the laser beam. The absorption coefficient gives an indication of the effect of the additive. As discussed in Section 6.3.1 an absorption coefficient in the range  $0.3\text{-}0.5\text{mm}^{-1}$  should provide laser heating to a depth of a few millimetres. The energy measured after transmission through different thicknesses of the samples is shown in Table 25. The absorption coefficient was derived from the transmission measurements using Beer's law as previously shown.

**Table 25, laser transmission measurements and calculated absorption coefficients for virgin HDPE as well as HDPE with different additives.**

Sample no	Description, wt%	Thickness/ mm			Absorption coefficient/ mm <sup>-1</sup>
		Transmission/ %			
1	HDPE no additive	0.18	3.15	3.20	0.35
		80.40	28.50	27.30	
2	HDPE CNT, 0.003	0.20	0.30	3.11	2.30
		59.50	47.20	0	
3	HDPE CB, 0.003	0.15	0.20	3.08	1.12
		68.80	67.40	2.65	
4	HDPE CW, 0.003	0.11	0.17	3.04	0.99
		76.80	74.40	4.30	

Required absorption coefficients were achieved by adding very small additions (0.003wt %) of carbon nanotubes, carbon black or Clearweld® absorber to the HDPE. HDPE alone showed a lower absorption coefficient (0.35mm<sup>-1</sup>). The absorption in the HDPE however reduces dramatically as the material is raised above the melting point. Therefore the additives retain absorption above the melting point of the HDPE. In addition it was observed that only 28% of the incident beam on a 3mm thick virgin HDPE sample was transmitted through it, which means corrections needed to be made when choosing laser powers to make welds as is described in the following sections.

#### **6.6. Heating of HDPE specimens**

The transmission trials were followed by heating trials using the laser radiation on one side of the waisted specimen while measuring temperature changes on either the side that was irradiated or the side opposite to it. The beam size was set to be slightly smaller than the wide end of the sample (approx. 88mm<sup>2</sup>). The beam power and time were controlled to allow a known amount of energy to be applied. The temperature of the sample was monitored during the irradiation using an infrared pyrometer directed to either the upper or lower surfaces as shown in Figure 79 and the results are given in the Table 26.

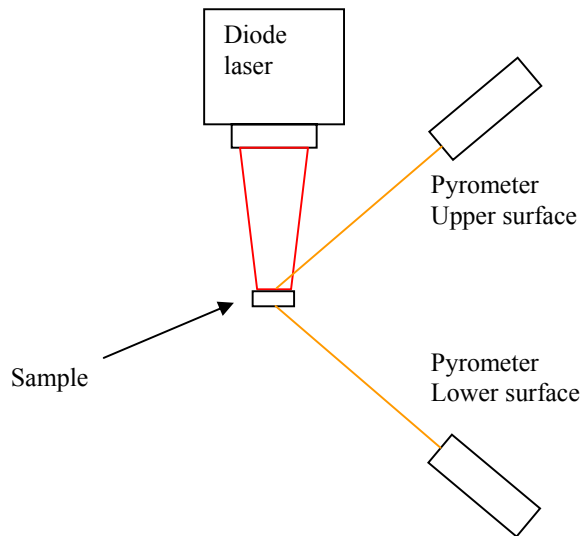


**Figure 79, equipment arrangement for temperature measurements during laser heating trials on flat strips of virgin and modified HDPE.**

The results showed that when these low concentrations of CB, CW or HBCNTs were used the material could be heated through thickness. Although the top and lower surface temperatures were not the same. Samples containing CB or HBCNT retained their high absorption properties throughout the exposure time whereas samples containing CW showed a reduction in their absorption characteristics when heated above a certain temperature (hence the initially greenish dye became transparent) and therefore larger part of the incident beam penetrated through these samples. Samples containing CB or HBCNT, therefore absorbed most of the incident radiation at or near their surface, with minimal beam penetration.

**Table 26, results of laser heating on the first batch of mixed samples. The duration and energy applied are for the whole heating cycle from room temperature. Upper surface refers to the surface of the sample exposed to the beam and lower surface is the reverse surface to that exposed to the beam.**

Sample no	Description, wt%	Power/W	Duration/s	Energy applied/Jmm <sup>-2</sup>	Maximum upper surface temperature/°C	Maximum lower surface temperature/°C
1	HDPE no additive	15	5	0.85	70	56
		15	10	1.70	105	77
		15	15	2.56	122	98
		15	20	3.41	130	110
		15	30	5.11	153	124
		15	60	10.23	192	163
		15	120	20.45	216	186
		15	180	30.68	227	191
4	HBCNT1, 0.003%	5	5	0.28	89	47
		5	10	0.57	152	63
		5	15	0.85	164	74
		5	20	1.14	216	82
		5	30	1.70	229	108
		5	40	2.27	261	100
10	CB, 0.003%	5	5	0.28	99	51
		5	10	0.57	129	69
		5	15	0.85	177	84
		5	20	1.14	183	101
		5	30	1.70	227	121
11	CW, 0.003%	5	5	0.28	85	47
		5	10	0.57	127	62
		5	15	0.85	143	79
		5	20	1.14	172	86
		5	30	1.70	178	109

The results confirm that while the HDPE without additive can be heated relatively effectively when it is below the melting point at approximately 125°C, the heating is much reduced above this temperature when the material is much more transparent to the

laser energy, as explained in the previous sections. This means that exposure times and /or energies almost five times higher are required compared with materials with absorbing additives. Furthermore, without any absorbers, the heating is not sufficiently high or fast to create a weld; longer exposures and higher laser intensities will cause degradation of the polymer surface and melting from the top as opposed to creating a weld. All the additives used were very effective at increasing the heating rate when the temperature was above 125°C. However the sample preparation process did not produce evenly dispersed absorbers in each specimen. In addition, the laser trials are conducted by transmission through a virgin HDPE sample which will scatter and absorb part of the incident beam. Therefore the amounts of absorber used in practice will need to be higher than the calculated amounts and were in the region of 0.1wt%. Also this meant that the absorption fraction at the interface was increased, which would compensate for the energy loss through the top surface of the weld without having to increase the welding power and cause possible damage to the top surface of the virgin HDPE.

#### **6.7. Initial welding trials**

Initial welding trials were carried out to understand the influence of welding parameters such as welding speed and laser power. The TTLW trials were carried out on different specimens using the same laser as used for the heating trials with a square beam spot of 3×4mm (1.2cm<sup>2</sup>). In addition a sliding clamping ring was used to apply pressure (approximately 1 Nmm<sup>-2</sup> at the work piece) to the samples interface during the welding process (as routinely used for TTLW of plastics using CW and CB). The parts were positioned and clamped using spacers due to the overlap geometry, as shown in Figure 80 to ensure that the clamping pressure was as homogeneous as possible.

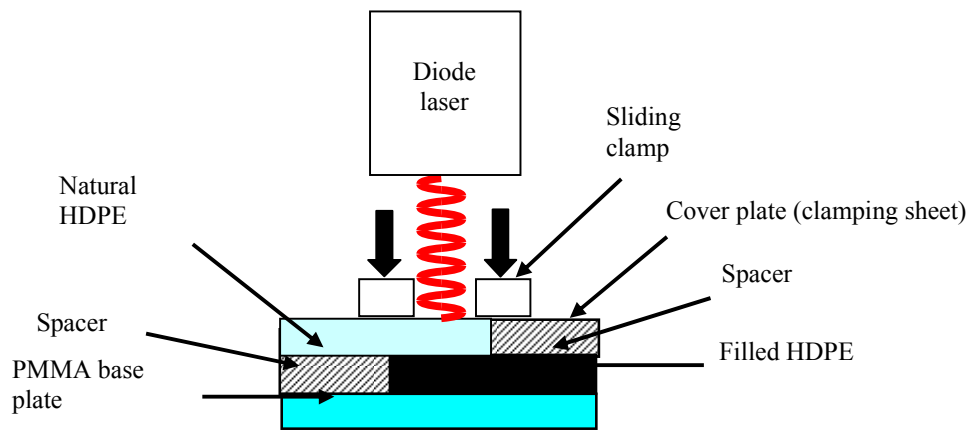


**Figure 80, configuration of the laser, clamping system and sample for the laser welding trials.**

Different welding speeds and powers were examined, with each condition repeated and tested three times for statistical confidence. The welds produced were evaluated only by pulling them apart by hand to see whether an integral joint was achieved or not. Initially the HBCNT samples were welded using a 50W laser power (P) at a  $1\text{ m min}^{-1}$  welding speed (v) based on the calculations for melt depth and weld temperature, but these conditions did not result in a weld. However, using 100W of power and a speed  $2.5\text{ m min}^{-1}$  resulted in a weld. These results are counterintuitive, because the  $P/v$  ratio for the first set of parameters was  $50\text{ W m}^{-1}\text{min}$  and for the second set that resulted in a weld, was  $40\text{ W m}^{-1}\text{min}$ . Further trials showed that a welding speed of  $3\text{ m min}^{-1}$  using a 100W laser power (i.e. a  $P/v$  ratio of  $33\text{ W m}^{-1}\text{min}$ ) also resulted in a weld. Similar results were obtained using CB; for example a welding power of 30W at  $1\text{ m min}^{-1}$  did not result in a weld, however a welding power of 100W at  $4\text{ m min}^{-1}$  ( $25\text{ W m}^{-1}\text{min}$ ) did result in a weld. A fewer number of trials were conducted with CW as the welding conditions for this absorber are well known by the author. Welding speeds of  $1\text{ m min}^{-1}$  at 70W power did not result in a weld; however increasing the power to 80W and using the same speed did. Table 27 shows a few of the initial trials carried out including the results.

**Table 27, some of the results from the initial welding trials.**

Absorber	Laser power/W	Welding speed/(m.min <sup>-1</sup> )	Weld	Power/speed	Power <sup>2</sup> /welding speed
CB	30	1	No	30.00	900
CB	40	1	Yes	40.00	1600
CB	40	2	No	20.00	800
CB	100	2.5	Yes	40.00	4000
CB	100	3	Yes	33.33	3333
CB	100	4	Yes	25.00	2500
CW	70	1	No	70.00	4900
CW	80	1	Yes	80.00	6400
CW	100	1	Yes	100.00	10000
CW	100	2	No	50.00	5000
HBCNT	30	1	No	30.00	900
HBCNT	40	1.5	No	26.67	1067
HBCNT	40	1	No	40.00	1600
HBCNT	40	2	No	20.00	800
HBCNT	40	3	No	13.33	533
HBCNT	50	1	No	50.00	2500
HBCNT	100	2.5	Yes	40.00	4000
HBCNT	100	3	Yes	33.33	3333
HBCNT	100	4	No	25.00	2500
HBCNT	100	5	No	20.00	2000

When comparing the values for P/v with the welding performance the results seemed inconsistent. However, if the results are compared with P<sup>2</sup>/v there is consistency. Power/speed is a measure of the heat applied to the weld. One would expect this to be a good measure for defining how to get a good weld, i.e. if the overall amount of energy applied per unit area remains constant with increasing speed one might expect the same weld results regardless of what the welding speed is. This is true as a first approximation and for small changes in laser power or welding speed. However, as the welding speed increases the required power does not change linearly with it because the weld has less depth and so less volume of material is heated at the higher speed. This can also be seen by rearranging Equation (50), where it can be seen than intensity squared is proportional to the thermal diffusivity as shown below

$$l = \frac{C\rho\Delta T(Xt_p)^{1/2}}{A_f t_p} \quad (67)$$

In other words heat does not diffuse quickly enough as the power increases significantly therefore a better approximation of the weld strength is given by using  $P^2/v$  as the variable instead of  $P/v$ .

### 6.7.1. Microscope images of the initial welds

Welds produced during the preliminary trials using dry powders were fractured and inspected under SEM. Results showed that the polymer was melted and the HBCNTs were embedded in the weld (Figure 81). Inspection of the weld interface did not show a distinct interface between the two substrates (Figure 82), which is a sign of a good melt entanglement.

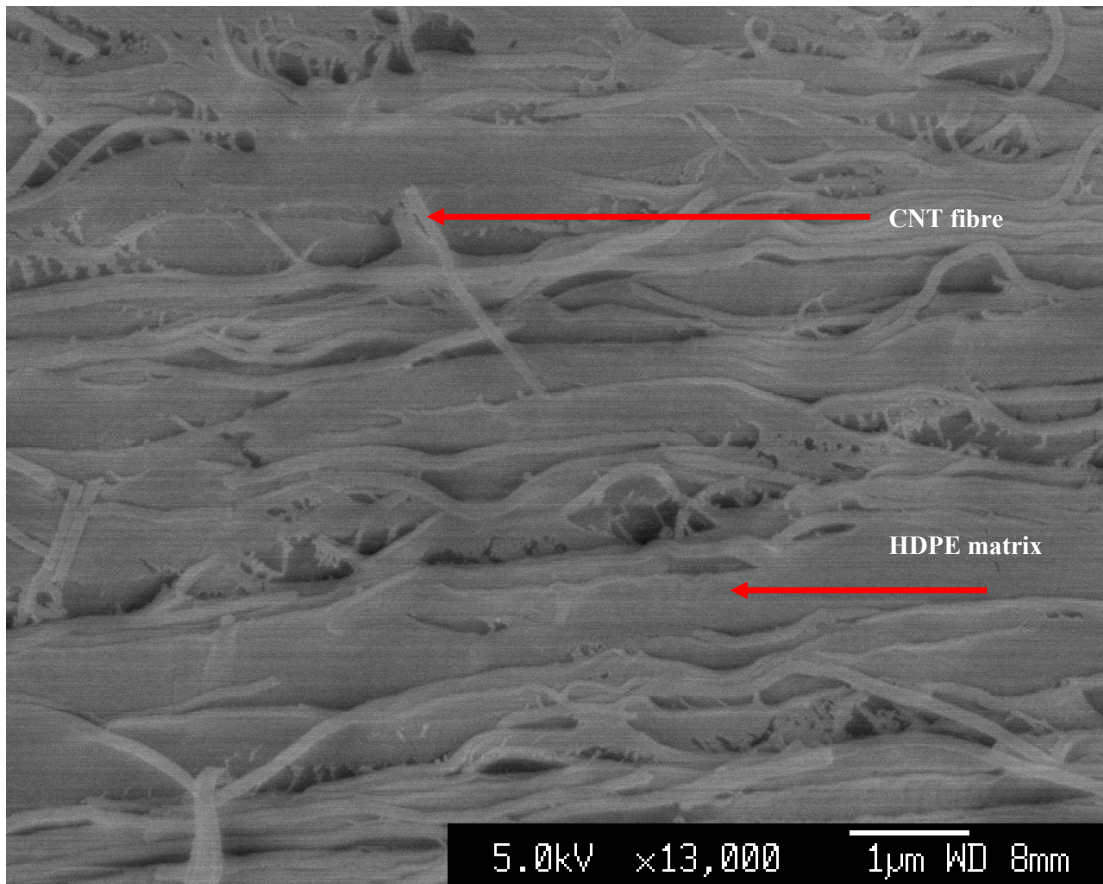


Figure 81, fracture surface of a HDPE welded specimen made with dry HBCNT powder at the interface.

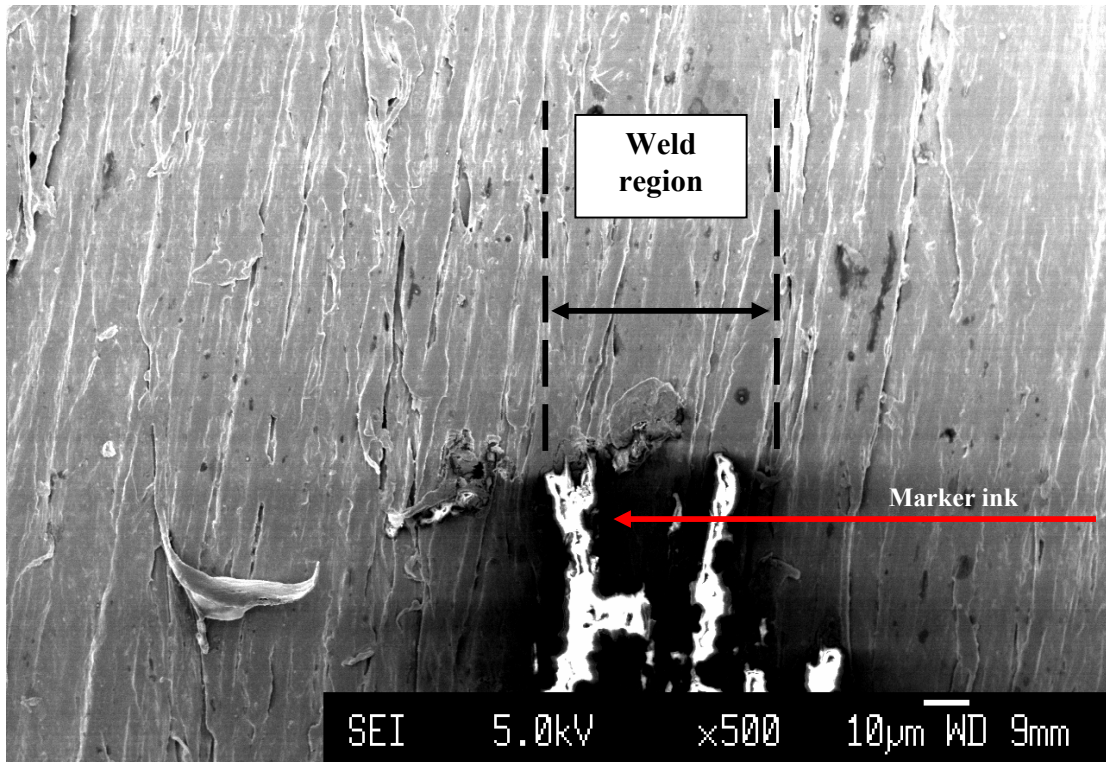
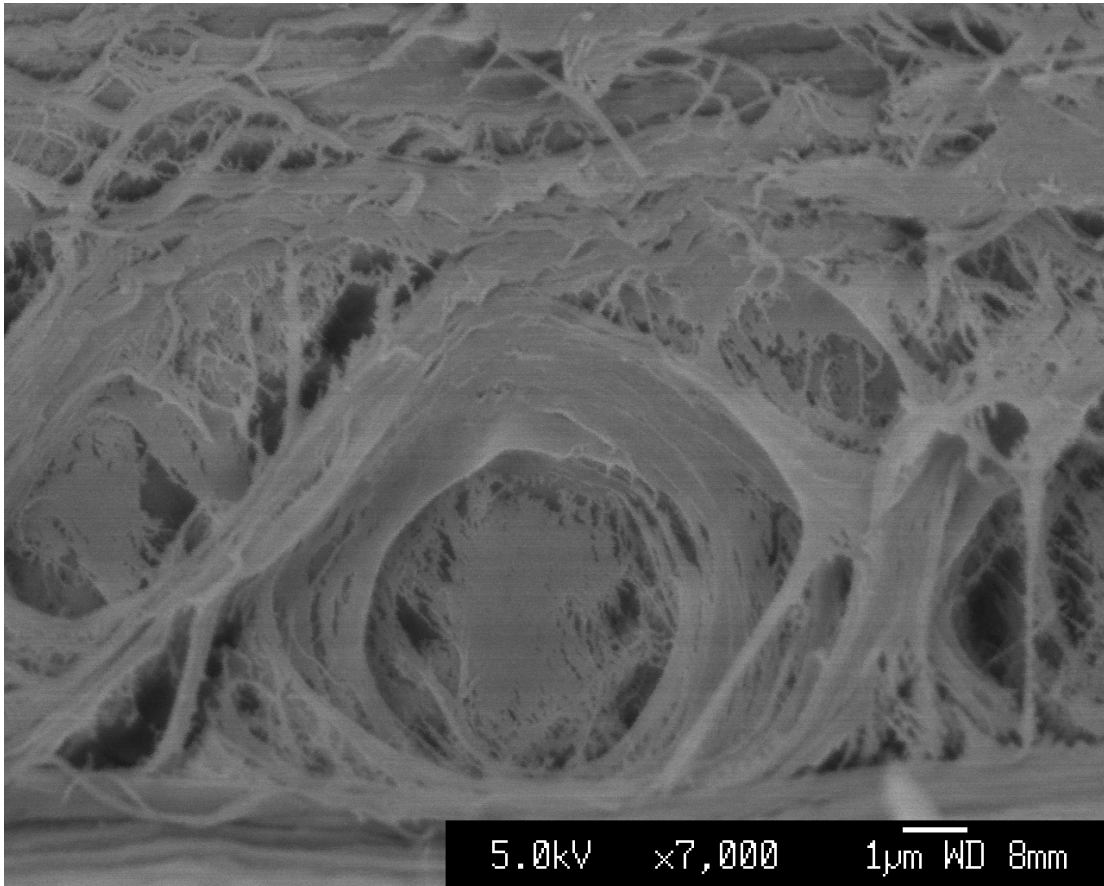


Figure 82, Weld interface of welded HDPE using HBCNT powder. The marker pen was used to highlight where the weld is as the welding interface could not be seen otherwise by SEM due to the consistent melt achieved during the process.

Lap shear tests were conducted on five samples made using HBCNTs and SEM examination of the failed surfaces showed large areas of sheared material and revealed polymer melt fusion as well as a HBCNT fibres wrapped in molten polymer as shown in Figure 83.



**Figure 83, Sheared part of a failed HDPE weld, made with dry HBCNT powder at the interface.**

## **6.8. Design of experiments**

As it could be clearly seen from the initial welding results there are a number of variables to consider for TTLW, and these variables have mutual influences. Assuming uniform properties of the HDPE to be welded, the factors that will affect the performance of the final weld are the welding parameters such as (power, spot size, welding speed, clamping pressure, etc) It is clear that each welding parameter has a lower and upper limit that results in a weld and these parameters are interrelated. Therefore, to find the optimal combination of these parameters, the welding experiments need to be extended and an unfeasible number of samples would have to be tested to be able to account for any interactions between the parameters if changed simultaneously or to find optimal conditions for making a weld or comparing the performance of the different absorbers. A design of experiment (DoE) approach was used, which is a statistical technique that provides a predictive outcome on the basis of the data derived; it is not based on physical

modelling. Thus, it can predict the outcome of the given data, although it does not explain why this occurs.

The software used for the DOE was Design-Expert from Stat-Ease. A Response Surface Methodology (RSM) was used, using a response surface, central composite design. RSM is a collection of statistical and mathematical techniques that are useful for developing, improving and optimising a process. The RSM graphical perspective is based on two groups of variables: independent variables and response variables. The independent variables are controllable variables, while the response variables measure the performance or quality characteristic of the process. For example the failure load (response variable) of a laser welded joint depends on a number of independent variables, including laser power and welding speed.

A set of experiments were therefore determined for each absorber using this method, as shown in Table 28. If power and speed were treated as separate parameters, the experimental design would generate a number of experiments (high power, low speed and low power, high speed) that would result in a weld with no strength. A parameter linking these variables was used, in order to limit the number of runs that would generate no weld. The parameters that were investigated were  $P^2/V$  ( $W^2 m^{-1} min$ ) and the laser power,  $P$  (W). The limits of these two parameters were determined from preliminary trials as discussed in Section 6.8, which were carried out to identify the range of laser powers and welding speeds that would give a weld for each absorber. Laser trials were then conducted using the parameters from the DoE (i.e. power and the welding speed) and the resultant welds were lap shear tested to evaluate their strength.

#### **6.8.1. Lap shear test results**

Each welded sample was lap shear tested and the value of load at break measured. Due to the slight variation in the specimen width for different samples the lap shear test results were normalised by dividing the resultant failure loads by the specimen weld length. The results of the lap shear tests are also listed in Table 28.

**Table 28, design of experiment test matrix, for the filled HDPE samples.**

<b>Absorber</b>	<b>P<sup>2</sup>/speed (W<sup>2</sup> m<sup>-1</sup> min)</b> <b>Variable 1</b>	<b>P(W)</b> <b>Variable 2</b>	<b>Fracture load/ weld length</b> <b>(N.mm<sup>-1</sup>), Response</b>
<b>CNT</b>	4547	72	54.5
	4000	100	26.3
	2469	72	34.7
	2469	72	17.8
	1003	45	0
	1000	100	0
	2469	72	18.5
	373	72	0
	4050	45	62.1
	2469	72	0
	2484	111	40
	2469	72	0
	2569	34	54.5
	<b>CB</b>	4547	72
4000		100	0
2469		72	0
2469		72	49.7
1003		45	0
1000		100	0
2469		72	31.7
373		72	0
4050		45	56.5
2469		72	32.3
2484		111	53.4
2469		72	31.9
2569		34	0
5000		50	42.9
<b>CW</b>	7500	75	51.7
	7469	110	0
	10000	100	49.1
	11029	75	57.9
	7500	75	48.1
	7500	75	50
	5000	100	0
	7500	75	48.3
	10000	50	53.5
	7500	75	0
	4050	45	61
	3961	75	0

The resultant weld strength data was input to the DOE as the response variable and models predicting the load/weld-length for each absorber as a function of power<sup>2</sup>/speed and power were determined.

For each type of absorber a relation linking the load at break/weld length with P<sup>2</sup>/v and P were determined, as listed below:

- CB: load at break/ weld length of weld =  $37.92531 + 0.010307 \times (P^2/v) - 0.60769 \times P$
- CW: load at break/weld length =  $32.57095 + 0.00707915 \times (P^2/v) - 0.66784 \times P$
- HBCNT: load at break/weld length =  $7.80461 + 0.01379 \times (P^2/v) - 0.25594 \times P$

It was then possible to plot the behaviour of the process for each absorber. Two cases were evaluated; constant welding speed and constant laser power. In each case, two values of welding speed and two values of laser power were taken into account. Figures 84 and 85, show the predicted evolutions of load at break/weld length as a function of laser power, for two different speeds of  $0.5 \text{ m}\cdot\text{min}^{-1}$  and  $1 \text{ m}\cdot\text{min}^{-1}$  respectively based on the DoE as well as the actual test data points under the same conditions based on Table 28.

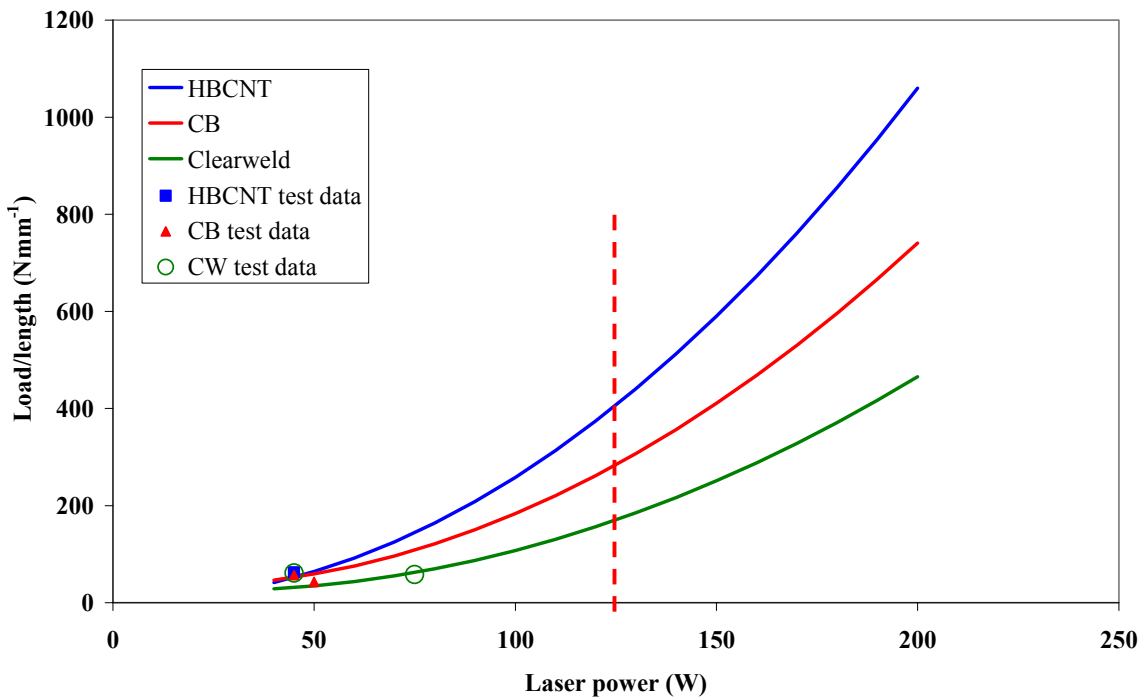


**Figure 84, failure load/ weld length as a function of laser power for a welding speed of  $0.5 \text{ m}\cdot\text{min}^{-1}$ .**

The predictions for the welding speed of  $0.5 \text{ m}\cdot\text{min}^{-1}$  are mostly in agreement with test data. However CW is predicted to generate the weakest welds at all powers compared with HBCNT and CB, where as the test data showed that the difference between the absorbers is very small at laser powers below 50W when welding at the speed of  $0.5 \text{ m}\cdot\text{min}^{-1}$  and indeed CNT produces strongest welds followed by CW and then CB under these conditions. Overall the predictions show that HBCNTs generate stronger welds than

CB or CW for a given amount of energy. The initial welding trials and general experience has shown that it is not possible to achieve high integrity TTLW in HDPE or other semi-crystalline polymers at low power intensities due to the large energy scattering of the beam energy. Therefore for industrial applications HBCNTs could be advantageous in terms of higher joint integrities compared with CB and CW for a given power, or indeed more energy efficient for a given weld strength. However it should be noted that the peak strengths would be similar for all the absorbers just at different weld conditions depending on the absorption properties. It should also be noted that 200W of laser power for welding might be extrapolating a bit far showing weld strength larger than the parent material. Such high powers in practice will overheat the sample, which will then show a reduction in the strength of the joint. This will be more of an issue with HBCNTs and CB than CW, because CW loses its absorption properties at high temperatures. A reasonable cut off power will be between 100 to 150W as indicated by the red dashed lines in Figures 84 and 85.

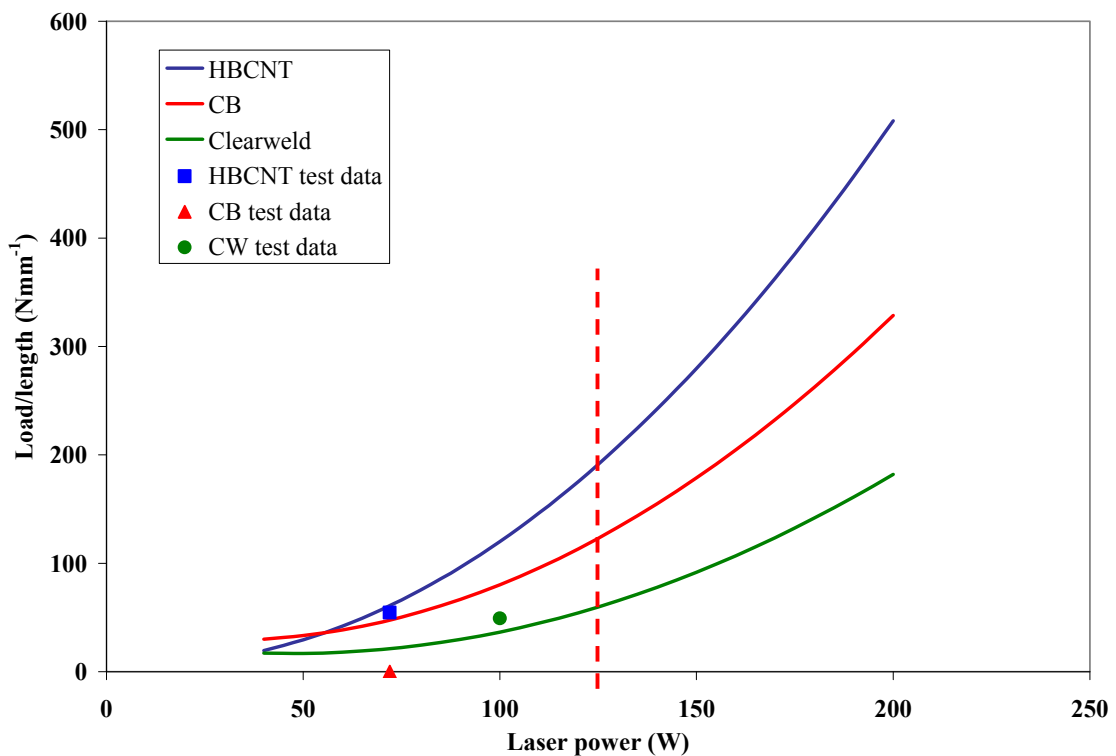


Figure 85, failure load/ weld length as a function of laser power for a welding speed of 1m.min<sup>-1</sup>.

Figure 85 shows the predictions of weld strength at welding speed of  $1 \text{ m min}^{-1}$  for different laser powers. The actual test data points for welds under the same conditions are also shown in the graph. It can be seen that the predictions for HBCNT and CW are reasonably accurate compared with actual data, while the weld strength result for CB seem to be lower than that predicted. In general it can be seen that HBCNT would result in stronger welds than the other absorbers under similar conditions.

As well as achieving the desired weld strength it is also important that the absorber used can enhance the welding productivity i.e. welds can be made as fast as possible. The predicted evolutions of load at break/weld-length as a function of welding speed was calculated and are plotted in Figures 86 and 87 for two different laser powers of 100W and 50W, respectively.

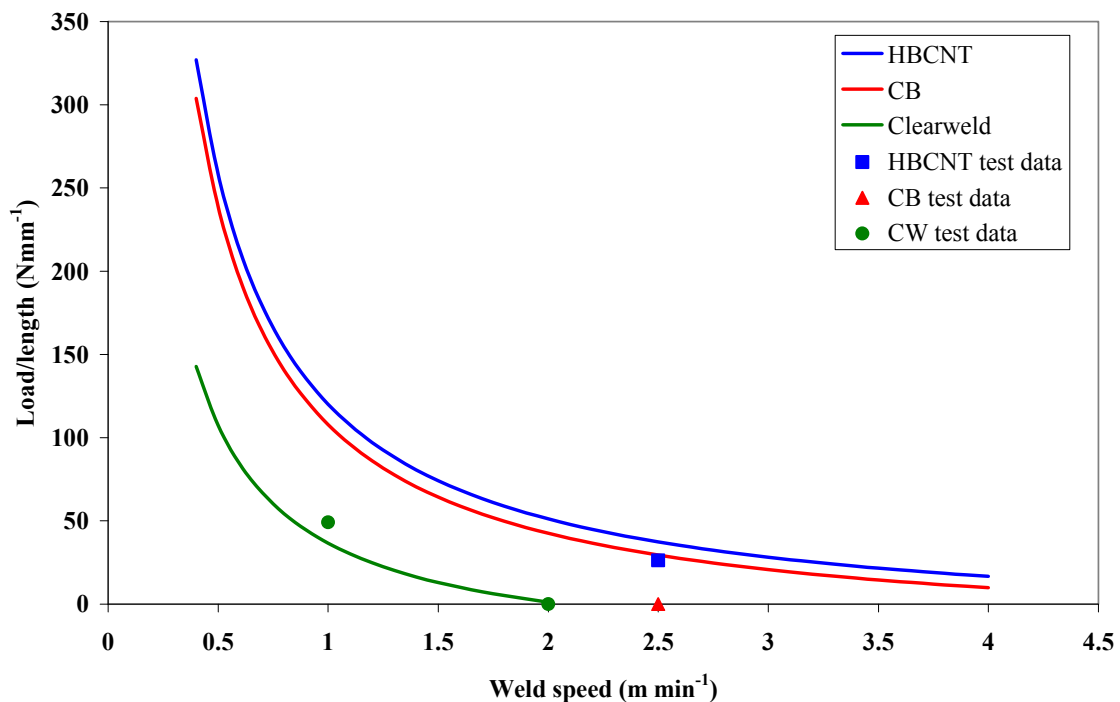


Figure 86, failure load/ weld length as a function of welding speed for a laser power of 100W.

For a power of 100W, the predicted results for CW seem to be consistent with the test data. HBCNT test result is also close to the predicted value, however the result achieved for the CB welded joint is again much below (in fact zero) the predicted values of strength. Although the model predicts that t HBCNT and CB will perform similarly it is more likely that HBCNT and CW result in good welds with HBCNT producing stronger

welds while CB will perform inferior to the other absorbers in terms of both weld strength and welding speed.

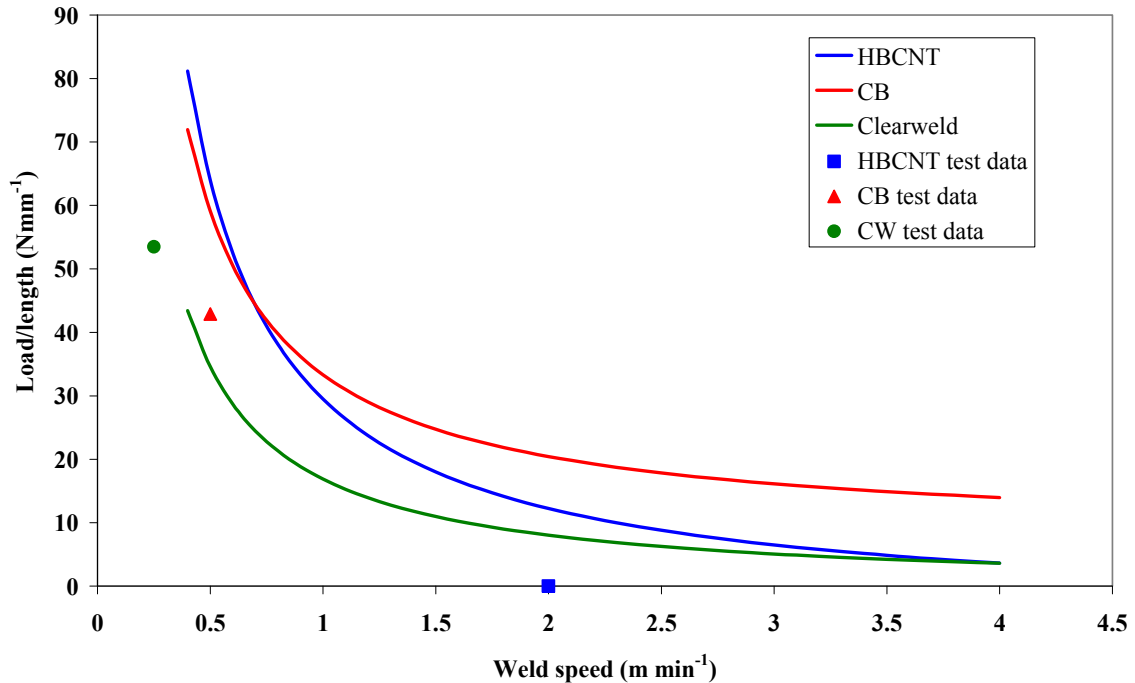


Figure 87, failure load/ weld length as a function of welding speed for a laser power of 50W.

Finally, for a laser power of 50W the performance of CW again seems to be consistent with predictions while test results for CB are again below the predicted values. HBCNTs is predicted to produce welds as good as CB at weld speeds below 1 m min<sup>-1</sup> and then fall in between CB and CW at higher welding speeds for the laser power if 50W. Unfortunately there are no test data points for HBCNT at 50W however the data point for 45W is shown on the graph for welding speed of 2m min<sup>-1</sup>, which did not result in a weld.

### 6.8.2. Melt depth

To examine the melt depth and compare it with the theoretical results, and to provide a comparison between the efficiency of different absorbers in creating molten material, three welds made with the same parameters (welding speed of 0.5 m min<sup>-1</sup> and a power of 45W), were sectioned and observed under a crossed polar transmission microscope. Polarising microscopy uses the interaction of an optically anisotropic material with polarised light. The microscope has a polariser unit in the illumination system and an

analyser between the object and the eye piece. The arrangement used in these experiments is crossed polars, where the plane of polarisation of the polariser and the analyser are perpendicular to one another. With no specimen or an isotropic specimen between the two polarisers, the field of view is dark as the analyser does not transmit any of the light, which has been transmitted through the polariser. However anisotropic materials are birefringent, and split the light that is passing through them into two plane polarised waves at right angle to one another. Birefringence is mainly due to the orientation of the polymer chains although it can also arise from the presence of different phases such as crystalline and amorphous phases in a semi-crystalline polymer. Such structures appear coloured under crossed polars and this depends on the light retardation. The welded samples were sliced to thin sections across the weld using a microtome to allow transmitted light microscopy. The samples were first cut to fit the microtome holder using a band-saw (no longer than 20mm and approximately 5-10mm high) and mounted in mounting compound with the face to be sectioned upwards. The samples were then left for the mounting compound to set after which several slices were cut until the sample surface was flat. A sample slice was then cut and placed on a slide covered with castor oil. All traces of the mounting compound were carefully removed using tweezers and a small brush, the sample was then covered with more oil and another slide and placed under the microscope. The light on the sample was then adjusted until it was bipolar and focused. The resultant images are shown in Figures 88-90.

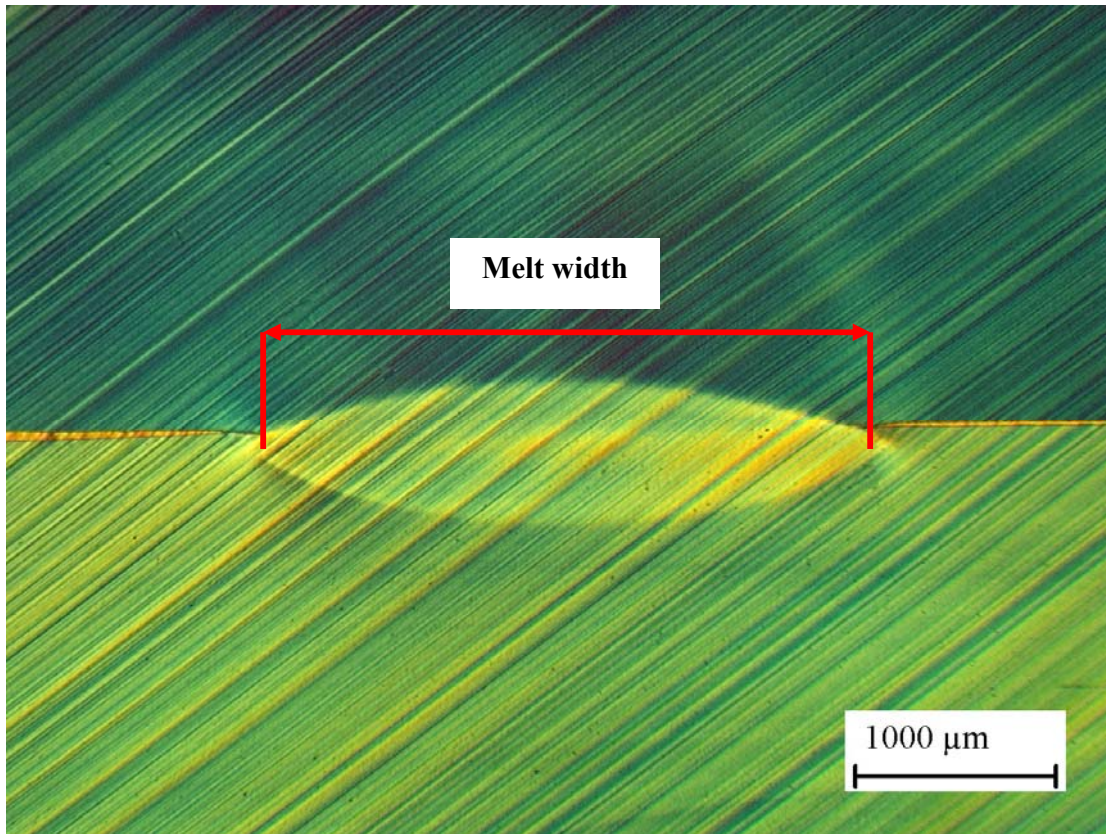


**Figure 88, microtome section of a weld made with 0.1wt% heat treated ball milled carbon nanotubes (HBCNT) incorporated in HDPE at welding speed of  $0.5 \text{ m min}^{-1}$  and 45W of power.**

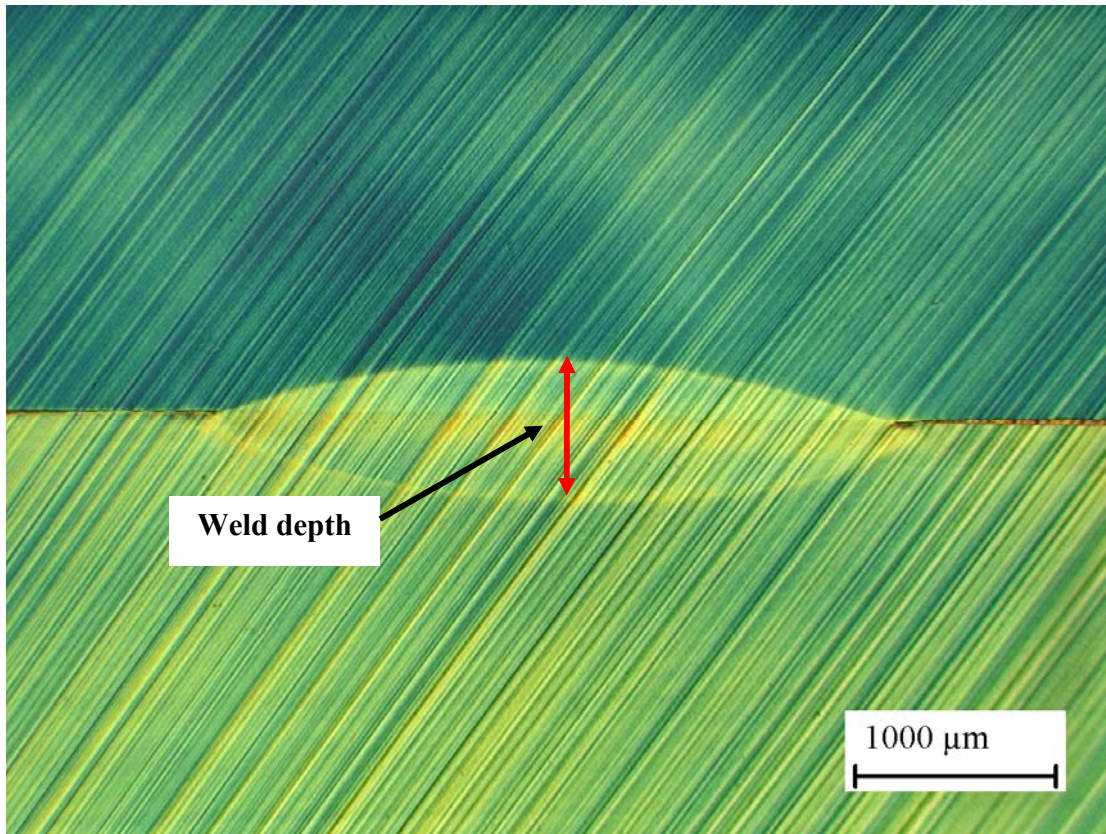
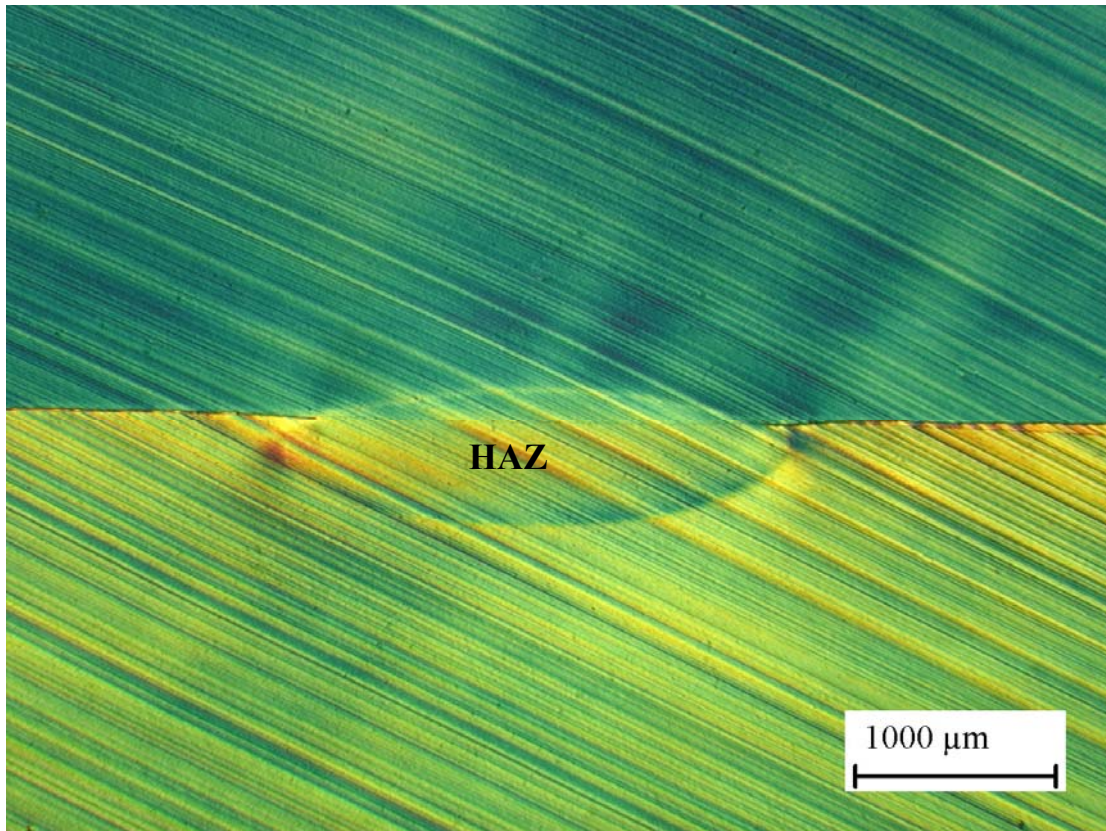


Figure 89, microtome section of a weld made with 0.1wt% carbon black (CB) incorporated in HDPE at welding speed of  $0.5 \text{ m min}^{-1}$  and 45W of power.



**Figure 90, microtome section of a weld made with 0.1wt% Clearweld (CW) absorber incorporated in HDPE at welding speed of  $0.5 \text{ m min}^{-1}$  and 45W of power.**

The colour difference in the top and bottom substrate is due to the light retardation, which arises from the difference in the birefringence of the two polymers because they were extruded in different batches and therefore have different chain orientation as well the fact that the upper surfaces in the Figures 88-90 have absorbers incorporated in them. Using transmission optical microscopy, the heat affected zone (HAZ) is indicated by the change in birefringence colour viewed between crossed-polarising optics, which indicates a change in the orientation of polymer molecules, probably due to residual stress generation as a result of a heating cycle in the constrained material. The lenticular HAZ section is characteristic of the process. The weld depths were 0.78, 0.69 and 0.67mm, for HBCNT, CB and CW respectively. The welds made with CW required welding speeds ( $0.2 \text{ m min}^{-1}$ ) at the same energy level to provide an integral weld. The best results for CB were achieved at slightly weld speeds of  $0.45 \text{ m min}^{-1}$ . At a welding speed of  $1 \text{ m min}^{-1}$ , HAZ depths of below approx. 0.1mm were associated with failure at the weld interface. The width of the melt was also measured for Figures 88 to 90, and were found to be,

3.06mm, 3.29mm and 2.5mm for HBCNT, CB and CW, respectively. The stronger welds therefore are related to the greatest depth of melt achieved by using HBCNTs as absorbers. The higher heat generated in the HDPE substrate containing HBCNTs compared with the other absorbers, and its confinement to the interface, also creates more melt in the virgin substrate compared with CB and particularly CW which allows more of the incident beam into the bulk of the material and creates less melt at the interface.

### 6.8.3. Scanning electron microscopy

Both surfaces of the welds made with HBCNTs were examined under SEM. Figure 91 shows the failed surface of the welded virgin HDPE.

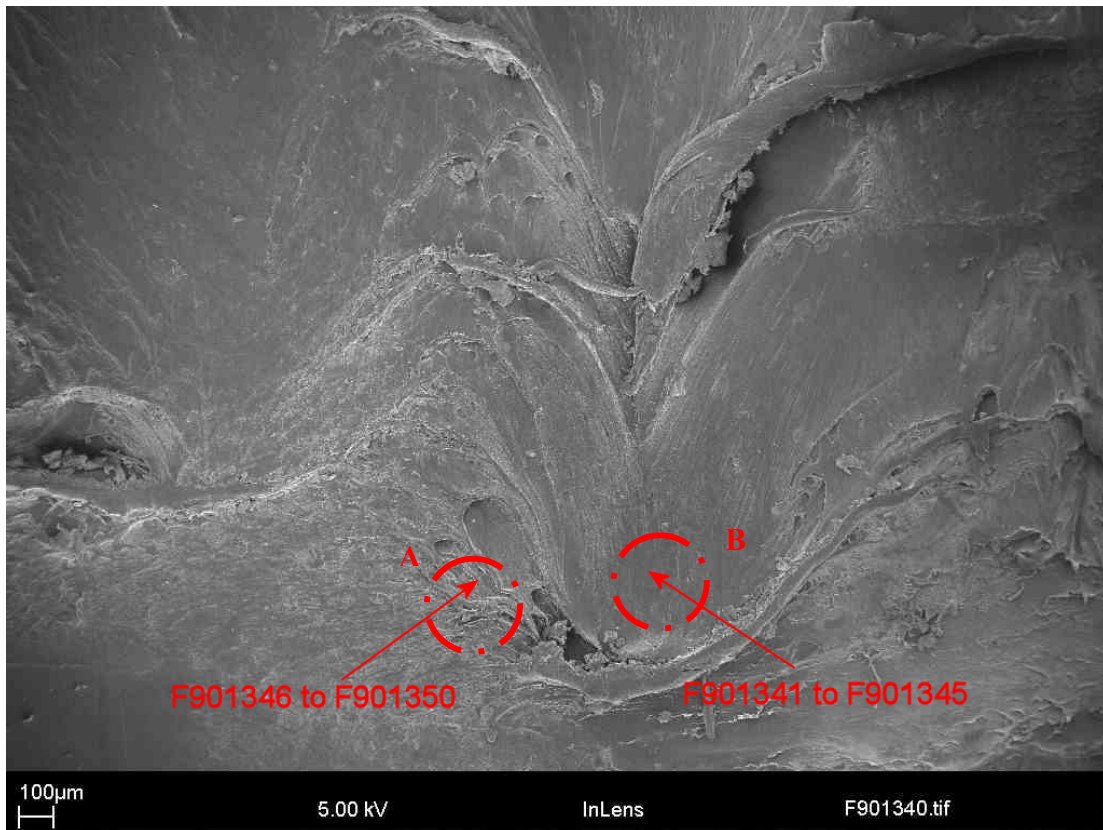
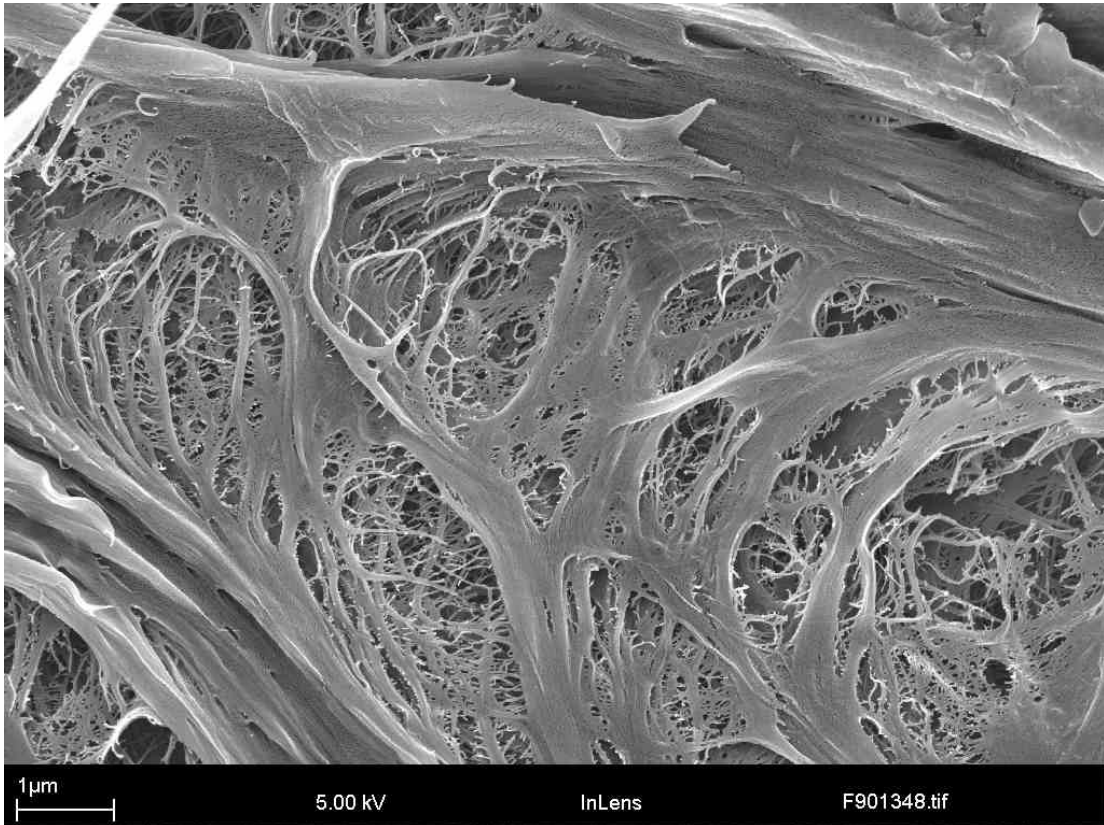


Figure 91, fracture surface of the welded virgin HDPE (F901346 to F901350 and F901341 to F901345 are the references for a number of images taken from the A and B Regions respectively).

Two distinct regions on the failed surface can be seen. One labelled A with large amounts of deformation and the other labelled B with a relatively flat appearance. Higher magnification of Region A is shown in Figure 92.



**Figure 92, high magnification image of Region A in Figure 91.**

This region seems to have undergone a large amount of shear during the lap shear test. This is due to the entanglement of the polymer chains and CNT fibres. A magnified image of Region B is shown in Figure 93.

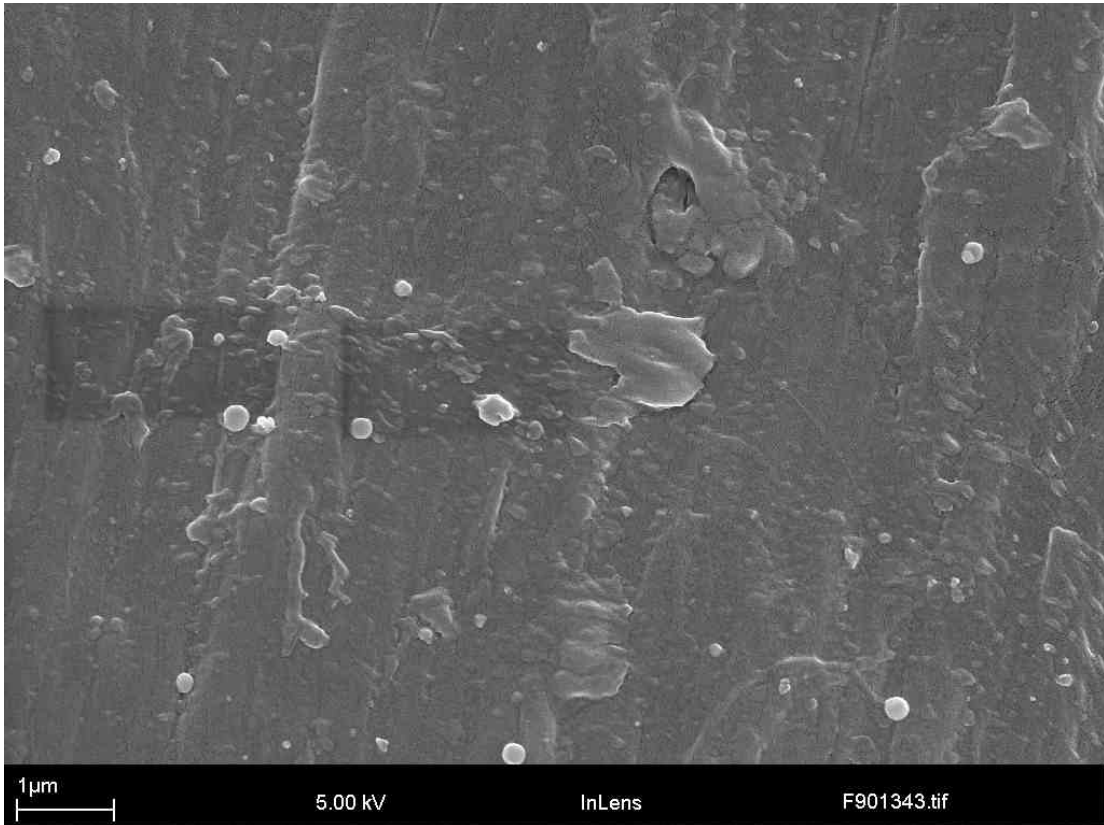


**Figure 93, high magnification image of region B in Figure 91.**

This region is more flat; however there are uneven surfaces in this region which are where small amounts of the molten polymer are left on the surface from the other substrate. Therefore the parts that were sheared off from one side are attached to the other side, meaning that the breaking of the weld does not happen exactly at the interface but shears near and around the interface through both sides of the weld. Figure 94 shows the failed surface of HDPE containing HBCNT absorbers.

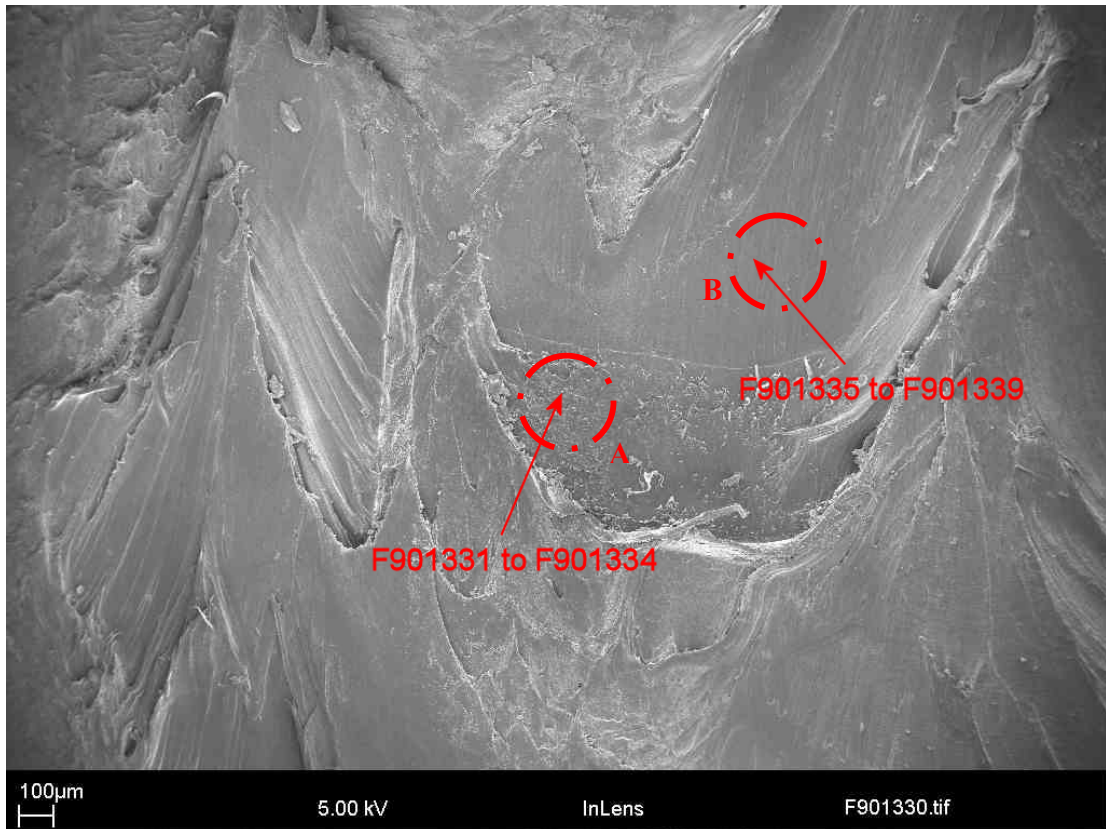


**Figure 94, failed HBCNT-modified HDPE substrate, (F901331 to F901334 and F901335 to F901339 are the references for a number of images taken from the A and B Regions respectively).**

Again two distinct regions on the failed surface can be seen. One labelled A with large amounts of deformation and the other labelled B with a relatively flat appearance. Higher magnification of Region A is shown in Figure 95.

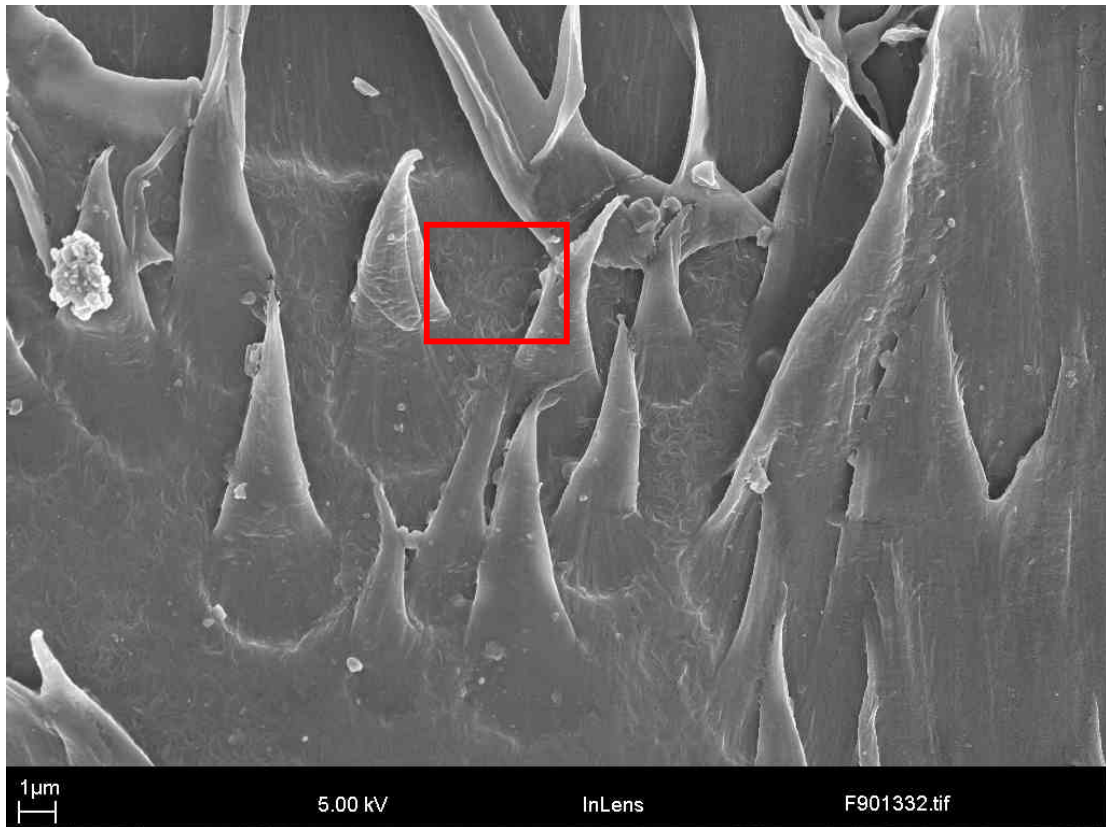


**Figure 95, high magnification image of Region A in Figure 94.**

This region seems to have undergone a large amount of shear during the lap shear test. However this time the material seems to have drawn out locally. This could be a result of HBCNTs reinforcing the polymer and make it very difficult to be removed during the shear test. Slight cracks were observed on the root of the cone shaped material in Figure 95 but they do not grow through thickness during the test. Also swirls of HBCNTs entangled with HDPE can be seen in the material, such as in the region highlighted with a red box in Figure 95. Areas of the failed surface examined showed HBCNTs wrapped in previously molten polymer and bridging the tearing gaps that were created during the lap shear tests. An example of this is given in Figure 96.

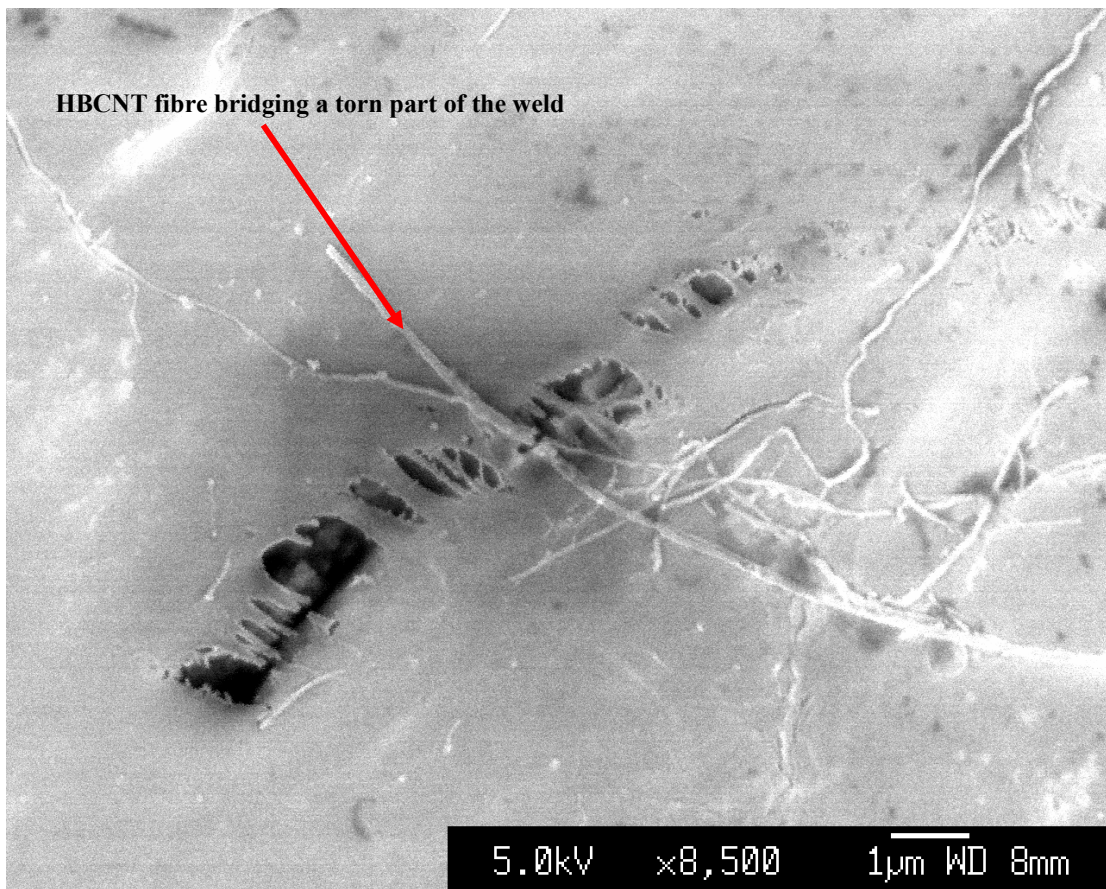


Figure 96, image of a HBCNT fibre bridging a sheared part of the weld.

A magnified image of Region B is shown in Figure 97. This region is more flat; however there are uneven surfaces on this region almost complementing the flat surfaces on the virgin HDPE, confirming that the breaking of the weld does not happen exactly at the interface but shears near and around the interface through both sides of the weld.

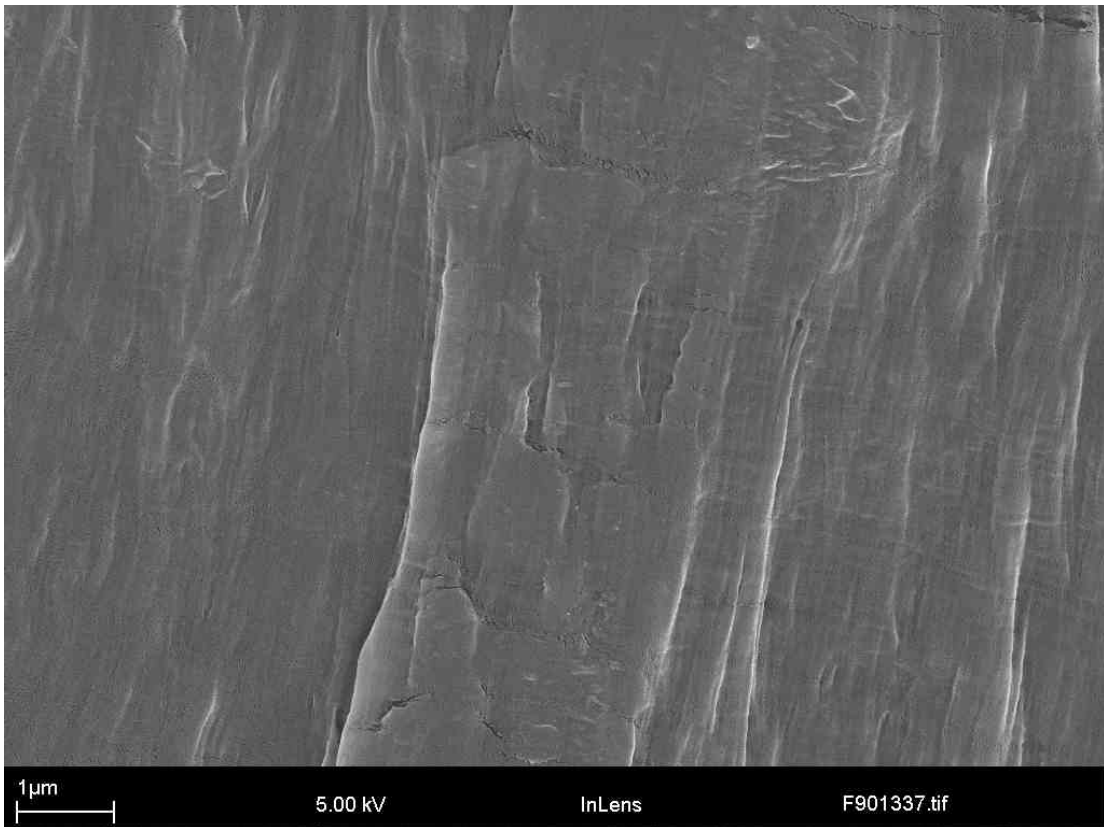


Figure 97, high magnification image of Region B in Figure 94.

### 6.9. Summary

Through transmission laser welding (TTLW) is a rapid method of producing welds between thermoplastic polymers. The process produces no weld flash and provides good control over the energy input and is therefore a desirable assembly process, particularly for more expensive plastic goods. As the laser beam needs to pass through the upper substrate, the materials properties in terms of absorption and scattering of light, greatly influence the required parameters for this welding process.

In particular the presence of crystallites and scattering points can greatly reduce the weldability of a material. This is because of two reasons; one is the fact that the scattering and absorption can cause direct bulk heating of the materials to be welded and can therefore melt or degrade the material particularly at the top surface as opposed to the interface, where the molten polymer is needed. This problem can be overcome by adding absorbers at the interface to be welded to focus the heat and also by choosing a laser wavelength where the polymers to be welded are most transparent i.e. NIR. However the

second issue is supplying enough energy to these absorbers which could mean large laser intensities to compensate for the light extinction caused by the upper surface.

Carbon nanotubes are very efficient absorbers of the diode laser radiation and, if positioned into such joints, they can absorb the laser energy and generate enough heat to produce a weld even at very low concentrations. HBCNTs were used based on the results of the dry heating trials described in Chapter 5, which showed these CNTs are more efficient in absorption and conversion of laser light into heat than the other forms of CNTs that were examined. High absorption and effective heat generation properties allowed welding of thick semi-crystalline cross-sections that are otherwise impossible using the TTLW process. The welds obtained using HBCNTs are sensitive to the form the absorber is applied to the joint. Spraying liquid suspensions of HBCNT absorbers into the joint is impractical due to agglomeration and entanglement of the tubes. The best way of incorporating these materials into the joint is by adding them into one of the substrates to be welded, through injection moulding or perhaps other manufacturing processes, which also ensures containment of these nanoparticles and mitigates any associated health and safety issues during welding.

It was seen that different welding process parameters influence the integrity of the joint achieved. These parameters are interlinked and the changing of one affects the limits and performance of the others. The most important of these parameters were laser power and speed. To make the evaluation of the influencing parameters and their interaction feasible, without conducting a large number of tests, a DoE method was used to minimise the number of required tests. After conducting the DoE, a selected number of welding trials were conducted and the resultant welds' lap shear strength were measured. Models were created to predict evolution of the joint strength with both power and welding speed. Using identical parameters and conditions HBCNTs was predicted and also in practice produced stronger welds than CB and CW for all laser powers at the speed of 0.5 and 1 m min<sup>-1</sup>. The model predictions and the test results were always in agreement for CW where as the weld strength test data for CB were always much below the predicted values. Although CNT seemed superior in terms of weld strength it is anticipated that

CW will perform at very high power intensities due to its loss of absorption with increasing exposure time.

The melt depths for welds made using the three different samples at 45W and 0.5m min<sup>-1</sup> were examined. HBCNTs showed the largest melt depth at both surfaces, compared with CB and CW, this is because of HBCNTs' absorption characteristics focusing the heat at the interface, while their fibrous geometry and high thermal conductivity allows the transfer of this heat to a greater depth of the material. This interface absorption helps melting of the virgin polymer and creates more or less the same amount of melt in the upper surface. The melt depth is slightly compromised when using CB at the same concentration due to their shape (agglomerated particles as opposed to fibres) and poorer thermal conductivity. For CW at the same concentration the interface absorption is not as good as the other two and significant amounts of the beam energy still transmit through the lower sample causing more uniform bulk heating but not generating large amounts of molten polymer in the top surface.

## Conclusions

MWCNTs are efficient absorbers of near infrared radiation, where the absorbed radiation is effectively and instantaneously converted into heat. The instantaneous heating of MWCNTs when irradiated by a laser is due to the excited electron-phonon coupling, which happens at picosecond time-scales. The laser radiation interacts primarily with conduction  $\pi$  electrons and the photon energy of NIR radiation at 940nm ( $1.32\text{eV} > E_g$ ) would mean that it can interact with semiconducting tubes as it would with metallic tubes.

The interactions between all the individual processes are complex and can be described by the Boltzmann's non-equilibrium transport equation. However in simple terms the collision between electrons and photons, which is the joule heating effect that the 940nm wavelength laser's electric field has on the MWCNTs' electrons, is balanced by the rate of change of the electron energy, thermalisation of the electronic gas through electron-electron coupling, and coupling with lattice phonons through electron-phonon collisions, which leads to the heating of the lattice. The two main responses measured in this study (through transmission and heating) are not always directly dependent in all cases, because sometimes parts of the beam are extinct from the radiation field without being absorbed or contributing to the increase in total internal energy of the sample. The extinction is mainly due to scattering by impurities or by the out of phase simultaneous emissions.

The absorption properties of the carbon nanotubes are dependent on the orientation of the nanotubes and were generally enhanced for those beams that were polarized parallel to the tube axis. This is partly because of the  $\pi$  Plasmons directionality, which enhances absorption in tube bundles and is certainly the case for heat-treated graphitized tube bundles. These vibrations are in the order of 0.5 - 3 eV and enhanced absorption peaks have been observed at 1.2eV, which is the same as photonic energies of 940nm wavelength laser radiation. For tubes that had not been heat treated inter-tube tunnelling could take place, which meant that irradiation parallel and perpendicular to the tube axis gave similar heating results.

The amount of laser absorption and heating at 940nm is dependent on the structure of MWCNTs and their crystallinity, size, degree of imperfection and presence of impurities. Different treatment processes cause, structural and chemical changes that affect the physical properties of the MWCNTs. These include variation in their heat capacity and in-air oxidation temperature, as well as their behaviour in a laser radiation field. More crystalline structures, such as those that had been subjected to a heat treatment, have higher heat capacities and oxidation temperatures as opposed to samples with higher iron content and defect densities (qualitatively measured by the Raman  $I_D/I_G$  ratio). The MWCNTs were highly reactive towards either oxygen or water to the extent that parts of their structure (perhaps lattices with imperfections and vacancies or amorphous regions) can react with even very small amounts of oxygen or water as long as temperatures between 600-1000°C (depending on the post production treatment method used) are achieved and in some cases sustained for a period of time. Such species may exist as adsorbed or trapped molecules on or in between carbon nanotube bundles, or as contaminations in the otherwise inert test environment, for example due to impurities in the helium test gas. The process is further catalysed by the presence of iron impurities, which have remained in the MWCNTs from the CVD process.

Laser heating is dependent mainly on the crystallinity of the tubes and the degree of imperfection, with no dependence on tube diameter, as the 940nm wavelength is larger than an average MWCNT diameter by a factor of 10 and can be taken as constant across the diameter distribution. There is however some contribution to absorption and heating behaviour from the length of the tubes, particularly for those tubes with a length in the same order as the radiation wavelength. For example, HBCNTs have an average length of about 1µm, which is almost the same as the laser radiation wavelength used in this work and therefore enhances their absorption properties through resonance coupling. In general, more graphitic heat-treated tubes seem to have higher values of temperature change in a laser field than those that are less crystalline and contain more imperfections and impurities. There is however a dependence on the energy intensity and the exposure times; while more crystalline tubes perform better at shorter exposures and higher intensities, for longer exposure times structures with more defects seem to be more effective in generating heat. This is thought to be due to lower time dependant excitation

saturation thresholds for a given laser beam intensity for more crystalline tubes reaching equilibrium quicker and at lower temperatures in addition to their higher thermal conductivity. Remnant iron catalyst impurities or the vacancies left by removing metal particles during the purification process would act as trap centres for electrons or holes and at high temperatures photo-excited carriers become long-lived due to the repetition of the trapping and de-trapping processes. Therefore at longer exposure times those MWCNTs, which had less perfect crystalline structures (e.g. as-produced MWCNTs) would generate more heat when irradiated with a laser beam. An exception to this are the HBCNTs, which heat significantly better than other samples at all beam intensities and for all beam exposure times, due to their short length and the additional resonance absorption mechanism.

The laser energy transmission through different samples seems to increase with reduction in graphitisation; highly graphitic and crystalline structures are ideal for light absorption. This can be observed directly by plotting the resultant Raman  $I_D/I_G$  ratios (a qualitative measure of the amount of defects in the MWCNTs crystal structure) against transmission, and increase in transmission with increase in structural imperfections can be seen unless impurities are present. Impurities seem to also play a role in scattering of light due to their small sizes and therefore reduce the transmitted light intensity. When measuring the heat generated by the aligned tubes when irradiated with a laser beam of 2.7J energy at 940nm wavelength and pulse duration of 100ms, there was a correlation between the heat generated and the amount of distortion in the tubes or the bundles structure (i.e. the Raman  $I_D/I_G$  ratios). The heating efficiency seems to decrease with an increase in the amount of distortion for this short exposure times.

Efficient absorption of NIR by MWCNTs had optical-limiting characteristics when in matrices such as water or ethanol, where significant light scattering was observed. The effects in transmission experiments on the samples were contributed to by the optical properties of the absorbers as well as the thermal properties of the matrix and their mutual interactions, resulting in nonlinear scattering effects including micro-bubble formation. Only the optical properties of absorbers that could be dispersed in water and ethanol with minimal agglomerations (i.e. acid-treated samples) and CB, could be

examined. The structures of such MWCNTs are already altered by the acid treatment process. There is an influence of concentration on the absorption properties of the suspensions, particularly in ethanol. However, they behave differently when dispersed in water and a percolation threshold cannot be reached due to the continuous removal of the absorbers from the suspensions via the water-gas reaction. This was further confirmed by higher extinction coefficient values for suspensions in water than in ethanol.

MWCNTs laser heating can be controlled to disintegrate them to CO and H<sub>2</sub> in aqueous environments by inducing a water-gas reaction using a laser beam at a wavelength of 940nm with a 100ms pulse of 2.3J, which is close to the safe exposure thresholds of skin. The concept was further proven by removing MWCNTs from between layers of bacon without causing any visible damage or detectable temperature change in the bacon samples.

Laser irradiation of MWCNTs in water causes localised heating and initiation of water-gas removal of the tubes without any considerable increase in the surrounding temperature. This is a promising method of removing nanotubes from living tissue using laser radiation within permissible exposure limits. Therefore selection of a radiation with sufficient power to turn the nanotubes into gas, but not so much power and for such duration that it would exceed permitted doses for the skin in particular is essential. The skin tolerance curves and the relationship between tissue penetration and wavelength curves, coupled with the need to heat the nanotubes towards 1140°C led to the use of a 940nm NIR laser capable of illuminating an area of 0.88cm<sup>2</sup> at a power of 23 Wcm<sup>-2</sup>, which for a 100ms pulse was close to the published safe limits. The validity of the water-gas reaction model for carbon nanotubes was tested using MTGA in a water-saturated helium environment and showed that carbon nanotubes can undergo water gas reaction in water saturated environments. The mass spectroscopy analysis confirmed the by-products of this reaction as hydrogen and carbon monoxide. The amount of energy and the temperature needed for the tubes to undergo such a reaction depends on two main factors; one is the structure and degree of crystallinity and the other is the presence of remnant iron particles that could act as a catalyst for the reaction. Carbon nanotubes that were more crystalline and had been heat treated required longer dwell times at higher

temperatures to react with water. The tubes that had not been treated and carried remnant iron from the production process reacted with water at a temperature around 670°C. It was possible to initiate the water gas reaction in aqueous suspensions of ACNTs using a NIR laser beam. It seems that most of the energy absorbed by the tubes is re-radiated and only a small part of it is consumed to drive the reaction; therefore the reaction can be driven at very small energy inputs and potentially within safe exposure limits for skin. The overall temperature rise of the aqueous sample after heating the ACNTs is small following pulse and below the temperature threshold damage to tissue as was demonstrated by laser pulses on layers of bacon with dispersed water suspensions of ACNTs between them.

Last but not least high absorption and effective heat generation properties of HBCNTs allowed welding of thick semi-crystalline cross-sections of HDPE, which is otherwise very challenging using the TTLW process with same concentrations of other absorbers. The welds obtained were sensitive to the form of the absorber applied to the joint, with the best way of incorporating them into the joint being adding them to one of the substrates to be welded, which also ensures containment of these nanoparticles and mitigates any health and safety issues associated with the welding process. The most important welding parameters were laser power and speed; it was found that the weld strength in 3mm thick HDPE samples is proportional to the square of laser power divided by welding speed. A DoE, coupled with welding and mechanical testing, revealed that, when using identical parameters and conditions, HBCNTs produce much stronger welds than CB and CW for laser powers of 50W and higher. However the model predictions for welds produced by CB were did not coincide with actual test data and appeared to be overestimating the strength of the welds produced by this absorber. There was a consistent agreement between test data for CW and the prediction made by the model. It can be concluded that HBCNT will produce the strongest welds; however, for high power inputs CW will be more appropriate as it loses its absorption properties as it is heated and reduces the risk of excessive heat generation at a given point in the interface which can otherwise result in the degradation of the polymer. The melt depths for welds made at 45W and 0.5m min<sup>-1</sup> using the three different absorbers were examined by using microtome sections. HBCNTs showed the largest melt depth compared with CB and CW

because of their high absorption characteristics focusing the heat at the interface, while their fibrous geometry and high thermal conductivity allows the transfer of this heat to a greater depth of the material. The interface absorption also helps melting of the virgin polymer and creates more or less the same amount of melt both surfaces.

#### **6.10. Outlook**

Considering the remote removal of carbon nanotubes from tissue, initial indications are that soft tissue would scatter the radiation significantly, so that the dose per unit area would decrease with depth, in addition to any absorption. It was found that 5 mm of bacon reduced the transmitted intensity to 30% of the incident value. This scattering should be measured on more realistic tissue models; although if it proves to be significant at depths of the order of 1 cm or more, compensation may be achieved by using higher power beams spread over a greater area of skin but then focused using a Fresnel lens positioned at the skin surface or use of very short intense pulses. In addition, the radiation protocols associated with prescribed therapy are likely to be considerably more generous than the recommended limits for casual exposure used as a basis for the experiments reported here. The final point is more esoteric. Is there any point in replacing an embedded nanotube with a local area of burn trauma, and a few pico litres of hydrogen and carbon monoxide? The minute volume of gas produced ( $\sim 20 \text{ nL m}^{-1}$  of nanotube) would presumably disperse and would not be present in quantities that would be toxic to the body as a whole, the burn damage in the adjacent tissue is likely to be very local and in any case there will be a measure of protection by a steam jacket. The central point, however, is that the presence of bio-persistent fibrous nanoparticles in the body, as has been experienced in the case of asbestos, is highly undesirable as the long-term irritation leads to cells producing oxidative agents such as cytokines, which can trigger inflammation and possibly in the longer term, cancer. The removal of such an irritant species, albeit with some collateral tissue damage that the body can accommodate, may be seen as highly preferable to the possibility of a long-term triggering of abnormal cell growth. Work should be undertaken on cell cultures and tissue to assess the exact nature of the local damage associated with radiation removal of MWCNTs, as well as the applicability of the method more generally.

Secondly, the feasibility study undertaken here on the use of carbon nanotubes as infrared absorbers for through transmission laser welding has only scratched the surface for this application. Current world production capacity for carbon nanotubes is well in excess of 1000 tonnes per annum, and as the unit price continues to drop these materials will be at competitive prices with conventional absorbers such as carbon black. It is believed that through further development and process/material optimisation MWCNTs can be used routinely for fabrication of plastics parts, creating welds at lower energy input, with faster welding speeds and through thicker sections of polymer. The further developments required should be focused on firstly more controlled and consistent ways of introducing CNTs to the weld interface. Optimising a process such as spraying or preparation of thin films will introduce the absorbers at the weld and reduce the amount of material needed, most of which is currently wasted as redundant absorbers incorporated in the bulk of the material. The same will go for producing consistent qualities of MWCNTs, which will reduce batch-to-batch variation and provide confidence in the use of these materials. Better understanding of the absorption and heating effects in carbon nanotubes also needs to be developed based on responses of single nanotubes with different structures and properties, perhaps by using techniques such as atomic force microscopy.

## References

---

- [1] Yang, Z. P. et al., 2007, Experimental observation of an extremely dark material made by a low-density nanotube array, *Nano Letters*, 0, 0, A - F.
- [2] Nair, R. R. et al., 2008, Fine structure constant defines visual transparency of graphene, *Science*, 320, 1308.
- [3] Ajayan, P. M. et al., 2002, Nanotubes in a flash - ignition and reconstruction, *Science*, 296.
- [4] Kam, N. W. S. et al., 2005, Carbon nanotubes as multifunctional biological transporters and near-infrared agents for selective cancer cell destruction, *PNAS*, 102, 33, 11600–11605.
- [5] Panchapakesan, B. et al., 2005, Single-wall carbon nanotube nanobomb agents for killing breast cancer cells, *Nanobiotechnology*, 1, 133-139.
- [6] Cherukuri, P. et al., 2006, Mammalian pharmacokinetics of carbon nanotubes using intrinsic near-infrared fluorescence, *PNAS*, 103, 18882–18886.
- [7] Shao, N. et al., 2007, Integrated molecular targeting of IGF1R and HER2 surface receptors and destruction of breast cancer cells using single wall carbon nanotubes, *Nanotechnology*, 18, 31510-19.
- [8] Ferrari, M., 2005, Cancer nanotechnology: Opportunities and challenges, *Nature reviews. Cancer*, 5, 161-171.
- [9] Chakravarty, P. et al., 2008, Thermal ablation of tumor cells with antibody-functionalized single-walled carbon nanotubes, *PNAS*, 105, 8697-8702.
- [10] Porter, A. E. et al., 2007, Direct imaging of single-walled carbon nanotubes in cells, *Nature nanotechnology*, 2, 713- 717.
- [11] Zhao, Y. et al., 2008, Are carbon nanotubes safe? *Nature nanotechnology*, 3, 191-192.
- [12] Schipper, M. L. et al., 2008, A pilot toxicology study of single-walled carbon nanotubes in a small sample of mice, *Nature nanotechnology*, 3, 216 -221.
- [13] Agnes B. Kane and Robert H. Hurt, 2008, The asbestos analogy revisited, *Nature nanotechnology*, 3, 378 -379.

- 
- [14] Poland, C. A. et al., 2008, Carbon nanotubes introduced into the abdominal cavity of mice show asbestos like pathogenicity in a pilot study, *Nature nanotechnology*, 3, 423-428.
- [15] Concise Science Dictionary, 1996, Oxford University Press.
- [16] Spencer, M.S. 1995, On the activation energies of the forward and reverse water-gas shift reaction, *Catalysis letters*, 32, 9-13.
- [17] Goldstein, M. 2008, Carbon monoxide poisoning, *Journal of emergency nursing*, 34, 538-42.
- [18] Baibarac, M. and Romero, P. G., 2006, nanocomposites based on conducting polymers and carbon nanotubes from fancy materials to functional applications, *Journal of nanoscience and nanotechnology*, 6, -14.
- [19] Wang, C. et al., 2007, strong carbon-nanotube-polymer bonding by microwave irradiation, *Advanced functional materials*, 17, 12, 1979-1983.
- [20] Dosser, L. et al., accessed on int line 2009, Transmission welding of nanocomposites with direct diode and Nd:YAG solid state lasers, [http://www.mlpc.com/documents/laser\\_welding\\_carbon\\_nanocomposites.pdf](http://www.mlpc.com/documents/laser_welding_carbon_nanocomposites.pdf) [accessed 10 of January 2010].
- [21] <http://www.farinfrared.eu> [accessed 17<sup>th</sup> October 2010]
- [22] Callister, W.D., 2003, *Materials science and engineering an introduction*, 6th ed, New York, Wiley and Sons.
- [23] Park, D., 1964, *Introduction to the quantum theory*, San Francisco, Mc-Graw-Hill, INC.
- [24] Wilson, J. and Hawkes, J.F.B., 1987, *Lasers principles and applications*, Hertfordshire, Prentice Hall International (UK) Ltd.
- [25] Loudon, R. 1973, *The quantum theory of light*, Clarendon press Oxford, Oxford university press London.
- [26] Tolstoy, V.P. et al., 2003, *Handbook of infrared spectroscopy of ultra thin films*, New Jersey, Wiley and Sons.
- [27] *Quantum Mechanics*, D.I. Blokhintsev, D.Reidel Publishing Company, Dordrecht-Holland, 1964.

- 
- [28] Bertolotti, M., 1983, *Physical processes in laser-materials interactions*, New York, Plenum Press.
- [29] George. C. Baldwin, 1966, *An introduction to non-linear optics*, Plenum Press, New York, 1969
- [30] Savage, J.A., 1985, *Infrared optical materials and their anti reflection coating*, Bristol, Adam Hilger Ltd
- [31] Gang Chen, 2005, *Nanoscale energy transport and conversion*, Oxford, UK.
- [32] Rethfeld, B. et al., 2002, Ultrafast dynamics of nonequilibrium electrons in metals under femtosecond laser irradiation, *Physical Review B*, 65, 214303.
- [33] Zhibin Lin and Leonid V. Zhigilei, 2006, Thermal excitation of d band electrons in Au: implications for laser-induced phase transformations, *Proc. of SPIE*, 6261, 62610U-10.
- [34] Terrones, M., 2004, Carbon nanotubes: synthesis and properties, electronic devices and other emerging applications, *International materials reviews*, 49, 6, 325-377.
- [35] Dresselhaus, M.S. et al., 2005, Raman spectroscopy of carbon nanotubes, *Physics Reports*, 409, 47–99.
- [36] Saito, R. et al., 2005, *Physical properties of carbon nanotubes*, London, Imperial College Press.
- [37] Harris, P.J.F., 1999, *Carbon nanotubes and related structures. New materials for the twenty-first century*, Cambridge, Cambridge University Press.
- [38] Radhakrishnan, G. et al., 2006, *Thin solid films*, 515, 1142–1146.
- [39] Ebbesen, T. et al., 1992, Large-scale synthesis of carbon nanotubes, *Nature*, 358, 220–222.
- [40] Endo, M. et al., 1993, The production and structure of pyrolytic carbon nanotubes (PCNTs), *J. Phys. Chem. Solids*, 54, 1841–1848.
- [41] Thess, A. et al., 1996, Crystalline ropes of metallic carbon nanotubes, *Science*, 273, 483–487.
- [42] Sing, C. et al., 2002, Production of aligned carbon nanotubes by the injection chemical vapour deposition method, *Physica B*, 323, 339–340
- [43] Singh, C. et al., 2003, Production of controlled architectures of aligned carbon nanotubes by an injection chemical vapour deposition method, *carbon*, 41, 359–368.

- 
- [44] Boskovic, B. O. et al., 2002, Large-area synthesis of carbon nanofibres at room temperature, *Nature materials*, 1, 165-168.
- [45] Kingston, C.T. et al., 2004, Efficient laser synthesis of single-walled carbon nanotubes through laser heating of the condensing vaporization plume, *Carbon*, 42, 1657–1664.
- [46] Maruyama, S. et al., 2003, Synthesis of single-walled carbon nanotubes with narrow diameter-distribution from fullerene, *Chem. Phys. Lett*, 375, 553–559.
- [47] Geng, J. et al., 2002, Synthesis of high purity single-walled carbon nanotubes in high yield, *Chem. Commun.*, 2666–2667.
- [48] Bachilo, S. M. et al., 2003, Narrow (n,m)-distribution of single-walled carbon nanotubes grown using a solid supported catalyst. *J. Am. Chem. Soc.* 125, 11186–11187.
- [49] Koziol, K. et al., 2005, Three dimensional internal order in multiwall carbon nanotubes grown by chemical vapour deposition, *Advanced materials*, 17, (6), 760-763.
- [50] O’Connell, M. J. et al., 2005, Chiral selectivity in the charge-transfer bleaching of single-walled carbon-nanotube spectra, *Nature Materials*, 4, 412-418.
- [51] Paradise, M. and Goswami, T., 2007, Carbon nanotubes – Production and industrial applications, *Materials and design*, 28, 1477–1489.
- [52] Iijima, S. et al., 1992, Pentagon, heptagon and negative curvature in graphite microtubule growth, *Nature*, 356, 776-778.
- [53] Endo, M. and Kroto, H. W., 1992, Formation of carbon nanofibres, *J. Phys. Chem*, 96, (17), 6941-6944.
- [54] Lambin, P.R., 2003, Electronic structure of carbon nanotubes, *Physique*, 4, 1009–1019.
- [55] Sergei, M. et al., 2002, Structure-assigned optical spectra of single-walled carbon nanotubes, *Science*, 298, 2361-2366
- [56] Hamada, N. et al., 1992, New one-dimensional conductors: Graphitic microtubules, *Physical review letter*, 68, 10, 1579-1581.
- [57] Choi, J. et al., 2001, Electronic band dispersion of vertically aligned multiwall carbon nanotubes, *Chemical physics Letters*, 349, 185-190.
- [58] Fischer, J. E. et al., 1997, Metallic resistivity in crystalline ropes of single-wall carbon nanotubes, *Physical review B*, 55, 8, 4921-4924.

- 
- [59] Eklund, P. C. et al., 1995, Vibrational modes of carbon nanotubes; spectroscopy and theory, *Carbon*, 33, 7, 959-972.
- [60] Osman, M. A., and Srivastava, D., 2005, Molecular dynamics simulation of heat pulse propagation in single-wall carbon nanotubes, *Physical review B*, 72, 125413, 1-7.
- [61] Pimenta, M. A. et al., 2007, Studying disorder in graphite-based systems by Raman spectroscopy, *Phys. chem. chem. Phys.*, 9, 1276–1291.
- [62] Dresselhaus, M. S., et al., 2010, Perspectives on carbon nanotubes and graphene Raman spectroscopy, *Nano Lett.*, 10, 751–758.
- [63] Hayashi, Y. et al., 2005, Synthesis and characterization of metal-filled carbon nanotubes by microwave plasma chemical vapor deposition, *Diamond & related materials* 14, 790– 793.
- [64] Rao, A. M. et al., 1997, Diameter-selective Raman scattering from vibrational modes in carbon nanotubes, *Science*, 275, 187-191.
- [65] Benoit, J.M. et al., 2002, Low-frequency Raman studies of multiwalled carbon nanotubes: experiments and theory, *Phys. Rev. B*, 66, 073417.
- [66] Masarapu, C. et al., 2005, Specific heat of aligned multiwalled carbon nanotubes, *Nanotechnology*, 16, 1490–1494.
- [67] Rositani, F. et al., 1987, Infrared analysis of carbon blacks, *Carbon*, 25, 3, 325-332.
- [68] Mellouki, I. et al., 2007, IR characterization of graphite black-coating for cryogenic detectors, *Infrared physics & technology*, 50, 58–62.
- [69] Margulis, V.I. and Gaiduk, E.A., 2001, Nature of near-infrared absorption in single-wall carbon nanotubes, *Physics letters A*, 281, 52–58.
- [70] Kuhlmann, U. et al., 1998, Infrared active phonons in single-walled carbon nanotubes *Chemical physics letters*, 294, 237–240.
- [71] Ugawa, A. et al., 2001, Far-infrared to visible optical conductivity of single-wall carbon nanotubes, *Current applied physics*, 1, 45-49.
- [72] Kamara's, K. et al., 2006, Far- and mid-infrared anisotropy of magnetically aligned single-wall carbon nanotubes studied with synchrotron radiation, *Infrared physics & technology*, 49, 35–38.
- [73] Wang, F. et al., 2005, The optical resonances in carbon nanotubes arise from excitons, *Science*, 308, 838-840.

- 
- [74] O'Connell, M. J. et al, 2002, Band gap fluorescence from individual single-walled carbon nanotubes, *Science*, 297, 593–596.
- [75] Itkis, M.E. et al., 2006, Bolometric infrared photoresponse of suspended single-walled carbon nanotube films, *Science*, 312, 5772, 413 – 416.
- [76] Castrucci, P. et al., 2006, Large photocurrent generation in multiwall carbon nanotubes, *Applied physics letters*, 89, 253107, 1-3.
- [77] Wang, Y. et al., 2004, Receiving and transmitting light-like radio waves: Antenna effect in arrays of aligned carbon nanotubes, *Applied physics letters*, 85, 13, 2607-2609.
- [78] Liu, L. and Zhang, Y., 2004, Multi-wall carbon nanotube as a new infrared detected material, *Sensors and actuators A*, 116, 394–397.
- [79] Vivien.L et al, 2001, Pulse duration and wavelength effects on the optical limiting behavior of carbon nanotube suspensions, *Optics Letters*, 26, 4.
- [80] Vivien.L, et al, 2002, Carbon nanotubes for optical limiting, *Carbon* 40 , 1789–1797
- [81] Izard.N et al, 2005, Influence of structure on the optical limiting properties of nanotubes, *optics Letters*, 30, 12, 1509.
- [82] Adrian Bejan and Allan D. Kraus, 2003, *Handbook of heat transfer*, Chapter 9: Boiling by John R Thome, John Wiley & Sons.
- [83] Lin, M. F. et al., 1999, Optical properties of well-aligned multiwalled carbon nanotube bundles, *Physical review B*, 61, 14114-14118.
- [84] Absorption spectroscopy of individual single-walled carbon nanotubes Stéphane Berciaud,<sup>a</sup> Laurent Cognet,<sup>a</sup> Philippe Poulin,<sup>b</sup> R. Bruce Weisman,<sup>c</sup> and Brahim Lounisa\*
- [85] William.Q, 2002, Theory of plasmons in carbon nanotube bundles, *Condens. Matter* 14 5239–5253
- [86] Kempa.K, 2002, Gapless plasmons in carbon nanotubes and their interactions with phonons, *Physical Review B* 66, 195406.
- [87] Young Lim.K et al, 2003, Laser Pruning of carbon nanotubes as a route to static and movable structures, *Advanced materials*, 15, 3.
- [88] Chiong Cheong.F et al, 2003, Large area patterned arrays of aligned carbon nanotubes via laser trimming, *Institute of physics publishing nanotechnology* 14, 433–437

- 
- [89] Singh, G. et al., 2007, Laser-induced exfoliation of amorphous carbon layer on an individual multiwall carbon nanotube, *Applied physics letters* 91, 033101.
- [90] Shirk, M.D., and Molian, P.A., 2001, Ultra-short pulsed laser ablation of highly oriented pyrolytic graphite, *Carbon*, 39, 1183–1193.
- [91] Joseph, M. et al., 2002, High temperature vapour pressure studies on graphite using laser pulse heating, *Carbon. letters to the editor*, 40, 2021 –2040.
- [92] Bassil, A. et al., 2006, Controlled laser heating of carbon nanotubes, *Applied physics letters*, 88, 173113, 1-3.
- [93] Dumitrica, T. et al., 2006, Breathing coherent phonons and caps fragmentation in carbon nanotubes following ultrafast laser pulses, *Physical review B*, 74, 193406, 1-4.
- [94] Ahir, S. V. et al., 2006, Infrared actuations in aligned polymer-nanotube composites, *Physical review B*, 73, 085420.
- [95] Jiang, H. et al., 2004, Thermal expansion of single wall carbon nanotubes, *Journal of engineering materials and technology*, 126, 265-270.
- [96] Petr, K., 2002, Nanoscale processing by adaptive laser pulses, *Physical review B*, 66, 241401, R, 1-4.
- [97] Lu, Y. et al., 2005, Nanoparticle-enhanced laser micromachining of polymeric nanocomposites, *Transactions of NAMRI/SME*, 33, 249.
- [98] Hertel, T. and Moos, G., 2000, Electron-phonon interaction in single-wall carbon Nanotubes: A time-domain study, *Physical review letters*, 84, (21),5002-5005.
- [99] Cronin, S. B. et al., 2006, Temperature dependence of the optical transition energies of carbon nanotubes: The role of electron-phonon coupling and thermal expansion, *Physical review letters*, 96, 127403.
- [100] Castro Neto, A. H. and Guinea, F., 2006, Electron-phonon coupling and Raman spectroscopy in disordered graphene, *Cond-Mat*, 3, 0608543, 1-4.
- [101] Yin, Y. et al., 2007, Optical determination of electron-phonon coupling in carbon nanotubes, *Physical review letters*, 98, 037404, 1-4.
- [102] Ago, H. et al., 1999, Work functions and surface functional groups of multiwall carbon nanotubes, *J. Phys. Chem. B*, 103, 8116-8121.

- 
- [103] Purcell, S. T. et al., 2002, Hot nanotubes: stable heating of individual multiwall carbon nanotubes to 2000 K induced by the field-emission current, *Physical review letters*, 88, 105502, 1-4.
- [104] Keidar, M. et al., 2006, Current-driven ignition of single-wall carbon nanotubes, *Letters to the editor / Carbon*, 44, 1013–1024.
- [105] Chiu, Y. H. et al., 2005, Ballistic phonon thermal transport in multiwalled carbon nanotubes, *Physical review letters*, 95, 226101, 1-4.
- [106] Adam, W. et al., 2007, Direct observation of Mode Selective electron-phonon coupling in suspended carbon nanotubes, *Nano letters*, 7, 12, 3618-3622.
- [107] Windle, A., 2007, Part III undergraduate course M6 Lecture 9: polymeric materials and carbon nanotubes.
- [108] Koziol, K., 2006, Carbon nanotube polymer scaffolds, PhD thesis, Department of Materials and Metallurgy, University of Cambridge, UK.
- [109] Andrews, R. et al., 2001, Purification and structural annealing of multiwalled carbon nanotubes at graphitization temperatures, *Carbon*, 39, 1681–1687.
- [110] Yudasaka, M. et al., 2001, Diameter enlargement of HiPco single-wall carbon nanotubes by heat treatment, *nano letters*, 1, 9, 487-489.
- [111] Katayama, T. et al., 2002, Multiwalled carbon nanotubes with bamboo-like structure and effects of heat treatment, 91, 10.
- [112] Shaffer, M. S. P. et al., 1998, Dispersion and packing of carbon nanotubes, *Carbon*, 36, (11), 1603–1612.
- [113] Barone, P. W. et al., 2005, Near infrared optical sensors based on single-walled carbon nanotubes, *Nature materials*, 4, 86-92.
- [114] Sandler, J. et al., 1999, Development of a dispersion process for carbon nanotubes in an epoxy matrix and the resulting electrical properties, *Polymer*, 40, 5967–5971.
- [115] Martin, C.A. et al., 2004, Formation of percolating networks in multi-wall carbon-nanotube-epoxy composites, *Composites science and technology*, 64, 2309–2316.
- [116] Zhang, J. and Gao, L., 2007, Dispersion of multiwall carbon nanotubes by sodium dodecyl sulfate for preparation of modified electrodes toward detecting hydrogen peroxide, *Materials letters*.

- 
- [117] Chakrapani, N. et al., 2004, Capillarity-driven assembly of two-dimensional cellular carbon nanotube foams, PNAS, 101, 12, 4009–4012.
- [118] Ahn, K. S. et al., 2004, In-situ rf plasma treatment of multi-wall carbon nanotubes with various reactive gases for enhanced field emission, Journal of the Korean Physical Society, 45, 1, 154-157.
- [119] Shaoming Huang and Liming Dai, 2002, Plasma etching for purification and controlled opening of aligned carbon nanotubes, J. Phys. Chem. B, 106, 3543-3545.
- [120] Lu, K. L. et al, 1996, Mechanical damage of carbon nanotubes by ultrasound, Carbon, 34, 6, 814.
- [121] Chakrapani, N. et al., 2004, Capillary-driven assembly of two-dimensional cellular carbon nanotube foams, PNAS, 101, . 4009-4012.
- [122] Matranga.C et al, 2003, Trapped CO<sub>2</sub> in carbon nanotube bundles, J. Phys. Chem. B, 107, 12930-12941,
- [123] Smith. M.R.Jr, 2003, Selective oxidation of single-walled carbon nanotubes using carbon dioxide, Carbon 41, 1221–1230.
- [124] Phys.J, 2005, Adsorption on carbon nanotubes studied using polarization-modulated infrared reflection-absorption spectroscopy, 109, 9970-9979.
- [125] <http://en.wikipedia.org/wiki/Carbon> [accessed the 5th of April 2010].
- [126] Lucas, A.A. et al., 2002, Colloquium: Optical simulations of electron diffraction by carbon nanotubes, Review of modern physics, 74, 1-10.
- [127] Leonard C. Thomas, Making accurate DSC and MDSC specific heat capacity measurements with the Q1000 Tzero DSC, TA Instruments, 109 Lukens Drive, New Castle DE 19720, USA.
- [128] Braidy.N et al, 2002, Oxidation of Fe nanoparticles embedded in single-walled carbon nanotubes by exposure to a bright flash of white light, Nano Lett., 2, 11.
- [129] Blaine, R. L. and Hahn, B. K., 1998, Obtaining kinetic parameters by modulated thermogravimetry, Journal of Thermal Analysis, 54, 695-70.
- [130] Xiaowei, L. et al., 2004, effect of temperature on graphite oxidation behaviour, nuclear engineering and design, 227, pp. 273-280.
- [131] Jean-Baptiste, D. et al., 1993, Carbon black science and technology, 2nd ed, New York, Marcel Dekker Inc.

- 
- [132] McKenzie, A. L. , 1990, Physics of thermal processes in laser-tissue interaction, Phys. Med. Biol., 35, 9, 1175-1209.
- [133] Boulnois, J. L., 1986, Photophysical processes in recent medical laser developments: a Review, Lasers in medical science © Bailliere Tindall, 1, 47-65.
- [134] Huang, X. et al., 2006, Cancer cell imaging and photothermal therapy in the near-infrared region by using gold nanorods, J. AM. CHEM. SOC., 128, 2115-2120.
- [135] Parish, J. A. and Anderson, R. R., 1983, Selective photothermolysis: Precise microsurgery by selective absorption of pulsed radiation, Science, new series, 220, 4596, 524-527.
- [136] Loo, C. et al., 2004, Nanoshell-enabled photonics-based imaging and therapy of cancer, Technology in cancer research & treatment, 3, 1, 33-40.
- [137] O'Neal, P. D. et al., 2004, Photo-thermal tumor ablation in mice using near infrared-absorbing nanoparticles, Cancer etters, 209, 71–176.
- [138] Kalra, A. et al., 2003, Osmotic water transport through carbon nanotube membranes, PNAS, doi:10.1073/pnas.1633354100.
- [139] Maniwa, Y. et al., 2007, Water-filled single-wall carbon nanotubes as molecular nanovalves, Nature materials, 6, 135-141.
- [140] Hummer, G. et al., Water conduction through the hydrophobic channel of a carbon nanotube, Nature, 414, 188-190.
- [141] McKenzie, A. L., 1990, Physics of thermal processes in laser-tissue interaction, Phys. Med. Biol., 35, 9, 1175-1209.
- [142] Nukiyama, S., 1934, The maximum and minimum values of heat Q transferred from metal to boiling water under atmospheric pressure, journal Japan Soc. Mech. Engrs 37, 367-374.
- [143] H. J. Ivey and D. J. Morris, 1962, AEEW-R Report 137.
- [144] Lienhard, J. H. and Dhir V. K. J., 1973, Heat Transfer 95, 152-158.
- [145] S. Glod et al, 2002, Int J. of Heat and Mass Transfer, 45. 367-379.
- [146] Kotz, C.J. Treichel, P. and Townsend, J.R., 2009. *Chemistry and chemical reactivity*. vol 2. Belmont California: Thompson Brooks.
- [147] Dorin B, et al., 2008, temperature measurement of carbon nanotubes using infrared thermography, Chem. Mater, 20, 4011-4016.

- 
- [148] Balberg I, Anderson CH, Alexander S, Wagner N. 1984, Excluded volume and its relation to the onset of percolation. *Phys Rev B*, 30, 7, 3933–43.
- [149] Paton, K. R and Windle, A. H., 2008, Efficient microwave energy absorption by carbon nanotubes, *Carbon*, 46, 1935-1941.
- [150] Carroll, D., 2008, Novel carbon nitride nanowire (CNW) conjugates for breast cancer treatment, U.S. army medical research and materiel command report, W81XWH-06-1-0681.
- [151] Der Ho, W., et al., 2005, Resonant frequency analysis of fixed-free single-walled carbon nanotube-based mass sensor, *Sensors and actuators A*, 126, 117–121.
- [152] TSeeger et al, 2003, Evolution of multiwalled carbon-nanotube/SiO<sub>2</sub> composites via laser treatment, *Nanotechnology*, 14, 184–187.
- [153] Potente, H. et al., 1997, Laser-transmission welding of PE-HD, *Kunststoffe*, 87, 3, 348-350.
- [154] <http://www.twi.co.uk/content/ksab002.html> [accessed, 25th of April. 2010]
- [155] Jones I and Wise R, 1998: 'Welding Method'. EP1117502.
- [156] Jones, I. A. and Olden, E. 2000, A thermal model for transmission laser welding of thermoplastic polymers, 77429.01/2000/1065.03, 1998-2000 CRP Programme 9805-9.
- [157] Readdy, A. F, 1973. *Plastics fabrication by ultraviolet, infrared, induction, dielectric and microwave radiation methods*, Plastics technical evaluation centre.
- [158] S Rostami and I A Jones, 2003, Process guidance and software for Clearweld®, TWI report 13205.02/03/1168.2.
- [159] M. Bystrzejewski, M. et al., 2010, Dispersion and diameter separation of multi-wall carbon nanotubes in aqueous solutions, *Journal of colloid and interface Science*, 345, 136-142.
- [160] Shercliff H R and Ashby M F: 'The Prediction of case depth in laser transformation hardening:'. *metallurgical transaction A*, volume 22A, 2469, 1991.
- [161] Dos Santos, W. N., 2007, Thermal properties of polymers by non-steady-state techniques, *Polymer Testing*, 26, 556–566.
- [162] Kennish, Y.C. et al, 2002, Heat flow model for laser welding of polymers, ANTEC, the society of plastic engineers 60th annual conference, Sanfrancisco, USA.